The effect of geometric frustration on some correlated electron systems

By

Rajarshi Tiwari

PHYS08200605004

Harish-Chandra Research Institute, Allahabad

A thesis submitted to the

Board of Studies in Physical Sciences

In partial fulfillment of requirements

for the Degree of

DOCTOR OF PHILOSOPHY

of

HOMI BHABHA NATIONAL INSTITUTE

June, 2013

STATEMENT BY AUTHOR

This dissertation has been submitted in partial fulfillment of requirements for an advanced degree at Homi Bhabha National Institute (HBNI) and is deposited in the Library to be made available to borrowers under rules of the HBNI.

Brief quotations from this dissertation are allowable without special permission, provided that accurate acknowledgement of source is made. Requests for permission for extended quotation from or reproduction of this manuscript in whole or in part may be granted by the Competent Authority of HBNI when in his or her judgment the proposed use of the material is in the interests of scholarship. In all other instances, however, permission must be obtained from the author.

Thesis Author:

Rajarshi Tiwari

DECLARATION

I, hereby declare that the investigation presented in the thesis has been carried out by me. The work is original and has not been submitted earlier as a whole or in part for a degree/diploma at this or any other Institution/University.

Thesis Author:

_____

Rajarshi Tiwari

Place: ALLAHABAD, INDIA

Date:

Certificate

This is to certify that the Ph.D. thesis titled "**The effect of geometric frustration on some correlated electron systems**" by **Rajarshi Tiwari** is a record of bonafide research work done under my supervision. It is further certified that the thesis represents independent and original work by the candidate.

Thesis Supervisor:

_____

Prof. Pinaki Majumdar

Place: ALLAHABAD, INDIA

Date:

Acknowledgments

Academic: Inspiring through arguments, warning through outcomes, and training for Life (one of his lesser known traits), could be the best description of my advisor. One thing I like about him the most is, his persistence to push my thought process in the right direction. With these compliments, I thank Prof. Pinaki Majumdar for his guidance and support through all these years, part of which led to this thesis.

I thank Prasenjit Sen, for his amazing course on numerical methods, from where large fraction of my programming experience originates. I would also like to thank the members of the condensed matter group, Sumathi Rao, G. V. Pai, T. P. Pareek for what I learnt from them. Interactions with Jayanti, Sudhir Gupta, Shashank Shalger, Anamitra, Kalpataru, Arijit Saha, Bindusaar, Prabuddha, Viveka Nand, Sanjay Amritiya, Girish, Nishita, Shailesh, Sanjoy Dutta, Saurabh, abhishek Joshi, Udit Khanna, Aditya, Utkarsh, Krishamohan, Uttam, Rishu, Siddharth on physics, computation, mathematics and life were blessings. I am thankful to my school friend Mukul Anand, to keep pushing me to go into science. I am thankful to the book seller in Jaunpur besides Nagar Palika inter college, who accidently made me opt science, as he said, and I quote "Go for science, you may become a Doctor, else you will be a conductor!". I am in debt to Vivek Tiwari from AU, for being a friend, and a trusted counselor. I am thankful for the HPC clusters at HRI, on which all the numerical calculations relevant to this thesis were done.

Administrative: I thank the administration of HRI, for their help and support. The administration here has a distinctive image of a human resource, that is not only helpful and cooperative, it actually gives you a feel of being at home among family. I specially thank Ravindra Singh, Yashpal Bhadauriya, Ajay Srivastava, Umakant Dwivedi, Amit Roy, Raj Gulati, Archana Tandon, Seema Agrawal, Amit Kulve, Anoop, Sanjeev, Pradeep (Pantry), and Saadhu for their help and support.

Social life Life at HRI represents a nice combination of freedom and responsibility. It gave me a lot of experience apart from physics, ranging from fun loving endavours like interest in computer programming, Hindi literature, writing poems in *shamshaan*: "शमशान् में बुझती लकड़ियों को देखता रहा, मुझको बवक़्त मेरा गुनाह याद आ गया।" to some of the very heavy responsibilities like organizing the marriage of my sister, and later my own. This wasn't possible without Nani ji, Mama ji, and my friends Rawan (Ram Lal Awasthi), Krodhi (Vikas Chauhan), and Yashpal, Ajay, Umakant, and Pradeep (Pantry).

My advisor Pinaki, my late mother, my maternal uncle *Laloo mama*, my maternal gandmother Kalyani Devi, Rawan and my wife Priyanka have been the source of my wisdom, and my conscience. Nobody else, has been able to tolerate me, and stay with me in my worse days.

To my mother

Shashi Bala Tiwari

Her favourite quote

ऐ मालिक तेरे बंदे हम,
ऐसे हों हमारे करम।
नेकी पर चलें और बदी से टलें,
ताकि हंसते हुए निकलें दम।

CONTENTS

The effect of geometric frustration on some correlated electron systems

Synopsis

The notion of geometric frustration emerged originally in the context of Ising spins with antiferromagnetic nearest neighbour interaction on a triangular lattice. The classic solution by Wannier clarified how long range order is suppressed by frustration in this case. One can generalise the situation to frustrated structures in higher dimensions, *e.g*, the pyrochlore or the face centered cubic (FCC) lattices, where neighbouring spins live on a tetrahedral motif. Such models, and their classical and quantum Heisenberg versions, have been intensely studied.

Correlation physics, on the other hand, grew out of the continuing study of many body systems over the last several decades, with a fresh impetus given by the discovery of high T_c superconductivity in the doped Mott insulator $La_{2-x}Sr_xCuO_4$. This thrust the Mott transition and the doped Mott insulator centerstage. It quickly became apparent that a large family of oxides, including the magnetoresistive manganites, the high thermopower cobaltates, *etc*, owed their exotic properties to electron correlation. The development of powerful tools like dynamical mean field theory (DMFT) and its combination with *ab initio* methods has clarified many aspects of correlation physics over the last two decades.

Correlated systems involve metals systems with *itinerant* electrons, while traditional frustrated systems are insulating magnets with *localised* electrons. There are broadly two situations where they intersect:

- One may have a 'two species' system, of electrons and local moments, where the local moments live on a frustrated structure and are Kondo (or Hund's) coupled to itinerant electrons.

- We could have a Mott insulator in a frustrated structure and the consider its metallisation, due to decreasing interaction.

The first situation arises in Kondo lattice like, or 'double exchange', models, while the second is described by the Hubbard model. In both cases the ideal frustrated situation arises in the absence of itinerant electrons. The interest is in clarifying how the *presence* of electrons in the Kondo lattice, or the approach to the insulator-metal transition in Mott-Hubbard systems modifies the physics. The 'two species' description is appropriate for the pyrochlores (iridates, *etc*) and double perovskites, while the Hubbard model is relevant for materials like the cluster compound $GaTa_4Se_8$ and A_3C_{60}.

The thesis addresses the interplay of correlation effects and geometric frustration in three cases: (i) the metallic double perovskites, (ii) the triangular lattice Hubbard model for the κ-BEDT organics, and (iii) the Mott transition in the face centered cubic (FCC) lattice. It is organised as follows.

Chapter.1 provides a quick review of the twin areas of (i) geometric frustration in magnets, and (ii) correlation driven phenomena in electron systems. We then review the intersection of these two in the context of materials like (a) the κ-BEDT based triangular lattice organics, (b) the FCC based Mott materials like the Ga cluster compounds, $GaTa_4Se_8$, the fullerides A_3C_{60}, and the double perovskites, and (c) the pyrochlore iridates and molybdates. While each family has its peculiarity, we focus on the following generic features:

- Magnetism: long range order, spin freezing, or a spin liquid state,

- Resistivity and its temperature dependence near the IMT,

- Charge dynamics and spectral weight transfer near the IMT,

- Anomalous Hall response, where relevant.

The experimental summary is followed by a discussion of the minimal models that are used for the materials above. There are broadly two kinds of models:

$$
\begin{aligned}
H_{KLM} &= H_0 + J \sum_i \mathbf{S}_i.\vec{\sigma}_i \\
H_{Hubb} &= H_0 + U \sum_i n_{i\uparrow} n_{i\downarrow}
\end{aligned}
$$

In both cases H_0 defines the non interacting (band) problem. $\vec{\sigma}$ is the electron spin operator. H_{KLM} refers to a Kondo lattice model where the local moments $\mathbf{S}_i$ live on a frustrated lattice, while H_{Hubb} refers to the Hubbard model with electron repulsion U. The KLM is a 'two species' model, involving spins and fermions, while the Hubbard model just involves interacting electrons (at half filling in our case). For the KLM, the usual approach is to use Monte Carlo (assuming the spins to be classical) while the Hubbard model is solved via variational Monte Carlo, cellular DMFT, or some form of cluster perturbation theory. We review the major results, leaving the detailed discussion to later chapters.

Chapter.2 describes the models that we use and the computational strategy. In the KLM case when the spins $\mathbf{S}_i$ are treated as classical, their correlations are controlled by the distribution

$$
P\{\mathbf{S}_i\} \propto Tr_{c,c^\dagger} e^{-\beta H_{KLM}}
$$

This trace is not analytically computable at strong coupling (large J) and we use a exact diagonalisation based Monte Carlo to sample $P\{\mathbf{S}_i\}$. Electronic properties are computed by diagonalising H_{KLM} in the equilibrium configurations of $P\{\mathbf{S}_i\}$.

The Hubbard problem looks very different, and, beyond weak coupling, has traditionally been handled via quantum Monte Carlo and exact diagonalisation. Methods like DMFT also ultimately resort to these tools. These methods have a size limitation, despite the enormous increase in computing power over the decades, and are still not able to access complex magnetic states. We employed a Hubbard-Stratonovich

(HS) transformation to decouple the Hubbard interaction in terms of auxiliary charge (ϕ_i) and spin ($\mathbf{m}_i$) fields, retaining full rotation invariance. We neglect the time dependence of these fields, keep the charge field ϕ_i at its saddle point value $U/2$, but retain the full spatial fluctuations in the $\mathbf{m}_i$. The Hubbard problem now looks like:

$$H_{Hubb}^{eff} = H_0 - U \sum_i \mathbf{m}_i \cdot \vec{\sigma}_i + \sum_i \mathbf{m}_i^2$$

This can be solved by the same tools as for the KLM. Neglecting time dependence in the Hubbard case is *an approximation* and we check its validity against exact answers wherever available.

Chapter.3 discusses our results on possible *non ferromagnetic* phases in the metallic double perovskites. These are materials of the form $ABO_3.AB'O_3 \equiv A_2BB'O_6$. They usually involve a transition metal ion, B, with a large magnetic moment, and a non magnetic ion B′. While many double perovskites are ferromagnetic, studies on the underlying model reveal the possibility of antiferromagnetic phases as well *driven by electron delocalisation.* We present a comprehensive study of the magnetic ground state and T_c scales of the minimal double perovskite model in three dimensions using a combination of spin-fermion Monte Carlo and variational calculations. In contrast to two dimensions, where the effective magnetic lattice is bipartite, three dimensions involves a geometrically frustrated face centered cubic (FCC) lattice. This promotes non-collinear spiral states and 'flux' like phases in addition to collinear anti-ferromagnetic order. We map out the possible magnetic phases for varying electron density, 'level separation' $\epsilon_B - \epsilon_{B'}$, and the crucial B′B′ (next neighbour) hopping t'.

Chapter.4 makes a transition to the half-filled Hubbard model in two dimensions, defined on an anisotropic triangular lattice. This structure is like a square with one diagonal. The hopping along the axes is t, and along the diagonal it is t'. While we have studied the entire phase diagram in terms of anisotropy, interaction strength, and temperature, we focus on the anisotropy regime appropriate to the $\kappa-$BEDT based organics. We study the interaction driven crossover, which mimics the effect of pressure (or composition change) in the organics. We use bandstructure data and the measured transport gap to determine the electronic parameters and obtain a consistent description of magnetism and the resistivity. We uncover a pseudogap phase between the 'ungapped' metal and the 'hard gap' insulator, predict the momentum dependence of quasiparticle broadening and pseudogap formation, and clarify how these features arise from incommensurate magnetic fluctuations in this frustrated system. Beyond the organic Mott problem, we have mapped out the metal-insulator transition and pseudogap formation over the entire $U - t' - T$ parameter space.

Chapter.5 discusses the Mott transition and magnetic properties of the Hubbard model on the FCC lattice. Like triangular motifs in two dimensions, the tetrahedral motifs on the FCC lattice frustrate Neel order in the Mott insulator. We discover that the low temperature state is a paramagnetic metal at weak interaction, an

antiferromagnetic insulator (AFI) with flux like order at intermediate interaction, and an AFI with 'C type' order at very strong interaction. Remarkably, there is a narrow window between the paramagnetic metal and the AFI where the system exhibits spin glass behaviour arising from the presence of disordered but 'frozen' local moments. The spin glass state is metallic at weaker interaction but shows crossover to pseudogap behaviour and an insulating resistivity with growing interaction. We make a qualitative comparison of our results with trends observed in a broad class of FCC and pyrochlore based materials, and attempt a detailed quantitative match for the Mott transition in the FCC compound $GaTa_4Se_8$.

List of Publications/Preprints

1. *Non-collinear magnetic order in the double perovskites: double exchange on a geometrically frustrated lattice.*
   Rajarshi Tiwari and Pinaki Majumdar
   Int. J. Mod. Phys. B **27**, 1350018 (2013).

2. *Exchange interactions and magnetic phases of transition metal oxides: benchmarking advanced ab initio methods.*
   T. Archer, C. D. Pemmaraju, S. Sanvito, C. Franchini, J. He, A. Filippetti, P. Delugas, D. Puggioni, V. Fiorentini, R. Tiwari, and P. Majumdar
   Phys. Rev. B **84** 115114 (2011).

3. *Visualizing the Mott transition.*
   Rajarshi Tiwari and Pinaki Majumdar
   Curr. Sci. Vol. **103** No. 5, 518 (2012).

4. *The crossover from a bad metal to a frustrated Mott insulator*
   Rajarshi Tiwari and Pinaki Majumdar
   arXiv:1301.5026

5. *Mott transition and glassiness in the face centered cubic lattice.*
   Rajarshi Tiwari and Pinaki Majumdar
   arXiv:1302.2922

CHAPTER 1

INTRODUCTION

1.1 Overview of frustration and correlation

Geometric frustration in magnetism is best understood in the context of the nearest neighbour Ising antiferromagnet on a triangular lattice. Variants of this, involving triangular motifs in higher dimensions, quantum spins, and more complex interactions, define this well explored field. All these systems are 'insulators', with no relevant charge degrees of freedom, and the nature of spin-spin interaction is predefined (otherwise the notion of frustration itself becomes ambiguous).

Correlated systems, as we will use the term in the thesis, involve itinerant electrons. The magnetic degrees of freedom, independently present or self generated, couple to these electrons. For us the magnetic degrees of freedom will reside on a traditional 'frustrated' structure, but the interaction between them is not necessarily short range antiferromagnetic. In fact when the electron system is ungapped the magnetic interaction is effectively long range.

For us, the frustrated lattice mainly serves to rule out Neel order. We generally do not know the spin-spin interaction, and need to solve the electron problem '*ab initio*' to infer the magnetic state. This is where the focus of the present thesis differs from the mainstream of frustrated magnetism.

In what follows we review, successively, some of the general features associated with frustration, correlation effects, the combination of the two, and then aspects of double perovskite and Mott phenomenology relevant for us.
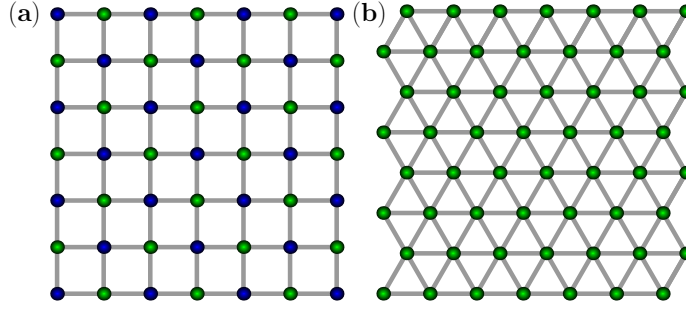
Figure 1.1: (a) The square lattice is bipartite as we can divide it into two sub-lattices, say blue and green, where neighbours of blue are only green (and vice versa). (b) In the triangular lattice such division is not possible.

1.1.1 Geometric frustration

To introduce the notion of geometric frustration let us start with the model of Ising spins ($\sigma_i = \pm 1$) on a lattice with nearest neighbour (NN) coupling J. The Hamiltonian is given by $E = J \sum_{ij \in NN} \sigma_i \sigma_j$. If $J < 0$ the ground state corresponds to all spins parallel, with total energy $E = -\frac{Nz|J|}{2}$, N being the number of lattice sites and z the number of nearest neighbours. Since $\frac{Nz}{2}$ is also simply the number of pair interactions, one says that in this ferromagnetic case all pairwise interactions are satisfied in the ground state.

When $J > 0$, one may naively expect that the ground state would correspond to all NN pairs being *anti-parallel*. However, in contrast to a ferromagnet, such an antiferromagnetic state may not exist for a given lattice. The existence of such a state in a lattice, with all pairwise interactions satisfied, is possible only when the lattice sites can be divided into two disjoint subsets (or sub-lattices) such that all neighbours of a site in one set belong to the other set. This is a geometric property of the lattice, and when it is satisfied we call the lattice bipartite. The nearest neighbours of a given site in such a lattice *are not themselves nearest neighbours of each other*, so a spin arrangement exists in which all NN pairs are anti-parallel. This state is the Neel antiferromagnet. It can occur, for example, on a square lattice (Fig.1.1(a)), and a simple cubic lattice.

A contrast is provided by the triangular lattice (Fig.1.1(b)), where the nearest neighbours of a given site are also themselves nearest neighbours. This prevents division of the lattice into two sub-lattices, the lattice is *non-bipartite*. Additional examples are the face centered cubic (FCC) lattice and pyrochlore lattice. On such a lattice, it is geometrically impossible to satisfy all the pairwise interactions, i.e., to have a Neel state. This situation where not all pairwise interactions can be satisfied,
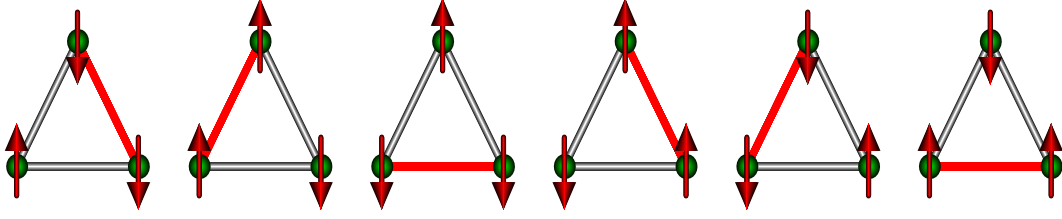
Figure 1.2: Possible anti-parallel arrangements in a three spin system. The sites are denoted by green circles, and spins by arrows. Each configuration has two satisfied bonds (gray line) and one unsatisfied bond (thick red lines).

due to lattice geometry, is called geometric frustration.

If not the "saturated" state, what kind of low energy magnetic configurations are available in a geometrically frustrated system? While this is a difficult question for an infinite lattice, let us look at the toy problem of three Ising spins with $J > 0$, Fig.1.2. There are six possible configurations with the lowest energy $E = -J$, shown in the figure, and in each of them one pair has parallel spins. With all bonds satisfied the lowest energy would have been $E = -3J$, instead of $-J$. Besides, the three site system has 6 fold degeneracy. The degeneracy of the ground state grows with system size. The classic solution of the Ising model on a triangular lattice, by Wannier [1] in 1950, clarified the following

1. The ground state energy of the antiferromagnetic triangular lattice Ising model is one third of the ferromagnetic case.

2. There is no singularity in the temperature derivative of the energy, i.e., specific heat, hence there is no 'Curie point'.

3. There is no long range order, the system is disordered at all temperatures.

4. The entropy at $T = 0$ is *finite* ($\frac{S(0)}{R} = \frac{2}{\pi} \int_0^{\pi/3} \ln(2\cos\omega)d\omega = 0.3383$).

Three years later, Kano *et al* [2], showed similar results for Ising spins on a Kagome lattice. In Fig.1.3 the total energy as function of temperature, calculated by Wannier is shown for the triangular lattice (left), while the right panel shows the Kagome result. For the ferromagnetic case, there is sharp decrease in the total energy, near a 'Curie point' T_c where the derivative, i.e., the specific heat has a singularity. For the antiferromagnetic case, however, the energy varies slowly, so the specific heat has a broad maximum instead of any singularity.

The phase diagram of the Ising model with nearest neighbour (J_1) and next neighbour (J_2) couplings, on the centered square lattice [3] and the Kagome lattice
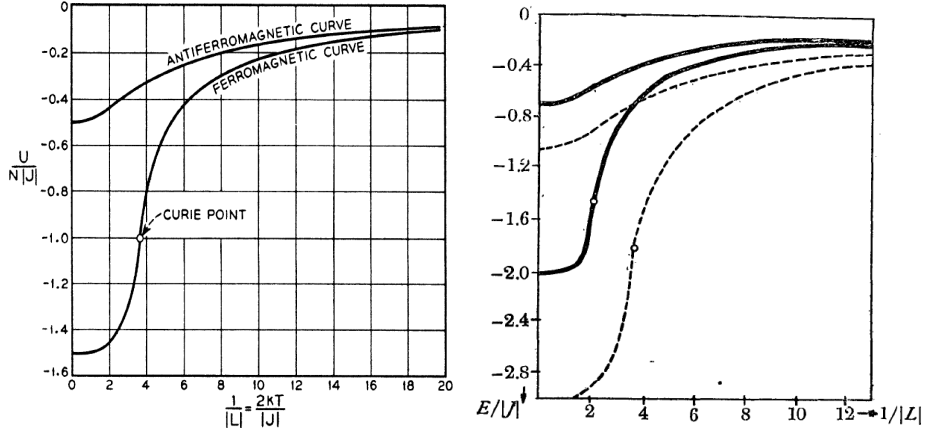
Figure 1.3: Temperature dependence of total energy for Ising systems. Left: Triangular lattice, from Wannier [1]. The lower(upper) curve is for ferromagnetic (antiferromagnetic) case. Right: Kagome lattice from Kano *et al* [2]. The solid set of lower(upper) curve is for ferromagnetic (antiferromagnetic) case, while the dotted curves are corresponding triangular lattice results.
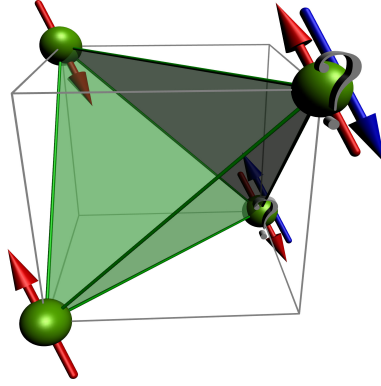
Figure 1.4: The tetrahedral unit, building block of the FCC and pyrochlore lattices.

[4], are shown in Fig.1.5. The centered square lattice shows non-monotonic phase boundary, where there is a 'reentrance' of AF phase between ferromangetic and paramagnetic phase. In Kagome lattice, the phase boundary is between ferromagnet and a *partially disordered* phase, in which central spins (blue dots) are free, with bigger reentrance window. The paramagnetic phase in the Kagome lattice also has two different kind of spatial fluctuations [5] probed via a spin glass order parameter proposed in [6], where one calculates overlap function $q_{\alpha,\beta} = \sum_1^N \langle\sigma_i\rangle_\alpha \langle\sigma_i\rangle_\beta / N$ and probability distribution for q, $P(q) = \sum_{\alpha,\beta} P_\alpha P_\beta \delta(q - q_{\alpha,\beta})$. The boundary of these two disordered phases is shown by the dotted line. This line is referred to as 'disorder line'. Reentrance, multiple thermal transition, and the presence of 'disorder line' has been seen in other models too. They are believed to be generic features of frustrated
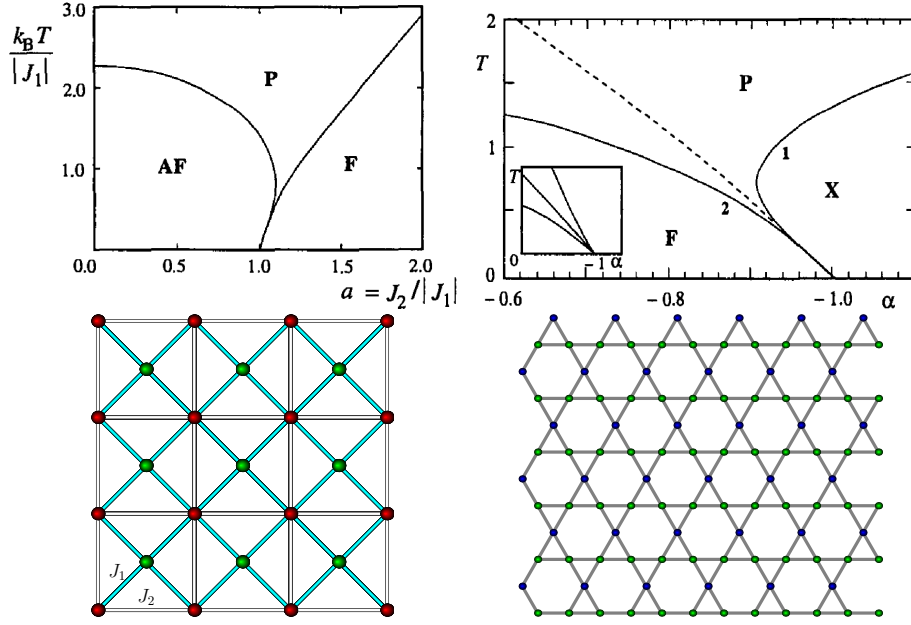
Figure 1.5: Temperature versus α $(= J_2/J_1)$ phase diagram for the antiferromagnetic Ising model on the centered square lattice [3] (left) and the Kagome lattice [4] (right). F, AF, P and X are respectively ferromagnet, antiferromagnet, paramagnet and partially ordered. Taken from Diep, *et al* [7]. The structure of the lattice are shown in the bottom.

systems in two and three dimensions. In three dimensions for the pyrochlore or the face centered cubic (FCC) lattices the neighbouring spins live on a tetrahedral motif (Fig.1.4) involving four triangular faces.

In case of classical Heisenberg spins (unit vectors) with AF coupling on a frustrated structure the total energy may be minimised by non-collinear or non-coplanar spin arrangements. While the Neel state cannot occur, the angular variables can allow other forms of long range order to occur. For example, on the triangular lattice one finds the well known 120^0 arrangement (Fig.1.6), and on the FCC lattice (where the ground state is actually degenerate) a 'C-type' phase is selected by thermal fluctuations. However, in many lattices like Kagome, checkerboard, and pyrochlore [8,9], the geometric frustration is more severe, and it prevents any long range order of the AF coupled NN Heisenberg model.

In these cases, when the ground state fails to sustain long range order, it may have disordered spin arrangements, with short range AF correlations, *e.g*, spin glasses or spin liquids. In a spin glass, below a certain temperature referred as 'glass transition temperature' or 'freezing temperature', T_g, the relaxation time of the spins diverges, and the spins are locked in a static random orientation. In the presence of quantum

Figure 1.6: The non-collinear 120^0 phase.

fluctuations these random orientations are no longer static, and result in spin liquid. In case of pyrochlores even the classical spins have $T_g \to 0$, an unusua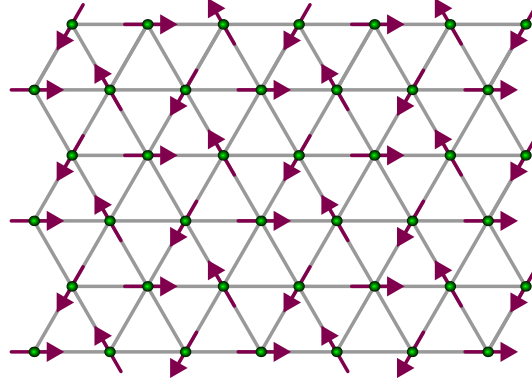l state referred as 'classical spin liquid' [8,9]. These situations, both in their classical and quantum versions, have been intensely studied [7–11].

While the triangular lattice with classical Heisenberg spins supports an ordered ground state, Fig.1.6, the Kagome lattice and the pyrochlore lattice, for example, do not. In these cases the Hamiltonian can be written as a sum of squares of the total spin, $\mathbf{S}_{tot}$, of individual units (tetrahedron in pyrochlore, and triangles in Kagome), which share only one vertex. The ground state is obtained by minimizing $\mathbf{S}_{tot}$ for every unit. This fixes relative angles within the unit but not the angles between neighbouring units, leading to a large ground state degeneracy due to this local freedom. In the Kagome lattice thermal fluctuations select a coplanar configuration [10, 11].

What about quantum effects? For a pair of *quantum* spins, with AF Heisenberg coupling, the ground state is anyway not a 'up-down' configuration but a singlet, *i.e,* a specific linear combination of the 'up-down' and 'down-up' states. Consider three quantum spins on a triangle with AF Heisenberg coupling. The ground state is four fold degenerate, with energy $-\frac{3}{2}J$, instead of six fold degenerate as in the classical Ising case with energy $-J$. These states are also linear combinations of 'up-down-up' states like $\frac{1}{\sqrt{2}}(|+-+\rangle - |-++\rangle)$, $\frac{1}{\sqrt{2}}(|+--\rangle - |-+-\rangle)$ etc. In the context of a lattice, quantum fluctuations of this kind allow the system to partly overcome the loss in energy due to classical frustration.

The quantum $S=\frac{1}{2}$ nearest neighbour Heisenberg antiferromagnet orders (at $T = 0$) on both the square and triangular lattice [12], though the order parameter is reduced by 40% and 50% respectively, compared to the classical result. The Kagome lattice is more frustrated than the triangular lattice [12–16].

28
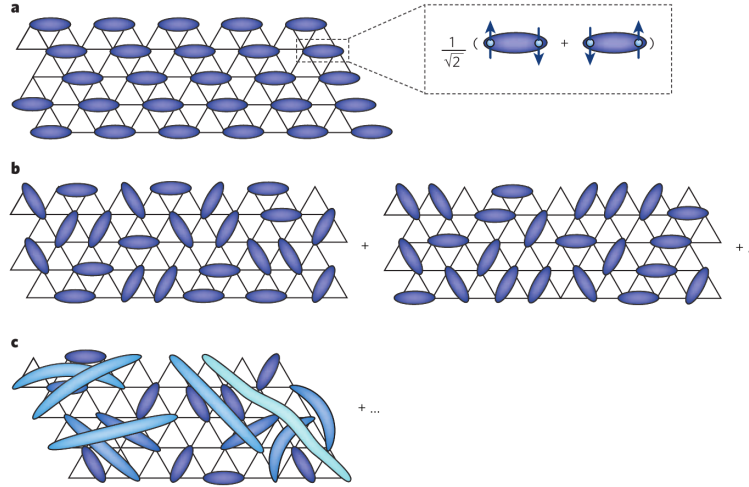
Figure 1.7: Cartoon of a valence bond crystal on the triangular lattice. (a) A regular arrangement of singlet bonds where blue ellipses denote the singlets. An RVB state is a superposition of many configurations of bond, which could be among (b) near neighbours, or (c) long distance apart. (From Balents [78])

Unusual ground states may also arise. The simplest object is a valence bond crystal (VBC), consisting of product of pairwise singlets of neighbouring spins (shown as cartoon in Fig.1.7.):

$$|(a,b)\rangle = \frac{1}{\sqrt{2}} \left(|a+\rangle|b-\rangle - |a-\rangle|b+\rangle \right)$$

In a valence bond two spins are maximally entangled. In the VBC, the state consists of static localized valence bonds, in which each spin is entangled with only one other. Several materials exhibit a VBC state [17–19], and are interesting as they provide an experimental way of studying Bose-Einstein condensation of magnons (which are triplet excitations of the singlet valence bonds) in the solid state. When these valence bonds are allowed to undergo quantum fluctuations, the ground state is a superposition of different pairings of spins into valence bonds (Fig.1.7(c)). If the distribution of these partitionings is broad, then there is no preference for any specific valence bond and the state can be regarded as a valence-bond 'liquid' rather than a crystal. This is generally called a resonating valence-bond (RVB) state [20].

The quantum Heisenberg antiferromagnet on checkerboard lattice shows long range plaquette order [21–23] at isotropic coupling while the Kagome antiferromagnetic is a spin liquid [12–16].

1.1.2 Electronic correlation

Electrons in a solid interact with each other and with the lattice vibrations. In case of narrow band materials, where a tight binding approximation is appropriate, short range repulsion between electrons may have important effects on electronic properties, producing magnetic moments and metal-insulator transition.

Early understanding and classification of materials in terms of their electrical character was based on band theory, where a completely filled or empty band results in insulating behaviour, while partially filled bands lead to metallic behaviour. However, it was found that several compound (e.g., NiO) do not respect this classification [24]. Some materials, which are nominally at 'half-filling' behave as insulators. Peierls [25] suggested that an insulating state could arise due to lattice period doubling which can arise from electron-phonon coupling induced dimerization. This could open a gap at the Fermi level.

In 1949 it was argued by Mott [26] that strong electron-electron interaction could prevent electron delocalisation, and lead to an insulating state, if the bandwidth fell below a critical value. This was the scenario for a Mott transition, made concrete later in terms of a minimal lattice model by Hubbard, *etc.*.

The Hubbard model [27] (also independently conceived by Gutzwiller [28] and Kanamori [29]) describes electron delocalisation in the presence of local repulsion. Originally introduced to address itinerant ferromagnetism [27] in transition metals, its usefulness now extends to describing metal-insulator transitions, antiferromagnetic order, and possibly d-wave superconductivity. Hubbard's several papers [30–34] worked out various limits of the model, and an approximate description of the Mott transition.

Although continuously studied since its introduction, the Hubbard model and the Mott insulator gained prominence with the discovery of high temperature superconductivity in the doped cuprate $La_{2-x}Sr_xCuO_4$ [35, 36]. This thrust the Mott transition and the doped Mott insulator center-stage.

It quickly became apparent that a large family of transition metal oxides, including the 'colossal' magnetoresistance manganites ($A_xA'_{1-x}MnO3$) [37, 38], the high thermopower cobaltates (Na_xCoO_2) [39], *etc*, owed their exotic properties to electron correlation [40–43]. The development of powerful tools like dynamical mean field theory (DMFT) and its combination with *ab initio* methods has clarified many aspects of correlation physics over the last two decades [44].

Important characteristics of these materials include: (i) the existence of several competing states, a typical example is the high T_c phase diagram in Fig.1.8,
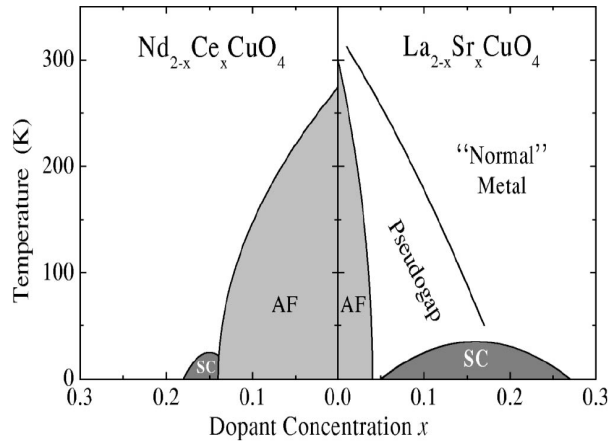
Figure 1.8: Phase diagram of the electron and hole doped superconductors, showing superconducting (SC), antiferromagnetic (AF), pseudogap, and normal metal regions. $x = 0$ is the half filled Mott insulating phase. (Damascelli [36])

(ii) strong sensitivity to perturbations like doping change, applied fields, disorder, and temperature, and (iii) the occurence of spontaneous nanoscale inhomogeneity.

1.1.3 Itinerancy and frustration

Correlation physics involves metallic systems with *itinerant* electrons, while traditional frustrated systems are insulating magnets with *localized* electrons. There are broadly two situations where they intersect:

- One may have a 'two species' system, of electrons and local moments, where the local moments live on a frustrated structure and are Kondo (or Hund's) coupled to itinerant electrons.

- We could have a Mott insulator in a frustrated structure and the consider its metallization, due to increasing bandwidth.

The first situation arises in Kondo lattice like, or 'double exchange', models, while the second is described by the Hubbard model. In both cases the ideal frustrated situation arises in the absence of itinerant electrons. The interest is in clarifying how the *presence* of electrons in the Kondo lattice, or the approach to the insulator-metal transition in Mott-Hubbard systems modifies the physics. The 'two species' description is appropriate for the pyrochlores $A_2B_2O_7$ (iridates, *etc*) and double perovskites $A_2BB'O_6$, while the Hubbard model is relevant for materials like the cluster compound $GaTa_4Se_8$ and A_3C_{60}. We review these quickly in the following sections.

31

1.2 Double perovskites

1.2.1 General introduction

The double perovskites (DP) constitute a large family of materials with the molecular formula $A_2BB'O_6$, where A is a large electro-positive element, B and B' are typically transition metals and O stands for Oxygen. They can be thought of as two units of perovskites, *i.e.*, $ABO_3 \cdot AB'O_3$. In most cases, they crystallize in alternating BO_6 and $B'O_6$ octahedra arranged in the rock-salt manner, as shown in Fig.1.9. The physical properties of double perovskites depend on

(a) The chemical combination B and B', and

(b) The ionic radius and valence of A.
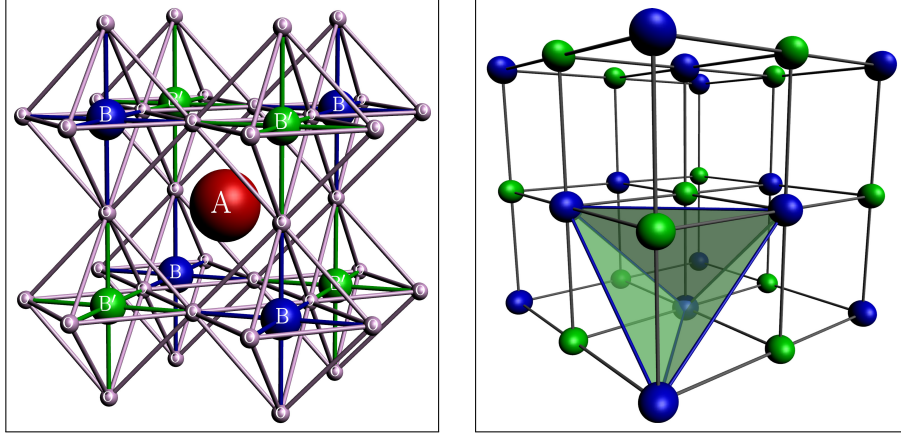
Figure 1.9: Left: The ordered double perovskite $A_2BB'O_6$ crystal structure, which consists of alternating pattern of BO_6, and $B'O_6$ octahedra, in rock-salt manner. Right: In the rock-salt B-B' arrangement, each sub-lattice is FCC.

They exhibit a number of magnetic and electronic states, for example high T_c ferromagnetic half-metal in Sr_2FeMoO_6 [45], high T_c ferromagnetic insulator in Sr_2CrOsO_6 [46], and frustrated antiferromagnetic insulators in La_2LiRuO_6 [47]. There are also exotic magnetic states like spin glass (Ba_2YReO_6 [48]) and valence bond glass Ba_2YMoO_6 [49].

1.2.2 Experimental results

Although studied for decades [50, 51] it was the discovery of high T_c ferromagnetism and half-metallicity in Sr_2FeMoO_6 [52] (SFMO) that led to renewed interest in the double perovskites. They display a wide variety of properties.

(a) SFMO is a high T_c half metallic ferromagnet with moderate low field magne-toresistance. Could be useful for spintronic and switching applications.

(b) La_2NiMnO_6 [53, 54], is a ferromagnetic insulator with $T_c = 270K$, and shows large magneto-dielectric response over a window $\sim 100 - 300K$ [55].

(c) Sr_2CrOsO_6 [46] is a ferromagnetic insulator with $T_c = 725K$, with one of the highest transition temperature reported.

Table 1.1: List of double perovskite materials

Perovskite	Crystal structure	Magnetism	T_c, T_N	Transport
Sr_2FeMoO_6	Tetragonal	FM	420K	Half metal
Ba_2FeMoO_6	Cubic	FM	345K	Half metal
Sr_2FeReO_6	Cubic	FM	400K	Half metal
Sr_2CrReO_6	Cubic	FM	635K	Half-metal
Sr_2CrOsO_6	–	FM	725K	Insulator
Ca_2CrReO_6	Monoclinic	FM	360K	Insulator
Ca_2FeReO_6	Monoclinic	FM	520K	Insulator
La_2NiMnO_6	Monoclinic	FM	280K	Insulator
Sr_2FeWO_6	–	AF	40K	Insulator
Sr_2FeCoO_6	Tetragonal	SG	75K	Insulator
Ba_2YMoO_6	–	VBG	0K	Insulator

The magnetism in the DP's arises from a combination of (i) Hund's coupling on the B, B′ ions and (ii) electron delocalisation. While there are important DP's where both B and B′ are magnetic ions e.g., La_2NiMnO_6, we will focus on materials where only one ion, say 'B', is magnetic. In this category, there are insulating DP's [47–49,56,57], which are mostly in the category of Mott insulators, and metallic DPs, for example Sr_2FeMoO_6 (SFMO).

Let us focus on metallic systems, where the effect of magnetic frustration is more interesting and much less explored. A good starting point is the SFMO, where the B atom (Fe) is magnetic while B′ (Mo) is non-magnetic. The ferromagnetism, and its applications in SFMO is well explored [58–62], but much less is known about the antiferromagnetism. Recent theoretical studies predicted that upon electron doping, SFMO should show a transition to a metallic antiferromagnetic state [63, 64]. The synthesis of lanthanum doped ($La_xSr_{2-x}FeMoO_6$) compounds have revealed signatures of antiferromagnetism at high doping [65].

The electronic structure of SFMO is shown in Fig. 1.10. The octahedral oxygen coordination splits the five d-orbitals into a threefold degenerate lower manifold t_{2g}
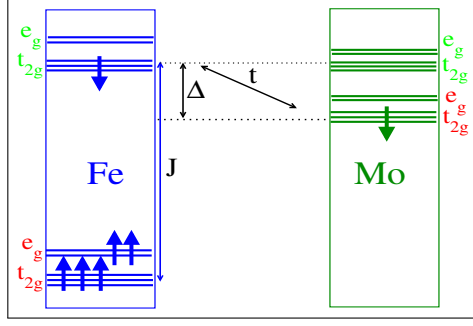
Figure 1.10: The relevant electronic levels of Sr_2FeMoO_6.

and the twofold degenerate higher energy e_g levels. The large Hund's splitting in Fe leads to high spin configurations, while for Mo, due to negligible Hund's splitting the level remain almost spin degenerate. SFMO exists in the mixed valent state involving (a) Fe^{3+}-Mo^{5+} in which Fe has 5 electrons filled in the lower, say up spin, orbitals and Mo has 1 electron in the lowest t_{2g} level, and (b) Fe^{2+}-Mo^{6+}, in which Fe has 5 electrons in the lower up spin levels, and one electron on the next higher 'down' t_{2g} level, and Mo levels are empty.

Based on the electronic structure established by Sarma *et al* [66], the lower t_{2g} and e_g band of Fe lie well below the Fermi level and contribute localized $S = \frac{5}{2}$ spin at each Fe site, while the the upper t_{2g} of Fe hybridize with the corresponding t_{2g} of Mo. The electron hopping amplitude t between the Fe, and Mo t_{2g} level, and the level difference Δ are the crucial ingredients that decide the band structure of the system. The next section discusses the origin of magnetic order.

1.2.3 Theoretical background

There have been several attempts at a theoretical understanding of the magnetism in these materials. These consist of (*i*) *ab initio* electronic structure calculations, and (*ii*) model Hamiltonian based approaches.

The *ab initio* calculations provide material specific information about the electronic structure [67], relevant energy scales and couplings like the hopping t, Hunds splitting and level difference Δ [64], and allow a rough mean field estimate of the T_c [68]. Unfortunately, these calculations are rather complicated for non-collinear magnetic phases that are likely in a frustrated magnetic lattice, which is the case for SFMO, where the localized moments lie on the FCC 'B' site sub-lattice. In such situations model Hamiltonian studies can provide some insight on possible ordered states.

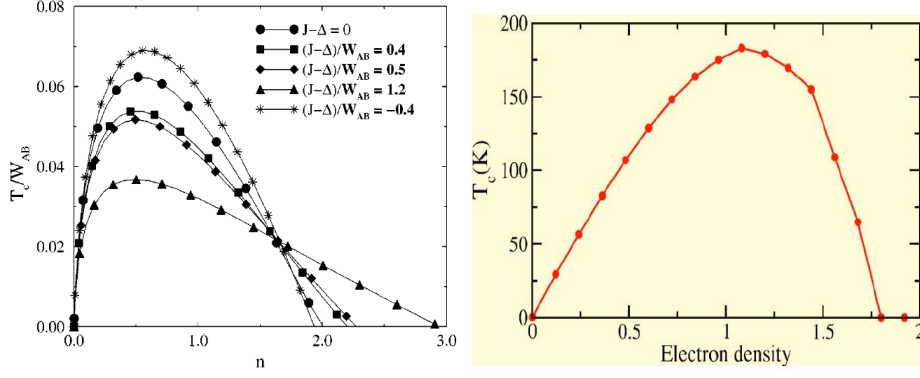Figure 1.11: Variation of magnetic T_c with band filling n. Left:(Millis [58]) in the $J \to \rho$ limit, for different values of $J - \Delta$ and $W_{AA}/W_{AB} = 0.6$, $W_{BB} = 0$. Right: (Brey [61]) for $J - \Delta = 0.3eV$, $t_{FeMo} = 0.3eV$, and $t_{MoMo} = 0.15$.

The band theory for DPs like SFMO is described as sum of three two-dimensional (2D) tight binding models, involving xy yz and zx planes, respectively, due to three t_{2g} bands. On the B sites the electrons are coupled to the localized spin. Since the three bands do not hybridize with themselves, and the hopping is planar for each band, the tight binding model has interesting two dimensionality. With this as the starting point and DMFT as the tool the T_c and window of stability for ferromagnetism was estimated by Millis *et al* [58, 59]. and Brey *et al* [61]. Another approach was variational mean field approach by Alonso *et al* [60] on a two dimensional single band model, and a finite temperature phase diagram was constructed between the ferromagnetic and the antiferromagnetic (AF) phase, highlighting the phase separation. However the nature of the AF phase was not mentioned.

Each of these efforts establish the stability window of ferromagnetic phase, beyond which AF phase was a possibility. The occurrence of non-ferromagnetic phases in spin-fermion problems has been known, and work based on the classical Kondo lattice [69–72] had revealed that variation in carrier density can lead to a wide variety of magnetically ordered phases.

Motivated by this a one band 'double perovskite' model had been studied in two dimensions [63].

$$H = \epsilon_B \sum_{i \in B} f^\dagger_{i\sigma} f_{i\sigma} + \epsilon_{B'} \sum_{i \in B'} m^\dagger_{i\sigma} m_{i\sigma} - t \sum_{\langle ij \rangle} f^\dagger_{i\sigma} m_{j\sigma} + J \sum_{i \in B} \mathbf{S}_i \cdot f^\dagger_{i\alpha} \vec{\sigma}_{\alpha\beta} f_{i\beta} \qquad (1.1)$$

The $f^\dagger$ and $m^\dagger$ denote respectively the creation operators on the magnetic B site (say Fe) and the non-magnetic B' sites (say Mo) with the 'on-site' energies ϵ_B and $\epsilon_{B'}$. t denotes the nearest neighbour hopping between the B-B' sites. The $\mathbf{S}_i$ are

35
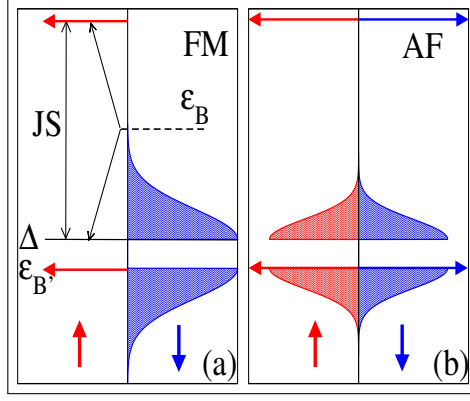
Figure 1.12: Schematic of the density of states in (a). the ferromagnetic, and (b). the antiferromagnetic ground states.

classical localized spins on the B site coupled to electronic spins through coupling $J \gg t$. Recalling the level scheme of SFMO in Fig.1.10, the effective level difference between B and B sites will be $\Delta = \epsilon_B - J\frac{S}{2} - \epsilon_{B'}$. One assumes $J \to \infty$ limit, keeping Δ finite. The parameter space for the problem includes the level difference Δ/t, electron density n, and and the temperature T/t. A schematic of the level scheme and the generic density of states (DOS) in the ferromagnetic and antiferromagnetic case is shown in Fig.1.12.

In the two dimensional model Sanyal *et al* [63] confirmed the existence of antiferromagnetic (AF) metallic, albeit collinear, phases. The magnetic phases are shown in Fig. 1.13. *Ab initio* calculations [64] in the full 3D situation have since confirmed the possibility of *collinear* antiferromagnetic metallic phases [64].

In three dimensions, however, the magnetic lattice becomes FCC! The frustrated character raises the intriguing possibility of doping driven *non collinear* antiferromagnetic phases. Part of this thesis will explore this issue in detail.
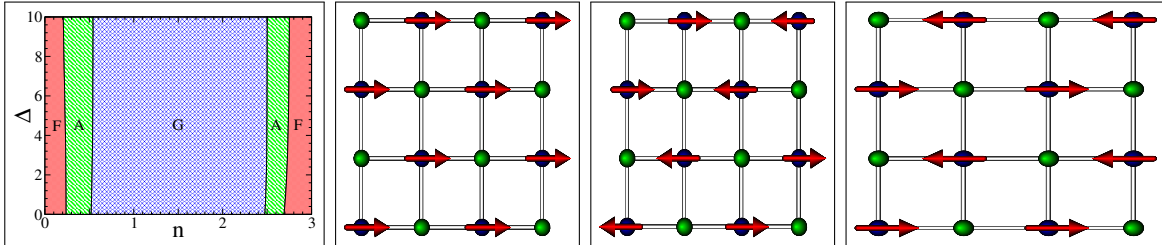
Figure 1.13: Left: The magnetic phase diagram of two dimensional model of ordered double perovskite, in electron density n and level difference Δ. Right: The snapshot of the magnetic phases, ferromagnet (F), A-type and G-type antiferromagnet.

1.3 Frustrated Mott systems

The Mott metal-insulator transition (MIT), and the proximity to a Mott insulator in doped systems, are crucial issues in correlated electron systems [73–76]. Correlated electronic systems involve strong short-range repulsion. At integer filling, the primary effect of correlation is the emergence of an insulating state where band theory predicts a metal. The nature of this insulating state is also different from the band insulator and involves non trivial magnetic correlations.

1.3.1 General introduction
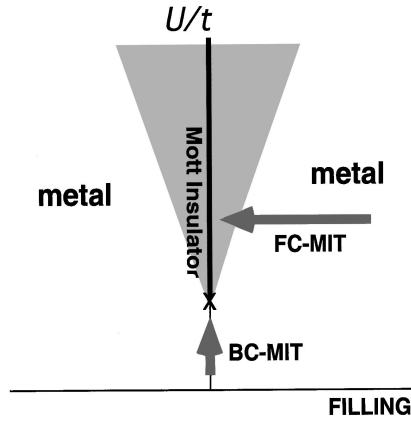
Figure 1.14: Schematic of the Mott metal insulator transition, showing the filling controlled (FC) transition and the bandwidth controlled (BC) transition. We will focus on the BC scenario in this chapter.

Understanding the transition from a metal to the Mott insulator, and the effect of doping the Mott state, are classic problems in quantum many-body physics. A minimal description is provided by the single band Hubbard model.

$$H = \underbrace{\sum_{ij,\sigma} \left[t_{ij} c_{i\sigma}^\dagger c_{j\sigma} + \text{h.c.} \right]}_{H_{TB}} + \underbrace{U \sum_i n_{i\uparrow} n_{i\downarrow}}_{H_U} \qquad (1.2)$$

The first term (say H_{TB}) denotes the kinetic energy involving the hopping amplitudes t_{ij}, usually restricted to nearest neighbours. A given lattice and choices of t_{ij} defines the density of states and bandwidth of the non-interacting systems. The second term, H_U, in equation (1.2) represents the interaction between electrons on the same site. Whether the model has a metallic or insulating ground state depends on the relative strength of interaction U/t and the electron density. A metal-insulator transition
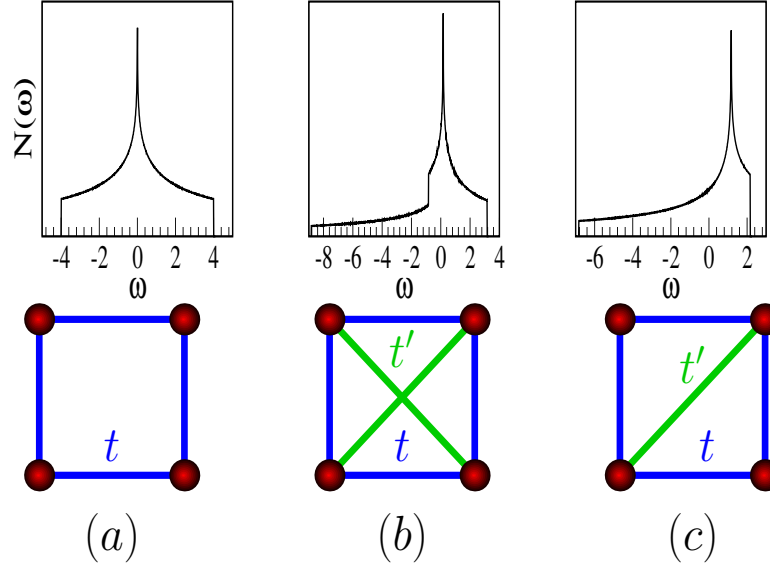
Figure 1.15: Schematics of the density of states (upper panel) and electron hoppings (lower panel) for: (a) square lattice with nearest neighbour hopping t, (b) square lattice with next nearest neighbour hopping t' too, and (c) triangular lattice with hoppings t,t'. The Fermi level at half filling is set to $\omega = 0$.

(MIT) can be caused, see Fig. 1.14, either by (a) filling control: varying the electron density towards $n = 1$ in a large U/t system, or (b) bandwidth control: increasing U/t staying at $n = 1$. In the present thesis we will explore only the bandwidth controlled transition.

While it is large U/t that is ultimately responsible for the Mott phase, the detailed behaviour of the system depends crucially on the symmetry of the underlying lattice, and the hopping parameters t_{ij}. This happens because weak coupling magnetic instabilities depend on nesting features in the Fermi surface, and the magnetism in the Mott phase depends on the lattice geometry. We set down simple features of a few tight binding systems to address the weak coupling physics.

(a) Square lattice with nearest neighbour hopping (t)

(b) Square lattice with nearest (t) and next nearest hopping (t')

(c) Triangular lattice, with anisotropic hoppings (t, t')

Fig.1.15 shows the schematics of hopping amplitudes t_{ij} and and corresponding density of states (DOS) $N(\omega)$ for the above three cases. Their dispersion relations and bandwidth are listed in table below.

Lattice	Hopping	Dispersion $\epsilon_{\mathbf{k}}$	Bandwidth W
Square lattice with nearest neighbour hopping	t	$-2t(\cos k_x + \cos k_y)$	$8t$
Square lattice with next nearest neighbour hopping	t, t'	$-2t(\cos k_x + \cos k_y)$ $-4t'(\cos k_x \cos k_y)$	$12t$ $(t' = t)$
Anisotropic triangular lattice	t, t'	$-2t(\cos k_x + \cos k_y)$ $-2t' \cos(k_x + k_y)$	$9t$ $(t' = t)$

Certain features of the DOS are noteworthy. All the systems (a)-(c) have a logarithmic singularity in DOS. Case (a) has particle-hole symmetry, absent in the other two. The location of the singularity, in terms of band filling, also differs between the three cases. We will see in the chapter 4, that large DOS near Fermi level results in stronger features in the Linhard susceptibility, which in turn triggers magnetic/charge instabilities in the presence of interactions.

To highlight the basic energy balance involved in the Mott transition we consider the following. The ground state of this tight binding system is the Fermi sea

$$|FS\rangle = \prod_{\mathbf{k}}^{\epsilon_{\mathbf{k}} \leq 0} c_{\mathbf{k}\uparrow}^{\dagger} c_{\mathbf{k}\downarrow}^{\dagger} |0\rangle \tag{1.3}$$

This by definition is uncorrelated, i.e., occupation of ↑-spin electron on a given site is independent of the occupation of ↓-spin electron on the same site. This means the $|FS\rangle$ has a lot of charge fluctuations and double occupancy. The expectation value of the interaction term H_U in the Fermi sea can be calculated as

$$E_U = \langle FS|H_U|FS\rangle = \langle FS|U\sum_i n_{i\uparrow} n_{i\downarrow}|FS\rangle = \frac{1}{4}NU \tag{1.4}$$

N being the number of lattice sites. The tight binding energy is just the sum of eigenvalues in the occupied part of the band, upto half filling. Assuming just nearest hopping t, we have $\epsilon_{\mathbf{k}} = -t\tilde{\epsilon}_{\mathbf{k}}$, where $\tilde{\epsilon}_{\mathbf{k}}$ is just a number, we have

$$E_{TB} = \langle FS|H_U|FS\rangle = 2\sum_{\epsilon_{\mathbf{k}} \leq 0} \epsilon_{\mathbf{k}} = -t \times \left(2\sum_{\tilde{\epsilon}_{\mathbf{k}} \leq 0} \tilde{\epsilon}_{\mathbf{k}}\right) = -N\alpha t \tag{1.5}$$

where, α is a number of order 1, which depends on the lattice geometry. The total energy per site, in the uncorrelated ground state is thus

$$\frac{1}{N}\langle FS|H|FS\rangle = \frac{1}{4}U - \alpha t \tag{1.6}$$

Now consider the state $|LOC\rangle$ which represents a one electron localized at every site, as would be appropriate deep in the Mott phase. The energy of this state is simply $\langle LOC|H|LOC\rangle = 0$. If we consider only the two limiting cases, $|FS\rangle$ and $|LOC\rangle$ the energies become equal at a $U/t|_c = 4\alpha$.

In reality, the metal suppresses double occupancy with increasing U, so it competes better with the localised state. This tends to push U_c higher, as observed in DMFT estimates. Intersite magnetic correlations, on the other hand, stabilise the insulator and tend to reduce U_c below DMFT estimates. So, while the argument for a Mott state at large U/t is quite general, the actual MIT and associated magnetic correlations are very lattice specific.

On a bipartite lattice the Mott transition is well understood in terms of magnetism and transport but the presence of triangular or tetrahedral motifs in the lattice brings in geometric frustration [77,78]. This disfavours long range order, and promotes complex electronic states with non-collinear, or incommensurate magnetic character. Their nature, and impact on the MIT, remain an outstanding problem. Such effects have seen some exploration in two dimensions, but hardly any in three dimensions. Below we briefly discuss some key experiments and existing theory in both these cases.

1.3.2   Two dimensional systems

1.3.2.1   Experiments

In two dimensions, a class of organic compounds provide a concrete testing ground for studying the effects of frustration on the metal-insulator transition [79,80]. These organics are quasi two dimensional (2D) materials, with molecular formula $\kappa-$(BEDT-TTF)$_2$X, where κ-(BEDT-TTF) (also known as κ-ET) is an organosulfer molecule (Fig.1.16 left), and 'X' is a halide like anion. The structural information is shown in Fig.1.16 (right box), where (a) shows that the crystal consists of alternating layers of the BEDT-TTF, and the same of halide X ions. In (b) we see the top view of the single layer consisting only of BEDT molecules, which are dimerized, so that the actual 'intra-dimer' distances are small compared to 'inter-dimer' distance. X being halide, each dimer has deficiency of electron, or a 'hole' carrier. If we imagine the dimer as a single 'site', then this structure lies on a triangular lattice (Fig.1.16(c)).

From *ab initio* calculations, the dimer site is known to be correlated, as the large lattice spacing, $\sim 11\mathring{A}$, leads to a low bandwidth, enhancing electron correlation effects. The inter-dimer hoppings are anisotropic in general, with one of the three
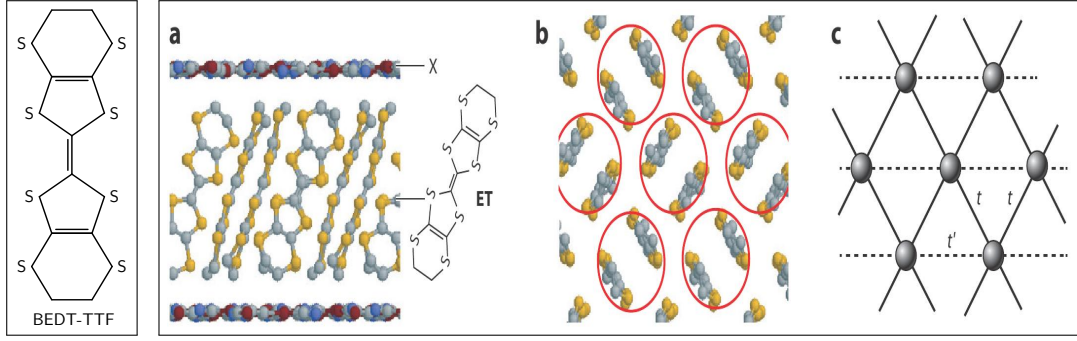
Figure 1.16: Left: Molecular structure of BEDT-TTF. Right: The crystal structure of the $\kappa-$BEDT compounds: (a) in plane view, (b) top view are shown. Assuming each dimer as a 'site' they lie on (c) a triangular lattice with anisotropic hoppings t,t'.

nearest neighbour differing from other two [81]. If we ignore the weak inter-layer coupling the low energy physics can be described by the single band Hubbard model in two dimensions on the anisotropic triangular lattice [81, 82].

In table 1.2 a material phase diagram is shown, constructed via *ab initio* methods [82] in which compounds are placed in $U/t-t'/t$ plane. The parameters are estimated with extended Huckel (EH) and density functional theory (DFT) calculations. A large number of these comounds are close to Mott transition, *i.e.,* can be metalized with moderate pressure. To give a few examples, materials like $\kappa-$Cl [83] and $\kappa-$CN [84], which are Mott insulators, undergo an insulator-metal transition (IMT) on hydrostatic pressure of order 20 Mpa. κ-$Cl_{1-x}Br_x$ shows an IMT as x increases above ~ 0.75 [85].

	X
A	$Cu_2(CN)_3$
B	$Cu[N(CN)_2]Cl$
C	$Cu[N(CN)_2]Br$
D	$Cu(CN)[N(CN)_2]$
E	$Cu(NCS)_2$
F	$Ag(CN)_2H_2O$
G	I_3
H	$k\text{-}(ET)_4Hg_{2.89}Br_8$
I	$k\text{-}(ET)_4Hg_{2.89}Cl_8$
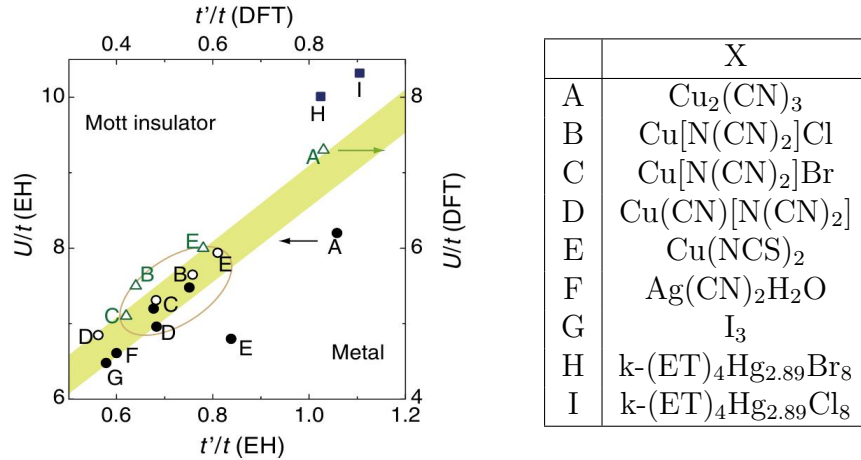
Table 1.2: Open circle: Extended Huckel (EH) calculations (120K), Closed circle: EH calculations (290K), Triangle: DFT calculations (taken from Shimizu *et al* [82])
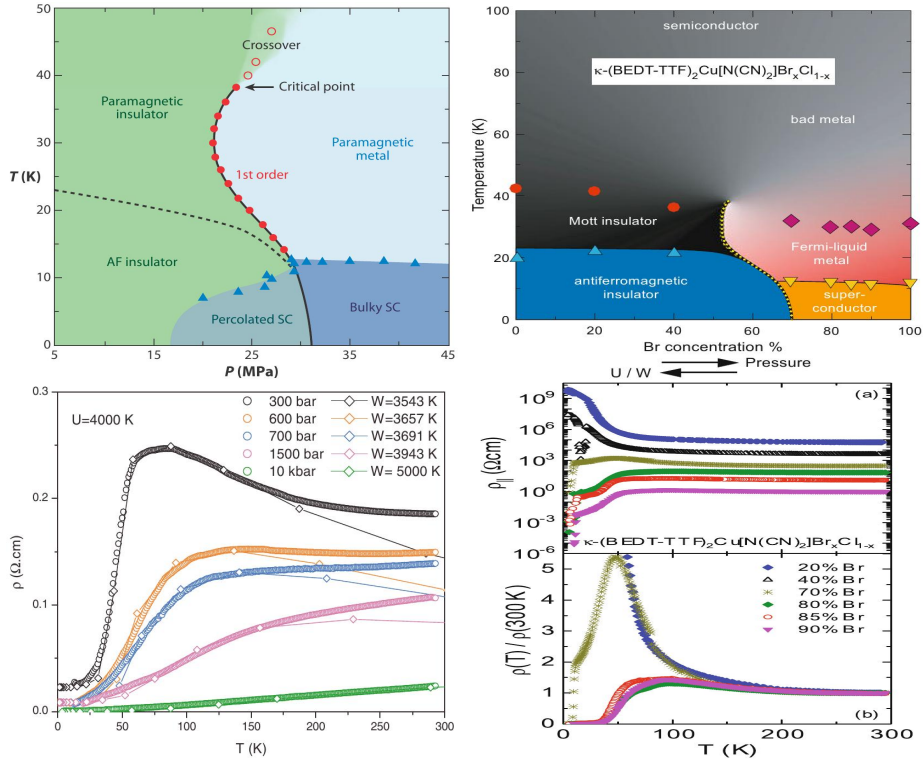
Figure 1.17: Top: The experimental phase diagram with pressure, and doping. Bottom: Corresponding transport measurement as function of temperature. In the second figure, the data from top to bottom are for x=0.2,0.4,0.7,0.8,0.85,0.9 and, the absolute values of resistivity are multiplied by 10, 10^2, 10^3, 10^4 and 10^5 respectively.

Fig.1.17 shows the experimental 'pressure-temperature' phase diagram of the κ-Cl with pressure and chemical doping, where the MIT boundary is estimated from conductivity measurements. The salient points about the experiments are:

- The metallic state is *very incoherent* above $T \sim 50$K, with $\rho \gtrsim 100$ mΩcm [85].

- The optical conductivity [86, 87] shows transfer of spectral weight from high frequency, $\sim U$, towards zero frequency and has non Drude character over a pressure window.

- The MIT boundary is non-monotonic, *i.e*, there is reentrance of insulating phase at higher temperature [84, 87]. See Fig.1.17 top row.

- NMR experiments suggests the presence of a pseudogap (PG) [88] in the single particle density of states near the MIT.

- The NMR also provides some insight into the magnetic correlations in the material [88–91].

42
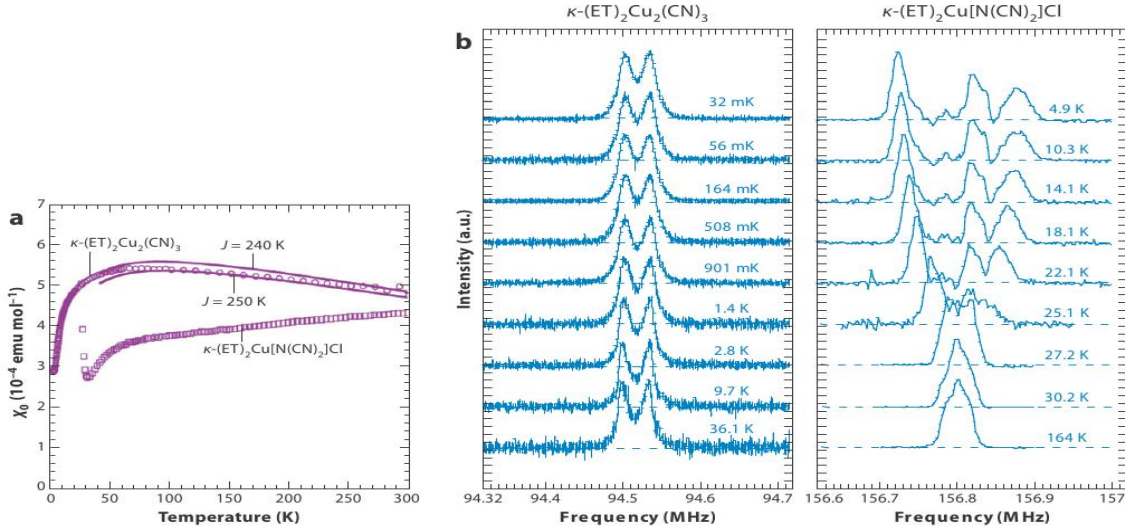
Figure 1.18: (a) Temperature dependence of the spin susceptibility for κ-CN, and κ-Cl. (b) ^{1}H-NMR spectra for single crystals of κ-CN, and κ-Cl under magnetic field applied perpendicular to dimer layer. (Taken from [84])

The information about the detailed magnetic state is limited. In Fig.1.18 (a) shows the magnetic susceptibility at ambient pressure for κ-CN, and κ-Cl (b) ^{1}H-NMR spectra of single crystals of the same. Fitting the susceptibilities of these two to Heisenberg model yields exchanges J=240K and 250K. The splitting of the lineshapes of the NMR spectra with lowering temperature indicates the onset of magnetic ordering, which is seen at rather low temperature $T = 27K$ in κ-Cl compared to exchange J, however the exact nature of magnetic order is not known. On the other hand, for κ-CN no change is observed down to $T = 32mK$ despite of rather large exchange J, suggesting the suppression of long range order because of (greater) frustration.

These unusual magnetic states would result in unique transport, optical, and spectral features. Our aim is to uncover the possible magnetic ground state on the frustrated structure and examine the impact of the finite temperature magnetic fluctuations on electronic spectra and transport.

1.3.2.2   Theoretical background

The single band Hubbard model is the starting point for approaching Mott physics. On the triangular lattice, specifically, there have been several studies [83, 92–103] to model organic physics. We quickly review these.

Method	VMC [95, 104]	ED [105, 155]	PIRG [106]	VCPT [102, 107]	DMFT [83, 96, 97]	CDMFT [98–101]
$t' - U$ Ground state	Yes	Yes	Yes	Yes	Not yet	Not yet
Finite T	No	No	No	No	Yes	Yes
Density of states	No	Yes	No	No	Yes	Yes
Transport/Optics	No	No	No	No	Yes	No*
Spatial correlations	Yes	No	No	No	No	limited

Table 1.3: Comparison of available many body methods to capture the Mott transition in the 2D triangular lattice. The left most column lists the indicators that we may wish to access to understand the system.

1.3.2.2.1 Ground state methods *Variational Monte Carlo* (VMC) minimises the energy by optimising the parameters in a variational wavefunction. The minimization of the energy is done via Monte Carlo sampling. This is a real space approach, limited however to small lattice sizes $N = 10 \times 10$. The reliability of these calculations crucially depend on the quality of trial wave functions. Luca *et al* [95] employed the VMC scheme optimizing two sets of wave functions derived from (a) a mean field Hamiltonian with AF correlations, and (b) BCS Hamiltonian. They concluded that for $t'/t = 0.85$ the MIT occurs at $U_c/t \sim 7.5$, and the insulating phase is a spin-liquid. Very recently [104] they have improved the variational set by taking spiral states. This results in qualitative change in the phase diagram, where at moderate insulating U the spin liquid was replaced by spiral antiferromagnets.

Exact diagonalization (ED) As the name suggest, involves numerical diagonalization of the many-body Hamiltonian, using Lanczos algorithm for large sparse matrices. The only limitation is that only lattices with a few sites (of order 16) can be studied. Clay *et al* [105] studied the Hubbard model at half filling, for all t/t' values on a 4×4 size, and established a phase diagram. They studied the nature of the states and concluded that the model does not exhibit superconducting state.

Path integral renormalization group (PIRG) method (Imada *et al* [106]) constructs an optimized ground state wave function $|\Phi\rangle$ as a linear combination $|\Phi\rangle = \sum_l c_l |\phi_l\rangle$ within the allowed dimension L, of the Hilbert space in a numerically chosen basis $\{|\phi_l\rangle\}$. The ground state is projected out after successive renormalization process in the path integral, in a manner in which both the coefficients c_l and the basis $|\phi_l\rangle$ is optimized.
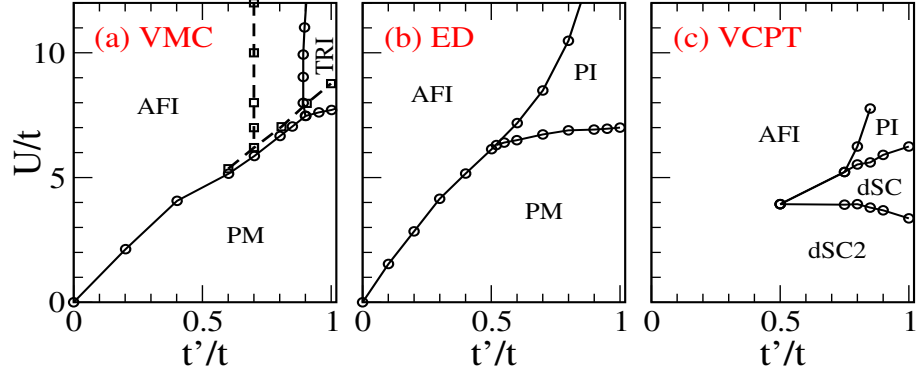
Figure 1.19: Ground state phase diagram of the Hubbard model on the anisotropic triangular lattice. Notation for the phases is standard, except TRI: 120^0 ordered insulator, and dSC: d wave superconductor.

Variational cluster perturbation theory (VCPT) divides the lattice into identical clusters of size N (say) with the inter-cluster hoppings, and evaluates one particle Green's function within the cluster numerically with open boundary conditions. The inter-cluster hoppings are treated perturbatively to recover the full Green's function $G(\mathbf{k}, \omega)$. Depending on the size N, short range correlations can be accessed in the system.(Sahebsara *et al* [102, 107]).

To have a feel on how some of these method compare when accessing the ground state, we show, in Fig.2.2 the ground state phase diagram using four different methods. (a) VMC by Luca *et al* [95, 104], (b) ED by Clay *et al* [105], and (c) VCPT by Sahebsara *et al* [102, 107].

1.3.2.2.2 Access to finite temperature has been usually with *dynamical mean field theory* (DMFT). It has been the method of choice [83, 96, 97], mapping the many body lattice problem to a many body *local* problem, supplemented by a self-consistency condition [108]. Some spatial correlations can be included via cluster DMFT [98–101]. Fig.1.20 shows phase diagram for anisotropic triangular lattice established by (a) Ohashi *et al* [99] for $t' = 0.8t$ using 4 site cluster based C-DMFT, and by (b) Liebsch *et al* [100] using 3 site cluster. They use the double occupancy $D_i = \langle n_{i\uparrow} n_{i\downarrow} \rangle$ to characterize the Mott transition.

Though the method captures the reentrance in MIT, as the Fig.1.20 shows, the understanding of its origin isn't present. Besides they present it in a limited window of t'/t.

We summarize below the results of the above methods, skipping the detailed
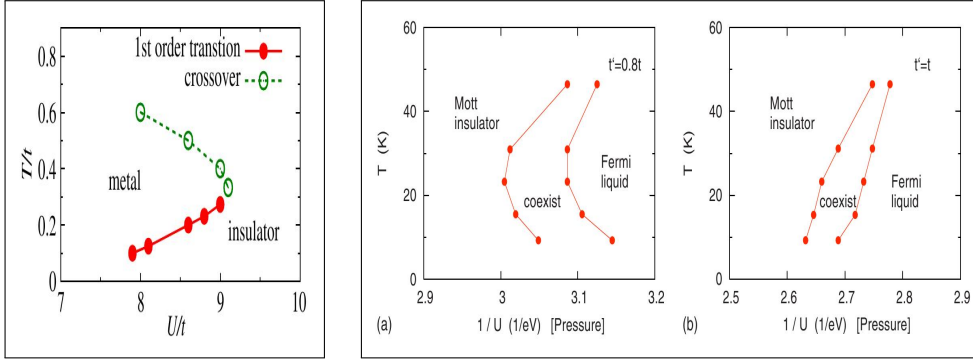
Figure 1.20: Finite temperature phase diagrams established by C-DMFT. Left: $t'/t = 0.8$ Right: (a) $t' = 0.8t$ and (b) $t' = t$

discussion for later in chapter 4. On triangular motif, the results in general depend on the degree of frustration and the specific method, but broadly suggest the following:

1. The ground state is a paramagnetic Fermi liquid at weak coupling, a 'spin liquid' or para-insulator at intermediate coupling, and an antiferromagnetic insulator at large coupling [92–95].

2. The qualitative features in optics [86] and transport [83] are recovered.

3. There could be a *reentrant insulator-metal-insulator transition* with increasing temperature for a certain window of frustration [99, 100].

4. A low temperature superconducting state could emerge [109–111], although Clay *et al* [105] deny this possibility.

The following are the open issues

- Most of the real space techniques are for $T = 0$, except DMFT which ignores spatial fluctuations. CDMFT does capture short range correlations but has not been generalised to handle complex magnetic states [99].

- There is very limited data on transport [83, 86], obtained mainly via DMFT. These do not capture the effect of magnetic correlations close to the Mott transition.

- Similarly, there is no study of the angular anisotropy of the pseudogap and its connection to magnetic correlations close to Mott transition.

We use a real space approach that is complementary to DMFT, handles spatial fluctuations and inhomogeneity well at finite temperature, and can provide a comprehensive answer to these questions.
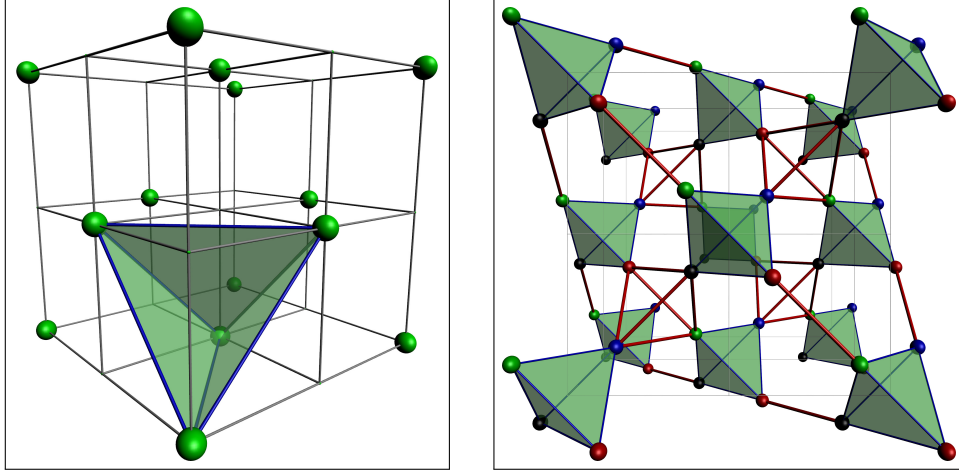
Figure 1.21: Left: FCC lattice, where green spheres denote the sites. The nearest neighbours form tetrahedral motif, which is the geometric ingredient for frustration. Right: pyrochlore lattice, seen as FCC lattice with a basis of four site tetrahedra (denoted by black, red, green and blue spheres). The nearest neighbours are connected by blue lines within the basis, and red lines among neighbouring basis.

1.3.3   Three dimensional systems

Three dimensional frustrated systems usually have tetrahedral connections. Examples are FCC and pyrochlore lattice (see Fig.1.21). Below we review the experimental literature, and theoretical development of these three dimensional frustrated correlated systems.

1.3.3.1   Experiments

While there has been intense exploration of frustration effects in two dimensions, as we saw in the last section, there is no organized body of work probing the interplay of geometric frustration and Mott physics in three dimensions. The systems with geometric frustration in 3D are realized on (a) the FCC lattice and (b) the pyrochlore lattice. In Fig.1.21, the lattice structure with nearest neighbour connection is shown for (a) the FCC lattice, which consists of edge sharing tetrahedra, and (b) the pyrochlore lattice, which consists of corner sharing tetrahedra.

There are, however, intriguing experiments on rather disparate systems whose common features do not seem to have been noticed, and no theoretical effort to connect them. The FCC examples include

1. Cluster compounds (CC) of formula AM_4X_8 [112–115], where A is usually Ga or Ge, M is transition metal and X is S or Se. In these compounds the

electronically active units are the 'cluster' M_4, which have one unpaired electron per cluster.

2. Some alkali fullerides of the form A_3C_{60} [116, 118, 119, 151], which have C_{60}^{3-} ions on FCC lattice. Cs_3C_{60} [118] for example, is magnetic insulator at ambient pressure, and becomes superconducting under pressure. It exists in two crystalline forms, one in which the anion is FCC, the other in which its BCC. At ambient pressure, the frustrated FCC polymorph has much lower Neel temperature $T_N = 2.2K$, compared to the BCC polymorph ($T_N = 46K$).

3. The site 'B' ordered double insulating perovskites, $e.g.$, Sr_2InReO_6 [57]. Many of these do not show long range order but spin-glass [47,48,56], or valence bond glass [49] character instead.

The pyrochlore examples include the molybdates $R_2Mo_2O_7$ [120–122], and iridates $Eu_2Ir_2O_7$ [123–126]. Most of these materials are insulators close to a Mott transition. They exhibit complex magnetic order, including a 'spin frozen' state, and have unusual Hall response [127] indicative of non coplanar order. They show have unusual temperature dependence in the resistivity - larger in metallic state at high temperature than the insulating state.

Compound	GaM_4Se_8	A_3C_{60}	$A_2BB'O_6$	$R_2M_2O_7$
Structure	FCC [112]	FCC, A15 [151]	FCC	Pyrochlore
Pressure studies	Hydrostatic	Hydrostatic, doping [116]	None	Hydrostatic [122, 126]
Reference state	Mott insulator	Mott insulator	Mott insulator or metal	Mott insulator or metal
Measurements	Resistivity, optical conductivity, Susceptibility	NMR [119]	Susceptibility [47, 48, 56, 57]	Resistivity [122, 126], Hall effect [127], Susceptibility [121]
Magnetic state	Glassy [112], Flux [113]	Supercond (FCC), AF (A15)	Spin glass [47, 48, 56, 57], VBS [49]	Spin glass [120–122]

Table 1.4: Summary of experimental results available on three dimensional frustrated compounds potentially close to a Mott transition.

Let us focus on the FCC cluster compounds which seem amenable to modelling within the single band Hubbard description.
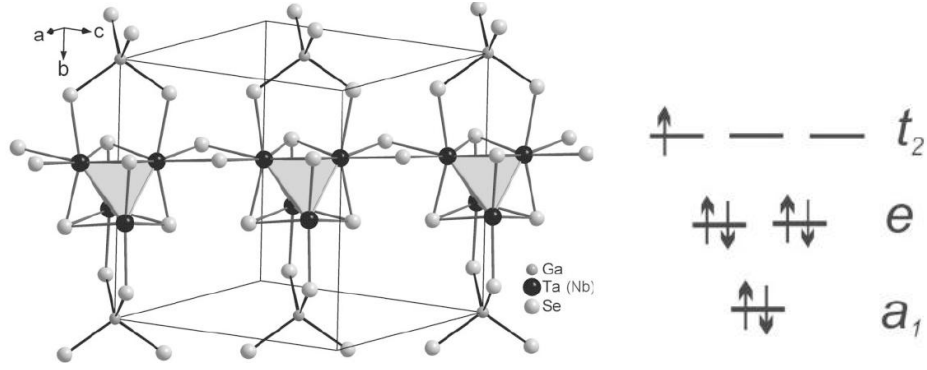
Figure 1.22: Left: Crystal structure of AM_4X_8 systems. Right: Molecular orbital scheme for bonding of M_4 clusters for seven electrons per cluster.

1.3.3.2 AM_4X_8 compounds

The crystal structure of the AM_4X_8 compounds, is shown in Fig.1.22 (left). The electronic correlation arise due to the large distance between M_4 clusters, $d_c > 4\mathring{A}$, compared to the intra-cluster distances. According to molecular orbital (MO) calculations, the d orbitals hybridize to form MOs which consist of three different bonding states (a) a non degenerate level a_1 followed by (b) two fold e and (c) three fold t_2 levels (see Fig.1.22 right panel). For A=Ga, we have 7 electron per cluster for M=V,Nb,Ta and 11 electrons for M=Mo. In both cases, the occupation of cluster levels corresponds to *one unpaired electron* per cluster. This is at the heart of the single band Hubbard description.

- Early measurements [114] on $GaNb_4Se_8$ and $GaTa_4Se_8$ revealed a pressure driven IMT at moderate pressure ($\sim 10 GPa$).

- At ambient pressure the materials are insulating with gaps $\sim 0.14eV$ and $0.1eV$, respectively.

- Increasing pressure ($\sim 10GPa$) leads to a phase with *large but finite resistivity at T=0*, and $d\rho/dT < 0$. This persists over a pressure window beyond which they behave like conventional metals (see Fig.1.23 left panel).

- A very recent optical conductivity measurement on $GaTa_4Se_8$ (Fig.1.23 right panel) indicates that the pressure driven transition involves large transfer of low frequency weight and should be thought of as a Mott transition.

- Few magnetic measurements on $GaNb_4Se_8$ [112] suggest a large Curie-Weiss constant ($\theta_{CW} \sim -300K$), but difficult to detect, suppressed non-collinear 'flux' like order [113].
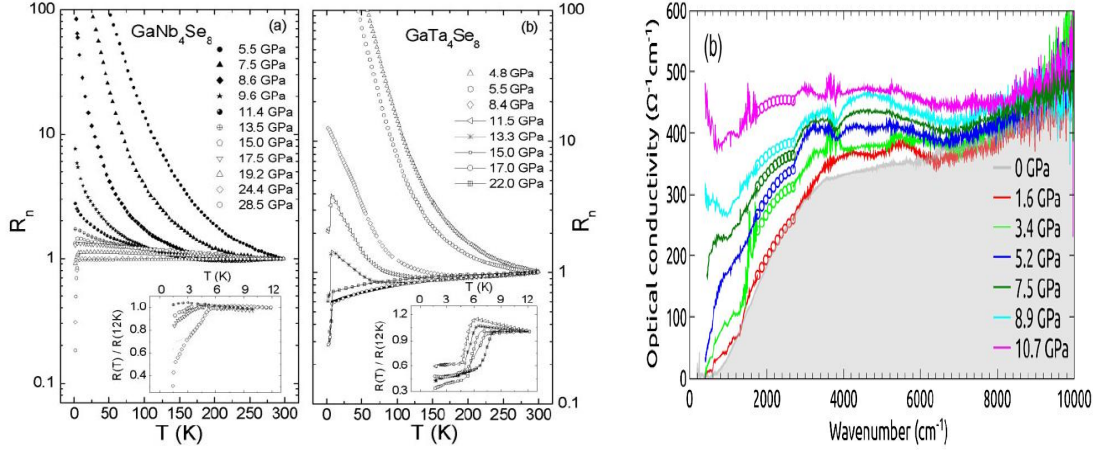
Figure 1.23:   Resistivity (left) and the optical conductivity (right) in AM_4X_8 systems

1.3.3.3   Theoretical background

One can understand the pressure driven Mott transition in the cluster compound, in terms of single band Hubbard model defined on the FCC lattice at half filling, where the M_4 clusters are mapped to a correlated site with Hubbard repulsion U and nearest neighbour electron hopping t. Qn the FCC lattice, surprisingly, there is hardly any theoretical work, except very early attempts using conventional static mean field theory [128]. A very recent paper, Phuoc *et al* [115], does present a DMFT based phase diagram, but there is no discussion about the nature of *spatial fluctuations*, which could play a crucial role in the frustrated system.

1.4   Agenda of the thesis

We have briefly reviewed the experimental background and theoretical progress in two situations:

(a) double exchange driven magnetism in double perovskites, and

(b) pressure driven metallisation of frustrated Mott insulators.

In both cases, the nature of magnetism has been a puzzle due to the frustrated lattice geometry. Establishing the nature of magnetic correlations and possible long range order, driven by electron delocalisation, defines the first task in the problems above.

The nature of the magnetic background affects the electronic spectrum and transport, quantifying this defines the second task. In particular, the metal-insulator

50

transition in the ground state, and a possible pseudogapped phase in the vicinity of the MIT, is one important issue. In addition, thermal fluctuations have a dramatic effect on the low frequency density of states, the angle resolved spectrum, the resistivity, and the optics. Establishing the behaviour of these indicators in our models, and comparing with available experimental data will be the major task.

There is a wealth of data in two dimensions from the organics, and some scattered data in three dimensional frustrated materials close to the Mott transition. We will use a Hubbard-Stratonovich decomposition to construct a 'lattice field theory' of electrons coupled to auxiliary moments and try to provide a qualitative overview and a detailed quantitative description of Mott physics in these systems, and compare in detail with available experimental data.

CHAPTER 2

MODELS AND METHOD

In this chapter we discuss the tools we have used for solving the two models that are relevant for us. These are, broadly, Kondo lattice type models relevant for the double perovskites, and the Hubbard model for the Mott transition. The first section introduces the models. This is followed by a discussion of the approximations we use to set up a tractable numerical problem. The section after discusses the numerical methods used. In the last section we describe the benchmarks against which we have tested our results.

2.1 Models

We consider two kinds of models:

$$H_{KLM} = \sum_{\langle ij \rangle \sigma} t_{ij} \left[c_{i\sigma}^{\dagger} c_{j\sigma} + \text{h.c.} \right] + J \sum_i \mathbf{S}_i . \vec{\sigma}_i \tag{2.1}$$

$$H_{Hubb} = \sum_{\langle ij \rangle \sigma} t_{ij} \left[c_{i\sigma}^{\dagger} c_{j\sigma} + \text{h.c.} \right] + U \sum_i n_{i\uparrow} n_{i\downarrow} \tag{2.2}$$

In both cases the first term (say H_0) defines the non-interacting (band) problem, $\vec{\sigma}$ is the electron spin operator. H_{KLM} refers to a Kondo lattice model where the local moments $\mathbf{S}_i$ live on a frustrated lattice, while H_{Hubb} refers to the Hubbard model with electron repulsion U. The KLM is a 'two species' model, involving spins and fermions, while the Hubbard model involves interacting electrons (at half filling in our case). For the KLM, the usual approach is to use a variant of classical Monte Carlo (assuming that the spins can be treated as classical) while the Hubbard model is solved via quantum Monte Carlo, cluster DMFT, or some form of cluster

perturbation theory. We discuss the KLM problem first in the next section, and then describe our approach to the Hubbard problem.

2.1.1 Kondo lattice systems

The Kondo lattice is a 'two-species' model, in which electrons delocalise on an underlying lattice, via hoppings t_{ij}, and couple locally to core spins $\mathbf{S}_i$. The core spins are supposed to arise from high spin states of electrons well below the Fermi level. The coupling between the electrons and spins, J, would be large in our system.

$$H_{KLM} = \sum_{\langle ij \rangle \sigma} t_{ij} \left[c_{i\sigma}^\dagger c_{j\sigma} + \text{h.c.} \right] + J \sum_i \mathbf{S}_i.\vec{\sigma}_i \qquad (2.3)$$

The electronic properties emerge as a function of spatial arrangements of spins. The probability $P\{\mathbf{S}_i\}$ of a spin configuration is decided by the electron free energy in that background.

$$P\{\mathbf{S}_i\} = \frac{Tr_{c,c^\dagger} e^{-\beta H_{KLM}}}{\int D\mathbf{S} \ Tr_{c,c^\dagger} e^{-\beta H_{KLM}}} \qquad (2.4)$$

To obtain $P\{\mathbf{S}_i\}$, one has to evaluate the trace over the fermions. This is analytically computable only in limiting cases, and in general one has to resort to some numerical scheme. We use an exact diagonalization based Monte Carlo (ED-MC) to sample the distribution $P\{\mathbf{S}_i\}$. The electronic properties are computed by diagonalizing H_{KLM} in the equilibrium configurations of the sampled $P\{\mathbf{S}_i\}$. The detailed procedure is discussed in Section 2.3.1.

2.1.2 The Hubbard model

The Hubbard model describes interacting electrons on a lattice, and is defined by

$$H = \sum_{\langle ij \rangle \sigma} t_{ij} \left[c_{i\sigma}^\dagger c_{j\sigma} + \text{h.c.} \right] - \mu \sum_i \hat{n}_i + U \sum_i \hat{n}_{i\uparrow} \hat{n}_{i\downarrow} \qquad (2.5)$$

t_{ij} is the hopping amplitude, usually taken to be non-zero only between nearest neighbours $\langle ij \rangle$ on a given lattice. It can be non-zero for further neighbours as well and for a specific material should be determined via *ab initio* calculation.

The Hubbard problem looks very different from the classical spin Kondo lattice. Beyond weak coupling it has been traditionally handled via quantum Monte Carlo and exact diagonalization tools. Approximate schemes like DMFT also ultimately

resort to these tools. These methods have a serious size limitation, despite the enormous increase in computing power over the last two decades, and are still not able to access complex magnetic states.

We use a new approach, discussed in the next section, which focuses on spatial order and its fluctuations and allows us to access large lattice sizes. It is approximate in nature, and maps the Hubbard problem at half filling to an effective Kondo lattice like problem.

2.2 Approximations

2.2.1 'Classical' approximation in the Kondo lattice

The model for that we will use for the double perovskites involves two sets of spatially alternating electronic levels connected by a hopping amplitude, with the electrons on one of these sites coupling to a core spin. This model involves two simplifications with respect to the real material.

(a) The conduction states in reality are orbitally degenerate.

(b) The core spin is a quantum degree of freedom.

In a material like SFMO the bands near the Fermi level are formed by 3 t_{2g} (xy, yz, zx) orbitals which delocalize in $x - y$, $y - z$, $z - x$ planes respectively. Multiple orbitals could, in principle, have a qualitative effect on the physics, as it does in the manganites via the Jahn-Teller distortion. The double perovskites do not seem to involve strong lattice effects and the orbital degeneracy survives. In this situation a single band model can describe the qualitative physics. In addition, a comparison to *ab initio* results, which include the full electronic structure, confirms the usefulness of the single band approach.

The local moment in SFMO has magnitude $S = 5/2$. So, while the original Kondo lattice model of $S = 1/2$ moments coupled to electrons essentially involves quantum dynamics of the spins, the double perovskite case can be approximated by treating the core spins as classical. The quantum effects can be built in later via a $1/S$ expansion [129].

2.2.2 Static approximation in the Hubbard model

The presence of two body interaction requires the use of approximations, or numerical tools, when studying the large U behaviour of the Hubbard model. We opt for an

auxiliary field decomposition that captures the mean field ground state but retains all thermal fluctuations. We use a Hubbard-Stratonovich (HS) transformation, below, to decouple the interaction in terms of auxiliary fields ϕ_i and $\mathbf{m}_i$ which couple to charge and spin densities respectively. The specific form of the decomposition was suggested by Hubbard [130,131] and explored further by Schulz [132]. It is motivated by the need to capture Hartree-Fock theory at saddle point, and retain the correct spin rotation invariance (and Goldstone modes). In terms of the Grassmann field $\psi_{i\sigma}(\tau)$, we have:

$$\exp\left[U\sum_i \bar{\psi}_{i\uparrow}\psi_{i\uparrow}\bar{\psi}_{i\downarrow}\psi_{i\downarrow}\right] = \int \prod_i \frac{d\phi_i d\mathbf{m}_i}{4\pi^2 U} \exp\left[\frac{\phi_i^2}{U} + i\phi_i\rho_i + \frac{\mathbf{m}_i^2}{U} - 2\mathbf{m}_i \cdot \mathbf{s}_i\right] \quad (2.6)$$

where charge and spin densities are defined as,

$$\rho_i = \sum_\sigma \bar{\psi}_{i\sigma}\psi_{i\sigma}, \quad \text{and} \quad \mathbf{s}_i = \frac{1}{2}\sum_{a,b} \bar{\psi}_{ia}\vec{\sigma}_{ab}\psi_{ib} \quad (2.7)$$

The partition function is now written as

$$Z = \int \prod_i \frac{d\bar{\psi}_{i\sigma}d\psi_{i\sigma}d\phi_i d\mathbf{m}_i}{4\pi^2 U} \exp[-\int_0^\beta \mathcal{L}(\tau)]$$

where, the Lagrangian $\mathcal{L}(\tau)$ is (all operators have τ dependence)

$$\mathcal{L}(\tau) = \sum_{i\sigma} \bar{\psi}_{i\sigma}\partial_\tau\psi_{i\sigma} + H_0(\tau) + \sum_i \left[\frac{\phi_i^2}{U} + (i\phi_i - \mu)\rho_i + \frac{\mathbf{m}_i^2}{U} - 2\mathbf{m}_i \cdot \vec{s}_i\right] \quad (2.8)$$

At half filling ($n = 1$), we make the following two approximations:

(a) We freeze the ϕ_i to its saddle point value $(U/2)\langle n_i \rangle = U/2$. This is motivated by the large U, which in the half-filled situation would penalise charge fluctuations. It is worth noting that away from half filling there would be ϕ_i fluctuations even at large U.

(b) We neglect the τ dependence of $\mathbf{m}_i(\tau)$ field but retain its full spatial dependence. This allows unbiased choice of the $T = 0$ magnetic state, and retains the thermal spin fluctuations on that state.

These two approximations lead to a model of electrons coupled to a the spatially fluctuating classical field $\mathbf{m}_i$. After making $\mathbf{m_i}$ dimensionless, by simple scaling

$\mathbf{m}_i \rightarrow \frac{U}{2}\mathbf{m}_i$, the half filled Hubbard model is mapped to the following effective Hamiltonian.

$$H = \sum_{\langle ij \rangle \sigma} t_{ij} \left[c_{i\sigma}^\dagger c_{j\sigma} + \text{hc} \right] + \sum_{i\sigma} (\frac{U}{2} - \mu)n_{i\sigma} - \frac{U}{2} \sum_i \mathbf{m}_i \cdot \vec{\sigma}_i + \frac{U}{4} \sum_i \mathbf{m}_i^2 \qquad (2.9)$$

where $\vec{\sigma}_i = \sum_{a,b} c_{ia}^\dagger \vec{\sigma}_{ab} c_{ib} = 2\mathbf{s}_i$. This model (equation (2.9)) has a classical part H_{cl}, and electronic part H_{el} describing electrons coupled to $\mathbf{m}_i$ fields, where -

$$H_{el} = \sum_{\langle ij \rangle \sigma} t_{ij} \left[c_{i\sigma}^\dagger c_{j\sigma} + \text{hc} \right] + \sum_{i\sigma} (\frac{U}{2} - \mu)n_{i\sigma} - \frac{U}{2} \sum_i \mathbf{m}_i \cdot \vec{\sigma}_i \qquad (2.10)$$

$$H_{cl} = \frac{U}{4} \sum_i \mathbf{m}_i^2 \qquad (2.11)$$

This resembles the KLM, with the crucial difference that the $\mathbf{m}_i$ are not of fixed magnitude. Nevertheless, the Kondo lattice like model for the double perovskites, and the approximate model derived from Hubbard, can be solved by the same tools.

Neglecting time dependence in the Hubbard case has several physical consequences that we will discuss later. In terms of advantages it allows:

- The access to non trivial magnetic states and captures their T_c scales accurately.

- It can access spectral and transport properties without any need for analytic continuation.

- It is not tied to long range order, and can describe a spin disordered Mott state and correlated metal as well.

2.2.3 Consequences of the approximations

The results of the KLM with $S = 5/2$ are well approximated by treating the spins as classical. Quantum effects, for example spin waves, can be extracted via a $1/S$ expansion [129].

For the Hubbard model, as we mentioned above, and would see in detail in Chapter 4, our approximate scheme allows access to the finite temperature physics rather well. However, the neglect of quantum dynamics of the auxiliary fields $\mathbf{m}_i$ results in: (a) missing the correlation effects in the ground state of the metal, overestimating its energy and underestimating the critical U/t for metal-insulator transition, and (b) missing a possible quantum spin liquid insulator [102, 103] at intermediate U/t. We will discuss these issues in the relevant chapter.

2.3 Numerical Methods

Both the models, the KLM (equation (2.3)) and effective Hubbard model (equation (2.9)), have one feature in common. They both describe the motion of electrons in the presence of spatially fluctuating classical fields, which are localized spins for KLM, and the auxiliary fields for the effective Hubbard model. Both problems are to be solved at strong coupling ($J/t \gg 1$ for KLM, or $U/t \gg 1$ for Hubbard model), which is well beyond the perturbative regime. In the absence of analytical tools one resorts to numerical methods. The numerical methods we use are broadly the following:

(a) Real space Monte Carlo, where one 'anneals' the classical fields from high to low temperature and samples the distribution of the classical field using Metropolis sampling.

(b) Variational minimization, in which we use a family of spatially periodic configurations of the classical variable and minimize the electronic energy over them.

As we discussed, the KLM (equation (2.3)) and effective Hubbard model (equation (2.9)), both describe electron propagation in a classical background of spins $\{\mathbf{S}_i\}$ of fixed magnitude (KLM), or the auxiliary fields $\{\mathbf{m}_i\}$ (effective Hubbard model). For a *given* configuration $\{\mathbf{m}_i\}$ (or $\{\mathbf{S_i}\}$), the electronic Hamiltonian H_{el} is quadratic in electronic operators, and one just needs to diagonalize it to get the single particle eigenvalues. The total energy of the system is sum of (i) the classical part and (ii) the electronic part which is sum of eigenvalues up to the chemical potential at $T = 0$, or the free energy at finite T.

However, the configurations $\{\mathbf{m}_i\}$ (or $\{\mathbf{S_i}\}$), themselves have to be determined from a certain distribution. At finite temperature, the thermal distribution of the fields is given by $P\{\mathbf{m}_i\}$ (or $P\{\mathbf{S}_i\}$):

$$P\{\mathbf{m}_i\} \propto Tr_{c,c^\dagger} e^{-\beta H_{el}} e^{-\beta H_{cl}} \tag{2.12}$$

The fermion trace is not analytically calculable when the magnetic coupling term is comparable to the kinetic energy and we need to converge towards the $P\{\mathbf{m}_i\}$ via an iterative combination of the Metropolis algorithm and exact diagonalisation. This is discussed next.
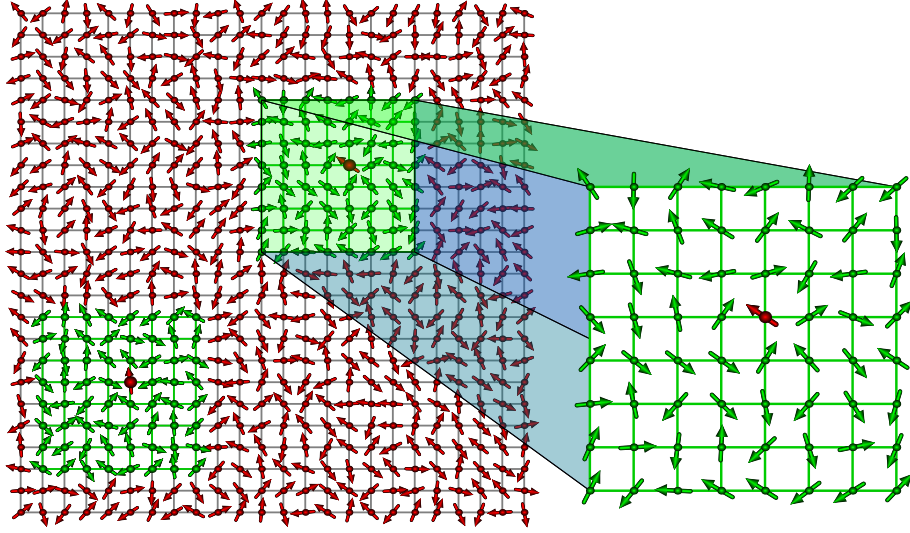
Figure 2.1: Visualization of the our cluster based update scheme.

2.3.1 Real space Monte Carlo

We set up the electronic Hamiltonian in real space basis for a given lattice size for an initial configuration of the classical field and attempt to 'update' this configuration. The energy cost of this update has to be computed through the free energy change of the entire system. The transition probability between configurations is $\propto \exp\left(-\beta(F' - F)\right)$, where F' and F are free energy in the attempted and initial configuration respectively. Computing $F' - F$ requires diagonalizing H_{el}. This involves an $\mathcal{O}(N^3)$ computational cost per update, *i.e*, the cost per MC sweep would be N^4. This limits the accessible lattice size to $N \sim 100$.

To access larger sizes within reasonable time we use a cluster algorithm (TCA) [133] for estimating the update cost. Here, rather than diagonalize the full H_{el} for every attempted update, we compute the update cost by diagonalizing a cluster (of size $N_c \sim 64$, say) around the reference site. This scheme has been extensively benchmarked [133] and works reasonably unless we are attempting to recover states with a large spatial period. A cartoon of the cluster scheme is shown in figure 2.1. The computational cost now scales as $N\mathcal{O}(N_c^3)$ which is linear in lattice size N. This lets us access large lattice sizes (24×24 in 2D (with $N_c = 8^2$), and $12 \times 12 \times 12$ (with $N_c = 4^3$) in 3D.

Once equilibrium is attained within the Monte Carlo scheme at a given temperature we use the MC configurations to calculate various properties of interest. Below we list some of the key indicators that we track in the KLM and Hubbard model.

2.3.1.1 Auxiliary field properties

- $P(m)$: This describes the magnitude distribution of the $\mathbf{m}_i$ fields:

$$P(m) = \frac{1}{N} \sum_i \langle \delta(m - |\mathbf{m}_i|) \rangle \qquad (2.13)$$

The sum is over all the lattice sites, and $\langle .. \rangle$ denote the average over thermally sampled field configurations. This quantity is irrelevant for KLM model, as the spins are fixed magnitude fields. For the Hubbard model it provides crucial insight into Mott physics.

- Structure factor $S(\mathbf{q})$: The angular correlation is accessed via the thermally averaged structure factor —

$$S(\mathbf{q}) = \frac{1}{N^2} \sum_{ij} \langle \mathbf{m_i} \cdot \mathbf{m_j} \rangle e^{i\mathbf{q} \cdot (\mathbf{X}_i - \mathbf{X}_j)} \qquad (2.14)$$

at each temperature. The onset of rapid growth in $S(\mathbf{q})$ at some $\mathbf{q} = \mathbf{Q}$, say, indicates a magnetic transition. The electronic properties are calculated by diagonalizing H_{el} on the full lattice for equilibrium $\{\mathbf{m}_i\}$ configurations. The nature of these correlations is characterized by the $\mathbf{q}$ at which the maximum.

2.3.1.2 Electronic properties

- Density of states (DOS) $N(\omega)$ at a given temperature is obtained by taking thermal average of the single configuration DOS over equilibrium $\mathbf{m}_i$ samples —

$$N(\omega) = (1/N) \sum_\alpha \langle \delta(\omega - \epsilon_\alpha) \rangle \qquad (2.15)$$

The ϵ_α above are the eigenvalues in a single equilibrium configuration.

- Optical Conductivity $\sigma(\omega)$: The conductivity is calculated using the Kubo formula (ref. [134]), which takes the form for a non-interacting disordered system

$$\sigma^{xx}(\omega) = \frac{\sigma_0}{N} \sum_{\alpha,\beta} \frac{n_\alpha - n_\beta}{\epsilon_\beta - \epsilon_\alpha} |\langle \alpha | J_x | \beta \rangle|^2 \delta(\omega - (\epsilon_\beta - \epsilon_\alpha)) \qquad (2.16)$$

where the current operator $\vec{\mathbf{J}}$ is

$$\vec{\mathbf{J}} = -i \sum_{i,\sigma,\vec{\delta}} \left[\vec{\delta} t_{\vec{\delta}} \, c^{\dagger}_{\mathbf{X}_i,\sigma} c_{\mathbf{X}_i+\vec{\delta},\sigma} - \text{h.c.})\right] \tag{2.17}$$

The d.c conductivity is the $\omega \to 0$ limit of the result above. $\sigma_0 = \frac{\pi e^2}{\hbar}$ in 2D and $\frac{\pi e^2}{\hbar a_0}$ in 3D (a_0 is the lattice spacing in the relevant direction). $n_\alpha = f(\epsilon_\alpha)$ is the Fermi function, and ϵ_α and $|\alpha\rangle$ are respectively the single particle eigenvalues and eigenstates of H_{eff} in a given background $\{\mathbf{m}_i\}$.

- Spectral function $A(\mathbf{k},\omega)$: We extract the thermal and spin averaged spectral function $A(\mathbf{k},\omega)$ as follows. The retarded Greens function

$$G_\sigma(\mathbf{k},t) = -i\theta(t)\langle\{c_{\mathbf{k}\sigma}(t), c^{\dagger}_{\mathbf{k}\sigma}(0)\}\rangle \tag{2.18}$$

can be simplified to the following

$$G_\sigma(\mathbf{k},t) = -i\theta(t)\sum_\alpha |\langle \mathbf{k}\sigma|\alpha\rangle|^2 e^{-i\epsilon_\alpha t} \tag{2.19}$$

where $\{|\alpha\rangle\}$ are the single particle eigenstates and ϵ_α are eigenvalues in a given $\{\mathbf{m}_i\}$ background. Doing the Fourier transform to frequency, one gets

$$G_\sigma(\mathbf{k},\omega) = \sum_\alpha \frac{|\langle \mathbf{k}\sigma|\alpha\rangle|^2}{\omega - \epsilon_\alpha + i0^+} \tag{2.20}$$

Then, we have the spectral functions as

$$A_\sigma(\mathbf{k},\omega) = -\frac{1}{\pi}\text{Im}G_\sigma(\mathbf{k},\omega) = \sum_\alpha |\langle \mathbf{k}\sigma|\alpha\rangle|^2 \delta(\omega - \epsilon_\alpha) \tag{2.21}$$

We average this over the sampled thermal configurations. The low frequency part of the spectral function $A_\sigma(\mathbf{k},\omega = 0)$ serves to identify the shape of the Fermi surface, and the hot and cold spot locations.

2.3.2 Variational minimization at $T = 0$

When the Monte Carlo suggests that the system is heading towards a state with periodic spatial behaviour, a simple way to access the possible ground state is to try a family of variational configurations. For simple enough configurations (discussed further on) the electronic model may be analytically solvable. Even when that is

not possible, the numerical cost of diagonalising a system of size N for N_{trial} configurations is $\sim N_{trial}N^3$, compared to the $N_{tempr}N_{sweep}N^4$ cost involved in the MC. N_{tempr} is the number of temperature points and N_{sweep} is the number of MC sweeps per temperature.

Taking our representation of the Hubbard model (equation (2.9)) and assuming a set of periodic configurations $\mathbf{m}_i$ defined by a magnitude m and period $\mathbf{q}$:

$$\mathbf{m}_i = m\big(\cos\mathbf{q}\cdot\mathbf{x}_i, \;\; \sin\mathbf{q}\cdot\mathbf{x}_i, \;\; 0\big) \tag{2.22}$$

we have

$$H_{el} = \sum_{\mathbf{x},\vec{\delta},\sigma} t_{\vec{\delta}}\left[c^\dagger_{\mathbf{x},\sigma}c_{\mathbf{x}+\vec{\delta},\sigma} + \text{h.c.}\right] - \frac{Um}{2}\sum_{\mathbf{x}}\left(e^{-i\mathbf{q}\cdot\mathbf{x}}c^\dagger_{\mathbf{x}\uparrow}c_{\mathbf{x}\downarrow} + e^{i\mathbf{q}\cdot\mathbf{x}}c^\dagger_{\mathbf{x}\downarrow}c_{\mathbf{x}\uparrow}\right) \tag{2.23}$$

This can be simplified by doing Fourier transformation to

$$H = \sum_{\mathbf{k}}\begin{pmatrix}c^\dagger_{\mathbf{k},\uparrow} & c^\dagger_{\mathbf{k}-\mathbf{q},\downarrow}\end{pmatrix}\begin{pmatrix}\epsilon_{\mathbf{k}} & -\frac{Um}{2} \\ -\frac{Um}{2} & \epsilon_{\mathbf{k}-\mathbf{q}}\end{pmatrix}\begin{pmatrix}c_{\mathbf{k},\uparrow} \\ c_{\mathbf{k}-\mathbf{q},\downarrow}\end{pmatrix} \tag{2.24}$$

Where $\epsilon_{\mathbf{k}}$ is the tight binding dispersion for the lattice. For an anisotropic triangular lattice this is given by $\epsilon_{\mathbf{k}} = -2t(\cos k_x + \cos k_y) - 2t'\cos(k_x + k_y)$. The eigenvalues can be readily obtained, and one gets

$$\epsilon_{\pm,\mathbf{k}} = \frac{1}{2}\left[\epsilon_{\mathbf{k}} + \epsilon_{\mathbf{k}-\mathbf{q}} \pm \sqrt{(\epsilon_{\mathbf{k}} - \epsilon_{\mathbf{k}-\mathbf{q}})^2 + U^2m^2}\right] \tag{2.25}$$

Once we get the dispersion, the total energy is

$$E(m,\mathbf{q}) = \sum_{\mathbf{k},\alpha=\pm}\theta(\mu - \epsilon_{\alpha,\mathbf{k}})\epsilon_{\alpha,\mathbf{k}} + \frac{U}{4}Nm^2 \tag{2.26}$$

To get the ground state, we minimize the total energy $E(m,\mathbf{q})$ with respect to the magnitude 'm' and vector $\mathbf{q}$. On a two dimensional $L \times L$ lattice, $\mathbf{q}$ can take L^2 values, as $\mathbf{q} = \frac{2\pi}{L}(q_x, q_y)$, where q_x, q_y are integers ranging from 0 to $L-1$. One can discretise m (bounded between $[0,1]$) into ~ 100 intervals. As we will see in the solution of the 2D Hubbard model this provides some intuition into the nature of possible magnetic order.
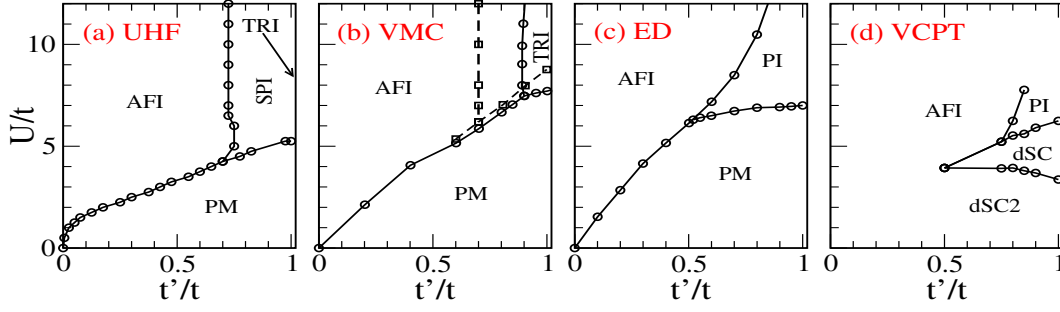
Figure 2.2: The ground state phase diagram obtained by different methods on the anisotropic triangular lattice. (a). Our auxiliary field based (unrestricted Hartree-Fock) result, (b). Variational Monte Carlo (VMC) by Luca *et al* [95, 104], (c). Exact diagonalisation (ED) by Clay *et al* [105], and (d). Variational cluster perturbation theory (VCPT) by Sahebsara *et al* [102, 107]. Within all schemes the ground state is a paramagnetic metal at weak coupling (and large t'/t), a Neel ordered antiferromagnetic insulator (AFI) at large U/t and small t'/t. The detailed character of the large U/t and large t'/t state varies between the methods [92–95].

2.4 Benchmarks

Here we discuss selected benchmarks for our methods. We first provide a quick comparison of our results with results from other methods (to be elaborated in individual chapters later), and then discuss issues of size dependence.

2.4.1 Comparison with other methods

For the double perovskite model in three dimensions there is no other theoretical effort probing the regime that we explore in this thesis. We will discuss the issue of size dependence of our results in the appropriate chapter.

For the Hubbard model in 2D, on the anisotropic triangular lattice, there is a significant body of work. We had summarised these in the first chapter. Here we provide a quick comparison of these results with the ground state obtained by our approach. This is to establish the basic usefulness of the auxiliary field approach. Detailed indicators at finite temperature will be taken up in Chapter.4.

The principal methods for the ground state include variational Monte Carlo (VMC) used by Luca *et al* [95, 104], exact diagonalization (ED) by Clay *et al* [105], and variational cluster perturbation theory (VCPT) by Sahebsara *et al* [102, 107].

Fig. 2.2 shows the comparison of results from these methods with that from the auxiliary field based minimisation (equivalent at $T = 0$ to unrestricted Hartree-Fock (UHF) theory). The qualitative trends in the UHF result match with that in the more
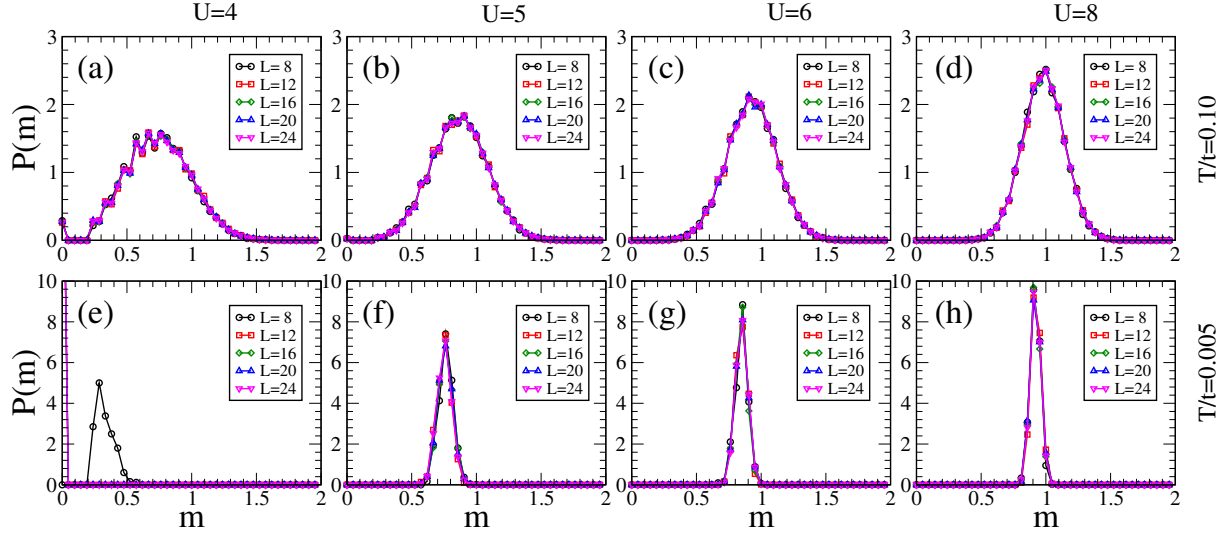
Figure 2.3: Lattice size L dependence of the field magnitude distribution $P(m)$ for the Hubbard model on triangular lattice with $t'/t = 0.8$. Four columns are for four representative values of $U = 4, 5, 6, 8$, at low temperature $T/t = 0.005$ ((a)-(d)) and high temperature $T/t = 0.10$ ((e)-(h)).

sophisticated approaches. At finite T, where the wavefunction based approaches have limited use, the auxiliary field scheme would have a distinct advantage.

Most of the finite temperature studies have employed dynamical mean field theory (DMFT) and its cluster variant (C-DMFT). DMFT recovers some of the generic features in transport [83] and optics [86] but does not capture the impact of magnetic correlations. C-DMFT has not been employed to explore response functions yet. We will compare our results to these wherever possible.

On the FCC lattice, there is hardly any theoretical work, except for a very early attempt using conventional static mean field theory [128]. A recent experimental paper [115] does present a DMFT based phase diagram but that again does not retain any of the magnetic correlations that would be important close to the Mott transition.

2.4.2   Size dependence within the MC

In this section we provide a discussion of the size dependence of our results in the 2D anisotropic triangular lattice Hubbard model, and establish that the 24×24 lattice that we use in Chapter.4 is adequate for most physical properties. This will allow us to focus on the physics issues there without digressing into questions of finite size.

In what follows we show results on the anisotropic triangular lattice at $t'/t = 0.8$
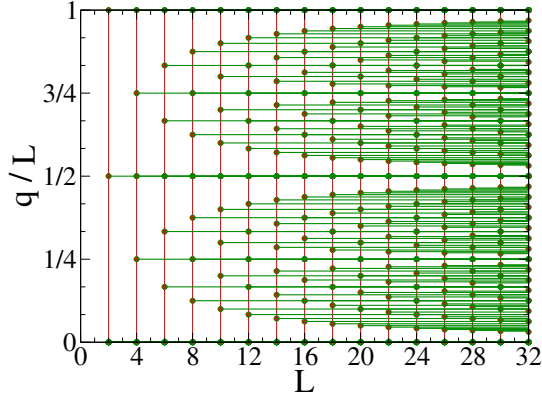
Figure 2.4: Lattice size L versus the allowed q values on the given lattice. Points on the vertical lines are the allowed values of the components (up-to 2π) on $L \times L$ lattice. Horizontal lines connect the same q values on different lattice sizes.

and focus on the magnetic indicators. Electronic properties are controlled by these.

Fig.2.3 shows the magnitude distribution $P(m)$ of the auxiliary fields $\mathbf{m}_i$, at two temperatures ($T/t = 0.1, 0.005$) for four representative values, $U/t = 4, 5, 6, 8$ across the Mott transition, for lattice sizes $L \times L$ with L ranging from 8 to 24. The distribution is broad at high temperature and sharply peaked at low temperature. The $P(m)$ is practically insensitive to lattice size L at all U at high temperature. At low temperature and large U the results are again independent of L but at the lowest U, close to the Mott transition value, the $L = 8$ data differs from the larger U results. Beyond $L = 12$ however even here the results are essentially size independent.

Figure 2.5: Lattice size L dependence of the structure factor $S(\mathbf{q})$ which describes the angular correlations of the $\mathbf{m}_i$ fields, for two representative values of (a) $U = 4$, when the ground state is non-magnetic, and (b) $U = 8$, when the ground state is in Mott insulating phase.

65
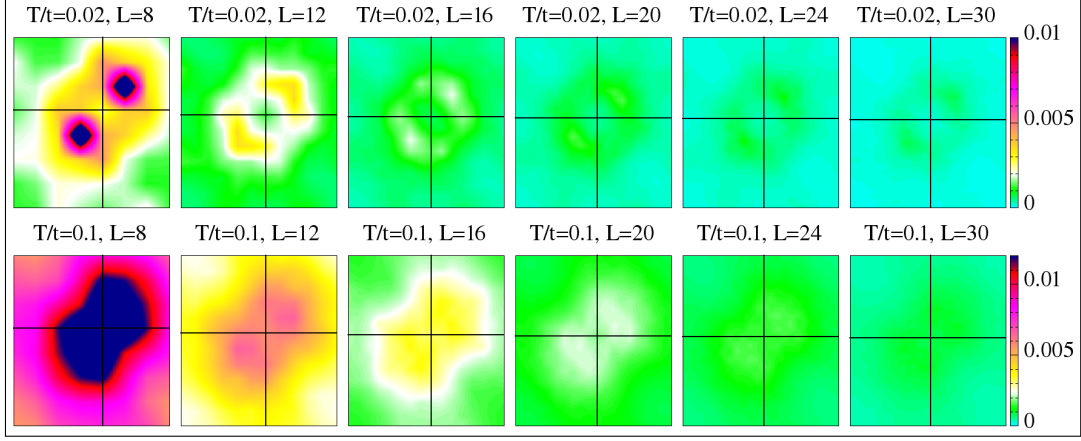
Figure 2.6: Lattice size L dependence of the full structure factor $S(\mathbf{q})$ for $U/t = 4$, at two temperatures $T/t = 0.02$ (low temperature, upper row) and $T/t = 0.1$ (high temperature, lower panel). q_x, q_y are along x, y direction in range $[0, 2\pi]$.
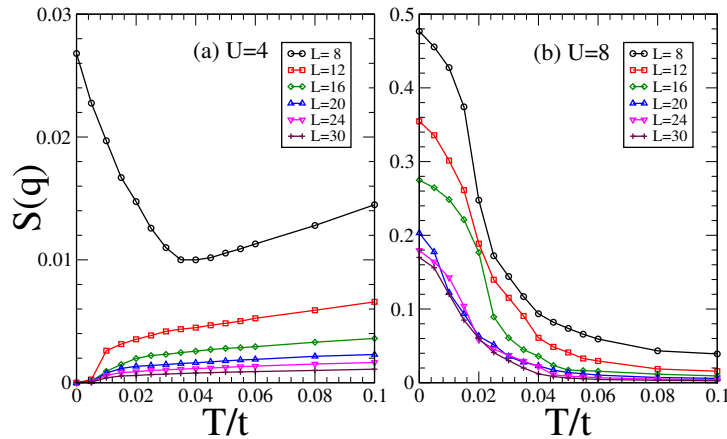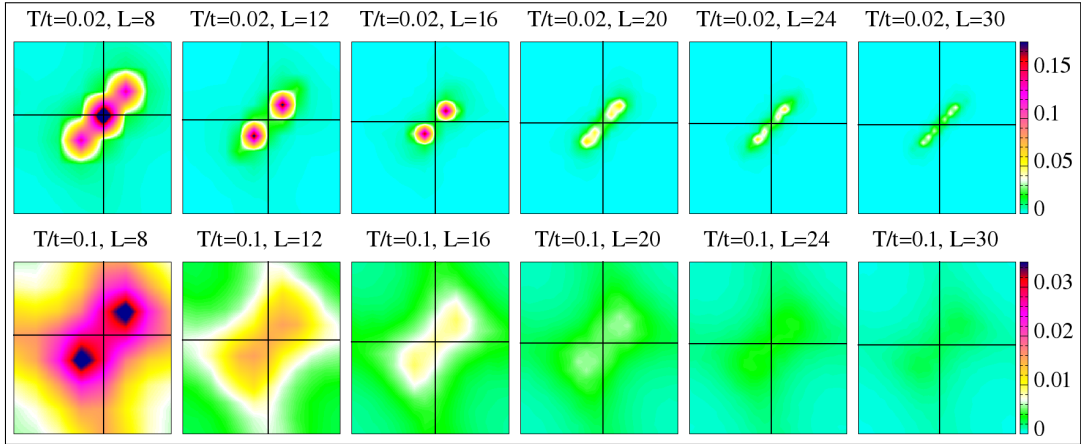

Figure 2.7: Lattice size L dependence of the full structure factor $S(\mathbf{q})$ for $U/t = 8$, in the same T, L set as figure 2.6. q_x, q_y are along x, y direction in range $[0, 2\pi]$.

We probed the underlying state more closely in terms of magnetic correlations, rather than the gross size distribution. The allowed values of momentum change with system size. On the $L \times L$ lattice the allowed $\mathbf{q}$ are given by $\mathbf{q} = 2\pi\left(\frac{q_x}{L}, \frac{q_y}{L}\right)$ where q_x, q_y are integers in the range $0, 1, 2, ...L - 1$. In Fig.2.4 we show the q_x, say, that are available for varying lattice size. For each choice of L the points on the vertical line indicate this.

The next figure shows the temperature dependence of the peak in the magnetic structure factor for two values of U and a wide range of L. The left panel establishes that there is no magnetic order (and in fact no magnetic moment) at $T = 0$ in the $U = 4$ problem. The $L = 8$ case shows a weak correlation, associated with the finite size effect highlighted for $P(m)$. The strength of correlation at finite temperature

66
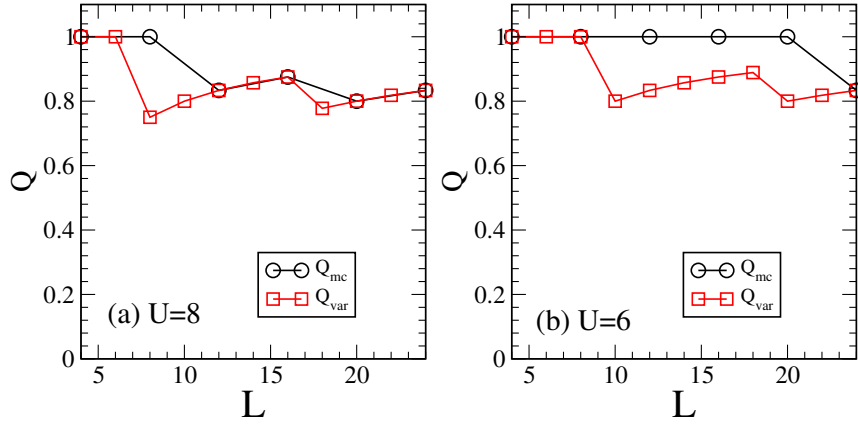
Figure 2.8: Lattice size L dependence of the structure factor $S(\mathbf{q})$ peak $\mathbf{q}$ from Monte Carlo and variational minimization, (a). $U/t = 8$, (b). $U/t = 6$. In general the minimising $\mathbf{Q}$ would be $\hat{x}Q_x + \hat{y}Q_y$. Within both the MC and the VC we get solutions that are roughly of the form $\hat{x}Q + \hat{y}Q$. This Q is plotted here, in units of π.

does depend on L but is reasonably stable by the time $L = 24$. For $U = 8$, right panel, the lower L values give significantly enhanced values, and strong size dependence, in the $S(\mathbf{q})$ peak, but the results stabilise for $L \geq 20$.

The full $\mathbf{q}$ dependence of $S(\mathbf{q})$ is quite instructive. Fig.2.6 shows the result at $U/t = 4$ and Fig.2.7 at $U/t = 8$, in each case for two temperatures, $T/t = 0.02$ and $T/t = 0.1$. The panels from left to right are for increasing L as indicated.

For $U/t = 4$, low T suggests ordering at a wavevector $\sim (0.8\pi, 0.8\pi)$ but this is systematically diminished with growing size. There are no moments and no order in the large L system. The higher T result suggests short range correlation and that pattern is reasonably stable with L. At this U/t we need $L \geq 20$ to get a reliable picture of the ground state.

At larger U, Fig.2.7, the moments are stable but the ordering pattern depends on L. $L = 8$ has a peak at (π, π), and weak satellites, suggesting Neel order. With increasing L however the peak shifts away from Neel order to $\mathbf{q} \sim (0.8\pi, 0.8\pi)$, a spiral state (weak a weaker peak in $S(\mathbf{q})$). Again for $L \geq 20$ the pattern is stable. Accessing the correct ground state even deep in the Mott window requires fairly large L. The high temperature data has a $\mathbf{q}$ dependence that is similar at all L, and is quantitatively stable for $L \geq 20$.

Overall, conclusions about the magnetic ground state and fluctuations can depend strongly on system size, but for $L = 24$ that we employ in 2D in most of the calculations the results are free of finite size artifacts.

Variational minimisation also involves a size dependence and we discover that

for $L \geq 20$ the VC results are reasonably stable and the Monte Carlo and VC based estimates are mutually consistent. Fig.2.8 compares the L dependence of the ordering wavevector at two U values and suggests that for $L = 24$ the conclusions are similar. Most of our MC results are at $L = 24$ but we have checked some data points at $L = 30$ as well.

The checks above will allow us to focus on the physics that emerges from our calculation without having to check for finite size artifacts frequently.

NON-COLLINEAR MAGNETIC ORDER IN THE DOUBLE PEROVSKITE

3.1 Introduction

In this chapter we discuss magnetism in the metallic double perovskites $A_2BB'O_6$. These involve a transition metal ion B, with a large magnetic moment, and a non magnetic ion B'. While many double perovskites (DP) in this category are ferromagnetic there are hints of antiferromagnetic phases at higher electron doping. These are driven by *electron delocalisation*, instead of the short range superexchange seen in magnetic insulators.

We will present a comprehensive study of the magnetic ground state and T_c scales of the minimal double perovskite model in three dimensions, using a combination of spin-fermion Monte Carlo and variational calculations. The model is defined on the three dimensional cubic lattice, where B and B' sites are in a rock salt pattern (Fig.3.1). The sublattice of the magnetic B atoms is face centered cubic (FCC) and geometrically disallows a Neel state. As a result, the antiferromagnetic tendency manifests itself as spiral order, or non-coplanar 'flux' like phases. We will map out the possible magnetic phases for varying electron density, the level separation between the B and B' ions, and the crucial B'-B' (next neighbour) hopping t'.

Previous study of double perovskites in two dimensions [63] revealed three collinear phases, namely ferromagnet (FM), a diagonal stripe phase (FM lines coupled antiferromagnetically) and a 'G type' phase (up spin surrounded by down and *vice versa*). In 2D the B sublattice is square and bipartite, so there is no frustration. If we had a 3D *simple cubic* B lattice the counterparts of the 2D phases would be FM, A type
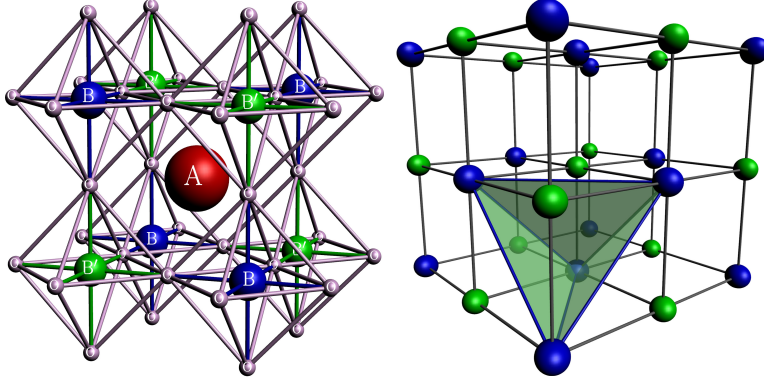
Figure 3.1: Left: The lattice structure of the ordered double perovskite $A_2BB'O_6$. Right: The same structure with oxygen removed, shows how B-B′ sites are arranged in rock-salt ordering. If the bottom corner (blue) atom is B, then its B nearest neighbours (connected by blue lines) are also nearest neighbours of each other. The triangles preclude Neel order.

(planar), C type (line like) and G type (Neel). The B ion lattice in 3D is FCC, so, while the FM and planar (A type) phases can exist, the C type phase is modified and the G type phase is disallowed.

Fig.3.1(right) indicates why it is impossible to have an 'up' (↑) B ion to be surrounded by only 'down' (↓) B ions, *i.e.*, the G type arrangement. Two B neighbours of a B ion are also neighbours of each other, frustrating G type order. The suppression of the G type phase, which occupies a wide window in 2D, requires us to move beyond collinear phases in constructing the phase diagram for 3D. We will discuss the variational family in Section 3.1.1.

Using a combination of Monte Carlo and variational minimization, our main results are the following:

- We map out the magnetic ground state at large Hund's coupling for varying electron density and B-B′ level separation. In addition to FM, and collinear A and C type order, the phase diagram includes large regions of non-collinear 'flux' and spiral phases and windows of phase separation.

- Modest B′B′ hopping leads to significant shift in the phase boundaries, and "particle-hole asymmetry".

- We provide an estimate of the T_c of these phases from the Monte Carlo where possible, or make a rough estimate based an energy difference calculation.

This chapter is organized as follows. In section 3.1.1 we define the effective single band model for the metallic double perovskites and describe the methods we use.

Section 3.2 discusses our results on the particle-hole symmetric model, and section 3.3 describes the effect of a introducing electron hopping t' between the non-magnetic sites. Section 3.4 discusses some issues of modeling the real double perovskites. We summarize and conclude the chapter in section 3.5.

3.1.1 Effective single band model

The alternating arrangement of B and B$'$ ions in the ordered cubic double perovskites is shown in Fig.3.1. We use the following one band model on that structure:

$$
\begin{aligned}
H = & \ \epsilon_B \sum_{i \in B} f_{i\sigma}^\dagger f_{i\sigma} + \epsilon_{B'} \sum_{i \in B'} m_{i\sigma}^\dagger m_{i\sigma} - \mu \hat{N} \\
& -t \sum_{\langle ij \rangle} \left[f_{i\sigma}^\dagger m_{j\sigma} + \text{hc} \right] + J \sum_{i \in B} \mathbf{S}_i \cdot f_{i\alpha}^\dagger \vec{\sigma}_{\alpha\beta} f_{i\beta}
\end{aligned}
\tag{3.1}
$$

The $f^\dagger$ correspond to the B ions and the $m^\dagger$ to the B$'$. ϵ_B and $\epsilon_{B'}$ are 'on-site' energy on the B and B$'$ sites respectively, $e.g.$, the t_{2g} level energy of Fe and Mo in SFMO. μ is the chemical potential and $\hat{N} = \sum_{i\sigma}(f_{i\sigma}^\dagger f_{i\sigma} + m_{i\sigma}^\dagger m_{i\sigma})$ is the total electron number operator. t is the hopping amplitude between nearest neighbour B and B$'$ ions. We augment this model later to study first neighbour B$'$−B$'$ hopping t' as well $(-t' \sum_{\langle ij \rangle \in B'}[m_{i\sigma}^\dagger m_{j\sigma} + \text{hc}])$. J arises from the Hund's coupling on the d shell. The Hund's coupling itself keeps the 5 core electrons polarised into a $S = 5/2$ state, and the exclusion principle forces the conduction electron spin to be antiparallel to this core spin. We will use $|\mathbf{S}_i| = 1$, and absorb the magnitude of $\mathbf{S}$ in J. $\sigma_{\alpha\beta}^\mu$ are the Pauli matrices.

The model has parameters J, ϵ_B, $\epsilon_{B'}$, and μ (or n). Since only the level difference matters, we set $\epsilon_{B'} = 0$. We have set $t = 1$, and use $J/t \gg 1$ so that the conduction electron spin at the B site is slaved to the core spin orientation. The B site levels are shifted to $\epsilon_B \pm J/2$ due to the strong on site coupling. To keep the difference between the lower B level and the B$'$ level finite we set the parameter $\epsilon_B = \Delta + J/2$, where Δ remains finite even as $J/t \to \infty$. We explore the phases as a function of n and Δ/t. We will present results for

(a) the nearest neighbour hopping model $(t'/t = 0)$ and

(b) when a non-zero B$'$-B$'$ hopping $t'/t = \pm 0.3$ is introduced.

A schematic for the on-site levels, and how they hybridize, is shown in Fig.3.2. The structural unit cell of the system has 2 atoms (one B, one B$'$), which amounts
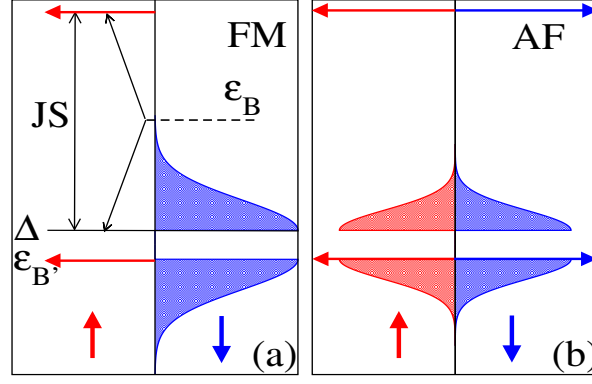
Figure 3.2: Level scheme and schematic band structure for the DP model when only B-B′ hopping is allowed. The arrows denote localized atomic levels. Red and blue denote ↑ and ↓ spins respectively. The atomic level scheme is shown in (a). where the spin degenerate B′ levels are at $\epsilon_{B'} = 0$ and the spin split B levels are at $\epsilon_B \pm JS/2$. We define the effective B level as $\Delta = \epsilon_B - JS/2$. When $JS \gg t$, the levels at $\epsilon_{B'}$ and Δ hybridize to create bands, shown for the FM case in (a), and for a collinear AF phase in (b).

to 4 atomic levels (2 up spin, 2 down spin). The two spin levels at the B site are separated by JS and overlap with 2 spin degenerate levels of the B′ site at $\epsilon_{B'} = 0$. We take Δ in the range (0-10). One B band become centered at Δ and second goes to $JS+\Delta$. In this situation the down spin B and two B′ bands overlap while up spin B band is always empty. The accessible electron density window includes the lowest three bands, so our electron density will be in the range $[0, 3]$ per formula unit.

To get a general feel of the band structure of the particle hole symmetric case, we notice that we have three levels (excluding the highest $f_\uparrow$ level at $JS + \Delta$ which remains empty and is redundant for our purpose) in atomic limit. These include one spin slaved $f_\downarrow$ level at Δ, and the two $m_\uparrow$, $m_\downarrow$, levels which overlap with the $f_\downarrow$ levels depending on the spin configurations. This overlap leads to electron delocalisation and band formation.

In the ferromagnetic case, Fig.3.2.(a), only one spin channel (say $m_\downarrow$) gets to delocalize through f sites and forms two bands, separated by a band gap of Δ, while other spin state (say $m_\uparrow$) is localized at 0.

For collinear AF configurations, the rough band scheme is as shown in Fig.3.2.(b). The conduction path gets divided into two sublattices, such that each spin channel gets to delocalize in one sublattice (in which all the core spins point in same direction, making the sublattice ferromagnetic.) See Fig.3.3(a)-(b), and Fig.3.3(c)-(d) for the details of the conduction path. In one such sublattice, only one of the ↑ or ↓ delocalized, the other remains localized. The roles of ↑ and ↓ are reversed in
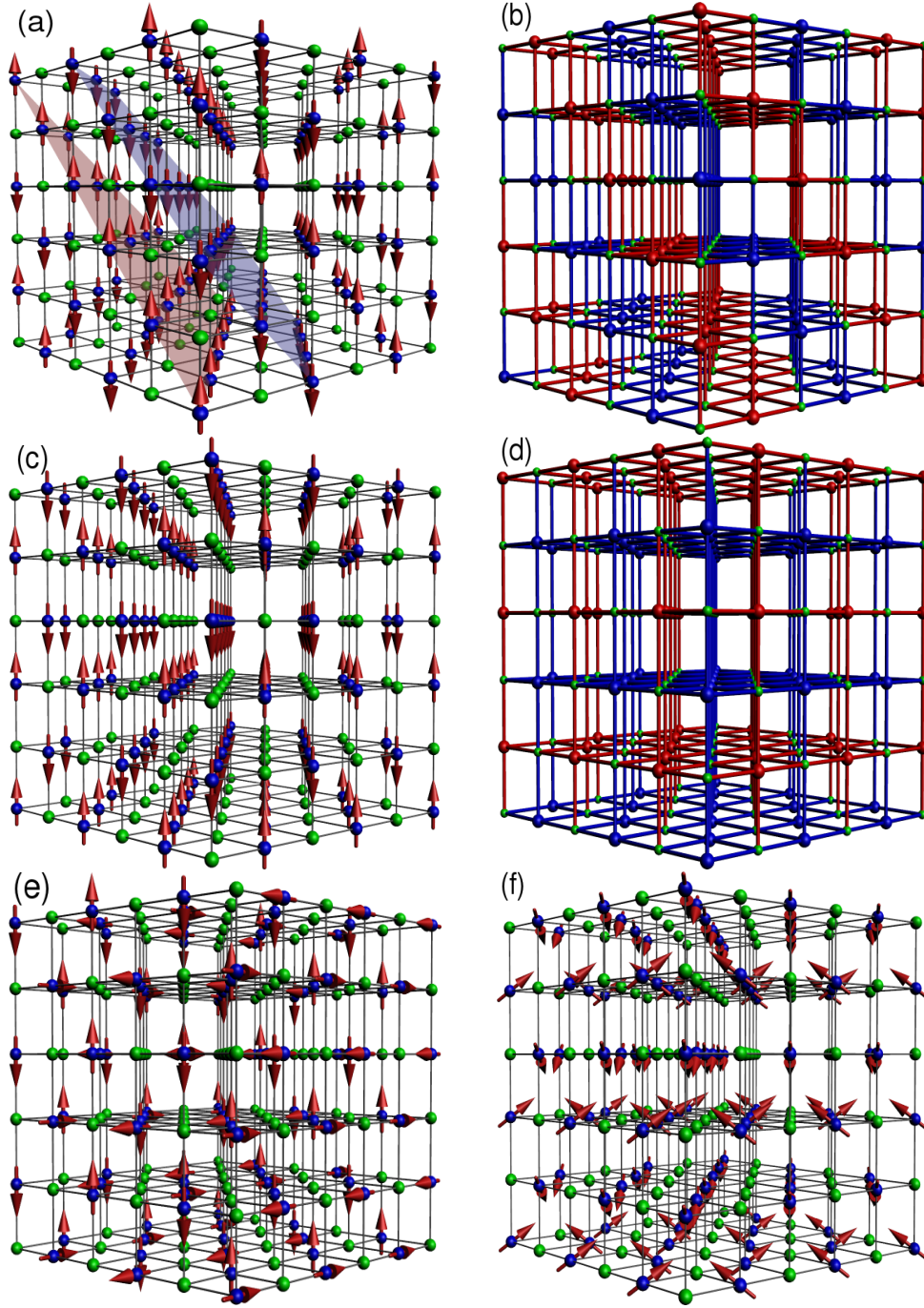
Figure 3.3: Core spin order, and corresponding electron delocalisation path. (a). 'A type' order: the spins are parallel within the 111 planes (shown) and anti-parallel between neighbouring planes. (b) The blue and red bonds show the electron delocalisation pathway for up and down spin electrons in the A type phase. The path is effectively two dimensional. (c) 'C type' phase with the spins parallel on alternating 110 planes, and anti-parallel on neighbouring planes. (d) The delocalisation path, consisting of the 110 planes and the horizontal 001 planes. (e) A typical spiral phase and (f) the 'flux' phase. Since the spin configurations are non-collinear the electrons delocalize over the whole system.

going from one sublattice to other, as a result one gets spin-degenerate localized and dispersive bands for AF phases.

3.1.2   Methods of solution

3.1.2.1   Monte Carlo

The model involves spins and fermions, and if the spins are 'large', $2S \gg 1$, they can be approximated as classical. This should be reasonable in materials like SFMO where $S = 5/2$. Even in the classical limit these spins are annealed variables and their ground state or thermal fluctuations have to be accessed via iterative diagonalization of the electronic Hamiltonian. As mentioned in chapter 2, we use a cluster based Monte Carlo (MC) method where the cost of a spin update is estimated via a small cluster Hamiltonian instead of diagonalizing the whole system [174]. We typically use a $12 \times 12 \times 12$ system with the energy cost of a move estimated via a $4 \times 4 \times 4$ cluster built around the reference site.

We principally track the magnetic structure factor to explore the nature of magnetic order

$$S(\mathbf{q}) = \frac{1}{N^2} \sum_{\mathbf{r},\mathbf{r}'} \langle \mathbf{S_r}.\mathbf{S_{r'}} \rangle e^{i\mathbf{q}\cdot(\mathbf{r}-\mathbf{r}')} \tag{3.2}$$

where $\langle ... \rangle$ denote thermal average. Although the magnetic lattice is FCC, the electrons delocalize on the combined B-B′ system which is a cubic lattice. Hence we define our wavenumbers $\mathbf{q}$ with respect to the full B-B′ lattice. As a result even a simple state like the ferromagnet corresponds to peaks at $\mathbf{q} = (0,0,0)$ and $\mathbf{q} = (\pi, \pi, \pi)$ and not just $\mathbf{q} = (0,0,0)$. This is because the spin field is also defined on B′ sites and it has to have zeros value on these sites.

The possibility of complex order in the ground state the Monte Carlo may require large annealing time, and involve noisy data. So, to complement the MC results we have also used a variational scheme discussed below.

3.1.2.2   Variational scheme

We now move to the variational approach. The variational states that we consider here are more complicated than that discussed in the last chapter, and are $\mathcal{O}(N^2)$ in number, so we need some caution in implementing the scheme. We compute the energy for periodic configurations where,

$$\mathbf{S_r} = p_\mathbf{r} \left(\hat{x} \sin\theta_\mathbf{r} \cos\phi_\mathbf{r} + \hat{y} \sin\theta_\mathbf{r} \sin\phi_\mathbf{r} + \hat{z} \cos\theta_\mathbf{r} \right) \tag{3.3}$$

with $\theta_{\mathbf{r}} = \mathbf{q}_\theta \cdot \mathbf{r}$ and $\phi_{\mathbf{r}} = \mathbf{q}_\phi \cdot \mathbf{r}$ with $p_{\mathbf{r}} = 1$ if $\mathbf{r} \in B$ and $p_{\mathbf{r}} = 0$ if $\mathbf{r} \in B'$. $\hat{x}$, *etc.*, are unit vectors in the corresponding directions.

The vector field $\mathbf{S_r}$ is characterized by the two wavevectors $\mathbf{q}_\theta$ and $\mathbf{q}_\phi$. For a periodic configuration, these should be $\mathbf{q}_\theta = \frac{2\pi}{L}(q_1, q_2, q_3)$ and $\mathbf{q}_\phi = \frac{2\pi}{L}(p_1, p_2, p_3)$, where q_i's and p_i's are integers, each of which take L values in $\{0, 1, 2, 3, ...L-1\}$. There are $\sim L^6$ ordered magnetic configurations possible, within this family, on a simple cubic lattice of linear dimension L.

The use of symmetries, *e.g.*, permuting components of q_θ, *etc.*, reduces the number of candidates somewhat, but they still scale as $\sim L^6$. For a general combination of $\mathbf{q}_\theta, \mathbf{q}_\phi$ the eigenvalues of H cannot be analytically obtained because of the non trivial mixing of electronic momentum states. We have to resort to a real space diagonalization. The Hamiltonian matrix size is $2N \times 2N$ (where $N = 2L^3$) and the diagonalization cost is $\sim N^3$. So, an exhaustive comparison of energies based on real space diagonalization costs $\sim N^5$, possible only for $N \leq 8^3$.

We have adopted two strategies: (i) we have pushed this '$\mathbf{q}_\theta, \mathbf{q}_\phi$' scheme to large sizes via a selection process described below, and (ii) for a few collinear configurations, where Fourier transformation leads to a small matrix, we have compared energies on sizes $\sim 100^3$.

First, scheme (i). For $L = 8$ we compare the energies of all possible phases, to locate the optimal pair $\{\mathbf{q}_\theta, \mathbf{q}_\phi\}_{min}$ for each μ. We then consider a larger system with a set of states in the neighbourhood of $\{\mathbf{q}_\theta, \mathbf{q}_\phi\}_{min}$. If we consider $\pm\pi/L$ variation about each component of $\mathbf{q}_{\theta,min}$, *etc*, that involves 3^6 states. The shortcoming of this method is that it explores only a restricted neighbourhood, dictated by the small size result. We have used $L = 12, 16, 20$ within this scheme.

The phases that emerge as a result of the above process are (i) FM, (ii) A-type, (iii) C-type, (iv) 'flux', and (v) three spirals SP_1, SP_2, SP_3. A-type consists of $(1, 1, 1)$ FM planes with alternate planes having opposite spin orientation (see Fig.3.3(a) left panel). If we convert each of these planes to alternating FM lines, so that the overall spin texture is alternating FM *lines* in all directions, we get C-type phase (see Fig.3.3(c)).

The 'flux' phase is different from the spiral families described using period vectors $\mathbf{q}_\theta, \mathbf{q}_\phi$. It is the augmented version of 'flux' phase used in cubic lattice double exchange model by Alonso *et al* (Table-I of ref. [71]). It has spin-ice like structure, and is described by

$$\mathbf{S}(\mathbf{r}) = \frac{p(\mathbf{r})}{\sqrt{3}}((-1)^{y+z}, (-1)^{z+x}, (-1)^{x+y})$$

Phase	Peak location in $S(\mathbf{q})$
FM	$(0,0,0),(\pi,\pi,\pi)$
A-type	$(\frac{\pi}{2},\frac{\pi}{2},\frac{\pi}{2}),(\frac{3\pi}{2},\frac{3\pi}{2},\frac{3\pi}{2})$
C-type	$(0,0,\pi),(\pi,\pi,0)$
Flux	$(\pi,0,0),(0,\pi,0),(0,0,\pi)$
	$(\pi,\pi,0),(\pi,0,\pi),(0,\pi,\pi)$
$\uparrow\uparrow\downarrow\downarrow$ phase	$(\frac{\pi}{2},0,0),(\frac{3\pi}{2},0,0),(\frac{\pi}{2},\pi,\pi),(\frac{3\pi}{2},\pi,\pi)$
SP$_1$:$\mathbf{q}_\theta=(0,\frac{\pi}{2},\pi),\mathbf{q}_\phi=0$	$(0,\frac{\pi}{2},\pi),(\pi,\frac{\pi}{2},0),(0,\frac{3\pi}{2},\pi),(\pi,\frac{3\pi}{2},0)$
SP$_2$:$\mathbf{q}_\theta=(0,\frac{\pi}{2},\pi)$	$(0,\frac{\pi}{2},\pi),(\pi,\frac{\pi}{2},0),(0,\frac{3\pi}{2},\pi),(\pi,\frac{3\pi}{2},0)$
$\mathbf{q}_\phi=(0,\frac{\pi}{2},0)$	$(0,0,\pi),(\pi,0,0)+(\pi,\pi,0)+(0,\pi,\pi)$
SP$_3$:$\mathbf{q}_\theta=(0,\frac{\pi}{2},\pi)$	$(0,\frac{\pi}{2},\pi),(\pi,\frac{\pi}{2},0),(0,\frac{3\pi}{2},\pi),(\pi,\frac{3\pi}{2},0)$
$\mathbf{q}_\phi=(\frac{\pi}{2},0,\frac{\pi}{2})$	$(\frac{\pi}{2},\frac{\pi}{2},\frac{3\pi}{2}),(\frac{3\pi}{2},\frac{3\pi}{2},\frac{\pi}{2}),(\frac{\pi}{2},\frac{3\pi}{2},\frac{3\pi}{2}),(\frac{3\pi}{2},\frac{\pi}{2},\frac{\pi}{2})$

Table 3.1: Candidate phases, the associated $\mathbf{q}_\theta,\mathbf{q}_\phi$, for the spirals, and the peak locations in the structure factor $S(\mathbf{q})$. All the $\mathbf{q}$ components have the same saturation value, given by $\frac{1}{2N_p}$, where N_p is the number of non-zero $\mathbf{q}$ peaks in the S(q). $N_p = 2$ for FM, A and C, $N_p = 4$ for $\uparrow\uparrow\downarrow\downarrow$ and SP$_1$,$N_p = 6$ for flux and $N_p = 8$ for SP$_2$ and SP$_3$. The factor of $\frac{1}{2}$ comes as we have half the spins at zero value, which halves the normalization.

The spiral SP$_n$ phases are characterized by commensurate values of $\mathbf{q}_\theta,\mathbf{q}_\phi$ (See Table 3.1 for details of periods and the S(q) peaks).

The simplest, SP$_1$ can be viewed as $\frac{\pi}{2}$-angle pitch in the (110),(101) and (011) directions. The other two spirals SP$_2$ and SP$_3$ are respectively C-type and A-type modulations upon SP$_1$. Just as flipping alternate $1,1,1$ planes in a FM leads to the A type phase, flipping the spins in the (111) planes alternatively in SP$_1$, leads to SP$_3$. Analogously, flipping FM lines in a FM and leads to C-type order - and a similar exercise on SP$_1$ leads to SP$_2$. This modulation is also seen in the $S(\mathbf{q})$ peaks of SP$_2$ and SP$_3$. See the Table 3.1, where all the three spirals have 4 S(q) peaks common, and SP$_2$ and SP$_3$ possess extra S(q) peaks of the A-type and C-type correlations.

In scheme (ii) we take collinear phases that occur in the phase diagram and compare their energy on very large lattices. This does not require real space diagonalization. The simple periodicity of these phases leads to coupling between only a few $|\mathbf{k}\rangle$ states. The resulting small matrix can be diagonalized and the eigenvalues summed numerically. We also included the 'flux' phase in this comparison. The details of this calculation, and the the magnetic phase diagram from comparison of FM, A, C and flux phases on large lattice size is discussed in Appendix A.

Particle hole symmetry in the model: The electrons move on the cubic lattice divided into two FCC sublattices each of consists of only B or B′ sites. For each of these sublattice, one can define particle-hole transformation [40] as $f_i \to f_i^\dagger$ and

$m_{i\sigma} \to -m_{i\sigma}^\dagger$. This transforms the Hamiltonian as

$$H_{particle}(\Delta, t, t') - \mu N \longrightarrow H_{hole}(-\Delta, t, -t') - (\mu - \Delta)N$$

When $t' = 0$, this simplifies to

$$H(\Delta, t) - \mu N \longrightarrow H(-\Delta, t) - (\mu - \Delta)N$$

This symmetry reflects in the phase diagram as the repetition of the phases after half-filling. Introducing the t' hopping destroys this symmetry, but a reduced symmetry still remains, which relates

$$(\Delta, t, t') \longrightarrow (-\Delta, t, -t')$$

This is reflected in the phase diagrams of particle-hole asymmetric case.

3.2 Results: nearest neighbour model

We now discuss the results in the particle-hole symmetric case, $i.e$, $t' = 0$. The $t' \neq 0$ situation is discussed in the next section. For each of these cases we first discuss the ground state phase diagram, then the nature of magnetic correlations at finite temperature, and finally the estimate of T_c.

Although the MC approach is 'unbiased', the results are are affected by finite size and the use of single spin based update. We use MC results to establish the dominant magnetic correlations in a parameter window and then explore these more carefully using the variational scheme. The MC based T_c estimate is also checked against a rough energy difference calculation that be implemented on the variational ground state.

3.2.1 Monte Carlo

We studied a $N = 12 \times 12 \times 12$ system using the cluster based update scheme. We used a large but finite J to avoid explicitly projecting out any electronic states [175], since that complicates the Hamiltonian matrix but allows only a small increase in system size. The magnetic phases were explored for $\Delta = 0$, 4 and 10.

In Fig.3.4, the magnetic ground state is shown, obtained via a combination of Monte Carlo and variational calculations. We see that the phase diagram is sym-
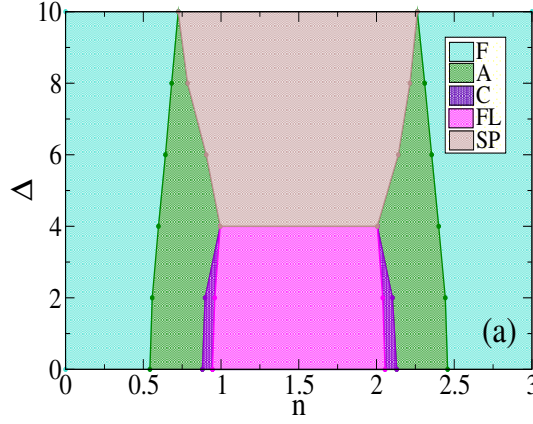
Figure 3.4: Magnetic ground state for varying electron density, n, and effective B-B$'$ level separation, for the model with only BB$'$, *i.e.*, nearest neighbour, hopping. The labels are: F (ferromagnet), A (planar phase), C (line like), FL ('flux') and SP (spiral). This figure does not show the narrow windows of phase separation in the model. The phase diagrams are generated via a combination of Monte Carlo and variational calculations on lattices of size up-to $20 \times 20 \times 20$.

metric in density. For small Δ, in the range $0 - 4$, we have FM, followed by A-type, C-type, and 'flux' phase. The order reverses as we go in the other half of the density window. The G-type phase which was largest stable phase in 2D (Fig.2 and Fig.5 in Ref. [63]) is almost taken over by the 'flux' phase. The stability of the 'flux' phase decreases with Δ and it does not show up for $\Delta > 4$. The phases that dominate the phase diagram are listed in table 3.1.

Two complications arise in the Monte Carlo approach in the present model. (i) Additional degeneracy of some AF phases: In addition to the usual spin rotation symmetry, the A-type and C-type phases have four fold degeneracy. The A-type phase for example can arise from planes that are normal to any of the four body diagonals (not just (111)). This leads to growth of domains with different orientation as the system is cooled and multiple peaks in the structure, table 3.2.

(ii) Geometrical frustration leads to the presence of multiple minima with similar energy and increases the equilibriation time.

Phase	Plane normal	$S(\mathbf{q})$
A_1	(1, 1, 1)	$(\frac{\pi}{2},\frac{\pi}{2},\frac{\pi}{2})+(\frac{3\pi}{2},\frac{3\pi}{2},\frac{3\pi}{2})$
A_2	(1,-1, 1)	$(\frac{\pi}{2},\frac{3\pi}{2},\frac{\pi}{2})+(\frac{3\pi}{2},\frac{\pi}{2},\frac{3\pi}{2})$
A_3	(1, 1,-1)	$(\frac{\pi}{2},\frac{\pi}{2},\frac{3\pi}{2})+(\frac{3\pi}{2},\frac{3\pi}{2},\frac{\pi}{2})$
A_4	(-1, 1, 1)	$(\frac{3\pi}{2},\frac{\pi}{2},\frac{\pi}{2})+(\frac{\pi}{2},\frac{3\pi}{2},\frac{3\pi}{2})$

Table 3.2: Peak location in the structure factors $S(\mathbf{q})$ for the four A-type phases
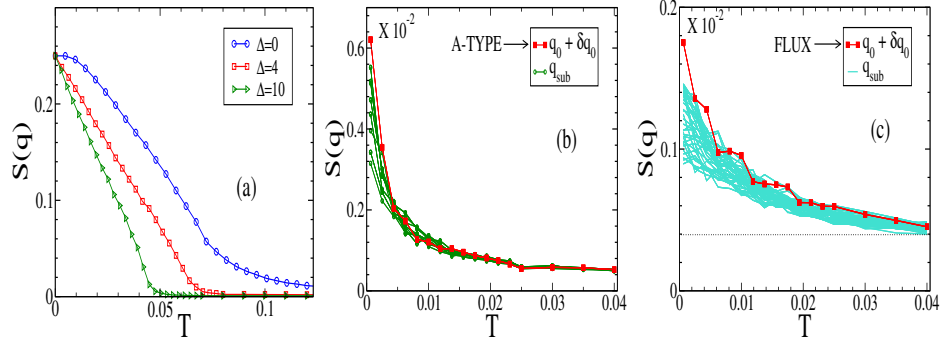
78

Figure 3.5: Temperature dependence of structure factor peaks for three typical densities and $t' = 0$. (a). The ferromagnetic order at $n = 0.2$ for $\Delta = 0$, 4, 10. (b). The growth of A type correlations (and the noise around the principal peak) at $n = 0.50$. The ordering wavevector $\vec{q_0}$ is listed in Table-3.1. $\delta\vec{q_0}$ are $\sim \mathcal{O}(\frac{1}{L})$ (c). 'Flux' type correlations at $n = 1.50$. The features are at and around the ordering wavevector in Table-3.1. Note the scale factors on the y axis in (b) and (c).

An illustrative plot of peak features in $S(\mathbf{q})$ as function of temperature T, is shown in Fig.3.5 for some typical densities. For FM, $S(\mathbf{q}_{FM})$ shows monotonic decrease of T_c with increasing Δ. For A-type and 'flux' phase, the $S(\mathbf{q})$ data shows a number of sub-dominant $\mathbf{q}$ peaks whose number keeps increasing as we move to more complicated phases with increasing density. These sub-dominant peaks arise due to a combination of (a) geometrical frustration and (b) our cluster based update.

In Fig.3.6 we show the full structure factor in the the three phases, namely FM, A-type and flux like. The data is visualized in following scheme. At every $\mathbf{q}$, a sphere is drawn, whose size, and colour scales with the value of $S(\mathbf{q})$. The colour scheme has white colour for the low values of $S(\mathbf{q})$, so that in the present scheme, only the most prominent $\mathbf{q}$ are displayed, and the smaller ones are essentially invisible.

For FM (Fig.3.6(a)-(b)), we see two bright spots at $(0, 0, 0)$ and (π, π, π) at low temperature, which correspond to the $\mathbf{q}$ values for ideal ferromagnet (see table 3.1). At higher temperature $T = 0.06t$, its weight goes down, but other $\mathbf{q}$ are still negligible, as the temperature is lower than T_c.

The A-type phase should ideally have peaks at $(\frac{\pi}{2}, \frac{\pi}{2}, \frac{\pi}{2})$, and $(\frac{3\pi}{2}, \frac{3\pi}{2}, \frac{3\pi}{2})$, or one of its symmetry related $\mathbf{q}$s (table 3.2). However, at low temperature, as in Fig.3.6(c) it has comparable weights corresponding to A_1 and A_4, and few subdominant neighbouring $\mathbf{q}$s. These weight quickly diminish with increasing temperature (Fig.3.6(d)).

The Fig.3.6(e) shows the structure factor at density where we expect the flux phase. Here the maximum weight lies close to $\mathbf{q}$ values corresponding to flux phase (table 3.1), but the weight is more dispersed, and there are a lot of sub-dominant
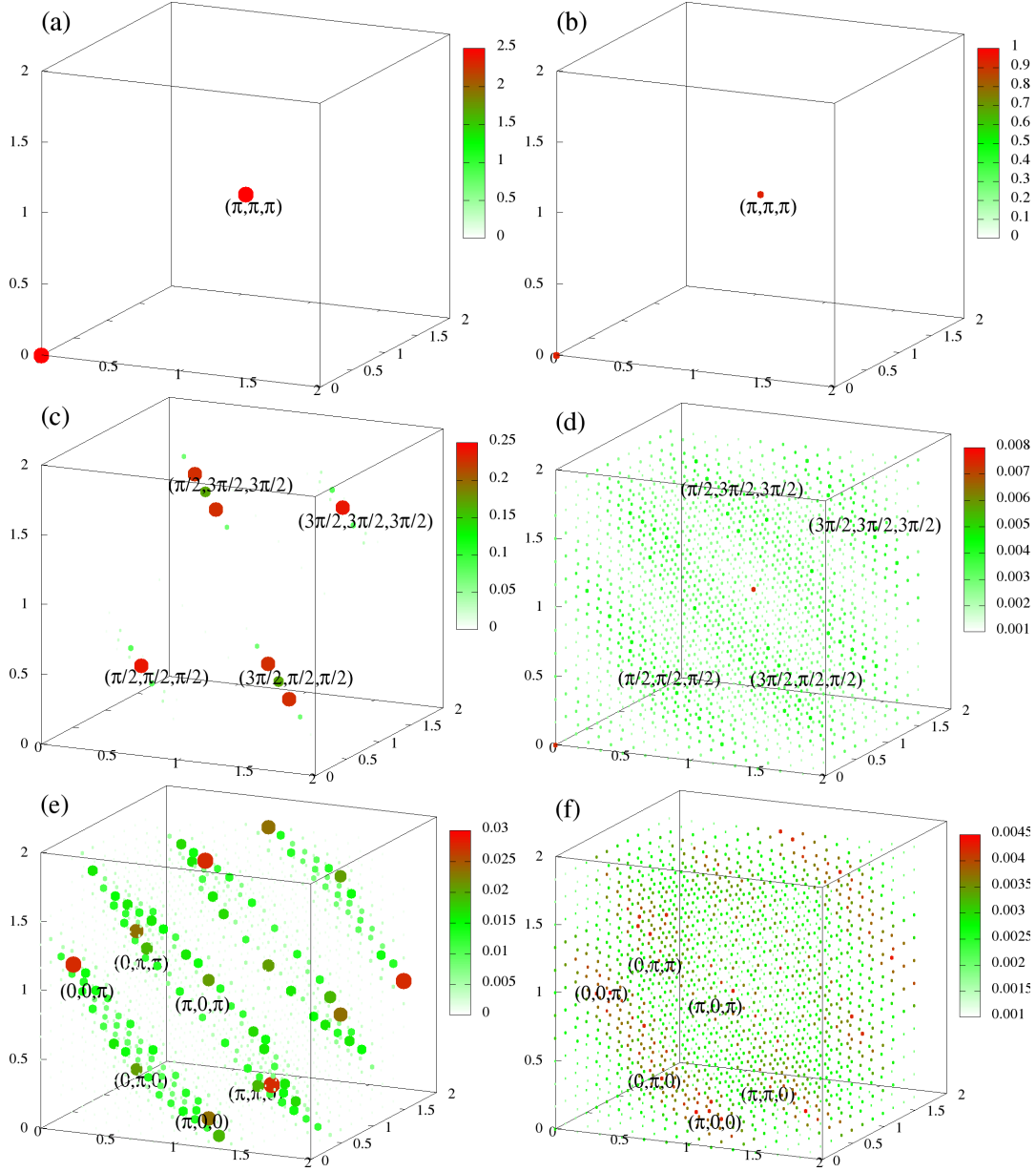
Figure 3.6: The full $S(\mathbf{q})$ at $T = 0$ (left column) and $T = 0.06t$ (right column). The momentum along each axis goes from $0 - \pi$. (a)-(b) is for FM, (c)-(d) is A-type, and (e)-(f) is for the flux like phase. The densities correspond to the same values as in Fig 3.5. In these scattered point plots, the colour and the size of the points at given $\mathbf{q}$ scales with the $S(\mathbf{q})$. The scaling is chosen different for each phase, but same for two temperatures. Because of the specific colour scheme chosen, the low values are small white circles, which are essentially invisible, highlighting only the higher $\mathbf{q}$ values. In each case (a)-(f), the three axes correspond to q_x, q_y, q_z respectively, and are in units of π, ie., they go from 0 to 2π.

$\mathbf{q}$s. With increasing temperature, they diminish quickly.

Using the structure factor data, we establish the $n - T_c$ phase diagram for $\Delta =$
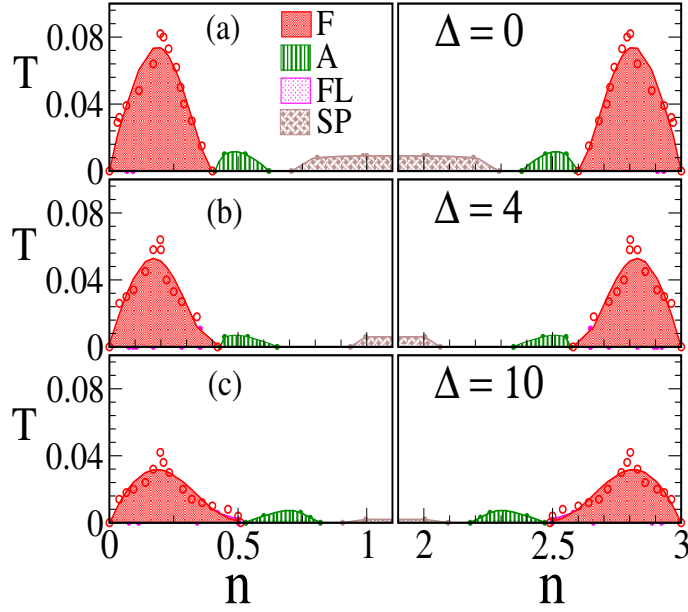
Figure 3.7: $n - T_c$ diagram for $\Delta = 0, 4, 10$ (top to bottom rows) as estimated from the Monte Carlo. Starting from low density $(n = 0)$ towards high density $(n = 1)$, we find FM with high T_c, thin window of A-type order with very low T_c compared to FM, followed by the 'flux' phase (at $\Delta = 0$) or 'spiral' (at larger Δ). The symbols are the actual MC estimated T_c, while the smooth lines are fit to the data.

$0, 4, 10$ that is plotted in Fig.3.7. The Monte Carlo captures mainly three collinear phases, namely FM, A-type, and a ↑↑↓↓ phase. The ↑↑↓↓ phase corresponds to two FM up planes followed by two FM down planes and so forth. As the carrier density is increased by increasing μ, we find a FM phase followed by the A-type AF. A ↑↑↓↓ phase appears in a thin window surrounded by FM itself. We suspected that this as a finite size effect, and a comparison with the energy of the FM on larger lattices (20^3), shows that the FM is indeed the ground state in the thermodynamic limit, and so we consider FM and ↑↑↓↓ collectively as FM only, and presence of ↑↑↓↓ is not indicated in the phase diagram.

The FM is stable at the ends of the density window, and its region of occurrence is slowly enhanced as we increase Δ, see Fig.3.4 as well. The T_c however decreases with increasing Δ since the degree of B-B′ mixing (and kinetic energy) decreases.

With increase in n the 2D system is known to make a transition to a line-like phase, and then a 'G type' phase (up spin surrounded by down, etc). The equivalent in 3D would be a progression from FM to a 'planar' (A type) phase, then a 'line like' (C type) phase and finally to a G type phase if possible. Numerical complexity and the geometric constraint modify the picture as below.

We do access the A type phase with some difficulty but our Monte Carlo cannot
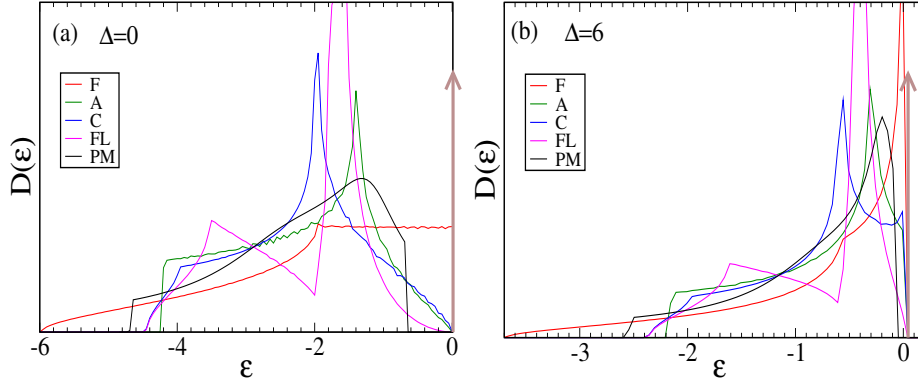
Figure 3.8: Density of states for the F, A, C, FL ('flux') and PM (paramagnetic) phases. (a) $\Delta = 0$ and (b) $\Delta = 6$. For both Δ the bandwidth decreases in the sequence: F, PM, C, FL, and A (FL and C have same bandwidth). The plot for $\Delta = 6$ is split in two parts, with the region between $\epsilon = [0, 6]$, with zero weight, omitted. The δ function arises from the localized B' level.

access the long range ordered C type phase. However, we see clear evidence of C type correlations in the structure factor. Comparing the energy of the ideal C type phase with the short range correlated phase that emerges from the MC we infer that C type order is indeed preferred over a parameter window. However, we cannot estimate a reliable T_c scale. In the next section we will see the variational results on the C type phase and get a rough estimate of the T_c.

The G type phase is geometrically disallowed on the B sublattice due to its FCC structure. An examination of the structure factor in the density window $n = [1, 2]$ suggests 'flux' like correlations at small Δ which evolves into a spiral at larger Δ. The frustration reduces the T_c of the phases in this density window compared to that of the FM. We can calculate the energy difference between a fully random spin configuration and the variational ground state. This δE serves as a crude measure of the T_c of the phase.

When $t' = 0$, the electron delocalisation happens through B-B'-B paths only (see the conduction paths, for example of collinear phases A and C in Fig.3.3(b) and 3.3 (d) respectively). In this case all the phases have an atomic level located at $\epsilon_{B'}(= 0)$ in the limit $J \to \infty$. This is directly seen in the density of states (DOS) of these phase. In Fig.3.8 we show the DOS for the F, A, C, 'flux' and paramagnet phases. This dispersionless level gives constant T_c in density region $n = [1, 2]$. This feature, and several others, are modified by finite B'-B' hopping, which leads to broadening of this level. It makes the DOS of the various magnetic phases asymmetric (in energy) and also destroys the particle-hole symmetry in the phase diagram.
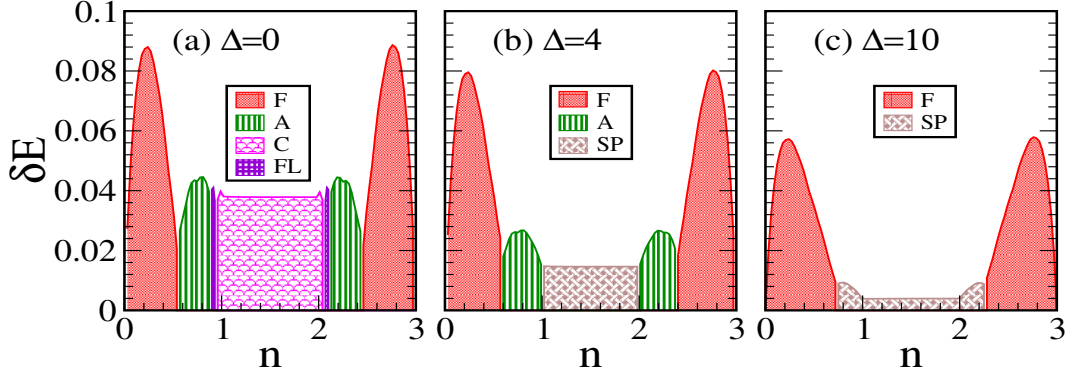
Figure 3.9:   The per site energy difference δE of the variational ground-state and the paramagnetic phase. This provides a rough estimate of the T_c. The parameters are $(a)\Delta = 0, (b)\Delta = 4, (c)\Delta = 10$ and $t' = 0$ in all cases. The sequence of phases from low density to middle is FM, A, C and 'flux' ($\Delta = 0$) or spiral ($\Delta = 4, 10$). The decrease in the 'T_c' with Δ is more drastic in AF phases.

3.2.2   Variational scheme

Using the variational scheme discussed earlier one can establish a ground state phase diagram. This is consistent, overall, with correlations that we see in the Monte Carlo, and now allows us to compare candidate phases on large sizes. This establishes the window of existence of the collinear phases, FM, A and C.

For the middle part of the density window no simple phase is suggested by the Monte Carlo. The variational scheme suggests the phases to be SP_1, SP_2, SP_3, and 'flux'. See the configurations in Fig.3.3(e)-(f) and $S(\mathbf{q})$ details from Table 3.1.

The variational scheme also allows a rough estimate of the T_c scale of the ordered state. Ideally, one should compute the energy of 'spin wave' configurations about the non trivial ground state, fit these to an effective Heisenberg model, and then work out the T_c of that model. Here we simply compute the 'binding energy' of each ordered phase, *i.e*, its energy gain with respect to the paramagnetic phase at the same electron density, and use the size normalised value as an estimate of T_c.

$$\delta E = (1/N)(E_{VC}(n) - E_{para}(n))$$

where E_{VC} corresponds to the variational minimum and E_{para} to the paramagnet.

This calculation is no substitute for the full MC, and is only meant to supplement the MC based T_c information and provide a rough estimate where MC is noise limited.
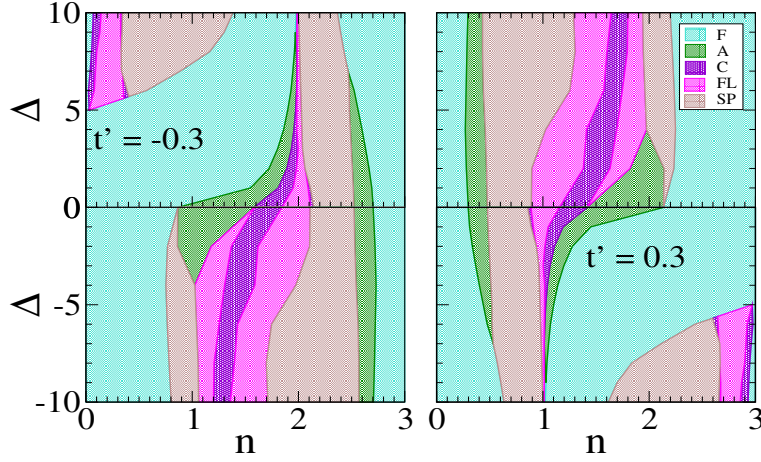
Figure 3.10: Ground state phase diagram in the presence of $t' = \pm 0.3$.

3.3 Results: next neighbour hopping

The model with only 'nearest neighbour' (BB$'$) hopping has a rich phase diagram. However, this has the artificial feature of a non dispersive level. In reality all materials have some degree of B$'$B$'$ [64] hopping due to larger size of B$'$ ion, and we wish to illustrate the qualitative difference that results from this hopping. We explored two cases, $t' = 0.3$ and $t' = -0.3$ for these particle-hole asymmetric cases.

The $n - \Delta$ ground state phase diagram for $t' = \pm 0.3$, obtained by a combination of MC, and variational calculation, is shown in Fig.3.10. Turning on t' has a significant effect on the phase diagram, compare with the $t' = 0$ case, Fig.3.4. The particle hole symmetry $(n \to 3 - n)$ is destroyed but a reduced symmetry $(n, \Delta, t') \to (3 - n, -\Delta, -t')$ still holds. The phase diagram is richer in the middle of the density window where crossing among various phases occurs at different densities. Due to the symmetry mentioned above it is enough to discuss the $\Delta > 0$ case with $t' = \pm 0.3$.

The A-type phase becomes very thin in the left, but unaffected by Δ, while in right side it widens up in the low Δ and gets replaced by the spiral quickly as we go up in Δ. 'flux' and C-type both become stable for high Δ with a gradual shift in the high density. For $t' = -0.3$, at very small Δ in the left and the middle part A-type and the spiral are major candidates with small window for C-AF and 'flux'. The behaviour in this part is not very sensitive to sign of t'.

Focusing on $t' = -0.3$, as go up from $\Delta = 0$ to $\Delta \sim 5$ the AF phases become less and less stable and are almost wiped out from the left part of the density, and FM becomes stable there. The largest stability window of FM occurs roughly near
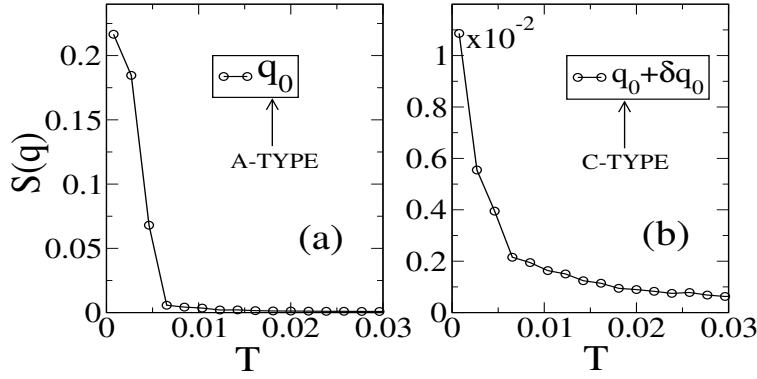
Figure 3.11: $S(\mathbf{q})$ for $t' = 0.3$ and $\Delta = 0$ at (a): a typical density $n \sim 0.5$ for A-type phase and (b): a typical density $n \sim 1.2$ for C type phase. A demonstration of $S(\mathbf{q})$ with no sub-dominant peaks, unlike at $t' = 0$.

$\Delta \sim 5$, where its stable up-to $n \sim 1.8$. Going further with higher Δ, FM looses its stability, from C type, 'flux' and spirals. However, there is very thin strip of stability of the FM in the band edge in the left part, and towards the middle density, there is re-entrance of the FM phase. In the right part of the density window we have FM, A type and spiral. Increasing Δ reduces the stability of A type to FM, making it vanish near $\Delta \sim 7$, while FM window keeps increasing with Δ.

Overall, $t'\Delta > 0$, shows a rich set of antiferromagnetic phases, while $t'\Delta < 0$, gives a ferromagnetic window, suppressing antiferromagnetic phases.

3.3.1   Monte Carlo

In Fig.3.11(a),(b) we show the structure factor data at two densities, for (a) A type and (b) C type phases, to demonstrate one remarkable difference from the particle-hole symmetric case. Fig.3.12 shows the full structure factor at low (T=0) and some high temperature ($T = 0.05t$) at the same densities for A and C type phases.

As we saw earlier in Fig.3.5 (temperature dependence) and Fig.3.6 (full $S(\mathbf{q})$) for $t' = 0$ the structure factor data were very noisy for AF phases, with many sub-dominant $\mathbf{q}$ peaks around the central peak. The saturation value for the A-type peak in the symmetric case was $\sim 10^{-2}$, while now it is ~ 0.2, close to the ideal value of 0.25! This is also evident for the full structure factor. Fig.3.12(a) shows clean peak at $(\frac{3\pi}{2}, \frac{\pi}{2}, \frac{\pi}{2})$ and $(\frac{\pi}{2}, \frac{3\pi}{2}, \frac{3\pi}{2})$, with other $\mathbf{q}$s essentially zero. The largest weights of C-type (Fig.3.12(c)) are close to $(\pi, 0, 0)$ and $(0, \pi, \pi)$, with very few subdominent $\mathbf{q}$s (recall table 3.1 for $\mathbf{q}$ values of clean phases).

The sharp change in the structure factor makes the identification of the T_c scale more reliable. Although inclusion of t' does not remove the noise completely, it is
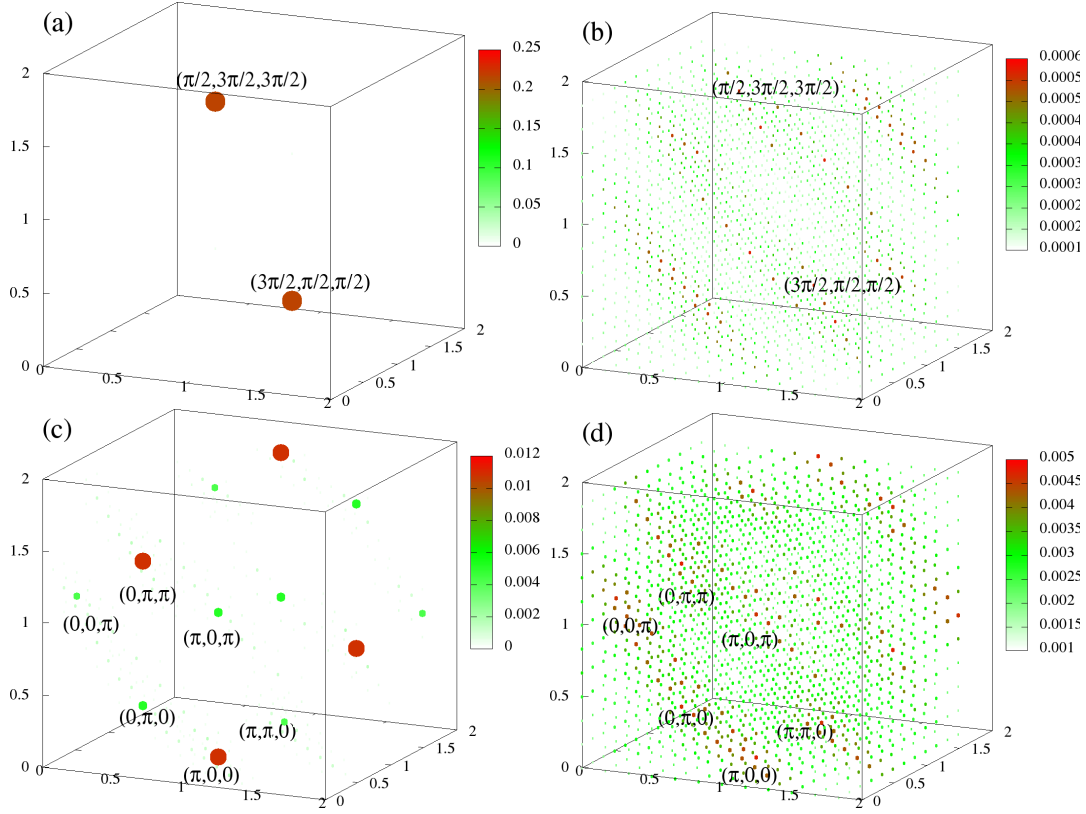
Figure 3.12: The full $S(\mathbf{q})$ at $T = 0$ (left column) and $T = 0.05t$ (right column) (a)-(b) is for A-type, (c)-(d) and is C-type at the same densities as Fig.3.11. The plotting scheme is same as in Fig.3.12. The scaling is chosen different for each phase, but same for two temperatures. The visible points denote the dominant $\mathbf{q}$ values. The three axes correspond to q_x, q_y, q_z respectively, and are in units of π, ie., they go from 0 to 2π.

reduced over a reasonable part of the phase diagram.

Fig.3.13(a) presents the $n - T_c$ phase diagram for $t' = 0.3$ and $\Delta = 0$ established from Monte Carlo, along with the δE from the variational approach (Fig.3.13(b)). In this case, the phases that appear as a function of density n are FM, A type, spiral, C type, A type and FM again. For FM, the window of stability gets reduced in the left (low density) part but enhanced in the right (high density) part. The ↑↑↓↓ phase appears again, but being a finite size artifact, is absorbed in the FM (and not shown).

The T_c is usually reduced, from the symmetric ($t' = 0$) case, as BB' hopping provides conduction paths that are non-magnetic. There is a wider space with moderate T_c for A type phase, located asymmetrically in density. It is more stable, in the right window, than left window. The correlations of spiral and C type phases are also captured with relatively less noise, see Fig.3.11(b) for example of C-type

Figure 3.13: Phase diagram obtained via Monte Carlo (left) and from the variational calculation (right) at $t' = 0.3$ and $\Delta = 0$.

correlation. The $n - T$ phase diagram for $t' = -0.3$ and $\Delta = 0$, can be obtained from transformation $n \longrightarrow 3 - n$, *i.e.*, reversing the density axis of Fig.3.13(a),(b).

3.3.2 Variational scheme

We also used the variational scheme to get an independent feel for the ground state and the δE for $t' = \pm 0.3$.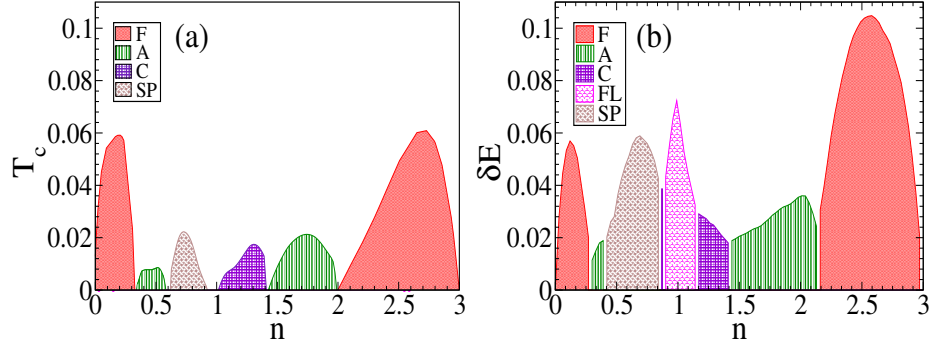 For $t' = 0.3$ the trends from MC are well reproduced by the variational scheme on large (20^3) systems at $\Delta = 0$. We observe reduced stability of FM at low density and enhancement at high density.

Note that the overall correspondence between the Monte Carlo and the variational approach is much better here than in the $t' = 0$ case, Fig.3.7 and the Fig.3.9.

In Fig.3.14 we have shown the $\delta E(n)$ calculated for 20^3 size, for $t' = \pm 0.3$. For $t' = 0.3$ and $\Delta = 0, 4, 10$ (Fig.3.14(a)-(c)) shows asymmetric δE (or T_c), for ferromagnet. The stability windows of the A type is enhanced, the large window of flux phase that was for $t' = 0$, is reduced in competition to spiral and C type. For the $t' = -0.3$, $\Delta = 0$ (Fig.3.14(d)) is just density reversed due to symmetry. However, the intermediate $\Delta = 4$ (Fig.3.14(e)) has a large stability window of ferromagnet. Here, though the Δ and t' are non-zero, due to unusually large stability window, the δE(or T_c) is large. For larger $\Delta = 10$ (Fig.3.14(f)), the ferromagnet appears in the middle and right with moderately reduced δE (or T_c), while the same is heavily suppressed for antiferromagnetic phases.

To summarize, from the MC and variational data we learn that, apart from asymmetry in the phase diagram, collinear FM and A type phases become stable in wide density window. Their T_c however is slightly reduced than the symmetric case. The S($\mathbf{q}$) data showing less noise for A, C type and spirals indicates that the energy landscape become 'smoother' by t' so that annealing process becomes easier
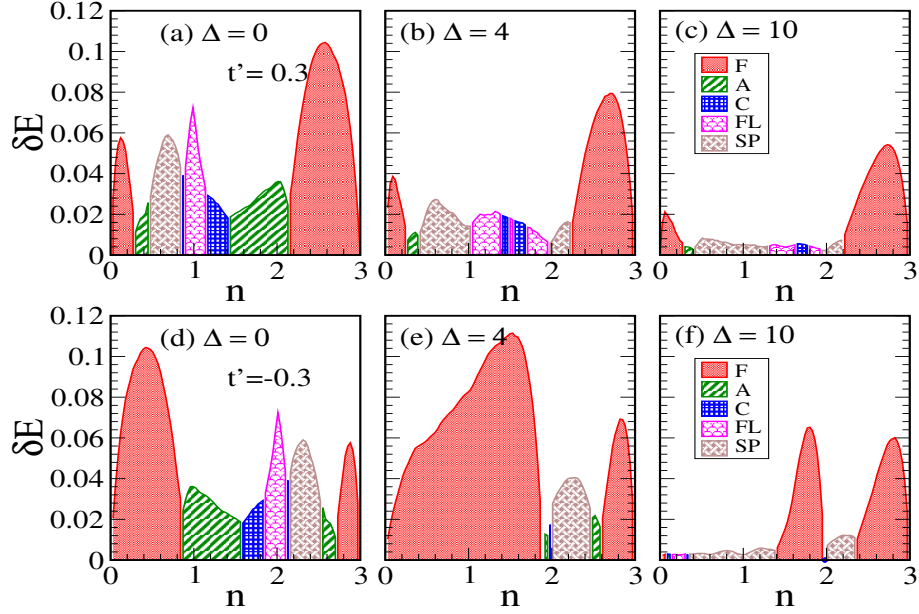
Figure 3.14: Asymmetric case, the energy difference δE of ground-state and paramagnetic phase. Top: $t' = 0.3$ The trends of δE match with T_c. Bottom: $t' = -0.3$ where FM is stable in the large portion of the density.

to get to the ground state. The energy differences δE as well as MC estimated T_cs show overall decrease with t'. This is understandable as, by introducing t' we allow electrons to more on the 'non-magnetic' sublattice B'. Now the energy of any phase, depends on the energy gain via the hopping process. From the nearest $f - m$ hopping, this gain scales as $\frac{t^2}{\Delta}$ subject to spin configurations, while the from the next nearest $m - m$ hopping, this gain simply scales as t', and doesn't care upon spin configurations. So more we increase t' and Δ, the more we are making the energy of the system insensitive to spin-configurations. The asymptotic limit of this is $\frac{t^2}{\Delta} \to 0$ when every phase has same energy as paramagnet.

In the couple of paragraphs below we try to create an understanding of how the phase diagram is affected by t'. Unfortunately we do not understand the effects over the entire density window yet.

For $t' = -0.3$, the FM loses its stability to AF phases even at low n. That is puzzling since one would expect the FM phase to have the largest bandwidth. We recall that in the $t' = 0$ case, there is a localized band coming from B' level for all the phases. The dispersion of this previously localized level causes the m and f to have a $\mathbf{k}$ dependent separation, which was Δ for all $\mathbf{k}$ in the symmetric case. The separation for these levels in the asymmetric case is $\Delta_{\mathbf{k}} = \Delta - \epsilon'_{\mathbf{k}}$, which varies from $\Delta - 12|t'|$, to $\Delta + 12|t'|$ in 3D. In 2D it varies from from $\Delta - 4|t'|$, to $\Delta + 4|t'|$.
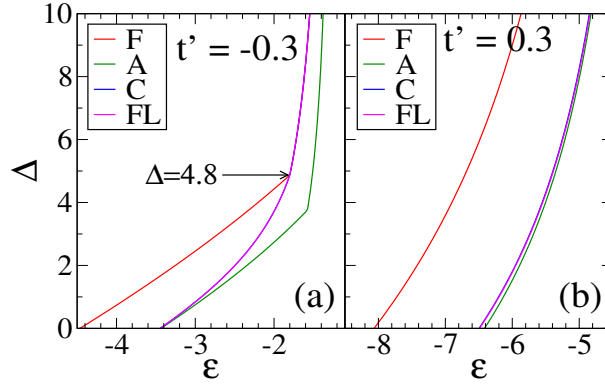
Figure 3.15: Asymmetric case, lowest eigenvalues plotted as function of Δ for the F,A,C and flux phases calculated from the dispersions. (a) $t' = -0.3$ and (b) $t' = 0.3$

Fig.3.15 shows the lowest eigenvalues of F,A,C and flux phases with Δ for $t' = \pm 0.3$ and we see how a crossing occurs at $t' = -0.3$.

We make a general observation about the change in the 'energy landscape' of the model, in the space of spin configurations, with changing t'. If $t' \gg t$ then the electrons could delocalize on the wide t' based band populating the non magnetic sites only. Magnetic order would make little difference to electronic energies and the energy landscape would be featureless. There are no ordered states as minimum in this landscape. Contrast to $t' = 0$, where delocalisation takes place necessarily through the magnetic sites and deep minima in in the landscape represent ordered states in real space. There are presumably shallow metastable states possible too.

At intermediate t' the ordered states are shallower, since the gain from magnetic ordering is lower, but the metastable seem to be affected even more, if the relative ease of Monte Carlo annealing is any indicator.

3.4 Discussion

The real double perovskites are multi-band materials, involving additional interaction effects and antisite disorder beyond what we have considered here. Nevertheless, we feel it is necessary to understand in detail the phase diagram of the 'simple' model we have studied, and then move to more realistic situations. In what follows, we first provide a qualitative comparison of the trends we observe with experimental data, and then move to a discussion of issues that are ignored in the present model.

3.4.1 Comparison with experiments

There is limited experimental signature [65] of metallic AF phases driven by the kind of mechanism that we have discussed. So, the comparison to experiments is, at the moment, confined to the T_c scales [177, 178] *etc*, of the ferromagnetic DP's.

From the *ab initio* calculations [64] the sign $t'/t \sim 0.4 > 0$ and $\Delta > 0$, so one can compare the right panel of Fig.3.4 qualitatively with experiments.

In a material like SFMO the electron density can be increased by doping La for Sr, *i.e*, compositions like $Sr_{2-x}La_xFeMoO_6$. This was tried [177] and the T_c increased from 420K at $x = 0$ to ~ 490K at $x = 1$. SFMO has threefold degeneracy of the active, t_{2g}, orbitals while we have considered a one band model. When we create a correspondence by dividing the electron count by the maximum possible per unit cell (3 in our case, 9 in the real material), in our units $x = 0$ corresponds to $n = 0.33$ and $x = 1$ to $n = 0.66$.

When $t' = 0$, as a function of n the T_c peaks around $n = 0.2$, Fig.3.7, quite far from the experimental value. However, in the presence of $t' = -0.3$ and $\Delta = 4$, Fig.3.14(e), the peak occurs above $n = 1$. So, modest t' can generate the ferromagnetic window that is observed, and produce a $T_c \sim 0.1t$. For $t \sim 0.5$eV, this is in the right ballpark.

Ray *et al* experimentally estimate the onset of AF order upon La doping to be $x \sim 1.1 - 1.5$, which corresponds to $n \sim 2.1 - 2.5$. Our onset of AF order, for Δ in [0-10], is $n \sim 0.5 - 0.75$, which for SFMO would be $n \sim 1.5 - 2.1$. This is quite close to experiments. However, inclusion of finite $t'/t > 0$, pushes this to lower values.

3.4.2 Additions to the model

(i) Effect of orbital variables: Apart from renormalization of the electron count, multiple orbitals could, in principle, have a qualitative effect. If the local orbital degeneracy is lifted by Jahn-Teller effect then the resulting 'orbital moment' could order in some situations. This orbital ordered (OO) background can modify electron propagation and the magnetic state. This is known to happen at some dopings in the manganites. Even there, however, the broad sequence of magnetic phases is consistent with predictions from a one band model. The double perovskites do not seem to involve strong lattice effects, the orbital degeneracy survives, and there is no orbital order. This suggests that there is even better chance of a one band model being qualitatively correct here, compared to the manganites.

Had there been strong OO effects, the spin-spin coupling in that background may

have picked up strong directionality, and the geometric frustration could have been irrelevant. This does not seem to happen in most double perovskites. Indeed, there are experiments on the insulating DP's [180–182] where the geometric frustration of the FCC lattice leads to a non trivial magnetic state, unrelieved by the presence of multiple orbitals.

We of course expect that the phase boundaries and T_c scales that we calculate would be affected by the orbital degeneracy. However, the trends in the phase diagram with increasing density simply reflect a growing AF tendency and the non coplanar phases emerge due to the impossibility of Neel order.

(ii) Antisite disorder: Attempts to increase n via A site substitution also brings in greater antisite disorder (B-B′ interchange) and even the possibility of newer patterns of A site ordering (!) complicating the analysis. For example, one would try compositions of the form: $A_{2-x}A'_x BB'O_6$, where A and A′ have different valence in an attempt to change n. The assumption is that the A′ only changes n without affecting other electronic parameters, *i.e*, A′ ions do not order and remain in an alloy pattern. This may not be true. In fact, at $x = 1$, the material AA′BB′O$_6$ may have a specific A-A′-B-B′ ordering pattern that affects electronic parameters in a non trivial way and one cannot understand this material as a perturbation on $A_2BB'O_6$. In such a situation one needs guidance from experiments and *ab initio* theory to fix electronic parameters as x is varied. All this before one even considers the inevitable antisite (B-B′) disorder and its impact on magnetism [179].

3.5 Conclusions

We have studied a one band model of double perovskites in three dimensions in the limit of strong electron-spin coupling on the magnetic site. The magnetic lattice in the cubic double perovskites is FCC and increasing the electron density leads from the ferromagnet, through A and C type collinear antiferromagnets, to spiral or 'flux' phases close to half-filling. We estimate the T_c of these phases, via Monte Carlo and variational calculation. The introduction of B′B′ hopping $t'/t \sim 0.3$ significantly alters the phase diagram and T_c scales and creates a closer correspondence to the experimental situation on DP ferromagnets.

MOTT TRANSITION ON THE ANISOTROPIC TRIANGULAR LATTICE

In chapter 1 we qualitatively described the emergence of a Mott insulating state due to increasing interaction in the half-filled Hubbard model. This chapter discusses the Mott transition on the anisotropic triangular lattice in detail. The lattice we use is shown in the Fig.4.1. In terms of electron hopping it is equivalent to a square lattice with nearest neighbour hopping t, and next neighbour hopping t' along the (1,1) direction only. $t' = 0$ leads to the usual square lattice, while $t' = t$ is the isotropic triangular lattice. t'/t defines the degree of hopping anisotropy in the triangular lattice.

4.1 Background

The Mott transition from a metal to an insulator, with increasing interaction strength, U, occurs at 'integer' filling in electron systems [73]. In the absence of magnetic in-
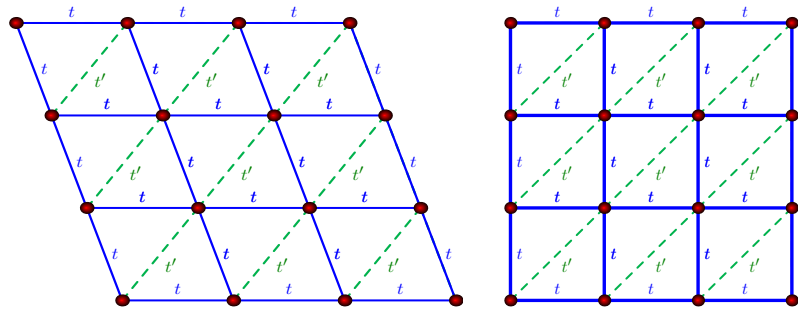

Figure 4.1:   Left: The triangular lattice with anisotropic hoppings t and t'. Right: The equivalent square lattice with the same set of hoppings.

stabilities this should occur when the interaction strength becomes comparable to the bare bandwidth. In most cases, however, this strong coupling effect is pre-empted by a magnetic instability, which occurs when the magnetic susceptibility $\chi(\mathbf{q})$ diverges. Within the random phase approximation (RPA), which arises naturally in the static Hubbard-Stratanovich scheme, the magnetic susceptibility is given by

$$\chi(\mathbf{q}) = \frac{\chi_0(\mathbf{q})}{1 - U\chi_0(\mathbf{q})} \tag{4.1}$$

If $\chi_0(\mathbf{q})$ has a peak at $\mathbf{q} = \mathbf{Q}$, then RPA predicts an instability at this wavevector at $U_c = 1/\chi_0(\mathbf{Q})$. If the predicted U_c is large then RPA may not be a good guide to the susceptibility of the interacting electron system. Also, if $\chi_0(\mathbf{q})$ is featureless in terms of its $\mathbf{q}$ dependence the instability argument is not useful.

The simplest case of a square lattice with nearest neighbour hopping t is well understood. There χ_0 diverges at $\mathbf{q} = (\pi, \pi)$ at $T = 0$ due to perfect nesting of the Fermi surface. As a result the magnetic instability occurs for infinitesimal U to a $\mathbf{Q} = (\pi, \pi)$ spin density wave state. The large U problem on this lattice also favours $\mathbf{Q} = (\pi, \pi)$ (Neel) order. The ground state turns out to be an antiferromagnetic insulator at all U, with the magnitude of the moment, and the single particle gap, increasing monotonically with U/t.

The presence of t' as in Fig.4.1, has the following effects:

- There is no longer any divergence in $\chi_0(\mathbf{q})$.

- For t'/t in the range $t'/t = 0 - 0.7$, the peak in $\chi_0(\mathbf{q})$ is still at $\mathbf{Q} = (\pi, \pi)$ (Fig.4.2 upper panel) and the system still prefers Neel order but beyond $U_c = 1/\chi_0(\mathbf{Q})$.

- For for $t' > 0.7t$, however, the maximum shifts significantly away from $\mathbf{Q} = (\pi, \pi)$ (Fig.4.2 lower panel), so, as we will discover, the system may exhibit spiral order.

- At strong coupling $U/t \gg 1$, the Mott localized phase is described by a $S = 1/2$ Heisenberg model. On the square lattice the resulting order is again at (π, π). With growing t'/t the progressively more frustrated structure reduces the stability of the Neel state. A spiral state may emerge at large t'/t.

- At a given $t'/$, the weak coupling and strong coupling wavevectors are in general not the same.
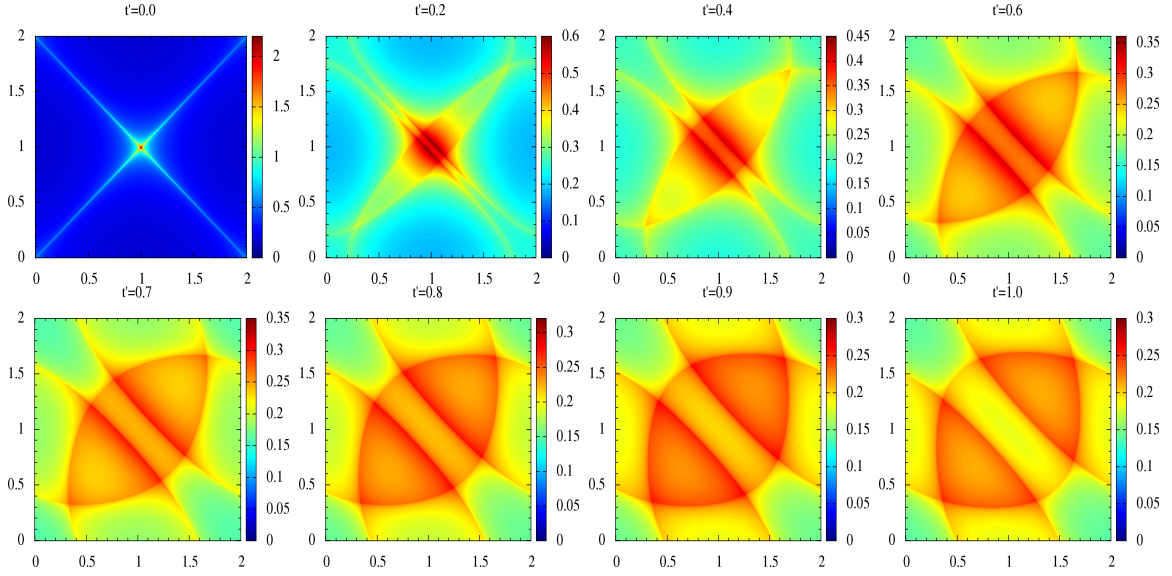
Figure 4.2: Non-interacting magnetic susceptibility $\chi_0(\mathbf{q})$ for anisotropic triangular lattice. We have q_x, q_y on the x and y axes, in units of π for each plot. The upper panel is for $t' = 0, 0.2, 0.4, 0.6$ where the maxima lies on, or around $\{\pi, \pi\}$, while in lower panel for $t' = 0.7, 0.8, 0.9, 1$ the maxima has shifted to incommensurate $\mathbf{q}$.

So, in contrast to the bipartite case, the dominant magnetic wave vector $\mathbf{Q}$ evolves from $\mathbf{Q}_0$ to $\mathbf{Q}_\infty$ as U/t changes at finite t'. When $\mathbf{Q}$ is typically incommensurate, as we will see later, it generates smaller gap compared to Neel order (for moments of the same size). This leads to the possibility of a magnetic metal at intermediate coupling.

In a two dimensional system thermal fluctuations prevent long range order at finite temperature, and quantum fluctuations could suppress order even at $T = 0$. Nevertheless an approximate solution of the magnetic problem, retaining classical thermal fluctuations can lead to valuable insight. In the present chapter we provide a comprehensive study of the Hubbard model in the anisotropic triangular lattice in the full t'/t range of [0-1] over a wide range of U/t.

We use a real space new approach to the Mott transition, using auxiliary fields, that emphasizes the role of spatial correlations near the metal-insulator transition (MIT). Our principal results, based on a combination of Monte Carlo (MC) on large lattices and variational minimization, are the following.

- We establish a ground state magnetic phase diagram in the $U/t - t'/t$ plane, and explore the finite temperature Mott transition by calculating transport and spectral functions at four representative cross sections of $t'/t = 0, 0.4, 0.8, 1$.

- The $U-T$ phase diagram is established for selected choice of t'/t. For $t'/t = 0.8$,

relevant for the κ-BEDT compounds, our results bear a strong resemblance to properties measured in these organics.

- At intermediate temperature, in the magnetically disordered regime, we obtain a strongly non Drude optical response in the metal, and predict a pseudogap (PG) phase over a wide interaction and temperature window.

- The electronic spectral function $A(\mathbf{k}, \omega)$ is *anisotropic* on the Fermi surface, with both the damping rate and PG formation showing a clear angular dependence arising from coupling to incommensurate magnetic fluctuations.

We start with the Hubbard model defined on the anisotropic triangular lattice, defined as in Fig.4.1 and use the square lattice geometry with anisotropic hopping t for nearest neighbours and t' for the next nearest neighbours. As discussed in section 2.1.2, we used Hubbard Stratonovich transformation to decouple the interaction term, and after a sets of approximation, we have the following effective Hamiltonian equivalent to equation (2.9) for the given hoppings:

$$
\begin{aligned}
H_{eff} = -t \sum_{\langle ij \rangle \sigma} \left[c_{i\sigma}^\dagger c_{j\sigma} + \text{h.c.} \right] - t' \sum_{(ij)\sigma} \left[c_{i\sigma}^\dagger c_{j\sigma} + \text{h.c.} \right] \\
+ \sum_{i\sigma} (\frac{U}{2} - \mu) n_{i\sigma} - \frac{U}{2} \sum_i \mathbf{m}_i \cdot \vec{\sigma}_i + \frac{U}{4} \sum_i \mathbf{m}_i^2
\end{aligned}
\tag{4.2}
$$

We will set $t = 1$ as the reference energy scale. $t' = 0$ corresponds to the square lattice, and $t' = t$ to the isotropic triangular lattice. The first two terms are just the tight binding parts for the anisotropic triangular lattice. Third term has constant shift of on-site energy. The last two terms are of crucial importance, in which the first term couples the electrons to the classical fields $\mathbf{m}_i$ with coupling $U/2$, and splits the on-site energy for two spins state by $\pm \frac{U|\mathbf{m}_i|}{2}$. The magnitude of the $\mathbf{m}_i$ field is controlled by the last term. μ controls the electron density, which we maintain at half-filling, $n = 1$. $U > 0$ is the Hubbard repulsion.

4.2   Ground state phase diagram

First, let study the ground state (T=0) behaviour of the system for generic value of U/t, and t'/t. As mentioned in the section 2.3.2, in order to get the ground state, one has to minimize the total energy at half filling $E\{\mathbf{m}_i\} = E_{el}\{\mathbf{m}_i\} + E_{cl}\{\mathbf{m}_i\}$ with respect to the $\mathbf{m}_i$ fields. In a brute force minimization, for N site lattice, this would
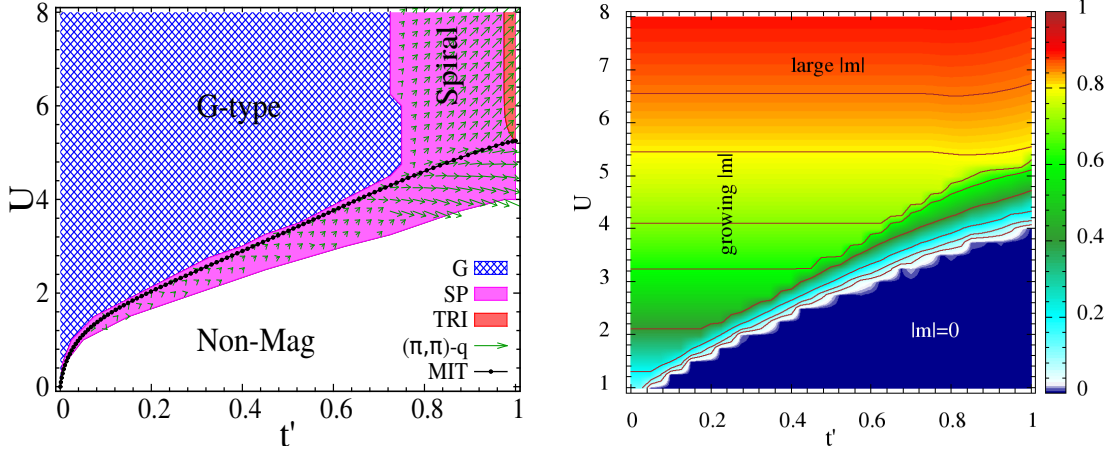
Figure 4.3: Left: The ground state phase diagram. The blue region denotes the Neel state characterized by $\mathbf{q} = (\pi, \pi)$. The thin red strip along $t' = 1$ denotes the three sub-lattice 120^0 spiral for which $\mathbf{q} = \left(\frac{2\pi}{3}, \frac{2\pi}{3}\right)$. The pink region represents incommensurate spirals at generic $\mathbf{q}$. A reduced scale of $\mathbf{q} - (\pi, \pi)$ shown as green arrows is drawn as illustration in the spiral region. The black line is the metal insulator boundary based on gap in the state, so that region below it is gapless/metallic. The lower white portion gives the non-magnetic $m = 0$ solution. Right: The color plot of the optimal m in the $U - t'$ plane. The contours are visual guide to constant m.

result in minimizing a function of $3N$ variable, which is an N-P hard problem, not to mention that calculation of the energy would involve numerical diagonalization for each $\mathbf{m}_i$ field. However, If we look for periodic solutions, the number of parameter to minimize with, becomes small and independent of system size N. Motivated by the simplicity to solve and generality, we chose the variational set described by $\mathbf{m}_i = m(\cos \mathbf{q} \cdot \mathbf{x}_i, \sin \mathbf{q} \cdot \mathbf{x}_i, 0)$ which describes a periodic field configuration, in which the magnitude of the field at each lattice site is m, and its angular direction have periodicity of the period vector $\mathbf{q}$. Once we restrict to this set, the total energy becomes the function of the magnitude m and the period $\mathbf{q}$, i.e., $E = E(m, \mathbf{q})$. Besides its calculation is fairly easy and we discussed it in section 2.3.2. For a given $(U/t, t'/t)$, one gets the optimal $(m, \mathbf{q})$ after minimizing the total energy, which characterizes the electronic nature of the state.

4.2.1 Magnetic phases

In Fig.4.3 (left) we have shown the ground state phase diagram, which summarizes the magnetic nature of the states in the $U - t'$ plane. The primary phases are collinear Neel order (G-type), incommensurate spiral (SP) and three sub-lattice 120^0
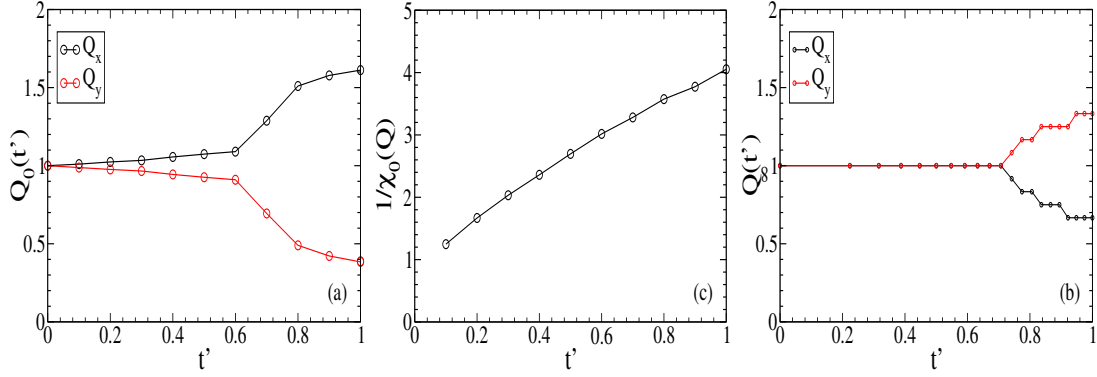
Figure 4.4: The magnetic instability wavevector inferred in the weak coupling limit (panel (a)), the corresponding $\chi_0^{-1} \sim U_c$ (panel (b)), and the Heisenberg limit wavevector (panel (c)). These results set the rough 'analytic' limits of the theory. A full optimisation based on the MC is needed at intermediate coupling. χ_0^{-1} should fall to zero as $t'/t \to 0$, accessing that requires calculation on much bigger lattices.

(at $t' = 1$), which have non zero m and $\mathbf{q}$ solutions. At lower U and larger t' one gets $m = 0$ solutions giving uncorrelated metallic (non-magnetic) state. The $t' = 0$ line stays at Neel order (G-type) for all U/t values upto $U/t = 0$, which continuously shrinks from the low U side following the MIT line, and eventually is destabilized against spirals at $t' \approx 0.7$. Beyond $t' \approx 0.7$, we have spiral whose period $\mathbf{q}$ gradually shifts from $\mathbf{q} = (\pi, \pi)$ to $\mathbf{q} = (\frac{2\pi}{3}, \frac{2\pi}{3})$, which is the ground state for large U limit for triangular lattice $t' = 1$. In fact, at large U it shifts along straight line connecting (π, π) and $(\frac{2\pi}{3}, \frac{2\pi}{3})$. The right panel of the figure we have shown the optimal m in the $U - t'$ plane. At lower U, the m stays constant in the Neel region, and starts decreasing once in the spiral region, and eventually vanishes. Thus in general, spiral phases have lower m as compared to Neel phase at given moderate U.

A quick understanding can be obtained by examining the weak coupling and strong coupling limits. Within the RPA scheme the peak in $\chi_0(\mathbf{q})$ decides the instability, as we have discussed before. Panel (a) in Fig.4.4 shows this wavevector $\mathbf{Q}_0(t'/t)$. Notice that it stays close to (π, π) for $t'/t \lesssim 0.6$ and then shifts quickly. The corresponding $\chi_0^{-1} \sim U_c$ is shown in panel (b). These decide the weak U instability and magnetic phase. For $U/t \gg 1$, deep in the Mott phase the system is a '$J - J'$' Heisenberg model, and the wavevector for that, labelled $\mathbf{Q}_\infty$ is shown in panel (c). Remember that $J'/J = (t'/t)^2$.

The band susceptibility was calculated on sizes upto 200×200, but capturing the divergence of χ as $t'/t \to 0$ requires much bigger lattices.
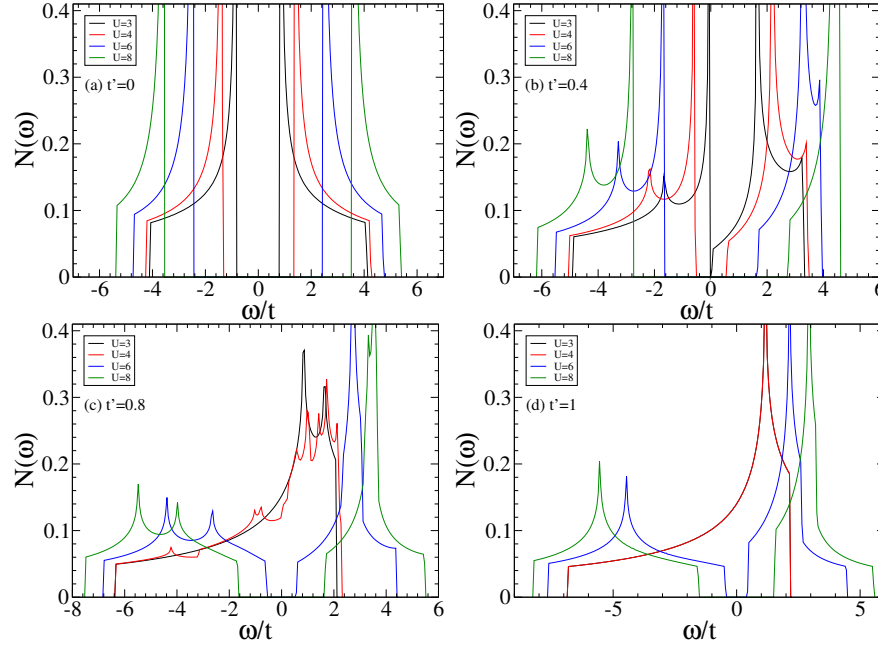
Figure 4.5: Density of states of the electron system at $T = 0$, using the variationally minimised background (which is roughly consistent with MC results).

4.2.2 Density of states

Recalling the tight binding dispersion $\epsilon_{\mathbf{k}} = -2t(\cos k_x + \cos k_y) - 2t' \cos(k_x + k_y)$, and the dispersion, we had for generic spiral state for given $\mathbf{Q}$ and m,

$$\epsilon_{\pm,\mathbf{k}} = \frac{1}{2} \left[\epsilon_{\mathbf{k}} + \epsilon_{\mathbf{k}-\mathbf{Q}} \pm \sqrt{(\epsilon_{\mathbf{k}} - \epsilon_{\mathbf{k}-\mathbf{Q}})^2 + U^2 m^2} \right]$$

one can easily see that, for $\mathbf{Q} = (\pi, \pi)$ (the Neel phase) $\epsilon_{\mathbf{k}} + \epsilon_{\mathbf{k}-\mathbf{Q}} = 0$ when $t' = 0$. Thus eigenvalues get divided into two sets with $\epsilon_{+,\mathbf{k}} = -\epsilon_{-,\mathbf{k}}$, so that the gap at half filling has a lower bound of Um (which is also the gap). Thus the Neel phase always has a gap for any nonzero value of m.

Given the optimised values of $\mathbf{Q}$ and m at a given U/t and t'/t the density of states can be readily generated. We show such results in Fig.4.5 for four values of t'/t, and $U/t = 3, 4, 6, 8$ in all four cases. It shows an insulating (gapped) state at all U when $t' = 0$, and the presence of a metal - with crossover to an insulating state at the larger t' cases.

While the specific bandstructure here arises from the presence of long range order in the background, the survival of the large U insulator at finite T is not related to order at all. The finite temperature discussion will highlight this.

A word about the gap. The expression $(\min\{\epsilon_{+,\mathbf{k}}\}$ - $\max\{\epsilon_{-,\mathbf{k}}\})$ whenever greater
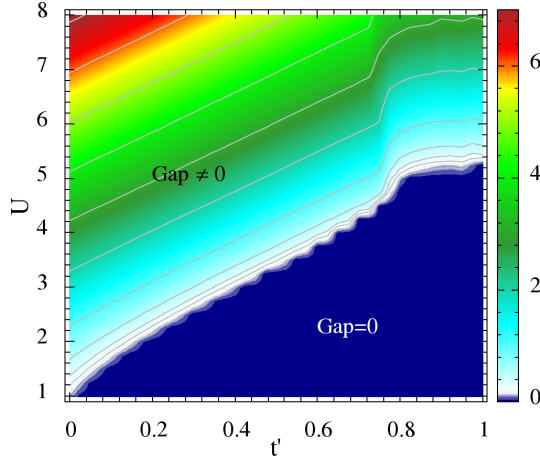
Figure 4.6:   The colour plot of the gap estimated in ground state.

than zero, gives the gap at half filling, but is difficult to calculate analytically for general value of t' and $\mathbf{Q}$. We have hence numerically calculated the gap for the ground state, which is shown in Fig.4.6. This suggests that spiral, which have lower m values compared to Neel phase, tend to have smaller gap, as a result the metal insulator boundary (shown as black line in the phase diagram in Fig.4.3) which is the locus of zero gap, has a positive slope with t'. Thus increasing t'/t reduces the insulating character, and if U/t is moderate, carries the system across the insulator to metal transition.

This summarizes the discussion of the ground state. As mentioned in the section 2.2.2, the effective model we used, reduces to unrestricted Hartree-Fock at $T = 0$, but with no assumption about the *translational symmetry*. It supports only static moment phases, usually either long range ordered, or non-magnetic ($m = 0$). However, when we raise the temperature from $T = 0$, the exact inclusion of the thermal fluctuations generated via the classical $\mathbf{m}_i$ fields, quickly improves the accuracy of the method with increasing temperature. In the next section we discuss the effect of the thermal fluctuations at finite temperature, on the $\mathbf{m}_i$ and their impact on electronic properties.

4.3   Finite temperature properties

We accessed the finite temperature physics of the effective model using the real space Monte Carlo sampling discussed in section 2.3.1, on $N = 24 \times 24$ lattice. The system was *annealed* from high enough temperature $T/t > 0.2$, to $T = 0$ in discretized intervals. At each temperature, large number of samples of $\mathbf{m}_i$ were generated from

the equilibrium distribution.

$$P\{\mathbf{m}_i\} = \frac{Tr_{c,c\dagger} e^{-\beta H_{el}} e^{-\beta H_{cl}}}{\int \mathcal{D}\mathbf{m} Tr_{c,c\dagger} e^{-\beta H_{el}} e^{-\beta H_{cl}}}$$

These were used to analyze the spatial correlation and the ordering tendency of the fields. The electronic properties like density of states, optical conductivity, DC resistivity, spectral function etc., were calculated by taking the thermal average over each of these individual $\mathbf{m}_i$ configurations. The system was studied for different degree of hopping anisotropy t' in the entire range of [0-1], and based the results of magnetic correlations, electronic properties and transport, we mapped out $U - T$ phase diagram.

4.3.1   Phase diagrams

Below, we first summarize our results using $U - T$ phase diagram. Then, we discuss in detail the spatial correlations of the fields in section 4.3.2. Then in the following sections we show how these correlations affect the electronic properties, specifically electronic density of states (section 4.3.4), transport (section 4.3.3), the spectral function and its anisotropy (4.3.5).

In Fig.4.7, we have shown the interaction(U)-temperature(T) phase diagram, drawn at four representative values of $t' = 0, 0.4, 0.8, 1$. The low temperature result is equivalent to UHF, and leads to a transition from an uncorrelated paramagnetic metal (PM) to an antiferromagnetic metal (AFM) at some $U = U_{c1}$, followed by antiferromagnetic insulator (AFI) at some $U = U_{c2} > U_{c1}$ (except when $t' = 0$). For $t' = 0$ and $t' = 0.4$, the AFI and AFM (for $t' = 0.4$) is simple Neel ordered, while for $t' = 0.8$ and $t' = 1$, its non-collinear phase with $\mathbf{q} \approx (0.85\pi, 0.85\pi)$, and $\mathbf{q} = (0.67\pi, 0.67\pi)$ respectively. At $t' = 0$, the AFI survives down to $U/t = 0$, with decreasing moment, and there is U_{c1}, and no AFM phase. The magnitude m_i is small in the AFM phase, and grows as U/t increases in the insulating (Mott) phase. The window of AFM slowly grows upon increasing t' as seen in the ground state variational phase diagram. However, the existence of the AFM, and the nature of order in the intermediate U/t Mott phase, could be affected by the neglected quantum fluctuations of the $\mathbf{m}_i$.

Finite temperature brings into play the low energy fluctuations of the $\mathbf{m}_i$. The effective model has the $O(3)$ symmetry of the parent Hubbard model so it cannot sustain true long range order at finite T. However, our annealing results suggest
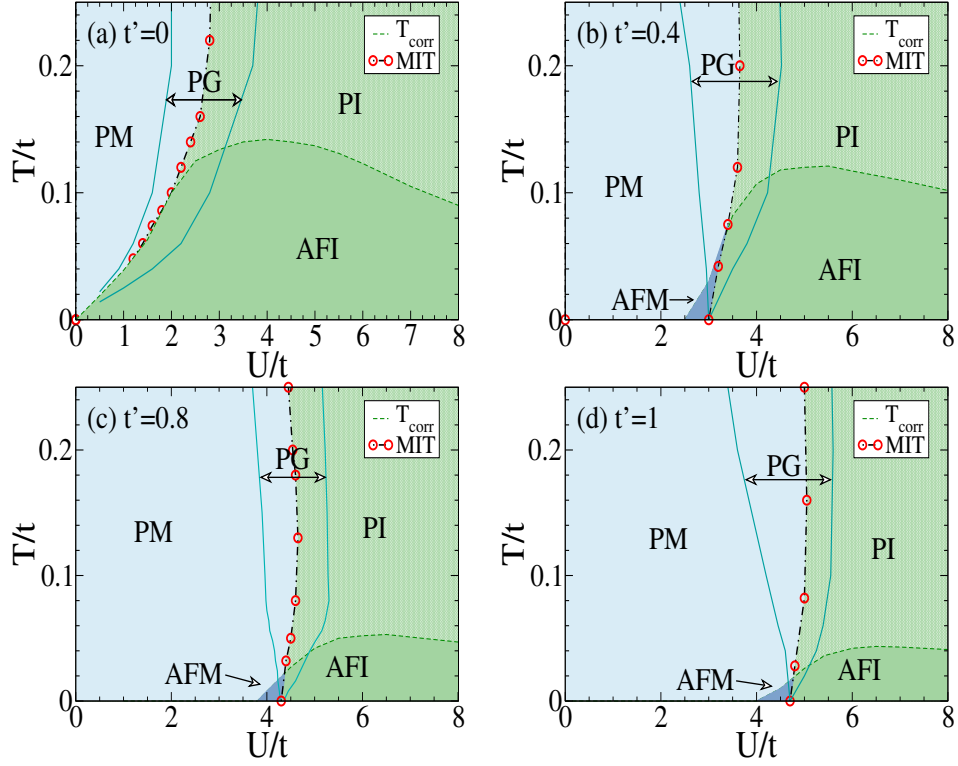
Figure 4.7: Finite temperature phase diagram, for four values of t'/t. (a) $t' = 0$, (b) $t' = 0.4$, (c) $t' = 0.8$, (d) $t' = 1$. The phases are paramagnetic metal (PM), paramagnetic insulator (PI), antiferromagnetic metal (AFM) and antiferromagnetic insulator (AFI). In (a), and (b) the AFM and AFI phases are simple Neel ordered, while in (c) and (d) these are non-collinear phases. PG indicates the pseudogap phase. T_{corr} indicates the temperature at which magnetic correlation length becomes larger than lattice size. The MIT line defines the crossover from metallic to insulating character, based on transport.

that magnetic correlations grow rapidly below a temperature T_{corr}, and weak inter-planar coupling would stabilize in plane order below T_{corr} (we have checked this explicitly). This scale increases from zero at $U = U_{c1}$, reaches a peak at some U_{max}/t, and falls beyond as the virtual kinetic energy gain reduces with increasing U. The U_{max} systematically increases with increasing t'/t, while the maximum T_{corr} at U_{max} systematically goes down.

We classify the finite T phases as metal or insulator based on the $d\rho/dT$, the temperature derivative of the resistivity. The dotted line indicating the MIT corresponds to the locus $d\rho(T, U)/dT = 0$. In addition to the magnetic and transport classification we also show a window around the MIT line where the electronic density of states (DOS) has a pseudogap. To the right of this region the DOS has a 'hard gap' while to the left it is featureless.

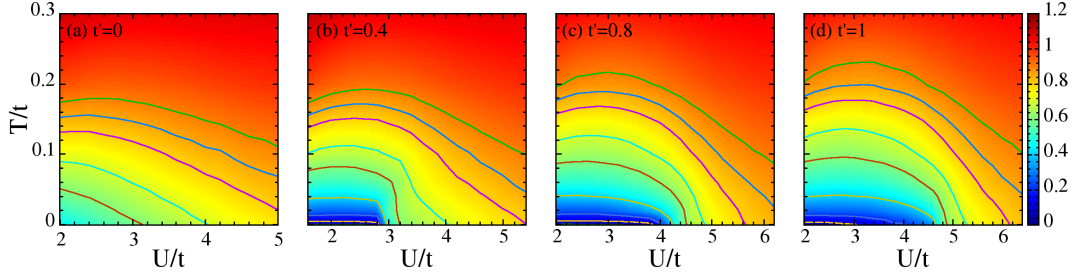Figure 4.8: The U dependence of $\bar{m}(T)$ for various temperatures, four representative values of t'. (a) $t' = 0$, (b) $t' = 0.4$, (c) $t' = 0.8$ and (d) $t' = 1$.

For $t' = 0$, the MIT line has a positive slope, which increases with temperature, and at very high temperature, the line becomes nearly vertical. However, for finite t' it becomes vertical at some moderately hight temperature T_{re}, after which the slope turns negative, showing re-entrant insulator-metal-insulator behavior with increasing T near $U \sim U_{c2}$. We discuss the details of the re-entrance later.

4.3.2 Auxiliary field correlations

We saw in the section 4.2, that the ground state is either magnetic, with non-zero fixed m and corresponding $\mathbf{q}$, or non-magnetic with $m = 0$. At finite temperature, the thermal excitations would generate fluctuations in the $\mathbf{m}_i$ configurations. This happens by allowing (a) differing magnitudes m_i of the fields at different sites and (b) randomized angles of the $\mathbf{m}_i$. These fluctuations, generate a variety of interesting states, as we saw in the last section. We will now try to see some trends in the nature of these fluctuations, in the $U - t'$ plane. As we will see in the subsequent sections, each have a different impact on electronic properties. Thus broadly we have two kind of fluctuations in the $\mathbf{m}_i$:

4.3.2.1 Magnitude distribution

When the ground state had non-zero m, and periodic angular variation given by $\mathbf{q}$, the excitations would generate states with non-uniform $\{m_i\}$, which will be distributed in some form around the average $\bar{m}(T)$. At very low temperature, $\bar{m}(T)$ will be very close to the ground state optimal value m, and systematically will *increase* with temperature. The ground state that had $m = 0$, would now generate non-zero $\{m_i\}$ distribution with increasing $\bar{m}(T)$ with temperature. In the Fig.4.8 we have shown the U dependence of $\bar{m}(T)$ at different temperatures for the four representative values of anisotropy t'. There is systematic increase in m with temperature at
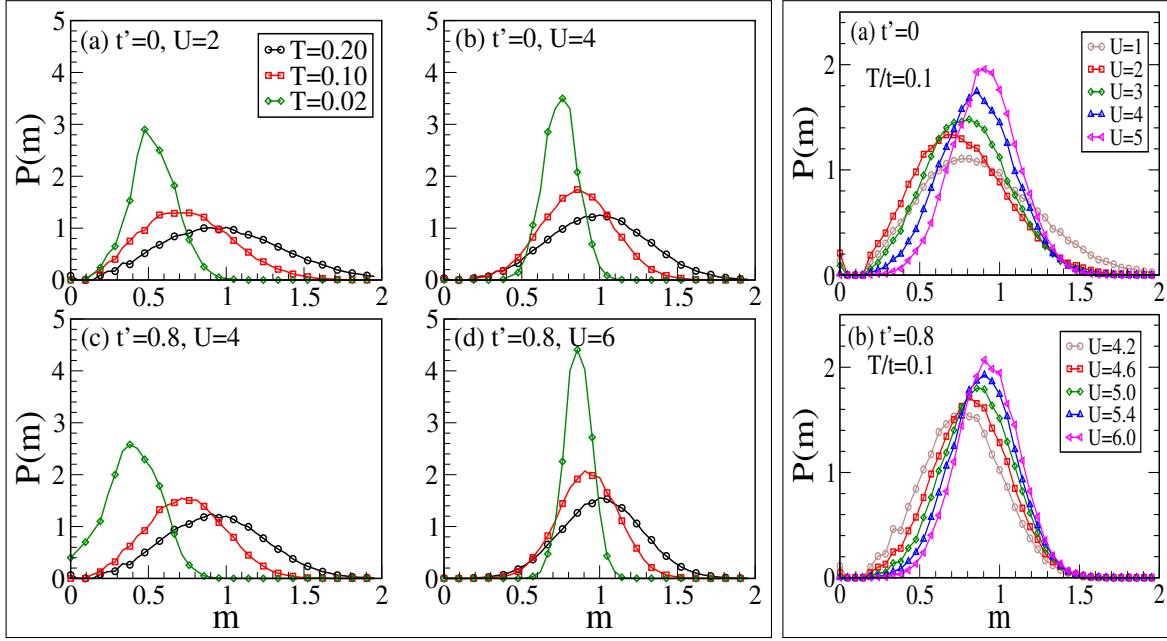
Figure 4.9: The magnitude distribution $P(m)$ at two values of t' plotted for values of U typical of weak and strong coupling and three temperatures each.

all U and t', however the rate of change of m is larger in metallic or low U. At very high temperature $T/t \geq 0.2$, the m becomes nearly independent of U.

The distribution of these m_i, denoted by $P(m, T, U)$ (or in short referred to as $P(m)$) is defined as following

$$P(m, T, U) = \langle\langle \frac{1}{N} \sum_i \delta(|\mathbf{m}_i| - m) \rangle\rangle \tag{4.3}$$

where $\delta(x)$ denotes the Dirac delta function, and $\langle\langle \ldots \rangle\rangle$ denotes the thermal average over equilibrium configurations. Lets see this first for the simplest case of square lattice $t' = 0$. In Fig.4.9 we have shown (a) the temperature dependence of the $P(m)$ at a fixed U, and (b) the U dependence at a fixed temperature. At T=0, $P(m)$ will be a delta function peaked at the optimal m. It progressively broadens around the mean, $\bar{m}(T)$, which itself increases with T. The U dependence in panel (b) shows that magnitude fluctuations are larger in lower U, while larger U, or more insulating systems have smaller magnitude fluctuations. This indicates that *the angular fluctuation are more crucial in insulating systems*. Although we have discussed it in the context of square lattice, these features of magnitude fluctuations are valid for all t'.

104

Figure 4.10: Snapshots of the auxiliary field magnitude, nearest neighbour angular correlation ($\mathbf{m}_0.\mathbf{m}_i$), and the structure factor $S(\mathbf{q})$. The left 3×3 panel is for $t' = 0$ and $U = 4$ (the square lattice with Neel order) and the right set is for $t' = 0.8$ and $U = 6$ (anisotropic triangular lattice with spiral order). Top row in each set is $m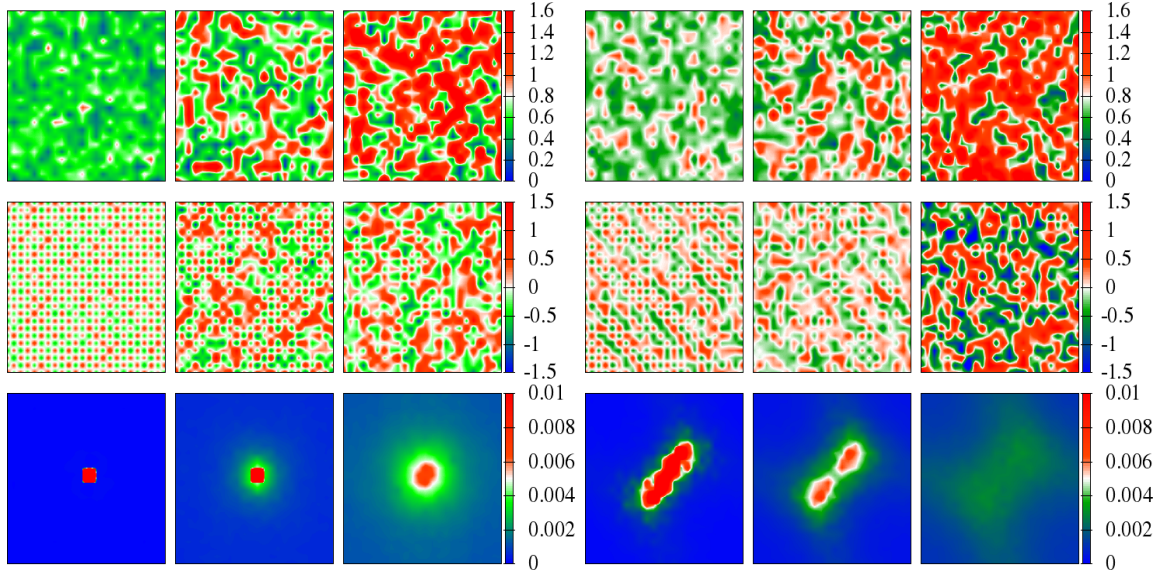_i$, next row is NN $\mathbf{m}_0.\mathbf{m}_i$, where $\mathbf{R}_0$ is a fixed reference site, third row is $S(\mathbf{q})$. Temperatures (from left to right) are $T/t = 0.02, 0.10, 0.20$.

4.3.2.2   Angular correlations

We calculate the following thermally averaged *structure factor* to proble angular correlation:

$$S(\mathbf{q}) = \frac{1}{N^2} \sum_{ij} \langle\langle \mathbf{m_i} \cdot \mathbf{m_j} \rangle\rangle e^{i\mathbf{q}\cdot(\mathbf{X}_i - \mathbf{X}_j)} \tag{4.4}$$

In a state of $\mathbf{m}_i$ with completely random angles, the structure factor $S(\mathbf{q}) = \mathcal{O}(\frac{1}{N^2})$ for all $\mathbf{q}$. However, as angles start to get correlated, some of the $\mathbf{q}$ increase at the cost of other, and the maximum value (at some $\mathbf{q}$s) of $S(\mathbf{q})$ starts to increase. Upon lowering the temperature, when the system goes under the magnetic transition, *the rapid growth of structure factor at some $\mathbf{q}$ is observed, whose onset temperature T_{corr} defines magnetic transition temperature.*

In Fig.4.10, we have shown the temperature dependence of the structure factor aided with some snapshots of the $\mathbf{m}_i$ fields. At very low $T = 0.02$, the m_i magnitudes almost uniform, their directions alternate in all directions as in Neel state, and the structure factor is sharply peaked at $\mathbf{q} = (\pi\pi)$. Progressively, upon increasing T, m_i is fluctuate, angular correlation weakens and the peak value of structure factor reduces, spilling its weight to neighbouring $\mathbf{q}$ values. The right 3×3 panel shows
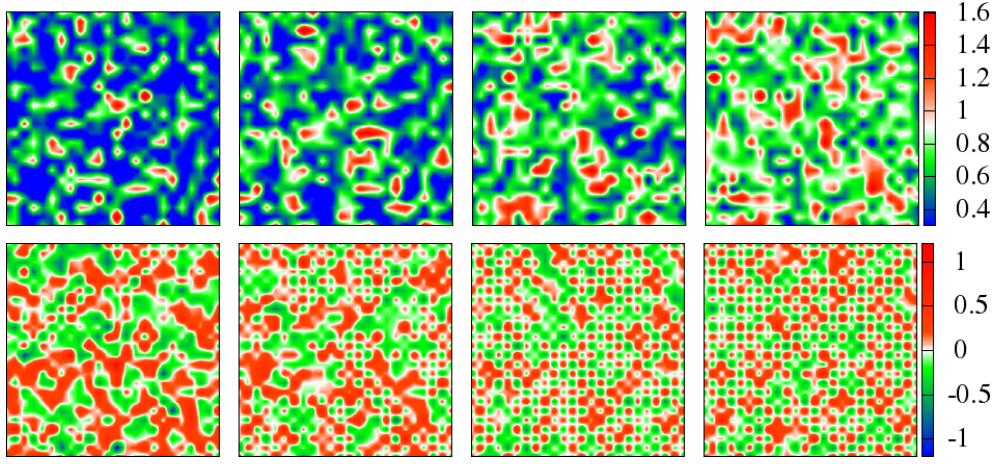
Figure 4.11: Snapshots of $\mathbf{m}_i$ fields showing U dependence of magnitude fluctuations and the angular correlation at $T = 0.1$, $U = 2, 3, 4, 5$, plotted on 24×24 lattice. Top row: Site dependent magnitude m_i. Bottom row: $\alpha_i = \mathbf{m}_i \cdot \mathbf{m}_0$, where $\mathbf{m}_0$ is field at some reference point. The electrons see these as typical configurations, as the system evolves from correlated metal with small U to antiferromagnetic insulator with large U.

similar data on the anisotropic case at $t'/t = 0.8$ where the reference state is now a spiral.

Next, in Fig.4.11 we have shown the evolution of the snapshots at a fixed temperature for different U at $t' = 0$. As the interaction strength increases, one observes the increase in the typical values of m_i and decrease in its fluctuations. Simultaneously, the angular correlations become stronger with U, evolving from a short range correlation at $U = 2$ to progressively better antiferromagnetic states at higher interaction strength ($U = 4, 5$).

To summarize, based on the results on the known square lattice, we know that, the fluctuations of the field increase with increasing temperature. The magnitude fluctuations are stronger at lower U, showing broader $P(m)$ compared to large U. The angular correlations are stronger in large U systems.

The nature of angular correlation becomes more complex, once we go to larger t' where the ground state has order at incommensurate $\mathbf{q}$. In Fig.4.12 we show the evolution of the structure factor at two temperatures, one at high temperature, and the other close to T_{corr}. First of all, the peaks are not at (π, π), but at incommensurate $\mathbf{q} \approx (0.85\pi, 0.85\pi)$, which the same $\mathbf{q}$, at which the ground state orders.

Besides, the spread is is larger compared to what we saw in square lattice at the same temperature. This means stronger angular fluctuations, and lower T_{corr}.
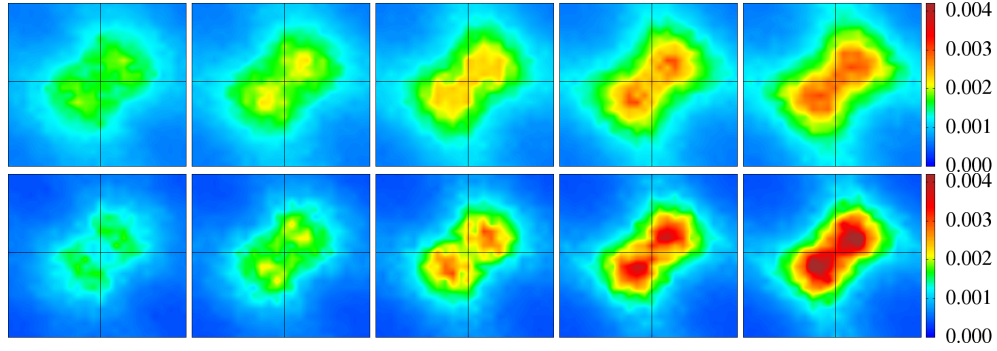
Figure 4.12: The structure factor $S(\mathbf{q})$ for $t' = 0.8$ plotted for increasing $U = 4.2, 4.4, 4.6, 4.8, 5.0$ (left to right), at two temperatures $T = 0.1$ (top row) and $T = 0.06$ (bottom row).

4.3.3 Transport and optical response

For the optical conductivity $\sigma(\omega, T)$, and the resistivity $\rho(T)$, we used the Kubo formula for optical conductivity. In Fig.4.13 we show the resistivity $\rho(T)$ computed from the Monte Carlo for varying U/t. Our resistivity is in units of $\rho_0 = \frac{\hbar c_0}{\pi e^2}$, c_0 being the lattice spacing.

In a full treatment of the Hubbard model, retaining the quantum fluctuations of $\mathbf{m}_i$, one would expect $\rho(T) \propto T^2$ in the metallic side. This is what DMFT produces, consistent with the experiments. Our resistivity also vanishes as $T \to 0$, modulo effects of finite annealing, but is described more by $\rho(T) \propto T$. This is an artifact of the classical approximation ($\langle m_i^2 \rangle \sim T$). However, as T increases the classical thermal fluctuations should provide an adequate description of the transport.

In Fig.4.14, we have shown the temperature evolution of the optical conductivity $\sigma(\omega)$, for for four values of t', and two values of U, $U = 4$ (left frame) and $U = 5$ (right frame). In a Drude metal, the optical conductivity would have maximum at $\omega = 0$, and quickly loose weight to higher frequency, while in a Mott insulator the optical conductivity would have a gap at low frequency, after which it would pickup weight which would have maxima near U. Its easy to see the following trends from the $\sigma(\omega)$:

- In both frames, (a) and (b) i.e., $t' = 0, 0.4$ are insulating with no weight at low frequency, and the maxima is peaked around $\sim U\bar{m}$. At low temperature, the gap is larger along the peak value. With increasing the temperature, progressively, the gap is decreased by the transfer of spectral weight at low frequencies, eventually having small Drude weight at high temperature. One

107
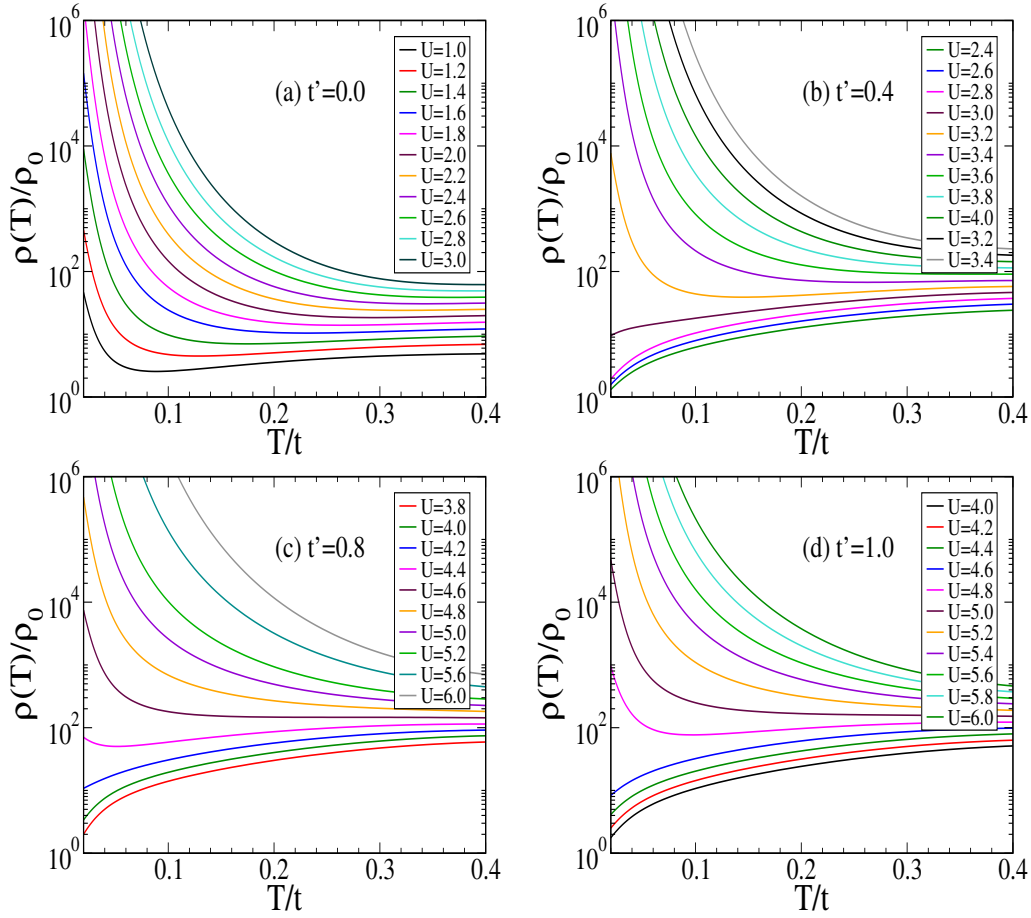
Figure 4.13: Temperature dependence of the resistivity $\rho(T)$ for different U in the neighbourhood of the MIT, plotted for the same four cross sections of t' as chosen in Fig.4.7 (a) $t' = 0$, (b) $t' = 0.4$, (c) $t' = 0.8$ and (d) $t' = 1$. The U values, shown here are chosen around the MIT, displayed in the legend.

can guess that this would correspond to a density of state with weak gap, or strong pseudogap with very low weight near the Fermi level, and the gap in the density of states would diminish, progressively with increasing temperature.

• In the left frame (c) and (d), i.e., $t' = 0.8, 1$ are metals having large weight at $\omega = 0$. The peak in $\sigma(\omega)$ is close to $\omega = 0$ in (c) while its exactly at $\omega = 0$ in (d). With increasing temperature, the Drude weight and the peak value decreases, and the peak locations moves to higher ω. The response at higher temperature, thus becomes *non-Drude metal*. This would correspond to 'weakly correlated metal' whose density of state, has large weight at Fermi level, which depletes progressively towards higher energies, forming pseudogap.

• In the right frame, (c) and (d) i.e., both have vanishing Drude weight, and

Figure 4.14: Temperature evolution of the optical conductivity $\sigma(\omega)$. The left and right boxes are for $U = 4$, and $U = 5$ respectively. The chosen cross sections of t' are (a) $t' = 0$, (b) $t' = 0.4$, (c) $t' = 0.8$ and (d) $t' = 1$. In each figure, three temperatures $T = 0.06, 0.1, 0.2$ are plotted.

most of the spectral weight surrounds $U\bar{m}$ The low frequency weight slowly increases with higher temperature, and the high ω weight, center around $U\bar{m}$ disperses. This one would expect very close to MIT, on the insulating side where the gap is vanishingly small. The density of state in such case would have very strong dip at Fermi level, with small weight at low energy.

In Fig.4.15, we show the optical conductivity $\sigma(\omega)$ at $T = 0.1t$ and $T = 0.2t$ as the interaction is varied across the Mott crossover, for $t' = 0.8$. Our first observation is the distinctly non Drude nature of $\sigma(\omega)$ in the metal, $U/t \lesssim 4.4$, with $d\sigma(\omega)/d\omega|_{\omega\to 0} > 0$. The low frequency hump in the bad metal evolves into the interband Hubbard peak in the Mott phase. The change in the lineshape with increasing T is more prominent in the metal, with the peak location moving outward, and is more modest deep in the insulator.

In the next section, we discuss the trends in the density of states (DOS) of the systems, as function of temperature and the interaction strength, and would explicitly show the trends we have guessed.

4.3.4   Density of states and pseudogap

In Fig.4.16, we have shown the temperature evolution of the density of state $N(\omega)$, for the same set of parameters as in the Fig.4.14. Its easy to see from the low temperature DOS, that (i) in both frames, (a) and (b) i.e., $t' = 0, 0.4$ are insulating in the ground state, showing hard gap. (ii) in the left frame (c) and (d), i.e., $t' = 0.8, 1$
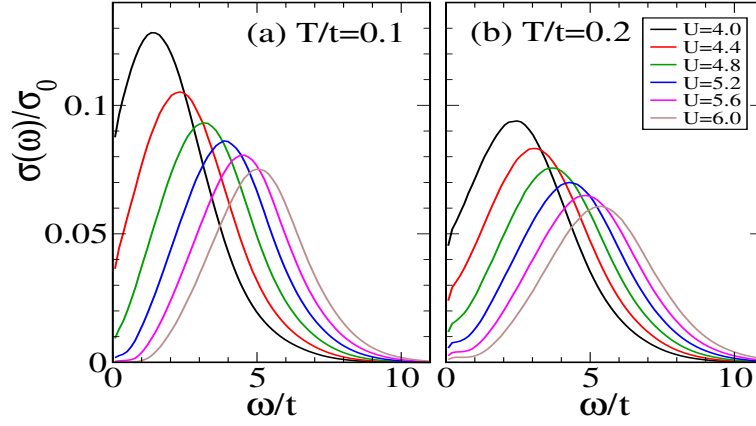
Figure 4.15: Optical conductivity at (a) $T = 0.1$, (b) $T = 0.2$ for U varying across U_c, for $t' = 0.8$. At these temperatures the $\sigma(\omega)$ is non Drude even in the 'weakly correlated' case $U \sim 4.0$. The finite frequency peak evolves into the Hubbard transition at large U.

are good metals, with large DOS at Fermi level. (iii) in the right frame, (c) and (d) i.e., both have strong dip in the DOS at the Fermi level. Evolution to higher temperature, increases the low frequency weight at Fermi level of an insulator, which results in narrowing the gap, and eventually a strong dip pseudogap phase. On the contrary, heating the uncorrelated metal (left frame (c) (d)), depletes the weight at Fermi level, thereby inducing a soft dip pseudogap, which becomes stronger at higher temperature.

At some fixed temperature, when we increase the interaction U, then at some $U = U_1(T)$, the magnetic fluctuations become strong enough to induce the pseudogap in the DOS, which deepens progressively with U, and at some $U = U_2(T)$, would become hard gapped. The local of these U_1 and U_2 defines the region containing the pseudogap, shown earlier in the finite T phase diagrams (Fig.4.7). The Fig.4.17 explicitly shows the crossover from the metal to the insulator involving a wide window of pseudogap, where the pseudogap window widens with increasing temperature. Here we have taken $t' = 0.8$, and chosen the U range across the MIT. One can see, that at $T = 0.1$ (Fig.4.17(a)) that $U = 4.0$ has a small dip at Fermi level (close to U_1), and $U = 5.6$ is on the verge of hard gap. At higher temperature $T = 0.2$ (Fig.4.17(b)), the dip in the $U = 4.0$ has increased, while $U = 5.6$ has slowly gained some spectral weight.

In general, in the region between the $U_1(T)$ line and the MIT line, the dip feature deepens with with T, and we have $\frac{dN(\omega=0)}{dT} < 0$, while in the region between MIT and $U_2(T)$ we have weak $\frac{dN(\omega=0)}{dT} > 0$. The PG arises from the coupling of electrons
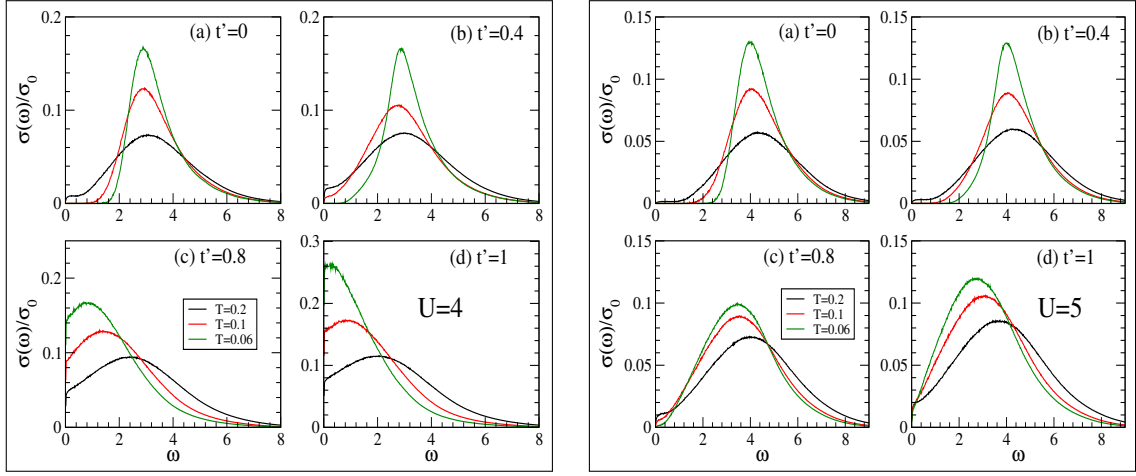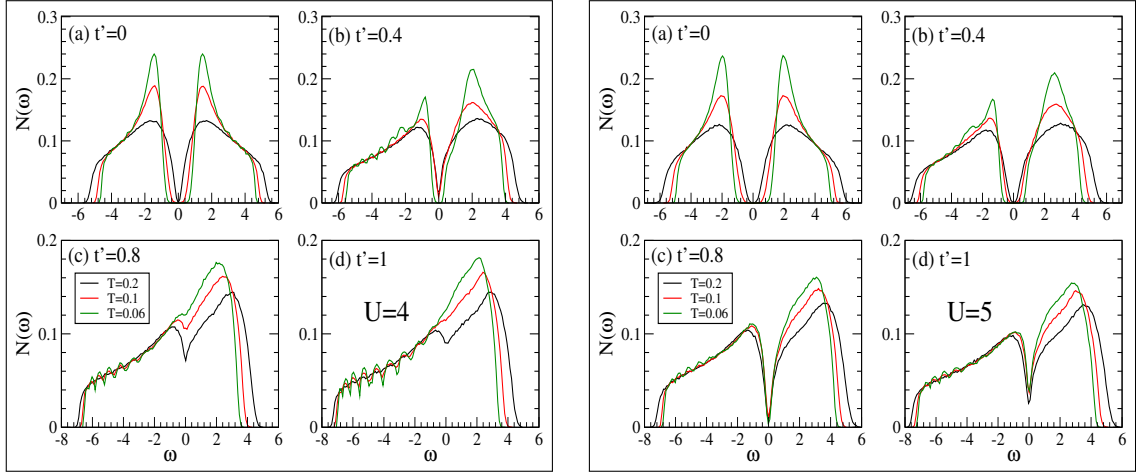
Figure 4.16: Temperature evolution of the DOS $N(\omega)$. The left and right boxes are for $U = 4$, and $U = 5$ respectively. The chosen cross sections of t' are (a) $t' = 0$, (b) $t' = 0.4$, (c) $t' = 0.8$ and (d) $t' = 1$. In each figure, three temperatures $T = 0.06, 0.1, 0.2$ are plotted.

to the fluctuating $\mathbf{m}_i$. A large m_i at all sites would open a Mott gap, independent of any order among the moments. Weaker m_i, thermally generated in the metal near U_{c1} and with only short range correlations, manages to deplete low frequency weight without opening a gap. Since the typical size $\langle m_i \rangle$ increases with T in the metal, we see the dip deepening at $U < U_c$.

In Fig.4.18, we show the map of DOS at the Fermi level $N(\omega = 0)$ over the entire $U - t'$ plane, at temperatures $T = 0.06, 0.1, 0.2, 0.3$, showing the evolution from the hight DOS in the metal to the vanishing DOS in the Mott phase through low finite DOS in the PG phase.
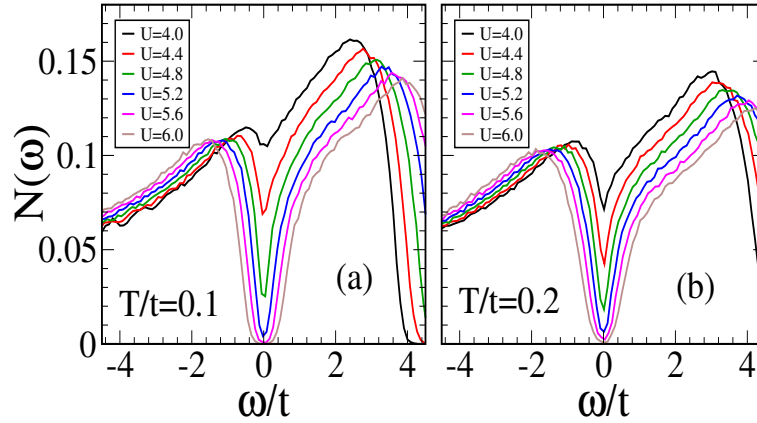
Figure 4.17: Density of states at $T/t = 0.1, 0.2$ for U varying across U_c. The dip in the DOS deepens with increasing T for $U/t \lesssim 4.8$. For larger U/t the system slowly gains spectral weight with increasing T. $t' = 0.8$
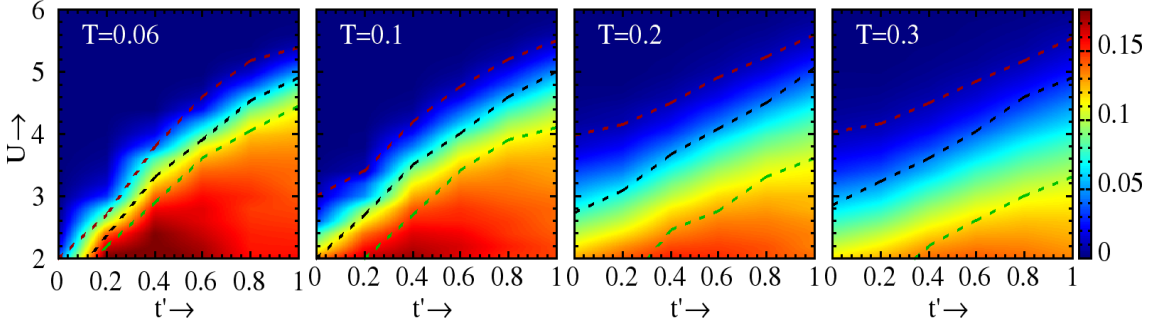
Figure 4.18: Map of the $N(\omega = 0)$, the DOS at Fermi level, in the $U - t'$ plane at four temperatures $T = 0.06, 0.1, 0.2, 0.3$. The black dotted line denotes the MIT crossover. The region between red and green dotted line represents the pseudogap region.

4.3.5 Angle resolved spectral functions

While the *size* of the $\mathbf{m}_i$ determine the overall depletion of DOS near $\omega = 0$ and the opening of the Mott gap, the *angular correlations* dictate the momentum dependence of the spin averaged electronic spectral function

$$A(\mathbf{k}, \omega) = \text{Im} \sum_{\sigma} (\frac{i}{\pi}) \int_0^{\infty} dt e^{i\omega t} \langle\langle \{c_{\mathbf{k}\sigma}(t), c_{\mathbf{k}\sigma}^{\dagger}(0)\}\rangle\rangle$$

Within a 'local self energy' picture, as in DMFT, $A(\mathbf{k}, \omega)$ should have no $\mathbf{k}$ dependence on the Fermi surface (FS). In that case we should have a $\mathbf{k}$ independent suppression of $A(\mathbf{k}, 0)$ with increasing U/t. However, inclusion of spatial fluctuations would be able to access the $\mathbf{k}$ dependence of the spectral function.

Below we first show the evolution of the $A(\mathbf{k}, 0)$, across the Mott transition, in connection with the angular correlations through the structure factor $S(\mathbf{q})$. We discuss two limiting cases (a) the square lattice $t' = 0$ in Fig.4.19, where the angular fluctuations are strong near (π, π), and (b) $t' = 0.8$ in Fig.4.20, where they are at incommensurate $\mathbf{q} \approx (0.85\pi, 0.85\pi)$. In both figures $T = 0.1$ data is shown, and U are chosen near the metal insulator crossover.

In both figures, the top row shows maps of $A(\mathbf{k}, 0)$ for $k_x, k_y = [-\pi, \pi]$, as increasing U/t transforms the bad metal to a Mott insulator. The first panel at $U/t = 4.2$ for (a) and $U/t = 2.0$ for (b) shows weak anisotropy on the nominal Fermi surface. The Fermi is square for $t' = 0$, while elliptical in shape for $t' = 0.8$ with minor axis along $(0, 0) \rightarrow (\pi, \pi)$ direction. At the next panel, the weak anisotropy is much amplified and the weight in the $(0, 0) \rightarrow (\pi, \pi)$ direction is distinctly larger. The actual position of th
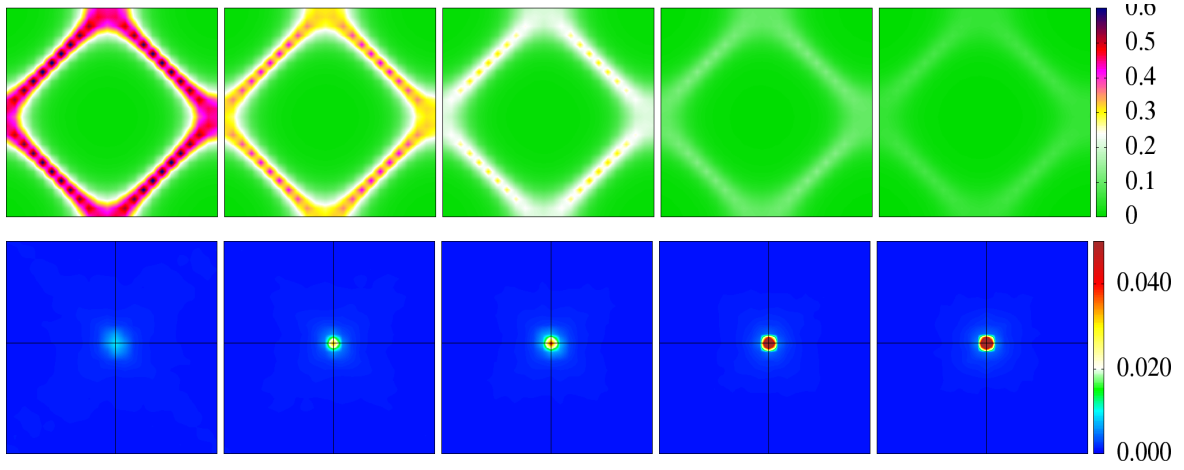
Figure 4.19: $t' = 0$ case. Top: Momentum dependence of the low frequency spectral weight in the electronic spectral function $A(\mathbf{k}, \omega)$ at $T/t = 0.1$. k_x, k_y range from $[-\pi, \pi]$ in the panels. Note the systematically larger weight near $\mathbf{k} = [\pi/2, \pi/2]$ and symmetry related points and smaller weight in the segments near $[\pi, 0]$ and $[0, \pi]$ and symmetry related points. $U/t = 2.0$, 2.2, 2.4, 2.6, 2.8, left to right. Bottom: $S(\mathbf{q})$ for the $\mathbf{m}_i$ fields for the same set of U/t. The q_x, q_y range from $[0, 2\pi]$. Note the very weak structure at $U/t = 2.0$ and the much larger and much sharper peak at $U/t = 2.8$.
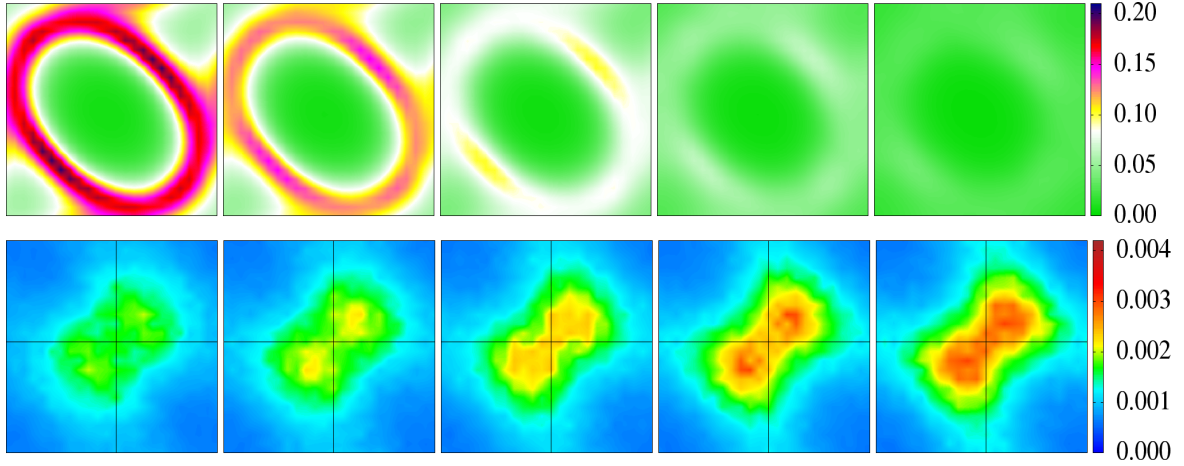
Figure 4.20: Top: Momentum dependence of the low frequency spectral weight in the electronic spectral function $A(\mathbf{k}, \omega)$ at $T/t = 0.1$. k_x, k_y range from $[-\pi, \pi]$ in the panels. Note the systematically larger weight near $\mathbf{k} = [\pi/2, \pi/2]$ and $[-\pi/2, -\pi/2]$ and smaller weight in the segments near $[\pi, 0]$ and $[0, \pi]$. $U/t = 4.2$, 4.4, 4.6, 4.8, 5.0, left to right. Bottom: Magnetic structure factor $S(\mathbf{q})$ for the auxiliary fields $\mathbf{m}_i$ for the same set of U/t. The q_x, q_y range from $[0, 2\pi]$. Note the very weak and diffuse structure at $U/t = 4.2$ and the much larger and differentiated structure at $U/t = 5.0$.

The next three panels basically show insulating states but without a hard Mott gap. Overall, the 'hot spot' where destruction of the Fermi surface seems to start is

113
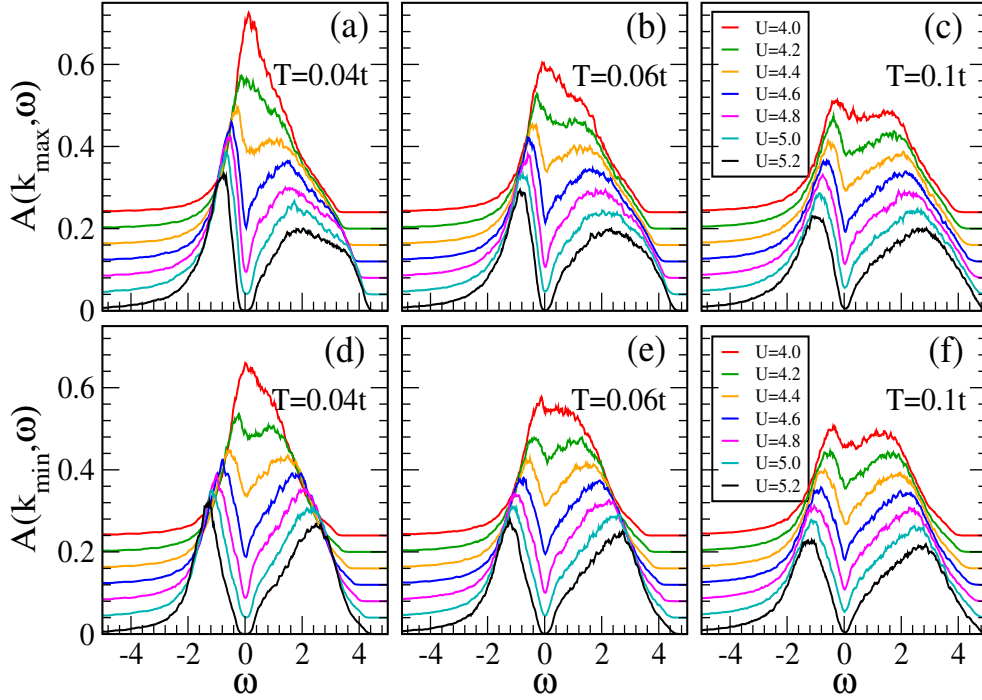
Figure 4.21:   Angle resolved spectral functions and $t'/t = 0.8$ highlighting the behaviour at the 'hot' and 'cold' spot on the Fermi surface.

at $(0, \pi)$, for the $t' = 0$ case, while the same for $t' = 0.8$ is near $\sim (0.64\pi, -0.64\pi)$ It ends near the 'cold spot', where the Fermi surface is strongest. The cold spot is near $(\pi/2, \pi/2)$, for $t' = 0$, and around $\sim (0.42\pi, 0.42\pi)$ for $t' = 0.8$. With increasing U the PG feature would form at the hot spot while the cold spot would still have a quasi-particle peak.

The second row in Fig.4.19,4.20 shows the structure factor $S(\mathbf{q})$ of the $\mathbf{m}_i$ fields at $T/t = 0.1$ for the same U/t as in the upper row. For $t' = 0$ the system is some what below T_{corr}, as a result magnetic correlation is large, hence the structure factor is quite sharp, around $\mathbf{Q} = (\pi, \pi)$, even though the order hasn't fully developed. For $t' = 0.8$, however, there is no magnetic order as the system is quite above its T_{corr}. Still, we can see the growth of correlations centered around $\mathbf{Q} \approx (0.85\pi, 0.85\pi)$ as U/t increases. The dominant electron scattering would be from $\mathbf{k}$ to $\mathbf{k} + \mathbf{Q}$, and the impact would be greatest in regions of the Fermi surface in the proximity of minima in $|\nabla \epsilon_{\mathbf{k}}|$. The location of the hot spots on the Fermi surface, and the momentum connecting them, indeed correspond to this scenario.

Fig.4.21 shows the full spectral function at the two points on the Fermi surface where the $\omega = 0$ spectral weight is either maximum (labelled $\mathbf{k}_{max}$) or minimum (labelled $\mathbf{k}_{min}$). The results are shown for $t'/t = 0.8$ but are generic as far as crossover
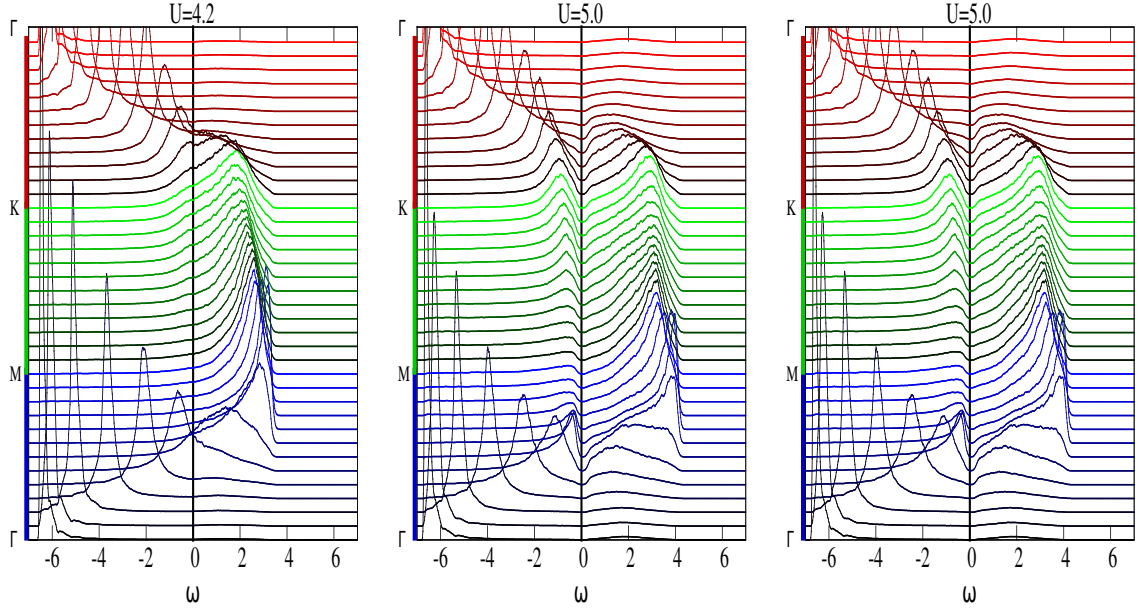
Figure 4.22: Angle resolved spectral functions and $t'/t = 0.8$ and $T/t = 0.04$ as U/t is increased across the Mott transition.

from a correlated metal to a Mott insulator are concerned. Notice the suppression of a broad 'quasiparticle' feature, visible at low U, as the interaction strength is increased, and the emergence of a pseudogap. The occurence of the pseudogap itself requires a magnetically disordered state, and could have been captured by a tool like DMFT. The *anisotropy* on the Fermi surface, however, arises from the momentum dependence of the self energy and requires a method that retains spatial correlations.

Fig.4.22 shows the spectral function for a complete momentum sweep across the Brillouin zone, as the system is taken across the finite temperature Mott crossover. In the left panel a quasiparticle peak is visible at all **k** while in the middle panel there is a pseudogap in the spectral functions (a clear two peak structure) as **k** crosses the Fermi level. This gets more prominent in the right panel.

4.3.6   Reentrant metal-insulator transition

In this section, we focus on an unusual reentrant feature in the phase diagram. We focus on $t' = 0.8$ and will comment on other parameter values at the end. Our main results on this issue are the following:

1. We observe that on the anisotropic triangular lattice there is indeed a window of interaction strength U, beyond the zero temperature metal-insulator transition at U_c,where the resistivity shows an insulator-metal-insulator (I-M-I) crossover

with increasing temperature.

2. The density of states (DOS) at the Fermi level *also has non monotonic behaviour with temperature,* and the two crossover scales $T_{IM}(U)$ and $T_{MI}(U)$ in the resistivity can be correlated with the behaviour of the DOS.

3. We relate the re-entrance to two competing effects in the underlying model and observe that re-entrance is absent on the square lattice, and is only weakly visible in the fully isotropic triangular lattice.

For $t' = 0.8$ the primary features are: (i) the transition from a paramagnetic metal (PM) to an antiferromagnetic metal (AFM) ground state at $U_{c1}/t \sim 3.9$ and then a transition to an antiferromagnetic insulator (AFI) at $U_{c2}/t = 4.3$, (ii) an increase in the magnetic correlation scale, T_{corr} from U_{c1} to $U \sim 6t$ and then a gradual decrease, and (iii) a wide pseudogap window around the finite temperature MIT line. Since we are interested in the metal-insulator transition and its salient features, we will identify U_{c2} with U_c and focus on a narrow window around it.
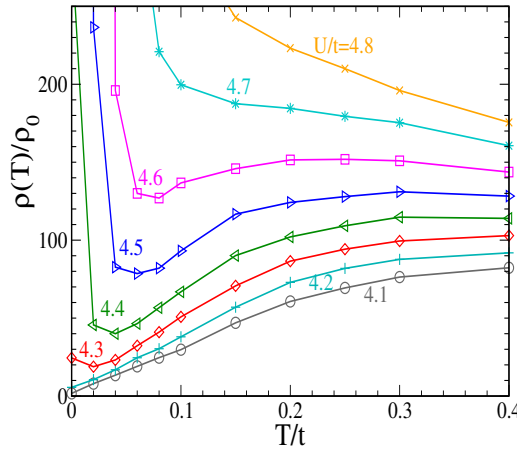
Figure 4.23: Temperature dependence of resistivity, $\rho(T)$ for interaction U in a narrow window around $U_c \sim 4.3t$. The values of U are displayed besides the curves.

Fig.4.23 show the resistivity $\rho(T)$ in the narrow window of U/t near the transition. We use this as our primary indicator of metallic or insulating behaviour. When $d\rho/dT > 0$ we call the system metallic, when $d\rho/dT < 0$ we call it insulating. Beyond the metal-insulator transition at $U_c \sim 4.3t$ the DOS in the ground state shows a finite gap. The resistivity $\rho(T)$ shows the following features:

1. For $U \lesssim 4.3t$ the resistivity increases monotonically with increasing T.

2. For $4.3t \lesssim U \lesssim 4.7t$ the resistivity first decreases with increasing T upto the insulator-metal crossover temperature, T_{IM}, increases from T_{IM} till the metal-insulator crossover T_{MI}, and then decreases slowly.

3. For $U \gtrsim 4.7t$ the resistivity decreases monotonically with temperature. The two scales $T_{IM}(U)$ and $T_{MI}(U)$ are shown further on in the phase diagram.
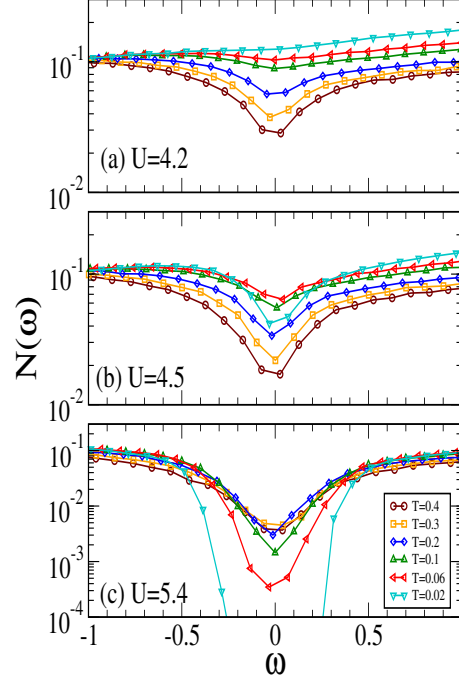
Figure 4.24: : Temperature dependence of the DOS at three typical interaction strengths. Top: monotonic suppression of the low energy DOS with increasing temperature in the metal at $U = 4.2t$. Middle: non monotonic behaviour of the low energy DOS with T at $U = 4.5t$, in the insulator-metal-insulator crossover window. Bottom: monotonic increase in the low energy DOS with increasing T 'deep' in the insulator at $U = 5.4t$.

Fig.4.24 shows the temperature dependence of the low energy DOS $N(\omega)$ at three representative interaction strengths.

1. The top panel shows the behaviour at $U = 4.2t$ where the ground state is metallic. In this case the DOS at the lowest temperature, $T = 0.02t$ is featureless, but increasing temperature leads to the appearance of a progressively sharper dip near $\omega = 0$. This is a regime of pseudogap formation due to strong magnetic fluctuations in metal, but $d\rho/dT$ remains positive at all T. The DOS at the Fermi level falls almost to $\sim 25\%$ of its $T = 0$ value on raising the temperature to $T = 0.4t$.
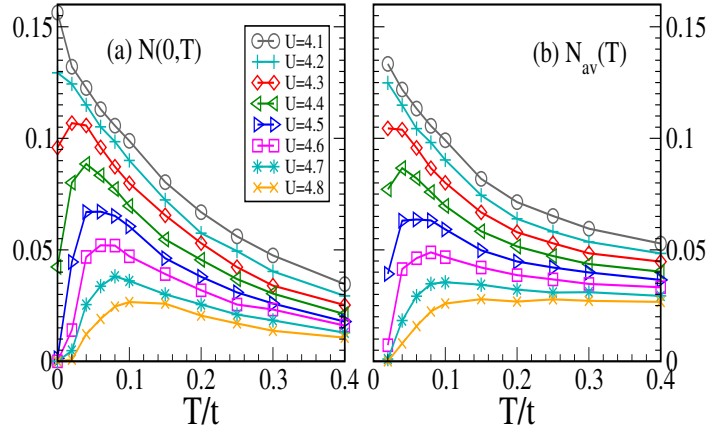
Figure 4.25: (a) Temperature dependence of the density of states at the Fermi level, $N(0)$, for varying U/t. (b) $N_{av}(T)$: the average of the density of states $N(\omega, T)$ over the low frequency window $\pm T$ around $\omega = 0$. Since the DOS has a sharp frequency dependence in the re-entrance window we think the low frequency average, rather than just $N(0)$, provides a better correspondence with transport.

2. The middle panel shows the DOS at $U = 4.5t$ where the ground state is insulating and the resistivity shows a thermally driven I-M-I crossover. At the lowest temperature that we show, $T = 0.02t$, there is a dip in the low energy density of states (up from a weak Mott gap at $T = 0$). The low frequency DOS gains weight till $T \sim 0.06t$, not surprising in a weak insulator, beyond which there is sustained *decrease* of low energy weight.

3. The bottom panel shows the behaviour deeper in the insulating regime $U = 5.4t$. Here the resistivity decreases monotonically with T (the highest U in Fig.4.23 is $4.8t$ but the similar behaviour holds at larger $U = 5.4t$ as well). The system starts with a hard gap at $T = 0$ which fills up slowly with increasing T. Even at the highest temperature the DOS is less than 10% of the non-interacting value.

Fig.4.25.(a) shows $N(0)$ the DOS at the Fermi level for varying interaction strength and temperature. The two metallic cases, $U/t = 4.1$ and 4.2 show monotonic decrease of $N(0)$ with T. The insulating cases $U/t \geq 4.3$ have $N(0) = 0$ at $T = 0$. They gain weight with increasing T, have a peak at some temperature $T_{peak}(U)$ and then decrease as in the metallic cases. For U/t much beyond the re-entrance window, $N(0)$ would rise (exponentially) slowly and monotonically with T. We have not shown that regime here.

The principal lesson from Fig.4.24 and Fig.4.25 is the *non monotonic temperature dependence* of the low energy density of states, in a manner that complements the
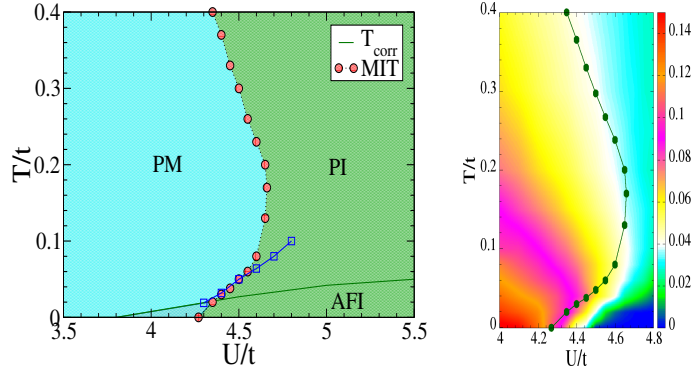
Figure 4.26: Left: Phase diagram emphasizing the re-entrant feature near U_c. The MIT line, $T_{MIT}(U)$, is the locus $\frac{d\rho(T,U)}{dT} = 0$. In the lower part, it indicates thermally driven IM crossover, which matches the $T_{peak}(U)$ (blue squares) reasonably (see text). Its upper part, indicates a MI crossover. Right: a colour plot of $N(0,T,U)$, with the $T_{MIT}(U)$ line superposed. There is reasonable match between the shapes of constant contour $N(0,T,U)$ and that of $T_{MIT}(U)$.

resistivity behaviour. Fig.4.25.(b) shows $N_{av}(T)$, the density of states averaged over temperature dependent low frequency, defined by

$$N_{av}(T) = \frac{1}{2T} \int_{-T}^{T} d\omega N(\omega, T)$$

Since the DOS has a sharp feature near $\omega = 0$, we feel this frequency averaged quantity, rather than $N(0,T)$ itself, may have a better correspondence with the conductivity. In fact, while $N(0)$ falls sharply with T even at $T \sim 0.4$, N_{av} flattens out, with a hint of *increase* at high T at large U.

Fig.4.26 shows the metal-insulator phase diagram and the associated thermal crossover scales. The ground state is an antiferromagnetic (spiral) metal for $4.3 \geq U/t \geq 3.9$, and an antiferromagnetic insulator for $U/t \geq 4.3$. The magnetic 'transition temperature' increases with U/t in the interval shown, and falls again for $U/t \geq 7$. The MIT line has re-entrant character, we label the lower part, with $dT/dU > 0$, as $T_{IM}(U)$ and the upper part, with $dT/dU < 0$, as $T_{MI}(U)$. One can see the from Fig.4.26 (left) that $T_{peak}(U)$ curve matches reasonably with $T_{IM}(U)$, while from Fig.4.26 (right) we see that $T_{MI}(U)$ more or less follows constant low frequency DOS contour.

In Fig.4.27, we have shown the distribution $P(m)$ of the magnitude of $\mathbf{m}_i$ fields (left) and the structure factor $S(\mathbf{q})$ (right) at few temperatures and three representative U values 4.2 (in the metal), 4.5 (in the re-entrant region) and 5.4 (in the insulator). The distribution $P(m)$ shows the growth of the mean value $\bar{m}$ with U at
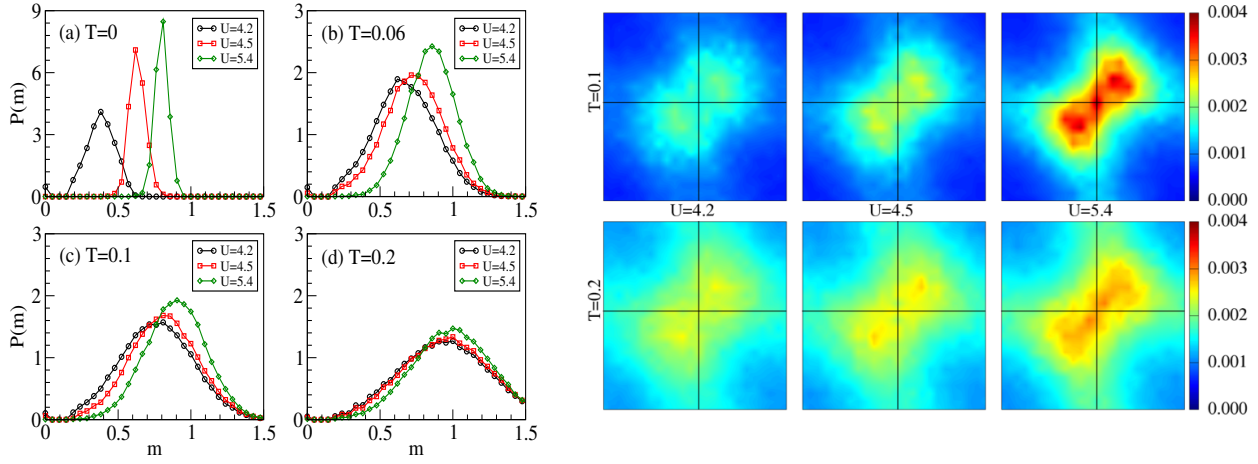
Figure 4.27: Left: $P(m)$ distribution at U=4.2 (metal), 4.5 (re-entrance window) and 5.4 (insulator) and T=0,0.06,0.1,0.2 . Right: The structure factor $S(\mathbf{q})$ arising from the spatial correlation of the $\mathbf{m}_i$ at same U values and T=0.1,0.2 . The q_x, q_y axes in the color plots are in range [0,2π], so the center is (π,π).

low T, and as we go to higher T, the distribution becomes more and more broader, and eventually all U start looking the same at very high temperature. The $S(\mathbf{q})$ plot demonstrates how angular correlations grow stronger with increasing U, and weaker with increasing temperature. At low T, $S(\mathbf{q})$ shows peak around $\mathbf{q}$=(0.85π,0.85π) and its conjugate $\mathbf{q}$, which corresponds to a non-collinear 'spiral' AF state. The closer the peak is to (π,π) (G-type phase), the stronger is the AF nature of the phase, and the sharper the peak, the stronger is the AF correlation.

In what follows we first try to create an understanding of the re-entrant feature in terms of the behaviour of the microscopic variables $\{\mathbf{m}_i\}$. We will then compare our results to CDMFT, and finally with the experimental situation.

The transport behaviour in Fig.4.23 is obviously correlated with the behaviour of the density of states seen in Fig.4.24 and Fig.4.25. The phase diagram and the associated contour plot for $N(0)$ in Fig.4.26 makes this correspondence more explicit. This allows us to shift focus to the behaviour of the low energy DOS, and analyze it in terms of the mean, variance, and angular correlation of the $\mathbf{m}_i$.

We would like to address three questions: (i) why is there a maximum in $N(0,T)$, how does it correlate with $T_{IM}(U)$? (ii) what determines the U dependence and the downward trend in $N(0)$ beyond $T_{IM}(U)$?, and (iii) why is there another M-I crossover at higher temperature?

It can be shown (at least numerically) that

1. When the $P(m)$ is sharply peaked, increasing AF correlations tends to increase

the gap in the DOS.

2. For given AF configuration, the gap increases with increasing $\bar{m}$

3. For a given strength of AF correlation, broadening of $P(m)$ tends to vanish the gap.

Its the competition between these mechanisms, which leads to the re-entrant behaviour, as we argue below.

Since the moments are AF ordered at low T, this leads to a growing spectral gap and a stronger insulating state with increasing U. With increasing T the $P(m)$ broaden and the mean value $\bar{m}(T, U)$ also increase. If the AF pattern had remained rigid with increasing T this would have *strengthened* the insulating state. However, the magnitude fluctuation and the angular randomness lead to a broadening of the spectrum, weakening of the gap, and growth in $N(0)$.

Beyond $T \sim 0.1t$ the angular disorder almost saturates and the slow growth of $\bar{m}(T, U)$ with T, leads to a loss of low energy spectral weight in *both in the metallic and insulating samples*. The peak in $N(0, T)$ therefore arises from a competition of growing $\bar{m}$ (tending to suppress $N(0)$) and growing randomness (that enhances $N(0)$).

4.4   Comparison with experiments

We saw in the previous sections, that triangular structure leads to frustrating magnetic interaction in the insulating phase. However, even if long range order is lost, short range spin correlations still have dramatical affect on the electronic properties near the MIT. The organic salts we mentioned in the section 1.3.2, provide a concrete test bed for this effect [79, 80]. The $\kappa-(\text{BEDT-TTF})_2\text{Cu}[\text{N(CN)}_2]$-X salts are quasi two dimensional (2D) materials where the BEDT-TTF dimers define a triangular lattice with anisotropic hopping [81]. The large lattice spacing, $\sim 11\mathring{A}$, leads to a low bandwidth, resulting in large U/t. For the X=Cl$_{1-x}$Br$_x$ family the frustration is moderate and a magnetically ordered state with $T_c \sim 30$K for $x = 0$ is obtained [154]. The low temperature state is an AFI for $x < 0.75$ and metallic for $x \gtrsim 0.75$ (with a superconducting (SC) instability at ~ 10K). The PM state is *very incoherent* above $T \sim 50$K: the resistivity [85] is large, $\gtrsim 100$mΩcm, the optical response has non Drude character [86, 87], and NMR [88, 89] suggests the presence of a pseudogap (PG). The detailed spectral features of this unusual state are not known.

In this section we attempt to connect the results of the triangular lattice Mott physics with available experiments on the $Cl_{1-x}Br_x$ family. We first, choose the electronic hopping parameters t, t' suggested, by *ab initio* calculations, and earliar theoretical attempts. We choose primary hopping $t \sim 65\text{meV}$ [81], and $t'/t = 0.8$. This would convert temperature expressed in units of t to that in Kelvin.

4.4.1 Parameter estimation

If we pretend, that applying 'pressure' or, in the present context, increasing the Br doping x, only reduces U/t, not t'/t, then we have U/t as function of x. For simplicity we will now denote U/t as U. The only one unknown now is the dependence of the interaction $U(x)$ on x. In the $Cl_{1-x}Br_x$ family it is observed that the transport gap can be fitted to $\Delta(x) \approx 800 - 1000x$ Kelvin [85], and for κ-Cl, upon pressure, it can be fitted to $\Delta(P) = 740 - 2P_{bar}$ [83]. We match this to the U dependence of our calculated gap, $\Delta(U)$, and infer $U|_{x=0} \sim 6$, where our calculated gap matches with the experiment. The MIT occurs at $x_c \sim 0.75$ and for us at $U \approx 4.6$. We used a quadratic polynomial fit for $U(x)$, and found that $U(x) = 6 - 1.35x - 0.4x^2$ reproduces the transport gap [85] estimated from the resistivity experiments. A similar fit is constructed for the hydrostatic pressure. The comparison is shown in Fig.4.28. The U range in resistivity in Fig.4.13(c) corresponds roughly to $x = [0, 1]$. Since $t = 65\text{meV}$, $T = 0.4t$ is approximately 300K.
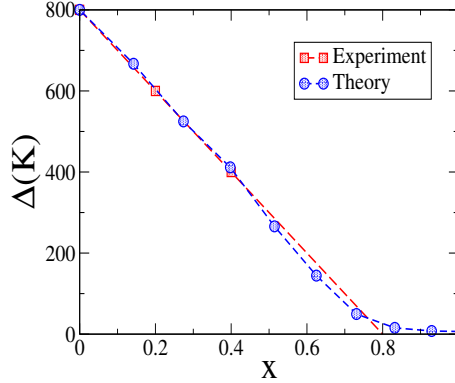
Figure 4.28: Comparison of the experimental and fitted Mott gap.
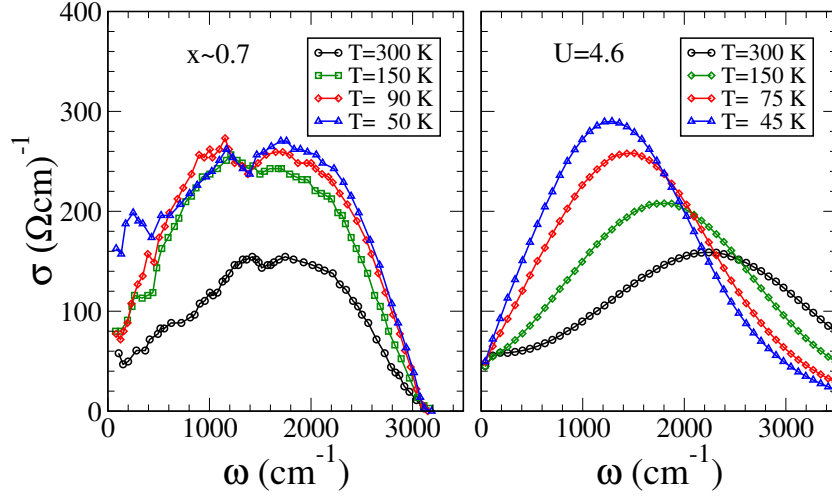
Figure 4.29: Comparison of the experimental and theoretical optical conductivity near the Mott transition. The experimental data at $x \sim 0.73$ is *extracted* from Fig.3 of Dumm *et al* [87].

4.4.2 Optical conductivity

The conductivity of the two dimensional system is first calculated as follows (ref. [134]), using the Kubo formula:

$$\sigma_{2D}^{xx}(\omega) = \frac{\sigma_0}{N} \sum_{\alpha,\beta} \frac{n_\alpha - n_\beta}{\epsilon_\beta - \epsilon_\alpha} |\langle \alpha | J_x | \beta \rangle|^2 \delta(\omega - (\epsilon_\beta - \epsilon_\alpha))$$

Where, the current operator J_x is

$$J_x = -i \sum_{i,\sigma} \left[t(c_{i,\sigma}^\dagger c_{i+\hat{x},\sigma} - \text{hc}) + t'(c_{i,\sigma}^\dagger c_{i+\hat{x}+\hat{y},\sigma} - \text{hc}) \right]$$

The d.c. conductivity is the $\omega \to 0$ limit of the result above. $\sigma_0 = \frac{\pi e^2}{\hbar}$, the scale for two dimensional conductivity, has the dimension of *conductance*. $n_\alpha = f(\epsilon_\alpha)$ is the Fermi function, and ϵ_α and $|\alpha\rangle$ are respectively the single particle eigenvalues and eigenstates of H_{eff} in a given background $\{\mathbf{m}_i\}$.

The experimental results are quoted as *resistivity* of a three dimensional material. If we assume that the planes are electronically decoupled then the three dimensional resistivity ρ_{3D} can be estimated from the resistance of a cube of size L^3. If the 2D resistivity is $\rho_{2D} = 1/\sigma_{2D}$, the resistance of a L^2 sheet is just ρ_{2D} itself. A stacking of such sheets, with spacing c_0 in the third direction, implies that the resistance of the L^3 system would be $R_{3D} = \rho_{2D}c_0/L$. By definition this also equals $\rho_{3D}L/L^2 = \rho_{3D}/L$. Equating the two, $\rho_{3D} = \rho_{2D}c_0$. Recalling that the normalizing
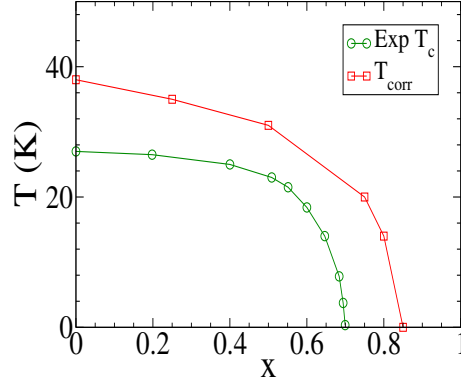
Figure 4.30: Comparison of the estimated T_{corr} and experimental T_c.

scale for the resistivity was $\rho_0 = \hbar c_0/\pi e^2$. Using $c_0 \sim 29\text{\AA}$, we have $\rho_0 \sim 380\mu\Omega\text{cm}$ for the organics.

The absolute magnitude of our metallic resistivity at $T \sim 0.4t$ is about $60\rho_0 \sim 25\text{m}\Omega\text{cm}$, while the experimental value is $\gtrsim 100\text{m}\Omega\text{cm}$ [85]. The difference could arise from electron-phonon scattering which is absent in our model. Limelette *et al* [83] presented a DMFT based resistivity result that compares favourably with experiments, but, apparently, involves an arbitrary scale factor.

We showed the U dependence of the optical conductivity in Fig.4.15, at $T/t = 0.1, 0.2$. For a rough comparison to organics, $T/t = 0.1 \equiv 80\text{K}$, $\omega/t = 5 \equiv 2500\text{cm}^{-1}$, and $\sigma/\sigma_0 = 0.1 \equiv 265\Omega^{-1}\text{cm}^{-1}$.

In the organics the experimenters have carefully isolated the Mott-Hubbard features in the spectrum by removing phononic and intra-dimer effects [87]. Since we have already fixed our t, t', U we have no further fitting parameter for $\sigma(\omega)$. The measured spectrum at $x \sim x_c$ and $T \sim 50-90\text{K}$ has a peak around $1500-2000\text{cm}^{-1}$. Using $U_c/t \sim 4.5$ and $T/t = 0.1$ we get $\omega_{peak}/t \sim 3.0$, which translates to $\sim 1500\text{cm}^{-1}$. The magnitude of our $\sigma(\omega)$ at ω_{peak} is $\sim 0.1\sigma_0 \sim 265\Omega^{-1}\text{cm}^{-1}$, since $\sigma_0 = 1/\rho_0 \sim 2650\Omega^{-1}\text{cm}^{-1}$. This is remarkably close to the measured value, $\approx 280\Omega^{-1}\text{cm}^{-1}$ (Ref. [87] Fig.3). In Fig.4.29, we have shown the temperature evolution of the optical conductivity near the Mott transition. In the $\text{Cl}_{1-x}\text{Br}_x$ the transition occurs around $x \sim 0.75$, while for us, it occurs around $U \sim 4.6$, or $x \sim 0.8$.

While the characteristic scales in $\sigma(\omega)$ match well with experiments, the experimental spectrum has weaker dependence on temperature and composition x. This could arise from the subtraction process and the presence of other interactions in the real material. Our result differs from DMFT [86], and agrees with the experiments, in that we do not have any feature at $\omega = U/2$. We have verified the f-sum rule numerically.
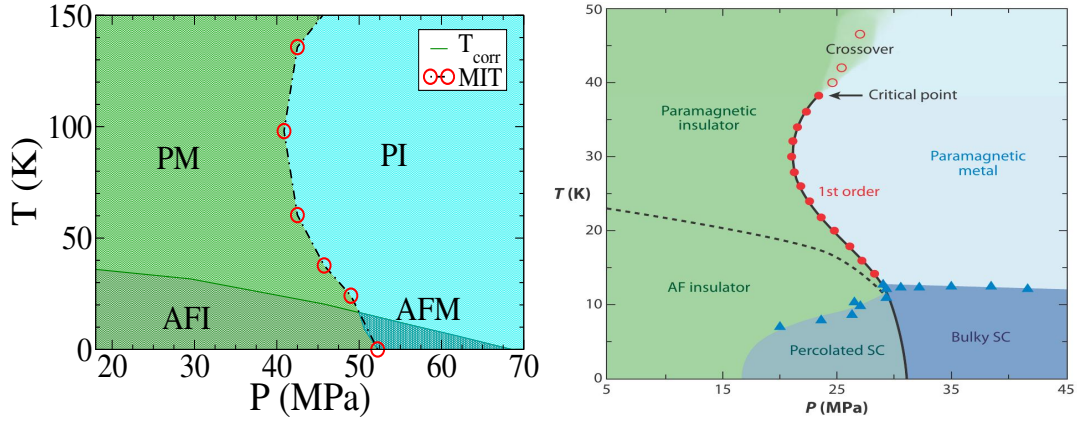
Figure 4.31: Comparison of the phase diagram with experiment.

4.4.3 Transition temperature

Finite temperature brings into play the low energy fluctuations of the $\mathbf{m}_i$. The effective model has the $O(3)$ symmetry of the parent Hubbard model so it cannot sustain true long range order at finite T. However, our annealing results suggest that magnetic correlations grow rapidly below a temperature T_{corr}, and weak inter-planar coupling would stabilize in plane order below T_{corr}. This scale increases from zero at $U = U_{c1}$, reaches a peak at $U/t \sim 6.5$, and falls beyond as the virtual kinetic energy gain reduces with increasing U (Fig.4.7(c)).

Since $U \sim 6.0$ at $x = 0$, from our results this would indicate that $T_{corr} \sim 0.05$, at $x = 0$, *i.e*, $T_{corr} \sim 35K$, not too far from the NMR inferred $T_c \sim 30K$. In Fig.4.30 we show a comparison of the experimental T_c and the T_{corr}.

4.4.4 Reentrant M-I transition

In the organics of the $\kappa-(\text{BEDT-TTF})_2\text{Cu}[\text{N(CN)}_2]$-X family in particular one observes an insulator-metal transition (IMT) in the ground state of the X=$\text{Cl}_{1-x}\text{Br}_x$ family at $x \sim 0.75$, and also a pressure driven IMT when X=Cl [79, 80]. While the increase in bandwidth, and so a decrease in the effective interaction, with increasing the 'pressure' is not unexpected, finite temperature brings to life *an unusual reentrance* [83, 85]. Over a narrow pressure window ($\sim$10Mpa), the insulating ground state 'metallises' with increasing temperature and then crosses over again to insulating behaviour at a higher temperature. In Fig.4.31, we show a comparison of the theory reentrance window with that of Kanoda *et al* [79]. For metals or insulators far from the critical interaction the behaviour is monotonic: metals show an increasing resistivity, while insulators show a decreasing resistivity with increasing temperature.

125

Cellular dynamical mean field theory (C-DMFT) studies suggest that geometric frustration could be responsible for the re-entrance effect that is observed [99, 100]. The specific predictions about interaction and temperature window, however, seem to vary widely with choice of the DMFT solver, and most of conclusions are based on the behaviour of the 'double occupancy' rather than the measurable transport and spectral features.

Our re-entrant window $\delta U = 0.4t$ near U_c, inferred from thermally driven I-M-I crossover, is equivalent to $\delta x = 0.2$. This is consistent with $\delta x \sim 0.2$ in the $Cl_{1-x}Br_x$ family [85]. The C-DMFT estimates of the re-entrant window varies widely, from $\delta U \sim 0.3t$ [100] to $\sim 1.2t$ [99].

4.4.5 Density of states

We saw, in section 4.3.4 that, the crossover from the bad metal to the insulator involves a wide window with a pseudogap in the electronic DOS, $N(\omega)$. One may have guessed this from the depleting low frequency weight in $\sigma(\omega)$, Fig.4.17 makes this feature explicit. We are not aware of tunneling studies in the organics, but the presence of a pseudogap has been inferred from NMR measurements [88]. Our results indicate a wide window, $U/t \sim [4, 5.3]$, where there is a distinct pseudogap in the global DOS. This suggests that the entire $x \sim [1.0, 0.35]$ window in the organics should have a PG. For $U/t \lesssim 4.6$ the dip feature deepens with increasing T, we have $dN(0)/dT < 0$ (compare panels (a) and (b), Fig.4.17), while for $U/t \gtrsim 4.6$ we have a weak $dN(0)/dT > 0$. The PG arises from the coupling of electrons to the fluctuating $\mathbf{m}_i$. A large m_i at all sites would open a Mott gap, independent of any order among the moments. Weaker m_i, thermally generated in the metal near U_{c1} and with only short range correlations, manages to deplete low frequency weight without opening a gap. Since the typical size $\langle m_i \rangle$ increases with T in the metal, we see the dip deepening at $U < U_c$.

4.5 Conclusions

We have explored in detail a method which retains the spatial correlations that are crucial near the Mott transition on a frustrated lattice. Using electronic parameters that describe the κ-BEDT based organics we obtain a magnetic T_c, metal-insulator phase diagram, and optical response that reproduces the key experimental scales. We uncover a wide pseudogap regime near the MIT, and predict distinct signatures

of the incommensurate magnetic fluctuations in the angle resolved photoemission spectrum.

While the 'higher temperature' results are likely to be a good approximant to the full quantum treatment, future work would involve a check on the stability of the unusual magnetic ground states to quantum fluctuations. The absolute value of U_c is also likely to be renormalised upward somewhat if further quantum effects are incorporated.

CHAPTER 5

MOTT PHYSICS AND GLASSINESS ON THE FCC LATTICE

In the previous chapter we saw how geometrical frustration in the triangular lattice disfavours Neel order and promotes complex non-collinear states. There are several families of compounds based on three dimensional frustrated lattices. The complexity of the these structures has prevented a detailed exploration of Mott physics and the possible magnetic phases.

5.1 Background

Unlike in two dimensions (2D), there is no organized body of work probing the interplay of geometric frustration and Mott physics in three dimensions (3D). In 3D there are intriguing experimental results on disparate systems [47–49,56,57,112–116, 118–127, 151], whose common features do not seem to have been noticed. The 3D frustrated Mott systems are realized on face centered cubic (FCC) and pyrochlore lattices. They both involve connected tetrahedra, disallowing Neel order in the insulating phase. The FCC examples include the Ga cluster compounds [112–115], alkali fullerides, A_3C_{60} [116, 118, 119, 151], and the double perovskites [47–49,56,57]. The pyrochlore examples include the rare earth molybdates [120–122] and iridates [123–127]. Most of these materials, at ambient pressure [160], are insulators close to a Mott insulator-metal transition (IMT). Despite the wide chemical variety, several striking features seem to be common:

1. *Magnetic state:* The Mott phase often has no long range magnetic order down to the lowest temperature, only short range antiferromagnetic correlations and

sometimes a hint of 'spin freezing' [47–49, 57, 120, 121]. However, many of these systems have large Weiss constant θ_{CW} (see table 5.1), suggesting strong antiferromagnetic exchange. This indicates a high degree of frustration in such systems.

Compound	Structure	θ_{CW} (K)	Reference
GaNb$_4$Se$_8$	FCC	300	[112, 113]
Cs$_3$C$_{60}$	FCC	105	[118]
Ba$_2$YRuO$_6$	FCC	571	[47]
Sr$_2$InReO$_6$	FCC	182	[57]
Ba$_2$YMoO$_6$	FCC	160	[49]
Y$_2$Mo$_2$O$_7$	Pyrochlore	200	[121]

Table 5.1: Curie constants θ_{CW} of some of the FCC and pyrochlore compounds.

2. *Unusual metal:* The Mott insulator can be driven metallic by applying pressure. The resulting state is a 'non Fermi liquid' - with anomalously large low temperature resistivity and a negative temperature coefficient [114, 122, 125, 126]. At high pressure 'normal' metallic behaviour is observed.

3. *Anomalous Hall:* Several of these systems have non-coplanar antiferromagnetic correlation. For example GaNb$_4$Se$_8$ [113] exhibits long range non-coplanar antiferromagnetic order with $T_c \sim 30K$. This can lead to anomalous Hall response, as already observed in the pyrochlore iridate Pr$_2$Ir$_2$O$_7$ [127].

4. *Spectral weight transfer:* The optical conductivity [115, 125] indicates that the insulator to metal transition involves transfer of spectral weight over a wide frequency window.

5. *Superconductivity:* Some of these systems, *e.g*, the cluster compounds [114] and the alkali fullerides [116, 118, 119, 151], show superconductivity at low temperature.

The first three features are direct consequences of frustration which promotes non-coplanarity and short range correlation, in contrast to collinear long range order. The last two are more generic to Mott physics. We will show that the single band Hubbard model on the FCC lattice helps us understand the connection between magnetism and transport in a subset of these materials [114, 115]. Based on our solution of the Mott problem on the FCC lattice we establish the following.

1. In the ground state, increasing interaction leads, successively, to transition from a paramagnetic metal (PM) to a spin glass metal (SGM), a spin glass

'insulator' (SGI), and then an antiferromagnetic insulator (AFI). The spin glass arises without the presence of any *extrinsic disorder*, consistent with several frustrated materials. The AFI has flux like order (defined later) at weaker coupling, and 'C type' order in the very strong coupling Heisenberg limit.

2. The T_c scales in the ordered phase, as well as the notional glass transition temperature T_{SG}, are a tiny fraction, $\sim$ a few percent, of the hopping scale due to the frustration.

3. While the AFI phase has a clear gap and divergent resistivity as temperature $T \to 0$, the spin glass insulator has a pseudogap in the density of states, non Drude optical response in the optical conductivity, and *large but finite resistivity* at $T = 0$ with with negative temperature coefficient ($d\rho/dT < 0$).

The results above, although obtained for the FCC lattice, have much in common with observations on the pyrochlores.

We have found little theoretical work on the magnetic phases or the Mott transition in the FCC lattice. A very early calculation explored a restricted set of mean field states [128] but, in contrast to 2D, there does not seem to be any cluster dynamical mean field theory (C-DMFT) result handling the combination of correlation and frustration.

As before we study the following model at half filling:

$$H = -t \sum_{\langle ij \rangle \sigma} \left[c_{i\sigma}^{\dagger} c_{j\sigma} + \text{h.c.} \right] - \mu \sum_i n_i + U \sum_i n_{i\uparrow} n_{i\downarrow} \qquad (5.1)$$

The $\langle ... \rangle$ denote nearest neighbours on the FCC lattice. We set $t = 1$ as the reference energy scale. μ controls the electron density, which we maintain at half filling $n = 1$. $U > 0$ is the Hubbard repulsion. Using the Hubbard-Stratonovich (HS) approach used in the last chapter, we get the following effective Hamiltonian H_{eff} which describes electrons moving in the spatially fluctuating background of classical $\mathbf{m}_i$ fields (where $\tilde{\mu} = \mu - \frac{U}{2}$)

$$H_{eff} = -t \sum_{\langle ij \rangle \sigma} \left[c_{i\sigma}^{\dagger} c_{j\sigma} + \text{h.c.} \right] - \tilde{\mu} N - \frac{U}{2} \sum_i \mathbf{m}_i \cdot \vec{\sigma}_i + \frac{U}{4} \sum_i \mathbf{m}_i^2 \qquad (5.2)$$

We can write this as sum of electronic and classical part $H_{eff} = H_{el}\{\mathbf{m}_i\} + H_{cl}\{\mathbf{m}_i\}$, where $H_{cl}\{\mathbf{m}_i\} = \frac{U}{4} \sum_i \mathbf{m}_i^2$. The $\{\mathbf{m}_i\}$ configurations follow the distribution

$$P\{\mathbf{m}_i\} \propto \text{Tr}_{cc^{\dagger}} e^{-\beta(H_{el} + H_{cl})} \tag{5.3}$$

Retaining the spatial fluctuations of $\mathbf{m}_i$ allows us to estimate T_c scales, and access the crucial thermal effects on transport. Within the static HS approximation H_{eff} and $P\{\mathbf{m}_i\}$ define a coupled fermion-local moment problem. This is similar to the 'double exchange' problem, with the crucial difference that the moments are self generated (and drive the Mott transition) and are not fixed in size.

As before we use a Monte Carlo technique, now on lattices upto $N = 12 \times 12 \times 12$ in size, with clusters of size $N_c = 4 \times 4 \times 4$. For characterising the magnetic state we calculate the thermally averaged structure factor $S(\mathbf{q})$ at each temperature. The onset of rapid growth in $S(\mathbf{q})$ at some $\mathbf{q} = \mathbf{Q}$, say, with lowering T, indicates a magnetic transition. Electronic properties like density of states, optical conductivity etc, are calculated by diagonalizing H_{el} on the full lattice for equilibrium $\{\mathbf{m}_i\}$ configurations. Since the MC ground state can be affected by annealing protocol, wherever possible we have tested it against variational choices of $\{\mathbf{m}_i\}$.

In the next section 5.2, we discuss the ground state. In section 5.3, we take up the finite temperature physics in detail, including the behaviour of the auxiliary fields, the density of states across the Mott transition, and transport and optical properties. This is followed by a section comparing our results with recent measurements on the FCC based Ga cluster compounds. We then conclude the chapter.

5.2   Ground state

At $T = 0$, the Monte-Carlo based sampling becomes the minimization process

$$\frac{\delta}{\delta \mathbf{m}_i} \langle H_{eff}\{\mathbf{m}_i\} \rangle = 0$$

Please note that $\mathbf{m}_i$ need not be periodic. We observe the following with growing U/t in the ground state.

1. At low U the minimization leads to a state with vanishing moments $m_i = |\mathbf{m}_i| = 0$. This holds for $U < U_{c1} \sim 4t$.

2. There is a weakly discontinuous transition to a state with non-zero m_i at U_{c1}. For $U_{c1} < U < U_{c2}$, where $U_{c2} \sim 6.7t$, the ground state involves finite m_i, with a finite width distribution $P(m, U)$ (see later) but no long range order. The system behaves like a spin glass (SG) with short range 'flux like' correlations.
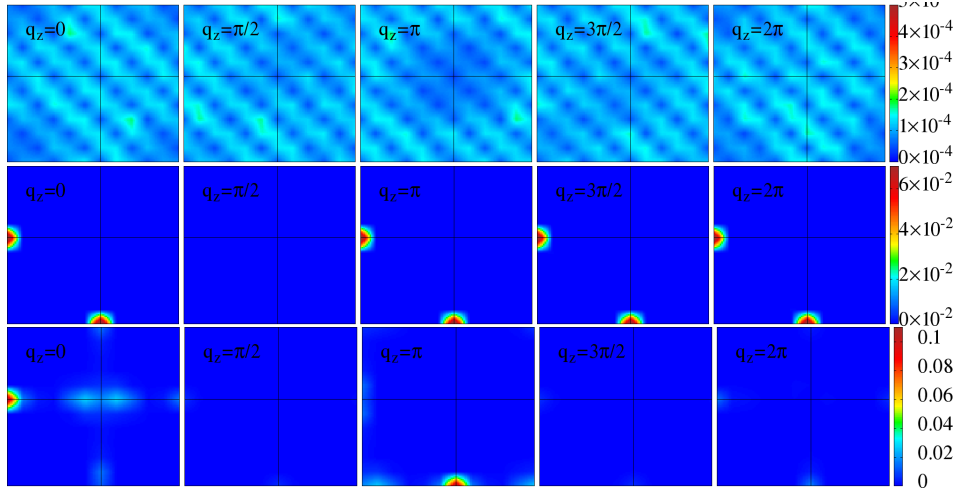
Figure 5.1: Two dimensional cross sections of the structure factor data $S(\mathbf{q})$ at low temperature, $T = 0.01$ for: top row: $U = 5$ in the spin-glass region, middle row: $U = 7$ for flux like order, and bottom: $U = 20$ for C type order. Each row has color plots of $S(\mathbf{q})$ in the q_x, q_y with selected $q_z = 0, \pi, \frac{\pi}{2}, \pi, \frac{3\pi}{2}..$

3. Beyond U_{c2} the ground state has long range flux like order till $U \sim 20t$, beyond which the virtual hopping generated exchange is effectively nearest neighbour and we obtain 'C type' order, as expected [165] for the AF Heisenberg model on the FCC lattice.

Fig.5.1 shows the structure factor that emerges from annealing the system to low temperature at three values of U. For $U/t = 5$, top row, the pattern does not show any signature of long range order but does have moments as Fig.5.2 reveals. At $U/t = 7$ the structure factor (middle row) shows flux like order, with a fairly large moment, while at $U/t = 20$ the magnetic order is C type.

At $U/t = 5$ the density of states, Fig.5.2 right panel, is almost featureless. The system is a metal, to be cross checked later via actual resistivity calculation. At the two larger values of U there is a clear gap in the spectrum and the system is an insulator. The DOS plots reveal that between the simple metal and the hard gap insulator there is a pseudogap phase. That turns out to have insulating resistivity as we will see later.

We now move to a quick analysis of the weak coupling and strong coupling phases using the same tools that we used for the triangular lattice.
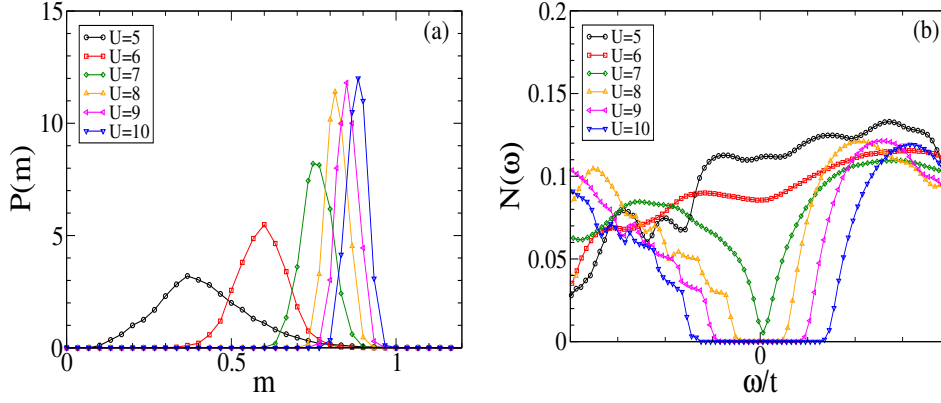
Figure 5.2: Low temperature behaviour: The left panel shows the distribution $P(m)$ of the magnitude of the moments. Right: the electronic DOS in the corresponding backgrounds. Notice the broad distribution with a small mean that arises at intermediate U, and the much sharper (ideally δ function) $P(m)$ at larger values of U. The DOS shows a pseudogap in the glassy phase.

5.2.1 Weak Coupling

In the 2D triangular lattice we could get some insight about the low U magnetic state by examining the RPA susceptibility based on $\chi_0(\mathbf{q})$. In that problem the peak location of χ_0 provided a hint about possible magnetic order.

We tried the same calculation in the FCC case but visualisation of the data is now more difficult. Instead of attempting to show a 3D plot of χ_0 we have shown cross sections of $\chi_0(\mathbf{q})$ in the q_x, q_y plane for various choices of q_z. The two rows in Fig.5.3 show data for the FCC (top row) and the simple cubic lattice (bottom row). The simple cubic case has a clear peak at (π, π, π) while the the FCC result shows a featureless χ_0 with the value ranging from $0.1 - 0.2$ as one moves over the Brillouin zone.

Remembering that at weak coupling we can use an effective model of the form

$$H_{eff}(\mathbf{m}) \sim \sum_{ij}(-\chi_{ij}^0\mathbf{m}_i.\mathbf{m}_j + \frac{|\mathbf{m}_i|^2}{U}\delta_{ij}) = \sum_q(-\chi_0(\mathbf{q}) + \frac{1}{U})|\vec{m}_\mathbf{q}|^2$$

to locate the instability, the χ_0 result suggests that a simple ordered state may not be the optimal solution. What we discover instead is that for U beyond a threshold U_{c1} the system generates a small moment which freezes into a glassy state (with short range flux like correlations), see Fig.5.1.

The moment is not large enough, near U_{c1}, to kill the metallic state, but it generates a residual resistivity. With growing U the density of states shows a pseudogap,
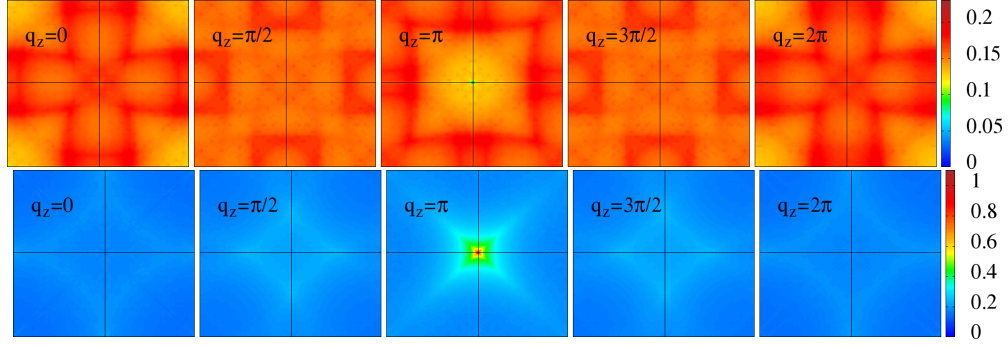
Figure 5.3: 2D cross sections of tight binding susceptibility $\chi_0(\mathbf{q})$ for (Top) the FCC lattice and (Bottom) the simple cubic lattice. The figures are in q_x, q_y planes, for selected q_z values shown in the figures in the range $[0, 2\pi]$.

and increasingly larger resistivity and for $U > U_{c2}$ the spectrum shows a hard gap. Within our resolution that is also where the moments order into a long range flux like pattern.

5.2.2 Strong coupling

At very strong coupling, deep into the Mott phase, the leading order virtual hopping process generates the effective model

$$H_{eff}(\mathbf{m}) = \sum_{ij} \frac{t_{ij}^2}{U} \mathbf{m}_i . \mathbf{m}_j$$

For nearest neighbour t_{ij} this is the classical antiferromagnetic Heisenberg model on the FCC lattice. Had we retained the quantum dynamics of the $\mathbf{m}_i$ we would have obtained the $S = 1/2$ quantum Heisenberg model. The classical

The classical model has been well studied [135–138], and extensive Monte Carlo results suggest the occurence of 'C type' order, see Fig.5.4, right. The nearest neighbour model has large degeneracy in $J(\mathbf{q})$ [135], however the thermal effects, and a small next nearest neighbour coupling, select collinear configuration.

Our results in the large U limit confirm this, and also generate the correct T_c scale $\sim 0.6t^2/U$. At weaker coupling but still in the Mott state we obtain a flux like configuration, Fig.5.4 left, as the ground state, probably because longer range hopping processes generate multispin couplings favouring non coplanar order.

135
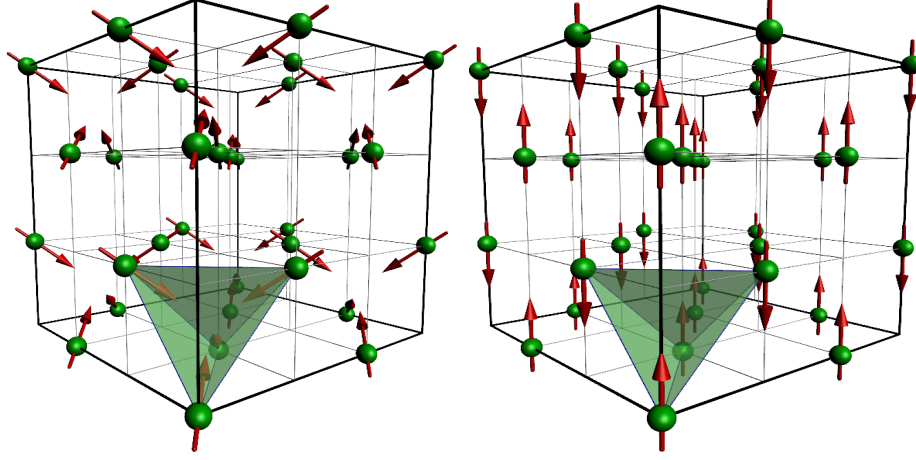
Figure 5.4: The $\mathbf{m}_i$ configuration in the flux state (left) and the C-type state (right). The FCC lattice points $\mathbf{X}_i$ are shown by green spheres, and the $\mathbf{m}_i$ fields by red arrows.

5.3 Finite temperature properties

5.3.1 Phase diagram

The ground state, as we have discussed, involves the sequence PM $\rightarrow$ SGM $\rightarrow$ SGI $\rightarrow$ AFI (flux and then C type) with increasing interaction. The main issues of interest in characterising the finite T phases are:

- The T_c, and glass transition scale T_g.

- The single particle DOS in terms of gap or pseudogap.

- The transport character, *i.e*, $d\rho/dT > 0$ or $d\rho/dT < 0$.

The nature of magnetic order and T_c is established from the structure factor peak. In the absence of a ordering peak in the structure factor the 'relaxation time' yields an estimate of freezing temperature. These are discussed in the next section.

Overall, the phase diagram Fig.5.5 indicates that T_c deep in the Mott phase follows the Heisenberg result, but is already significantly different by the time $U/t = 10$. For $U \lesssim 9t$ the size of the local moment itself diminishes rapidly, due to increase in itinerancy, and the T_c falls sharply.

Below $U_{c2} \sim 6.7t$ we have a glassy phase where, the $\mathbf{m}_i$ field seem to freeze at low temperature. We make a crude estimate of the 'freezing temperature' from the MC based local relaxation time [163], $\tau_{av}(T, U)$ (discussed in the next section 5.3.2). If the system undergoes an ordering transition, on lowering T, there is a rapid growth

Figure 5.5: The $U - T$ phase diagram. In ground state, upon increasing U/t, the system goes from PM (with no local moments) to successively, spin glass SGM, SGI (with disordered local moments), then to ordered AFI. At finite temperature the system also has a paramagnetic (Mott) insulating (PI) phase. The magnetic transition temperature T_c, and the spin glass freezing temperature T_{SG} (see text), are indicated. We show the extrapolation of the $T_c \sim 0.6\frac{t^2}{U}$ asymptote, that describes the $U/t \gg 1$ transition, to highlight the large deviation from the short range Heisenberg result. The PG region involves a pseudogap in the density of states.

in τ_{av} accompanied by a growth in the structure factor $S(\mathbf{q})$ at the $\mathbf{q}$'s associated with long range order (LRO).

For a glass transition, one observes similar growth in τ_{av}, without any signatures in $S(\mathbf{q})$. For $U > U_{c2}$ we observe LRO as well as a rapid increase in τ_{av} at a single temperature $T_c(U)$. For the window $U_{c1} < U < U_{c2}$, however, τ_{av} rises, at a temperature we call $T_{SG}(U)$, *without associated LRO.* We have also 'heated' the system up from $T = 0$ and discovered that any assumed ordered state is quickly destabilized, while the m_i moments themselves survive. T_{SG} varies in the manner shown in Fig.5.5, vanishing for $U < U_{c1}$ where there are no local moments. The freezing scale monotonically increases from $U/t \sim 4$ and matches the T_c of the flux phase at $U/t \gtrsim 7$.

The large U/t regime is obviously gapped due to the presence of large moments, which prevent double occupancy, and the small U/t regime has a density of states that is weakly renormalised with respect to the band result. At intermediate U, where the moments are small **and** disordered the electron spectrum only shows a suppression of weight at the Fermi level and not a full gap. This window is marked as PG in the phase diagram. Any mean field treatment of the magnetic problem
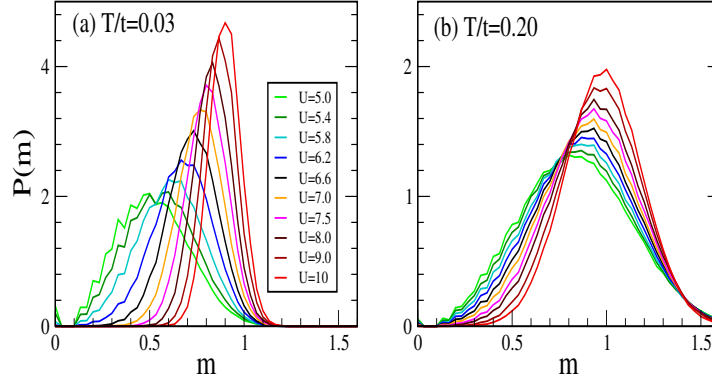
Figure 5.6: U dependence of the $P(m)$ distribution at (a) T=0.03t showing weak $\bar{m}$, and broad distribution around it in the correlated metal to, progressively stronger $\bar{m}$, and sharper distribution in the AFI with increasing U. (b) The same for T=0.2t, where all the U have progressively become broader and with higher $\bar{m}$, as compared to those in (a).

would have yielded a 'band structure' for the electrons. The novelty in the present case, with respect to the triangular lattice situation, is that the PG window survives down to $T = 0$ due to the presence of disordered local moments. The DOS will be shown in detail in a later subsection.

The 'metallic' and 'insulating' characterisation is done by examining the temperature derivative $d\rho/dT$. We will see the detailed resistivity later. For the moment notice that in addition to the obvious crossover from insulating to metallic behaviour with decreasing interaction we can have an I-M crossover (in a narrow U/t window) by increasing temperature as well.

5.3.2 Auxiliary fields

We first consider the magnitude distribution of the auxiliary field. In Fig.5.6 and Fig.5.7 we have shown the evolution of $P(m)$ of the auxiliary fields $\mathbf{m}_i$. Fig.5.6(a) and 5.6(b) show the U dependence, respectively, at low temperature, $T = 0.03$, and high temperature, $T = 0.2$. Fig.5.7(a)-(c) shows the temperature evolution at three representative values of U, (a) $U = 5.2t$ when the system is a SG metal, (b) U=6.2t, and (c) U=6.7t when in SG insulator. The trends in the broadening of the distribution with increasing temperature and interaction strength are qualitatively same as in two dimensions.
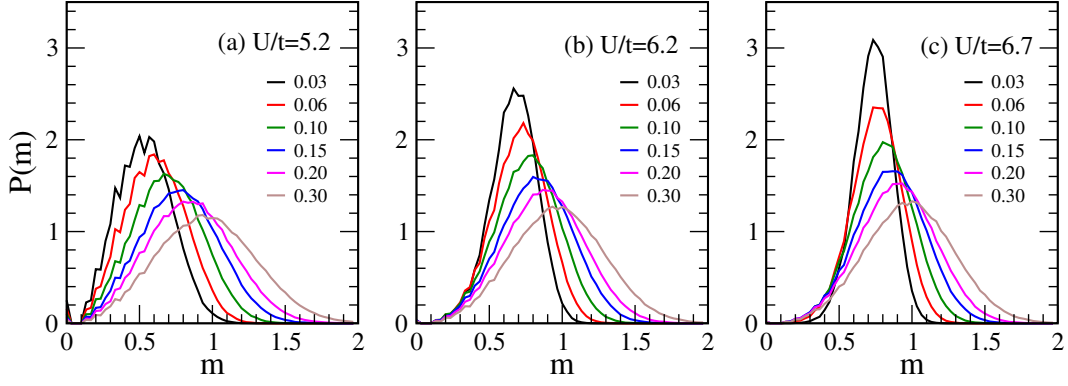
Figure 5.7: Temperature dependence of the $P(m)$ distribution at three fixed U in the SG window. (a) $U = 5.2t$, (b) $U = 6.2t$ and (c) $U = 6.7t$.

We calculate the structure factor $S(\mathbf{q})$

$$S(\mathbf{q}) = \frac{1}{N^2} \sum_{ij} \langle \mathbf{m_i} \cdot \mathbf{m_j} \rangle e^{i\mathbf{q} \cdot (\mathbf{r}_i - \mathbf{r}_j)}$$

for the angular spatial correlation, and the average relaxation time τ_{av} to get the correlation in the 'MC' time.

$$\tau_{av}(T, U) = \frac{1}{N} \sum_i \int_0^{t_{max}} dt \langle \mathbf{m}_i(0).\mathbf{m}_i(t) \rangle \tag{5.4}$$

In Fig.5.8 we have shown the temperature dependence of the structure factor and the relaxation time. The onset of rapid growth in $S(\mathbf{q})$ at some $\mathbf{q}$, defines onset of long range order, while the particular sets of $\mathbf{q}$s define the precise nature of the order. The onset of rapid growth in τ_{av}, shows the tendency of 'freezing' of the auxiliary fields $\mathbf{m}_i$ in the 'MC' time. The freezing temperatures, T_{SG} and the magnetic transition temperature T_c are marked in the figure as onset of growing $S(\mathbf{q})$ and τ_{avg} respectively. Beyond U_{c2}, till $U \lesssim 20$, we get a 'flux', phase, after which we get the 'C type' antiferromagnetic phase, which have the growing set of $\mathbf{q}$ mentioned in the table 5.2. The nature of these states is shown in Fig.5.4.

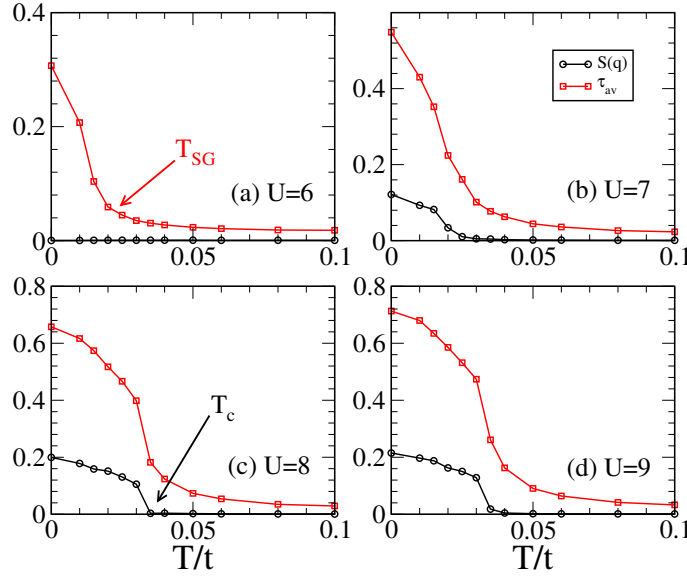| Phase	$\mathbf{q}$
Flux	$(\pi,\pi,0),(0,0,\pi),(\pi,0,\pi),(0,\pi,0),(0,\pi,\pi),(\pi,0,0)$
C type	$(\pi,\pi,0),(0,0,\pi)$

Table 5.2: The $\mathbf{q}$s for the flux and C type

Figure 5.8: Temperature dependence of $\tau_{av}(T,U)$, and $S(\mathbf{q})$ at $\mathbf{q}_{flux}$. (a) $U=6$ where, $S(\mathbf{q})$ shows no growth, down to $T=0$ for any $\mathbf{q}$, while τ_{av} starts growing around $T \sim 0.03$. (b)-(d) for $U=7,8,9$ respectively, where $S(\mathbf{q})$ and τ_{av} both grow at the same temperature ($T_c = T_{SG}$).

5.3.3 Density of states

While in the insulating phase ($U > U_{c2}$) the system would have a gapped density of states (DOS), and in the metallic ($U < U_{c1}$) case is likely to have a featureless DOS, the glassy window in between may have unusual spectral features. Fig.5.9.(a)-(b) shows the DOS for varying U/t at $T = 0.03t$ and $T = 0.20t$, respectively. For lack of space in the figure, the colour codes for U/t are marked in panel (b) only. In panel (a), for $U \lesssim U_{c1}$ the DOS is featureless, but for $5.4 < U/t < 7.5$ it displays a pseudogap (PG), and for higher U/t there is a clear gap. The large U/t phase is magnetically ordered at this temperature. At the higher temperature in panel (b), where there is no trace of magnetic order, the PG feature extends over a much larger U/t window. The weaker U 'metals' in (b) have a deeper PG compared to panel (a), while the weak gap insulators now have a PG feature rather than a hard gap. Panel (b) essentially illustrates the paramagnetic Mott transition on the FCC lattice.

Panels 5.10.(a)-(c) show the T dependence of the DOS for three typical U/t in the glassy window, where the ground state has frozen local moments. They all share the feature of thermally induced loss of low frequency weight which shows up at $\omega \sim U$. There is markedly less change with T on the negative frequency side, particularly in panels (b) and (c), compared to positive frequencies. This is due to the large asymmetry in the tight binding DOS of the FCC lattice. There is a subtle
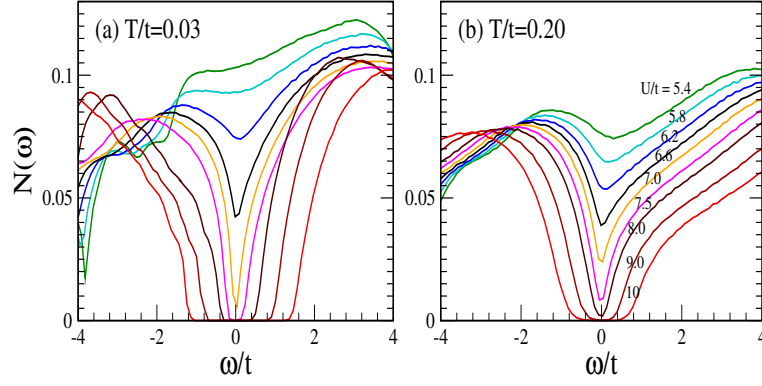
Figure 5.9: *U* dependence of density of states $N(\omega)$ at (a) *T*=0.03*t* showing the crossover from correlated metal to AFI through a wide pseudogap window, and (b) *T*=0.2*t*, where the crossover is between the PM and a PI through a much wider pseudogap window.
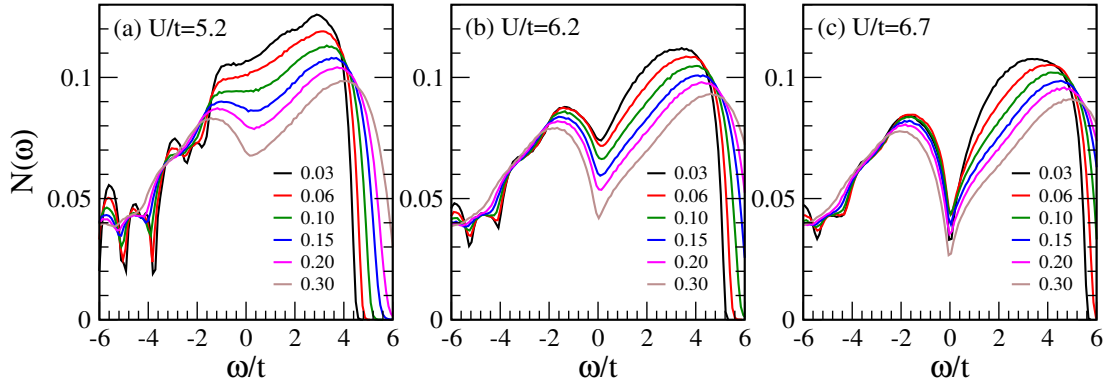

Figure 5.10: Temperature dependence of density of states $N(\omega)$ at three fixed *U* in the SG window. See the thermally induced PG at weak $U = 5.2t$ (a), the presence of the PG at $T = 0$ itself for (b) *U*=6.2*t* and (c) *U*=6.7*t*.

low energy difference between panels (a)-(b) and panel (c). In (a)-(b) the loss in low frequency weight, within $\omega \sim \pm t$ is monotonic with *T*. In panel (c), however, which neighbours the AFI, the low frequency weight first *increases* with *T*, upto $T \sim 0.1t$, and then again diminishes at higher temperature. Modest change of temperature, $T \sim 0.1t$, leads to large asymmetric shift of spectral weight from $\omega \sim 0$ to $\omega \sim U$.

5.3.4 Transport and optics

Fig.5.11 shows the resistivity $\rho(T, U)$. For $U < U_{c1}$ the resistivity is metallic ($\rho(T = 0) = 0$) and and increases with temperature ($d\rho/dT > 0$). For $U > U_{c2}$ the system is gapped at $T = 0$, hence zero temperature resistivity diverges ($\rho(T = 0) \to \infty$), with negative temperature coefficient ($d\rho/dT < 0$). These are the obvious metallic
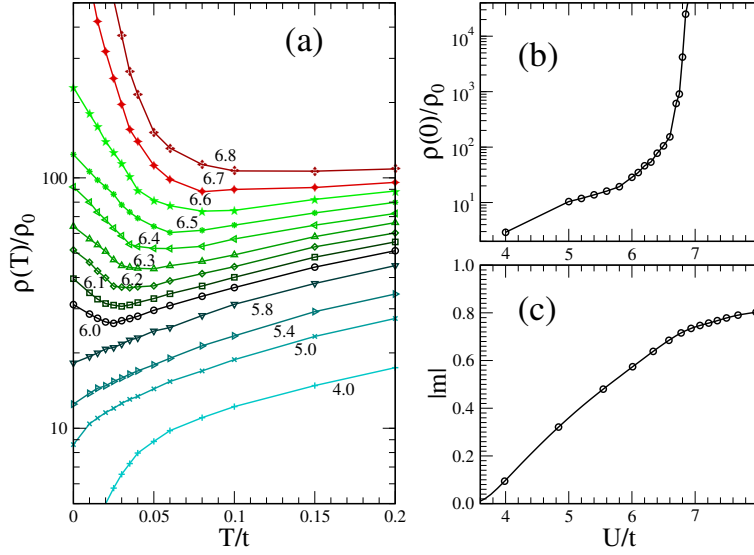
141

Figure 5.11: (a) T and U dependence of the resistivity, calculated in units of $\rho_0=\frac{\hbar a_0}{\pi e^2}$, a_0 being the lattice spacing (for $a_0 \sim 3\text{Å}$, $\rho_0 \sim 60\mu\Omega\text{cm}$). The PM window ($U<U_{c1}$) is metallic and the $T=0$ resistivity $\rho(0)$ vanishes. In the SGM phase ($U_{c1}<U<U_c$) is metallic, but $\rho(0)$ is finite. In the SGI phase ($U_c<U<U_{c2}$) $\rho(0)$ is finite, insulating and rapidly grows with U. For $U>U_{c2}$ the ground state has 'flux' order and a gapped spectrum (insulating), $\rho(0)$ is infinite. For the weakly insulating ground states ($(U-U_c)/U_c \ll 1$) increasing T leads to a crossover to metallic state. (b) The variation of the $\rho(0)$ with U/t. (c) The same for average moment m at $T=0$.

and insulating behaviour that one expects across a correlation driven transition. For $U_{c1} < U < U_{c2}$, however, the $T = 0$ resistivity is *finite*, with positive slope ($d\rho/dT > 0$) for $U_{c1} < U < U_c$, where $U_c \approx 5.8t$, and with negative slope ($d\rho/dT < 0$) for $U_c < U < U_{c2}$. This behaviour would usually not be expected in a translation invariant system, and arises because of the scattering of electrons from the 'frozen' local moments in the SG phase. The growth of $m(U)$, the mean magnitude of m_i, leads to the enhanced scattering with increasing U and finally the divergence of $\rho(0)$ due to the opening of a gap. The variation of $\rho(0)$ and m with U/t are shown in panels (b) and (c) respectively. We characterize the system as metallic, at a given T and U, when the slope $d\rho/dT > 0$, and insulating when $d\rho/dT < 0$. With this convention, an 'insulator' may have finite spectral weight at $\omega = 0$ in the optical conductivity $\sigma(\omega)$.

Fig.5.12, and 5.13 show the optics for the same parameter choice as the DOS figure. Panels (a)-(b) show the evolution of $\sigma(\omega)$ across the metal-insulator transition, between the PM and AFI at $T = 0.03t$, and between the PM and PI at $T = 0.20t$. There is a clear window of non Drude response at low T, roughly corresponding
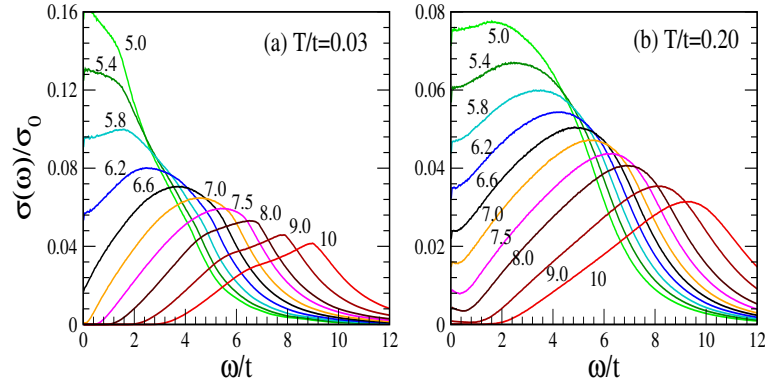
142

Figure 5.12: Optical conductivity $\sigma(\omega)$ in units of $\sigma_0 = \frac{1}{\rho_0}$, on the same U,T set as Fig.5.9(a)-(b). On increasing U/t, at low T (a) the response evolves from a Drude metal to the Mott AFI through a non Drude regime, and at large T (b) it shows similar evolution from the PM to a PI, where no Drude peak is visible down to $U = 5t$. The peak locations have moved to higher ω, and overall scales of $\sigma(\omega)$ are halved.
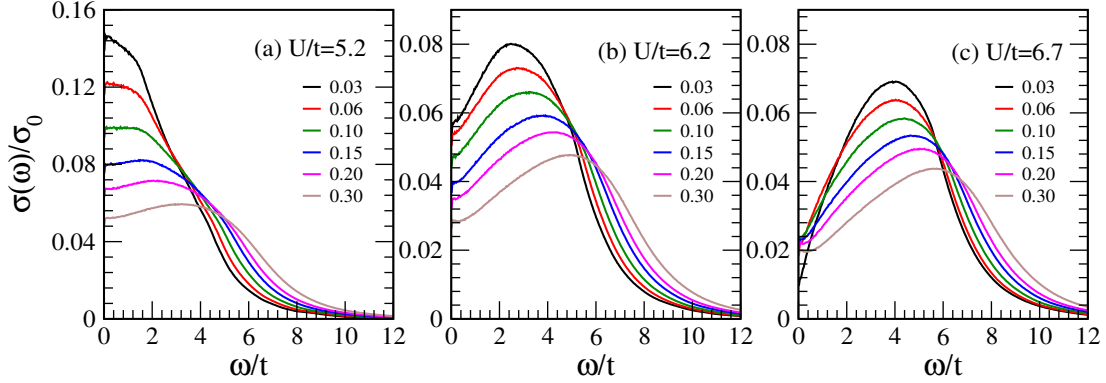
Figure 5.13: Temperature dependence of the Optical conductivity $\sigma(\omega)$ at the same U set as Fig.5.9(a)-(c) in the SG window. The weak moment system (a) shows essentially broadening of Drude response with increasing T. The larger moment system (b) shows a non Drude response with low ω weight suppressed with T. Panel (c) shows an SG with large $\rho(0)$. The very low ω weight (on the scale of the PG) *increases with T*, while the weight at $\omega \sim U$ reduces with increasing T.

to the PG regime in Fig.5.9.(a). In 5.12.(b) the non Drude window in U/t has increased as in Fig.5.9.(b) with a general suppression in the magnitude of $\sigma(\omega)$. The Fig.5.13(a)-(c) show the suppression of low frequency optical weight, with some of it appearing at $\omega \gtrsim U$. Unlike the single particle DOS, the total optical weight is not conserved and varies with the kinetic energy. At $U/t = 6.7$, the very low frequency optical response is non monotonic in T, showing a quick increase and then a gradual suppression. This directly relates to the behaviour of $\rho(T)$ in Fig.5.11.(a).

5.3.5   Discussion

We have highlighted a host of magnetic, transport and spectral features associated with Mott phenomena on the FCC lattice. However, like all many body methods, our approach too is approximate. We touch upon the possible shortcomings before attempting to relate our results to experiments.

Ground state: The ground state that we access through MC is equivalent to the unrestricted Hartree-Fock (UHF) result, but *with no assumptions about translational symmetry*. It is easy to see some of the qualitative effects of dynamical fluctuations in $\mathbf{m}_i$ and ϕ_i, that we have neglected, at $T = 0$. These would have the following consequences:

1. They would convert the $U < U_{c1}$ band metal to a correlated metal.

2. They would introduce quantum spin fluctuations in the large U antiferromagnetic phases.

3. They would possibly shift U_{c1} to a larger value, since the correlated metal competes better with the local moment phase, and would survive to larger U.

4. The intermediate window 'spin glass' that appears within the static approximation might be converted to a spin liquid with slowly fluctuating moments. A recent calculation on the triangular lattice demonstrates how longer range and multi-spin interactions arise on a frustrated Mott insulator and can lead to a spin liquid ground state [167].

We have tried various Monte Carlo protocols, and they all seem to lead to a spin glass state at intermediate coupling. However, it would be useful to check the size dependence in more detail, and also possible metastability of this state.

Thermal effects: Our approach captures the correct thermal fluctuations of the $\mathbf{m}_i$, without any assumption about long range order in the background. This in turn allows us to capture a T_c that has the qualitatively correct U dependence. With growing temperature, but staying at $T \ll U$, these classical thermal fluctuations should reasonably describe the magnetic background, and its effect on the electrons. Our results suggest the organization of a broad class of experiments.

1. We find that a non-coplanar spin configuration dominates the Mott phase, and pressure induced metalization leads to a weak moment 'spin frozen' state with

short range non-coplanar correlations. This is consistent [113, 116, 119] with observations on GaTa$_4$Se$_8$, FCC A$_3$C$_{60}$, and double perovskite materials.

2. Beyond the pressure driven IMT the materials exhibit [114, 122, 124, 125] very high $\rho(0)$, and $d\rho/dT < 0$. Our results show how this can arise from the presence of disordered local moments strongly coupled to the itinerant electrons, leading to large scattering. In the Ga cluster materials these local moments emerge from correlation effects, while in the pyrochlores [122] they are already present as localized a_{1g} electrons.

3. The very recent optical measurement [115] in GaTa$_4$Se$_8$ shows pronounced non Drude character in the metal near the IMT. This is consistent with our optics results for the PM to PI transition.

The correspondence above allows us to make two broad predicitions about Mott transition in these frustrated systems: (i) There should be a wide PG regime beyond the insulator-metal transition, persisting to $T = 0$. This should be visible in tunneling and photo-emission spectra, and (ii) the thermally induced shift of single particle spectral weight would be *extremely asymmetric*. Weight at low positive frequencies is shifted to the scale of $\omega \sim U$, while the negative frequency spectrum remains almost unaffected. We have not probed the anomalous Hall response due to flux like correlations or possible superconductivity.

Let us now move to a quantitative comparison of our results with data available on the FCC based Gallium cluster compounds.

5.4 Comparison with experiments

5.4.1 Parameter estimation

The recent optical experiments on the cluster compound GaTa$_4$Se$_8$ [115] show confirmation of a pressure driven Mott transition, consistent with earlier resistivity results [114], and suggest the appropriateness of a single band description. They also allow an estimate of the interaction strength, through optical conductivity data. The electronically active Ta$_4$ clusters live on a face centered cubic (FCC) motif, providing a clean example of an IMT in a three dimensional frustrated structure in, apparently, a single band context.

GaTa$_4$Se$_8$ had recently attracted attention due to electric field induced insulator to metal switching. Much, however, remains unknown about these materials, except

(i) the unusual low temperature transport feature, near the IMT [114], of very large residual resistivity with a negative temperature coefficient, and (ii) the possibility of a non-coplanar ('all in all out') order at $T \sim 30$K in $GaNb_4Se_8$. Neither of these are commonplace for materials near a Mott transition, and, we argue, arise from the interplay of frustration and correlation effects.

In this section, we use the single band Hubbard description for these materials, and 'calibrate' the pressure (P) dependence of electronic parameters (see later) based on the optical conductivity data.

The band structure calculations that accompany the recent optical measurement suggest that despite the complex chemistry *only one band*, arising primarily from Ta $5d$ levels, is adequate to describe the tight binding electronic structure. That does not necessarily mean that nearest neighbour (NN) hopping will describe the electronic structure in detail, but for simplicity we assume that only NN hopping provides an adequate starting point. The next task is to obtain a pressure dependent calibration, $t(P)$, for the hopping and estimate the interaction strength U.

The experimental optical conductivity, $\sigma_{exp}(\omega, P)$, shows a peak at $\omega_p \approx 550$meV when $P = 0$. The peak frequency reduces slowly as P increases to 10 GPa. For the insulating $P = 0$ sample $\sigma_{exp}(\omega)$ basically probes the inter Hubbard band transitions, prompting the authors to infer that $U \approx 550$meV. In principle U could be pressure dependent but apparently the Ta_4 clusters, from which the U arises, do not significantly compress with P. In that case the P driven Mott transition would arise from changing bandwidth. The authors indeed provide GGA based results for the bandwidth and interpret their results for $\sigma_{exp}(\omega)$ in terms of single site dynamical mean field theory (DMFT).

We proceed slightly differently. We treat U as a pressure independent constant, close to but not necessarily 550meV. We treat t as a P dependent parameter so that the key features, *i.e*, (i) the peak location ω_p, and (ii) the magnitude at the peak, $\sigma(\omega_p)$, match between $\sigma_{exp}(\omega)$ and the theory result $\sigma_{th}(\omega)$. Specifically, we want $\omega_p(P)|_{expt} \approx \omega_p(t(P), U)|_{th}$ and $\sigma_{exp}(\omega_p, P) \approx \sigma_{th}(\omega_p, t(P), U)$, at $T = 300$K. The quality of the match, for our choice of $t(P)$ is shown in Fig.5.14 and discussed further on. We find that $U = 500$meV, and $t(P)$ ranging from 50meV at $P = 0$ to 70meV at $P = 10$ GPa leads to a reasonable match. We use the estimated U and $t(P)$ to fix a *temperature independent* calibration for electronic parameters in terms of P. From now on we phrase the theory results directly in terms of absolute temperature (Kelvin) and pressure (GPa) without always referring to U/t.

Fig.5.14 shows the optical conductivity comparison. The left panel shows the
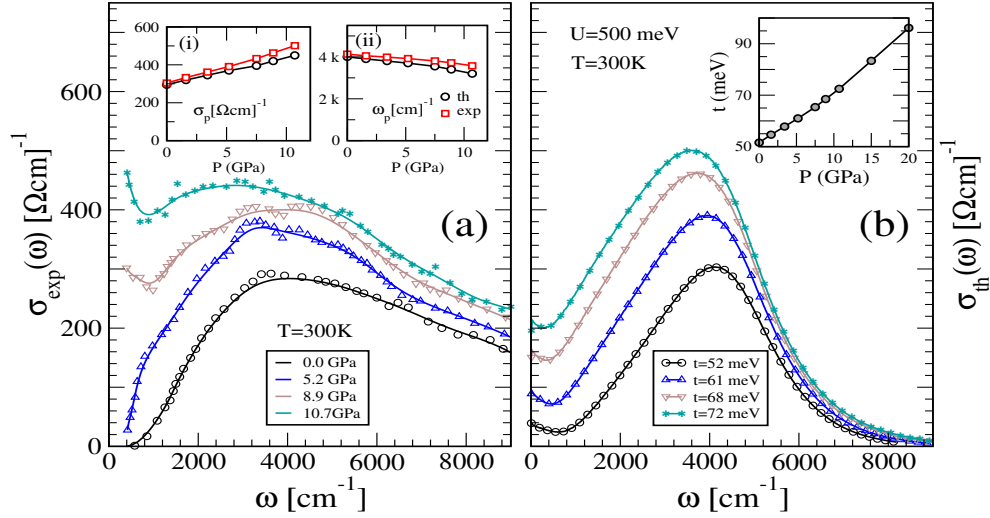
146

Figure 5.14: Comparison of the optical conductivity for calibrating the electronic parameters. (a) Experimental result $\sigma_{exp}(\omega)$ measured in $GaTa_4Se_8$ at various pressures and $T = 300$K. The data is obtained by subtracting out the inter-band contribution as quantified in the experimental paper. (b) Our result $\sigma_{th}(\omega)$ for $U = 500$meV and hopping parameters t chosen to mimic the pressure dependence in the experiments. Insets to panel (a), (i): comparison of the mid infrared peak height in $\sigma(\omega_p)$ between theory and experiment, (ii): comparison of the peak location ω_p. Inset to (b): our choice of hopping parameter t as function of pressure.

measured value $\sigma_{exp}(\omega, P)$, where we have subtracted a pressure independent high frequency contribution as quantified by the experimenters. This was suggested by them so that the result could be analyzed within a 'one band' scenario, removing Ta-5d to Se-4p transitions. The right panel shows our $\sigma_{th}(\omega, t(P))$, where $t(P)$ has been chosen as in the inset to panel (b), and $U = 500$meV and $T = 300$K. The $t(P)$ calibration has been chosen to get a reasonable fit to the peak location, inset (ii) in panel (a), and the peak height, inset (i) in panel (a). We had varied the choice of U to optimize the overall fit. Although the peak features match, note that $\sigma_{exp}(\omega, P)$ has a slower fall at high frequency, compared to the theory result. This possibly arises from the background subtraction process mentioned earlier and highlights the difficulty of separating intra-band and inter-band effects at high frequency. Having determined the electronic parameters by fitting $\sigma(\omega)$ at high temperature we now test the usefulness of the FCC Hubbard description by comparing the *temperature dependence* of the d.c resistivity between experiment and theory.
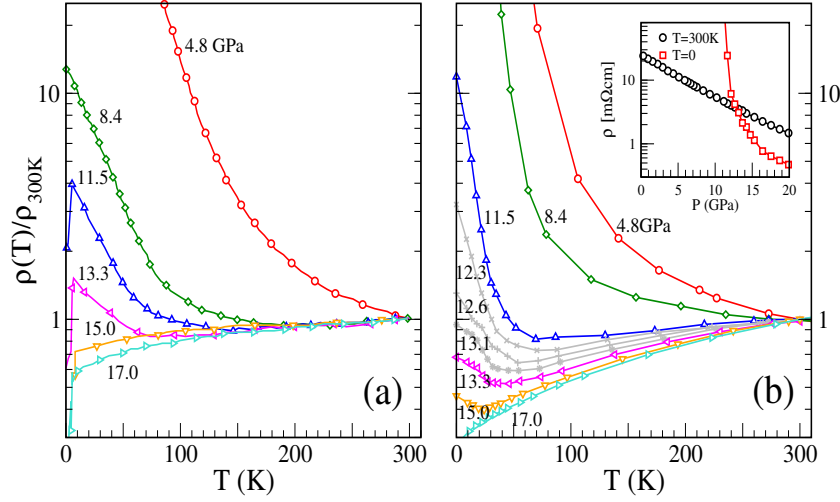
Figure 5.15: (a). The resistivity $\rho(T)$ in GaTa$_4$Se$_8$, normalized to its value at 300K, for different pressures. Notice the intermediate pressure window where $\rho(T)$ is headed for a finite value at $T = 0$ with $d\rho/dT < 0$. (b). The 'pressure' and temperature dependence of the theoretically estimated resistivity, using the calibration shown in Fig.1. The pressures that correspond to experiment are marked, and we also show data for intermediate pressure values in the anomalous regime. The inset to panel (b) shows the absolute value of the model resistivity at $T = 0$ and $T = 300$K. Note that we have no phonon contribution or impurity scattering in the theory.

5.4.2   Comparing the resistivity

Fig.5.15 shows the resistivity, the left panel shows the experimental result $\rho_{exp}(T, P)$, normalized to $\rho_{exp}(300K, P)$, while the right panel shows the theoretical result $\rho_{th}(T, P)$ similarly normalized. Note that our fit to the high frequency feature in $\sigma(\omega)$ in no way constrains the d.c resistivity. First the obvious features: (i) At low pressure, $P = 4.8$ GPa, both ρ_{exp} and ρ_{th} diverge as $T \to 0$. The experimental charge gap is estimated at 100meV, our estimate at low temperature is about 105meV (it weakens slowly with T). (ii) For $P \gtrsim 15$ GPa both ρ_{exp} and ρ_{th} show usual metallic behaviour with $d\rho/dT > 0$. The experimental result has a higher $T \to 0$ value probably due to the presence of impurity scattering.

Over an intermediate pressure window, 8 GPa $\lesssim P \lesssim 14.0$ GPa, however, ρ_{exp} shows a large $T \to 0$ value, with $d\rho/dT < 0$. It seems some scattering or localization mechanism survives in the system even after the charge gap is destroyed by pressure. Our result ρ_{th} has a similar window, over a slightly different pressure range, 11.6 GPa $\lesssim P \lesssim 16.0$ GPa. While the numerical values for ρ_{th} and ρ_{exp} at a given pressure differ, the match in the qualitative trend is remarkable. The inset to panel (b) shows the absolute value of ρ_{th} at $T = 0$ and $T = 300$K. The high T resistivity decreases
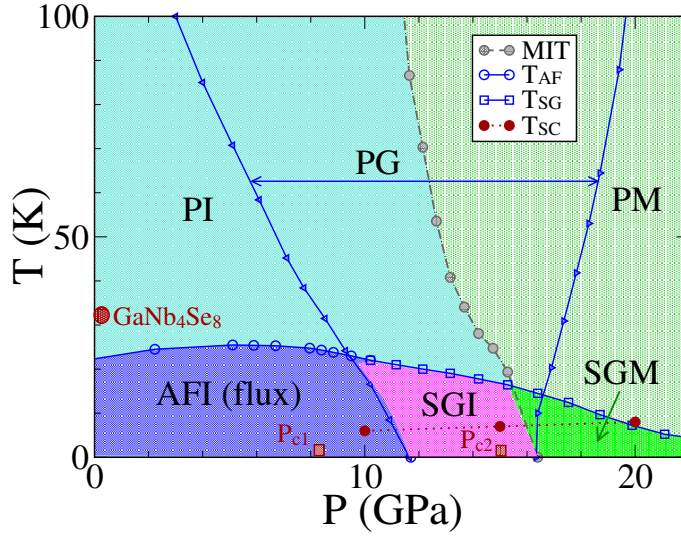
148

Figure 5.16: The pressure-temperature phase diagram of $GaTa_4Se_8$ based on our result. The predicted ground state is a non-coplanar (flux) state for $0 < P < 11.5$ GPa, and disordered local moment phase (spin glass) for $11.5 < P < 20$ GPa. The spin glass would have insulating character for $P < 16$GPa and metallic for $P > 16$ GPa. At $P = 0$ the flux phase has transition temperature $T_{AF} \approx 23$K. The T_{AF} slightly increases with P and beyond $P \sim 10$ GPa is replaced by a spin glass temperature T_{SG}. At high temperature the $P \lesssim 4$ GPa phase would be a paramagnetic insulator (PI), the $P \gtrsim 20$ GPa phase would be a paramagnetic metal, while the wide window in between would be pseudogapped (PG) with metallic or insulating character as shown. Available data from experiments is marked in red: (i) the slightly lower bandwidth material $GaNb_4Se_8$ is believed to have flux like order with $T_{AF} \approx 30$K, (ii) the critical pressures P_{c1} and P_{c2} for change in transport character are indicated, (iii) The superconducting transition $T_{SC} \sim 6-8$K is marked.

smoothly with increasing P, $i.e$, decreasing U/t. The low T resistivity varies more dramatically, with a metal-insulator transition at $P \sim 11.5$ GPa and a 'bad metal' (or weak insulator) phase for $11.5 < P < 16$ GPa. We feel the correspondence between ρ_{exp} and ρ_{th} is a strong test of the model. There is no way that just a fit to the high temperature $\sigma_{exp}(\omega)$ would automatically reproduce the complicated pressure and temperature dependence of ρ_{exp}. 'Impurity' and electron-phonon scattering are not included in our model.

5.4.3 Predicted magnetic phases

Fig.5.16 shows our prediction for the $P - T$ phase diagram of $GaTa_4Se_8$ based on our solution of the FCC Mott problem and the $t(P)$ calibration. We also superpose experimental data where available. Let us first comment on the ground state: (i) We
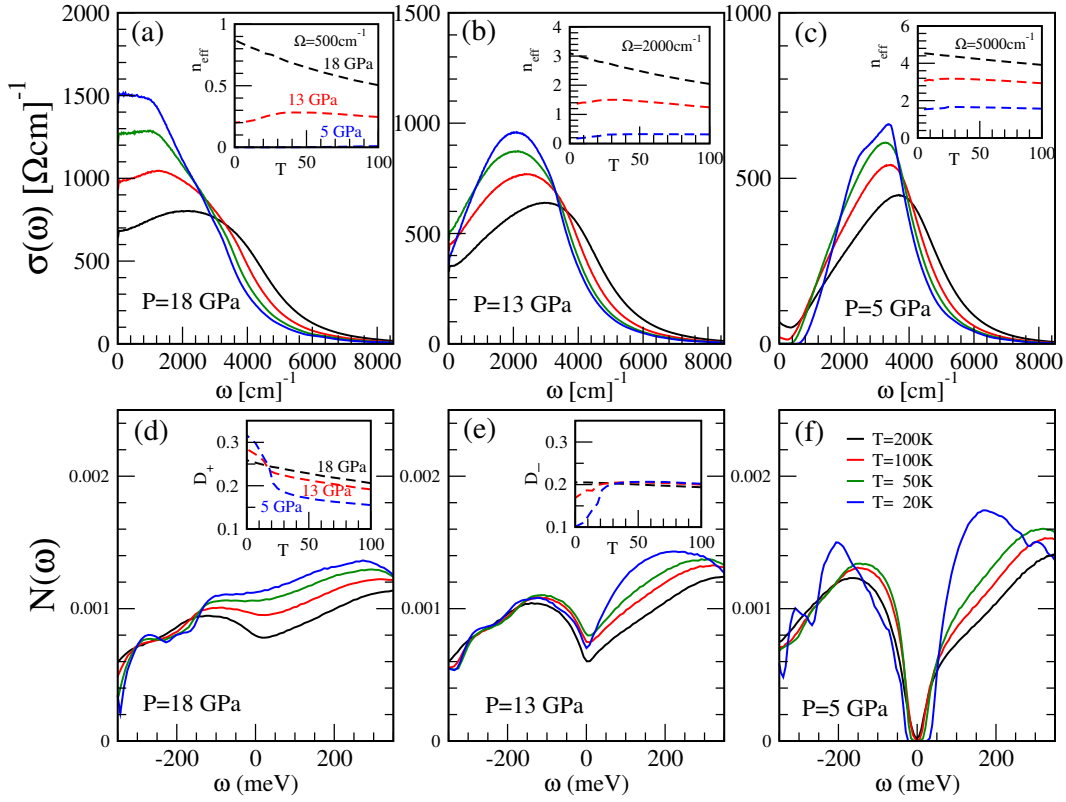
Figure 5.17: Predicting the temperature dependence of the optical conductivity (top row) and the single particle density of states (bottom) in the vicinity of the insulator-metal transition. 5GPa is in the Mott phase and 18 GPa is in the metal.

suggest an antiferromagnetic insulating (AFI) state with non-coplanar 'flux' order for $P \lesssim P_{c1} \sim 11.5$ GPa. (ii) Beyond P_{c1} and upto $P \sim 20$ GPa (beyond which we do not want to push $t(P)$) we see a disordered local moment (spin glass) phase. The magnitude of the moments decreases with increasing P. The spin glass would be insulating (SGI) for $P_{c1} < P < P_{c2}$, where $P_{c2} \sim 16$ GPa, with an electronic pseudogap and $d\rho/dT < 0$. Beyond P_{c2} there should be a spin glass metal (SGM) with a featureless density of states and $d\rho/dT > 0$. Experimentally, the transport inferred $P_{c1} \sim 8$ GPa, while $P_{c2} \sim 15$ GPa. These are quite comparable to our $P_{c1} \sim 11.5$ GPa and $P_{c2} \sim 16$ GPa.

The transition temperature T_{AF} at $P = 0$ is ≈ 23K, rises slightly with P, and beyond $P \sim 10$ GPa is replaced by a spin glass transition temperature T_{SG}. While we do not know of measurements on the magnetic state in $GaTa_4Se_8$ the slightly smaller bandwidth $GaNb_4Se_8$ 'orders' at $T \sim 30$K at $P = 0$, into, apparently, a flux like state. This point is marked at $P = 0$, as suggestive of what one could examine in $GaTa_4Se_8$.

5.4.4 Predicted spectral features

Fig.5.17 shows the temperature dependence of the optical conductivity and the DOS at three pressures. The three pressures we choose are (a) $P = 18$ GPa, corresponding to a metallic ground state, (b) $P = 13$ GPa, corresponding to a spin glass 'insulating' ground state, and (c) $P = 5$ GPa where the ground state should be AFI. Note that the available optical data only shows the P dependence at $T = 300$K, so the results for $\sigma(\omega)$ in Fig.5.17.(a)-(c) are detailed predictions for what to expect in the temperature dependence. The temperature legend, common to all panels, is shown in panel (f).

Panel (c) shows the behaviour of $\sigma(\omega)$ at $P = 18$ GPa as T increases from 20K to 200K. The low T response is Drude like, with a peak at $\omega = 0$, but for $T \geq 50$K there is the hint of the peak shifting to finite ω and the non Drude character is quite prominent at $T = 200$K.

5.5 Conclusions

We have provided a comprehensive study of the Mott transition on the geometrically frustrated FCC lattice. Our results indicate that magnetic frustration can lead to a translation symmetry broken 'two fluid' state of itinerant electrons and disordered local moments between the paramagnetic metal and the antiferromagnetic insulator. The disordered phase involves an anomalously large residual resistivity, non Drude optical response, and a single particle pseudogap. The results establish a conceptual scheme for approaching 3D frustrated materials. We have made a quantitative description of the pressure driven Mott transition, in the cluster compounds AM_4X_8, based on the recent optical conductivity data, by calibrating the pressure in terms of the bandwidth of the materials.

DISPERSION FOR ORDERED PHASES

Here we show how to calculate dispersion for selected ordered phases, which have relatively small unit cells. We define the unit cell for each phase, and go to $k-$space where the Hamiltonian becomes block diagonal.

A.1   Spectrum for collinear phases

The Hamiltonian can be diagonalized by Fourier transformation. We write the Hamiltonian H as $H = H_0 + H_J$, where, H_0 is given by,

$$
\begin{aligned}
H_0 &= \sum_{\vec{X}\sigma}[\epsilon_1 f^\dagger_{\vec{X},\sigma} f_{\vec{X},\sigma} + \epsilon_2 m^\dagger_{\vec{X}+\vec{a_1},\sigma} m^\dagger_{\vec{X}+\vec{a_1},\sigma}] - t \sum_{\vec{X},\sigma,\vec{\delta}\in\text{NN}} (f^\dagger_{\vec{X},\sigma} m_{\vec{X}+\vec{\delta},\sigma} + \text{h.c.}) \\
&\quad -t' \sum_{\vec{X},\sigma,\vec{\delta}\in\text{NNN}} (m^\dagger_{\vec{X}+\vec{a_1},\sigma} m_{\vec{X}+\vec{a_1}+\vec{\delta},\sigma} + \text{h.c.})
\end{aligned} \tag{A.1}
$$

and H_J is given by

$$
H_J = J \sum_{\vec{X}} \vec{S}(\vec{X}) \cdot \vec{\sigma}_{\alpha,\beta} f^\dagger_{\vec{X},\alpha} f_{\vec{X},\beta} \tag{A.2}
$$

The lattice vector $\vec{X}$ is defined as $\vec{X} = n_1\vec{A_1} + n_2\vec{A_2} + n_3\vec{A_3}$ with $A_i, i = 1, 2, 3$ as the primitive lattice vectors ($A_1 = (2, 0, 0)$, $A_2 = (1, 1, 0)$, $A_3 = (0, 1, 1)$), defining the periodicity of lattice with the 2 site unit cell. With this periodicity, the unit cell has one 'f' and one 'm' site at $(0, 0, 0)$ and $(1, 0, 0)$ respectively. Now doing a Fourier transform on 'f' operators (similarly for 'm's)

$$
f^\dagger_{\vec{X},\sigma} = \frac{1}{\sqrt{N}} \sum_{\vec{k}} f^\dagger_{\vec{k},\sigma} \exp(i\vec{k} \cdot \vec{X}) \tag{A.3}
$$

This simplifies the non-magnetic part H_0 as follows,

$$H_0 = \sum_{\vec{k},\sigma} \left[(\epsilon_2 + A'_{\vec{k}}) m^\dagger_{\vec{k},\sigma} m_{\vec{k},\sigma} + \epsilon_1 f^\dagger_{\vec{k},\sigma} f_{\vec{k},\sigma} + (A_{\vec{k}} f^\dagger_{\vec{k},\sigma} m_{\vec{k},\sigma} + \text{h.c.}) \right]$$

$$= \sum_{\vec{k},\sigma} \left(f^\dagger_{\vec{k},\sigma}\ m^\dagger_{\vec{k},\sigma} \right) \begin{pmatrix} \epsilon_1 & A_{\vec{k}} \\ A_{\vec{k}} & \epsilon_2 + A'_{\vec{k}} \end{pmatrix} \begin{pmatrix} f_{\vec{k},\sigma} \\ m_{\vec{k},\sigma} \end{pmatrix} \tag{A.4}$$

Which is reduced to 2×2 block. the amplitudes $A_{\vec{k}} = -2t(\cos k_x + \cos k_y + \cos k_z)$ and $A'_{\vec{k}} = -4t'(\cos k_x \cos k_y + \cos k_y \cos k_z + \cos k_z \cos k_x)$ are just the cubic and FCC dispersions.

Next, we have to simplify the H_J part. For the collinear phases, $\vec{S}(\vec{X})$ can be expressed as $\vec{S}(\vec{X}) = (0, 0, e^{i\vec{q}\cdot\vec{X}})$. For FM, $\vec{q}$ is trivially $(0,0,0)$. For A-type, $\vec{q} = (\frac{\pi}{2}, -\frac{\pi}{2}, \frac{\pi}{2})$, while for C-type $\vec{q} = (0, \pi, -\pi)$. Now, plugging this value of $\vec{S}(\vec{X})$ in H_J and doing the Fourier transform for the H_J, we get,

$$H_J = J \sum_{\vec{x}} \sigma f^\dagger_{\vec{k},\sigma} f_{\vec{k}+\vec{q},\sigma} \quad ; \sigma = \pm 1 \tag{A.5}$$

Now $\vec{q} = 0$ for FM, so H_J becomes diagonal. Thus total Hamiltonian H still remains 2×2 block, and the eigenvalues for the FM are solutions of the following 2×2 block

$$H_{2X2}(\vec{k}, \sigma) = \begin{pmatrix} \epsilon_1 + J\sigma & A_{\vec{k}} \\ A_{\vec{k}} & \epsilon_2 + A'_{\vec{k}} \end{pmatrix} \tag{A.6}$$

For A-type and C-type phases, we get matrix elements connecting $|\vec{k}, \sigma\rangle \to |\vec{k} + \vec{q}, \sigma\rangle \to |\vec{k}, \sigma\rangle$, so that now we get to solve following 4×4 block

$$H_{4\times4}(\vec{k}, \sigma) = \begin{pmatrix} \epsilon_1 & J\sigma & A_{\vec{k}} & 0 \\ J\sigma & \epsilon_1 & 0 & A_{\vec{k}+\vec{q}} \\ A_{\vec{k}} & 0 & \epsilon_2 + A'_{\vec{k}} & 0 \\ 0 & A_{\vec{k}+\vec{q}} & 0 & \epsilon_2 + A'_{\vec{k}} \end{pmatrix} \tag{A.7}$$

From these we obtain the spectrum for F,A,C phases on large ($\sim 100^3 - 500^3$) lattices, which can be used to calculate the density of states, phase diagram, phase separation windows etc.

154

A.2 Spectrum for the 'flux' phase

The unit cell for the 'flux' phase has $4B$, and $4B'$ atoms lying on the corners of the cube. The primitive lattice vectors become $A_i = \{(2,0,0), (0,2,0), (0,0,2)\}$ At finite J, the same procedure (as for collinear phases) will reduce the Hamiltonian into 16×16 block. To make life a bit simple, we use the J$\to \infty$ limit on the Hamiltonian for the 'flux' phase, which is same as used in [63] except its the 3D version.
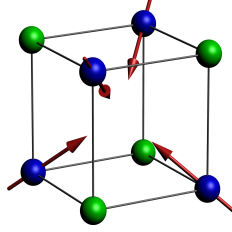

Figure A.1: Unit cell structure for the Flux phase

This gives us 4 spin-less f_i levels and 8 $m_{i,\sigma}$ levels in the unit cell, which upon simplification reduces to 12×12 block. With the basis $\left(\begin{array}{cc} f_i(k) & m_{i\uparrow}(k) \end{array} \right)_{i\in\{1,2,3,4\}}$ The Hamiltonian breaks into 12×12 block given as follows

$$H = \begin{pmatrix}
\Delta & 0 & 0 & 0 & t_{1\uparrow}a_1 & t_{1\downarrow}a_1 & t_{1\uparrow}a_2 & t_{1\downarrow}a_2 & 0 & 0 & t_{1\uparrow}a_3 & t_{1\downarrow}a_3 \\
0 & \Delta & 0 & 0 & t_{2\uparrow}a_2 & t_{2\downarrow}a_2 & t_{2\uparrow}a_1 & t_{2\downarrow}a_1 & t_{2\uparrow}a_3 & t_{2\downarrow}a_3 & 0 & 0 \\
0 & 0 & \Delta & 0 & t_{3\uparrow}a_3 & t_{3\downarrow}a_3 & 0 & 0 & t_{3\uparrow}a_2 & t_{3\downarrow}a_2 & t_{3\uparrow}a_1 & t_{3\downarrow}a_1 \\
0 & 0 & 0 & \Delta & 0 & 0 & t_{4\uparrow}a_3 & t_{4\downarrow}a_3 & t_{4\uparrow}a_1 & t_{4\downarrow}a_1 & t_{4\uparrow}a_2 & t_{4\downarrow}a_2 \\
t_{1\uparrow}^*a_1 & t_{2\uparrow}^*a_2 & t_{3\uparrow}^*a_3 & 0 & 0 & 0 & t_{12} & 0 & t_{23} & 0 & t_{13} & 0 \\
t_{1\downarrow}^*a_1 & t_{2\downarrow}^*a_2 & t_{3\downarrow}^*a_3 & 0 & 0 & 0 & 0 & t_{12} & 0 & t_{23} & 0 & t_{13} \\
t_{1\uparrow}^*a_2 & t_{2\uparrow}^*a_1 & 0 & t_{4\uparrow}^*a_3 & t_{12} & 0 & 0 & 0 & t_{13} & 0 & t_{23} & 0 \\
t_{1\downarrow}^*a_2 & t_{2\downarrow}^*a_1 & 0 & t_{4\downarrow}^*a_3 & 0 & t_{12} & 0 & 0 & 0 & t_{13} & 0 & t_{23} \\
0 & t_{2\uparrow}^*a_3 & t_{3\uparrow}^*a_2 & t_{4\uparrow}^*a_1 & t_{23} & 0 & t_{13} & 0 & 0 & 0 & t_{12} & 0 \\
0 & t_{2\downarrow}^*a_3 & t_{3\downarrow}^*a_2 & t_{4\downarrow}^*a_1 & 0 & t_{23} & 0 & t_{13} & 0 & 0 & 0 & t_{12} \\
t_{1\uparrow}^*a_3 & 0 & t_{3\uparrow}^*a_1 & t_{4\uparrow}^*a_2 & t_{13} & 0 & t_{23} & 0 & t_{12} & 0 & 0 & 0 \\
t_{1\downarrow}^*a_3 & 0 & t_{3\downarrow}^*a_1 & t_{4\downarrow}^*a_2 & 0 & t_{13} & 0 & t_{23} & 0 & t_{12} & 0 & 0
\end{pmatrix} \tag{A.8}$$

Where the symbols in the above are defined as

$$\alpha = \sqrt{\frac{\sqrt{3}+1}{2\sqrt{3}}}; \quad \beta = \sqrt{\frac{\sqrt{3}-1}{2\sqrt{3}}}; \quad z = \frac{1-i}{\sqrt{2}}; \quad a_1 = 2\cos k_1; a_2 = 2\cos k_2; a_3 = 2\cos k_3$$

$$t_{12} = -4t'\cos k_1 \cos k_2; t_{23} = -4t'\cos k_2 \cos k_3; t_{13} = -4t'\cos k_1 \cos k_3;$$

$$t_{1\uparrow} = t_{2\uparrow} = -t\alpha; t_{3\uparrow} = t_{4\uparrow} = -t\beta; t_{1\downarrow} = -t_{2\downarrow} = tz\beta; t_{3\downarrow} = -t_{4\downarrow} = -tz^*\alpha$$

This gives us $H(\mathbf{k})_{12\times12}$, which is very difficult to diagonalize analytically, but still saves us from diagonalizing full real-space matrix of $\mathcal{O}(\mathcal{N})$ size, and reduces the problem to $\mathcal{O}(\mathcal{N})$ number of diagonalizations of 12 sized matrix.

The comparison of energies using the $\epsilon_{\mathbf{k}}$ obtained for F,A,C and flux phases, one can draw the magnetic phase diagram for large lattice size ($N \sim 400^3$). The figure A.2, shows the phase diagram, which can be compared to that obtained through real space calculations done on 20^3 size.
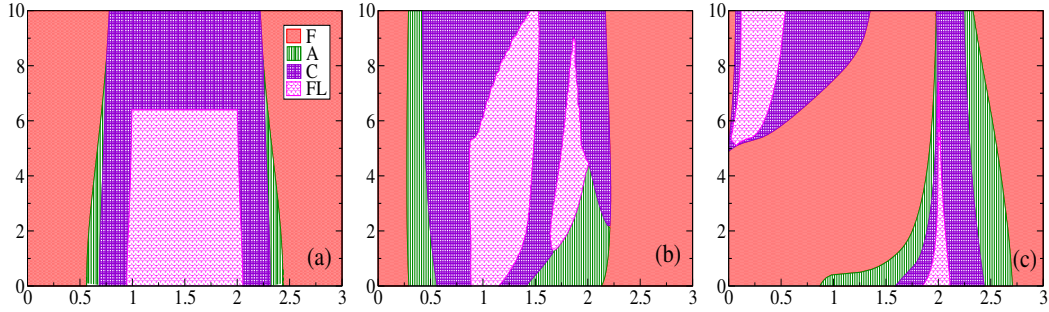

Figure A.2: Colour online: Phase diagram based on k space based diagonalisation for $t' = 0, 0.3, -0.3$. System size $N = 160^3$. Here we can only use F, A, C and 'flux' phase as candidate states but some of the complexity of more elaborate phase diagrams, Fig.2, are already present.

FCC LATTICE SETUP

On the FCC lattice, the primitive lattice translation vectors are

$$\vec{A}_1 \ = \ (0,1,1), \qquad \vec{A}_2 \ = \ (1,0,1), \qquad \vec{A}_3 \ = \ (1,1,0) \qquad \text{(B.1)}$$

All the points on FCC lattice are expressed in integer units of these, i.e., $\vec{X} = n_1\vec{A}_1 + n_2\vec{A}_2 + n_3\vec{A}_3 = (n_2 + n_3, n_3 + n_1, n_1 + n_2) = \vec{X}(n_1, n_2, n_3)$. Each site has 12 neighbours $X + \delta$, where

$$
\begin{aligned}
\delta \ = \ & (\ 1,\ \ 1,\ \ 0), (-1, -1,\ \ 0), \\
& (\ 1,\ \ 0,\ \ 1), (-1,\ \ 0, -1), \\
& (\ 0,\ \ 1,\ \ 1), (\ 0, -1, -1) \\
& (\ 1, -1,\ \ 0), (-1,\ \ 1,\ \ 0), \\
& (\ 1,\ \ 0, -1), (-1,\ \ 0,\ \ 1), \\
& (\ 0,\ \ 1, -1), (\ 0, -1,\ \ 1)
\end{aligned}
$$

Now lets see how the neighbours are labeled

$$
\begin{aligned}
N_1 \ &= \ X(n_1, n_2, n_3) + (1,1,0) = (n_2 + n_3, n_3 + n_1, n_1 + n_2) + (1,1,0) \\
&= \ (n_2 + (n_3 + 1), (n_3 + 1) + n_1, n_1 + n_2) = X(n_1, n_2, n_3 + 1)
\end{aligned}
$$

Or,

$$N_1 \ = \ X(n_1, n_2, n_3) + (1,1,0) = X(n_1, n_2, n_3 + 1)$$

Similarly, one gets the other five as

$$
\begin{aligned}
N_2 &= X(n_1, n_2, n_3) + (-1, -1, 0) = X(n_1, n_2, n_3 - 1) \\
N_3 &= X(n_1, n_2, n_3) + (1, 0, 1) = X(n_1, n_2 + 1, n_3) \\
N_4 &= X(n_1, n_2, n_3) + (-1, 0, -1) = X(n_1, n_2 - 1, n_3) \\
N_5 &= X(n_1, n_2, n_3) + (0, 1, 1) = X(n_1 + 1, n_2, n_3) \\
N_6 &= X(n_1, n_2, n_3) + (0, -1, -1) = X(n_1 - 1, n_2, n_3)
\end{aligned}
$$

Next, we have,

$$
\begin{aligned}
N_7 &= X(n_1, n_2, n_3) + (1, -1, 0) = (n_2 + n_3, n_3 + n_1, n_1 + n_2) + (1, -1, 0) \\
&= ((n_2 + 1) + n_3, n_3 + (n_1 - 1), (n_1 - 1) + (n_2 + 1)) = X(n_1 - 1, n_2 + 1, n_3)
\end{aligned}
$$

Or,

$$
N_7 = X(n_1, n_2, n_3) + (1, -1, 0) = X(n_1 - 1, n_2 + 1, n_3)
$$

Similarly the other neighbours are labeled as

$$
\begin{aligned}
N_8 &= X(n_1, n_2, n_3) + (-1, 1, 0) = X(n_1 + 1, n_2 - 1, n_3) \\
N_9 &= X(n_1, n_2, n_3) + (1, 0, -1) = X(n_1 - 1, n_2, n_3 + 1) \\
N_{10} &= X(n_1, n_2, n_3) + (-1, 0, 1) = X(n_1 + 1, n_2, n_3 - 1) \\
N_{11} &= X(n_1, n_2, n_3) + (0, 1, -1) = X(n_1, n_2 - 1, n_3 + 1) \\
N_{12} &= X(n_1, n_2, n_3) + (0, -1, 1) = X(n_1, n_2 + 1, n_3 - 1)
\end{aligned}
$$

Thus if we label the sites (n_1, n_2, n_3), the first six neighbours have labels, $(n_1 \pm 1, n_2, n_3)$,$(n_1, n_2 \pm 1, n_3)$, and $(n_1, n_2, n_3 \pm 1)$, and the second six neighbours have labels $(n_1 \pm 1, n_2 \mp 1, n_3)$,$(n_1 \pm 1, n_2, n_3 \mp 1)$, and $(n_1, n_2 \pm 1, n_3 \mp 1)$.

Thus, the 12 neighbours of the FCC lattice correspond to 12 'neighbours' in the 'label' lattice, first six of which are nearest neighbours, and second six of which are 6 selected next-nearest neighbours. So, though we need to define actual spin configurations on the FCC lattice, the corresponding Hamiltonian of FCC lattice is equivalent to that defined on the 'label' lattice.

		NN		
δ	δ'	J_x	J_y	J_z
(1, 1, 0)	(0, 0, 1)	-t	-t	0
(-1,-1, 0)	(0, 0,-1)	t	t	0
(1, 0, 1)	(0, 1, 0)	-t	0	-t
(-1, 0,-1)	(0,-1, 0)	t	0	t
(0, 1, 1)	(1, 0, 0)	0	-t	-t
(0,-1,-1)	(-1, 0, 0)	0	t	t
(1,-1, 0)	(-1, 1, 0)	-t	t	0
(-1, 1, 0)	(1,-1, 0)	t	-t	0
(1, 0,-1)	(-1, 0, 1)	-t	0	t
(-1, 0, 1)	(1, 0,-1)	t	0	-t
(0, 1,-1)	(0,-1, 1)	0	-t	t
(0,-1, 1)	(0, 1,-1)	0	t	-t
		NNN		
δ	δ'	J_x	J_y	J_z
(2, 0, 0)	(-1, 1, 1)	-t'	0	0
(-2, 0, 0)	(1,-1,-1)	t'	0	0
(0, 2, 0)	(1,-1, 1)	0	-t'	0
(0,-2, 0)	(-1, 1,-1)	0	t'	0
(0, 0, 2)	(1, 1,-1)	0	0	-t'
(0, 0,-2)	(-1,-1, 1)	0	0	t'

Table B.1:   The neighbours on fcc lattice

BIBLIOGRAPHY

[1] G. .H. Wannier, Phys. Rev. **79**, 357 (1950)

[2] Kenzi Kano, and Shigeo Naya Prog. Theor. Phys. **10**, 158 (1953)

[3] V. Vacks, A. Larkin and Y. Ovchinnikov, *Sov. Phys.* JETP **22** 820 (1966), T. Morita, *J. Phys.* A **19** 1701 (1987), T. Chikyu and M. Suzuki *Prog. Theor. Phys.* **78** 1242 (1987).

[4] P. Azaria, H. T. Diep, and H. Giacomini, Phys. Rev. Lett. **59**, 1629 (1987), M. Debauche, H. T. Diep, Phys. Rev. B **46**, 8214 (1992).

[5] M. Mzard, G. Parisi, N. Sourlas, G. Toulouse, and M. Virasoro, Phys. Rev. Lett. 52, 11561159 (1984)

[6] Giorgio Parisi, Phys. Rev. Lett. **50**, 1946 (1983).

[7] H. T. Diep, Frustrated spin systems, World Scientific (2005)

[8] R. Moessner and J. T. Chalker, Phys. Rev. B **58** 12049 (1998),

[9] R. Moessner and J. T. Chalker, Phys. Rev. Lett. **80** 2929 (1998).

[10] David A. Huse and Andrew D. Rutenberg, Phys. Rev. B **45** 7536 (1992).

[11] J. T. Chalker, P. C. W. Holdsworth, and E. F. Shender, Phys. Rev. Lett. **68** 855 (1992).

[12] P. Lecheminant, B. Bernu, C. Lhuillier, L. Pierre, and P. Sindzingre, Phys. Rev. B **56**, 2521 (1997)

[13] Michael Hermele, Ying Ran, Patrick A. Lee, and Xiao-Gang Wen, Phys. Rev. B **77**, 224413 (2008)

[14] Simeng Yan *et al.* Science **332**, 1173 (2011).

[15] Stefan Depenbrock, Ian P. McCulloch, and Ulrich Schollwock, Phys. Rev. Lett. **109** 067201 (2012).

[16] Yasir Iqbal, Federico Becca, Sandro Sorella, and Didier Poilblanc, Phys. Rev. B **87**, 060405(R) (2013).

[17] Iwase, H., Isobe, M., Ueda, Y. & Yasuoka, H. J. Phys. Soc. Jpn **65**, 23972400 (1996).

[18] Azuma, M., Hiroi, Z., Takano, M., Ishida, K. & Kitaoka, Y. Phys. Rev. Lett. **73**, 34633466 (1994).

[19] Kageyama, H. et al. Phys. Rev. Lett. **82**, 31683171 (1999).

[20] Anderson, P. W. Mater. Res. Bull. **8**, 153160 (1973).

[21] J.-B. Fouet, M. Mambrini, P. Sindzingre, and C. Lhuillier, Phys. Rev. B **67** 054411 (2003).

[22] Wolfram Brenig and Matthias Grzeschik, Phys. Rev. B **69**, 064420 (2004).

[23] S. Moukouri, Phys. Rev. B **77** 052408 (2008).

[24] J. H. de Boer and E. J. W. Verway, Proc. Phys. Soc. London Sec. **49**, 59 (1937).

[25] R. Peierls, Proc. Phys. Soc. London Sec. **49**, 72 (1937).

[26] N. F. Mott, Proc. Phys. Soc. London Sec. **62**, 416 (1949).

[27] J. Hubbard Proc. R. Soc. London Ser. **A276**, 238 (1963)

[28] M. C. Gutzwiller, Phys. Rev. Lett. **10**, 159162 (1963).

[29] J. Kanamori, Prog. Theor. Phys. **30**, 275289 (1963).

[30] J. Hubbard Proc. R. Soc. London Ser. **A277**, 237 (1963).

[31] J. Hubbard Proc. R. Soc. London Ser. **A281**, 401 (1963).

[32] J. Hubbard Proc. R. Soc. London Ser. **A285**, 542 (1963).

[33] J. Hubbard Proc. R. Soc. London Ser. **A296**, 42 (1963).

[34] J. Hubbard Proc. R. Soc. London Ser. **A296**, 100 (1963).

[35] Dagotto, *Rev. Mod. Phys.* **66**, 763 (1994), Lee *et al*, *Rev. Mod. Phys.* **78**, 17 (2006).

[36] Damascelli *et al*, Rev. Mod. Phys. **75**, 473541 (2003).

[37] Tokura, Y. (ed.), Colossal Magnetoresistive Oxides, CRC Press, (2000).

[38] Salamon *et al*, *Rev. Mod. Phys.* **73**, 583-628 (2001).

[39] M. Lee *et al*, Nature Mater. **5** 537-540 (2006)

[40] P. Fazekas, *Lecture Notes on Electron Correlation and Magnetism*, World Scientific (1999).

[41] Peter Fulde, *Electron Correlations in Molecules and Solids*, Springer series in solid state sciences (1995).

[42] Peter Fulde, *Correlated Electrons in Quantum Matter*, World Scientific (2012).

[43] P. W. Anderson, Science **177**, 393 (1972).

[44] Georges *et al*, *Rev. Mod. Phys.* **68** 13 (1996).

[45] Y. Tomioka, T. Okuda, Y. Okimoto, R. Kumai, and K.-I. Kobayashi, Phys. Rev. B **61** 422 (2000)

[46] Y. Krockenberger, K. Mogare, M. Reehuis, M. Tovar, M. Jansen, G. Vaitheeswaran, V. Kanchana, F. Bultmark, A. Delin, F. Wilhelm, A. Rogalev, A. Winkler, and L. Alff. Phys. Rev. B 75, 020404 (2007).

[47] T. Aharen, *et al.*, Phys. Rev. B **80**, 134423 (2009).

[48] T. Aharen, *et al.*, Phys. Rev. B **81**, 064436 (2010).

[49] M. A. de Vries, A. C. Mclaughlin, and J.-W. G. Bos, Phys. Rev. Lett. **104**, 177202 (2010).

[50] M. T. Anderson, K. B. Greenwood, G. A. Taylor, and K. R. Poeppelmeier. Progress in Solid State Chemistry, 22, 197 (1993).

[51] For reviews, see D. D. Sarma, Current Op. Solid St. Mat. Sci.,**5**, 261 (2001), D. Serrate, J. M. de Teresa and M. R. Ibarra, J. Phys. Cond. Matt. **19**, 023201 (2007).

162

[52] K.-I. Kobayashi, T. Kimura, H. Sawada, K. Terakura, and Y. Tokura. Nat 395, 677, (1998).

[53] M.A. Subramanian N.S. Rogado, J. Li. Advances in Materials 17, 2225 (2005).

[54] H. Das, U. V. Waghmare, T. Saha-Dasgupta, and D. D. Sarma. Phys. Rev. Lett. 100, 186402, (2008).

[55] D. Choudhury, P. Mandal, R. Mathieu, A. Hazarika, S. Rajan, A. Sundaresan, U. V. Waghmare, R. Knut, O. Karis, P. Nordblad, and D. D. Sarma, Phys. Rev. Lett. **108** 127201 (2012).

[56] C. R. Wiebe, J. E. Greedan, G. M. Luke, and J. S. Gardner, Phys. Rev. B **65**, 144413 (2002).

[57] H. Gao, *et al.*, Phys. Rev. B **83**, 134406 (2011).

[58] A. Chattopadhyay and A. J. Millis, Phys. Rev. B **64**, 024424 (2001).

[59] K. Phillips, A. Chattopadhyay, and A. J. Millis, Phys. Rev. B **67**, 125119 (2003).

[60] J. L. Alonso, L. A. Fernndez, F. Guinea, F. Lesmes, and V. Martn-Mayor, Phys. Rev. B **67**, 214423 (2003).

[61] L. Brey, M. J. Caldern, S. Das Sarma, and F. Guinea, Phys. Rev. B **74**, 094429 (2006).

[62] V. Singh and P. Majumdar, Eur. Phys. Lett. 94, 47004 (2011).

[63] P. Sanyal and P. Majumdar, Phys. Rev. B 80, 054411 (2009).

[64] P. Sanyal, H. Das, and T. Saha-Dasgupta, Phys. Rev. B 80, 224412 (2009).

[65] S. Jana, C. Meneghini, P. Sanyal, S. Sarkar, T. Saha-Dasgupta, O. Karis, and S. Ray, Phys. Rev. B **86**, 054433 (2012).

[66] Sarma *et al*, *Phys. Rev. Lett.* **85**, 2549 (2000).

[67] D. D. Sarma, P. Mahadevan, T. Saha-Dasgupta, S. Ray, and A. Kumar. Phys. Rev. Lett. 85, 2549 (2000).

[68] T. K. Mandal, C. Felser, M. Greenblatt, and J. Kübler. Phys. Rev. B **78**, 134431 (2008).

[69] M. Hamada and H. Shimahara. Phys. Rev. B **51**, 3027 (1995).

[70] D. F. Agterberg and S. Yunoki. Phys. Rev. B 62, 13816 (2000).

[71] J. L. Alonso, J. A. Capitán, L. A. Fernández, F. Guinea, and V. Martín-Mayor. Phys. Rev. B 64, 054408 (2001).

[72] K. Pradhan and P. Majumdar, Europhys. Lett. **85**, 37007 (2009).

[73] N. F. Mott, *Metal-Insulator Transitions*, Taylor and Francis (1990).

[74] A. Georges, G. Kotliar, W. Krauth and M. J. Rozenberg, Rev. Mod. Phys. **68** 13 (1996).

[75] M. Imada, A. Fujimori and Y. Tokura, Rev. Mod. Phys. **70** 1039 (1998)

[76] E. Dagotto, Rev. Mod. Phys. **66**, 763 (1994).

[77] N. P. Ong and R. J. Cava, Science **305** 52 (2005).

[78] L. Balents, Nature **464** 199 (2010).

[79] K. Kanoda and R. Kato, Annu. Rev. Condens. Matter Physics. **2** 167 (2011).

[80] B. J. Powell and R. H. McKenzie Rep. Prog. Phys. **74**, 056501 (2011).

[81] H. C. Kandpal, *et al.*, Phys. Rev. Lett. **103** 067004 (2009).

[82] Y. Shimizu, M. Maesato and G. Saito, J. Phys. Soc. Jpn. **80** 074702 (2011).

[83] P. Limelette, *et al.*, Phys. Rev. Lett. **91** 016401 (2003).

[84] Kanoda *et al*, Annu. Rev. Condens. Matter Physics. **2** 167 (2011).

[85] S. Yasin, *et al.*, Eur. Phys. J. B. **79** 383 (2011).

[86] J. Merino, *et al.*, Phys. Rev. Lett. **100** 086404 (2008).

[87] M. Dumm, *et al.*, Phys. Rev. B. **79** 195106 (2009).

[88] B. J. Powell, E. Yusuf, and R. H. McKenzie, Phys. Rev. B. **80** 054505 (2009).

[89] A. Kawamoto, K. Miyagawa, Y. Nakazawa, and K. Kanoda, Phys. Rev. B. **52** 15522 (1995).

[90] K. Miyagawa, A. Kawamoto, Y. Nakazawa, and K. Kanoda, Phys. Rev. Lett. **75** 1174 (1995).

[91] Y. Shimizu, K. Miyagawa, K. Kanoda, M. Maesato, and G. Saito, Phys. Rev. Lett. **91** 107001 (2003).

[92] H. Morita, S. Watanabe and M. Imada, J. Phys. Soc. J **71** 2109 (2002).

[93] T. Watanabe, H. Yokoyama, Y. Tanaka, and J. Inoue, Phys. Rev. B **77** 214505 (2008).

[94] K. Inaba, A. Koga, S. Suga, and N. Kawakami, J. Phys.: Conf. Ser. **150** 042066 (2009), T. Yoshioka, A. Koga and N. Kawakami, Phys. Rev. Lett. **103** 036401 (2009).

[95] L. F. Tocchio, A. Parola, C. Gros, and F. Becca, Phys. Rev. B **80** 064419 (2009).

[96] K. Aryanpour, W. E. Pickett, and R. T. Scalettar, Phys. Rev. B. **74** 085117 (2006).

[97] D. Galanakis, T. D. Stanescu and P. Phillips, Phys. Rev. B. **79** 115116 (2009).

[98] O. Parcollet, G. Biroli and G. Kotliar, Phys. Rev. Lett. **92**, 226402 (2004).

[99] T. Ohashi, T. Momoi, H. Tsunetsugu, and N. Kawakami, Phys. Rev. Lett. **100** 076402 (2008).

[100] A. Liebsch, H. Ishida, and J. Merino, Phys. Rev. B. **79** 195108 (2009).

[101] T. Sato, K. Hattori and H. Tsunetsugu, J. Phys. Soc. Jpn. **81** 083703 (2012).

[102] P. Sahebsara and D. Senechal, Phys. Rev. Lett. **100**, 136402 (2008).

[103] H. Y. Yang, A. M. Lauchli, F. Mila and K. P. Schmidt, Phys. Rev. Lett. **105**, 267204 (2010).

[104] L. F. Tocchio, H. Feldner, and F. Becca, R. Valenti, and C. Gros, Phys. Rev. B **87** 035143 (2013).

[105] R. T. Clay, H. Li, and S. Mazumdar, Phys. Rev. Lett. **101**, 166403 (2008).

[106] Masatoshi Imada, and Tsuyoshi Kashima, J. Phys. Soc. Jpn. **69** 2723 (2000).

[107] P. Sahebsara and D. Senechal, Phys. Rev. Lett. **97**, 257004 (2006).

[108] Antoine Georges, and Gabriel Kotliar, Phys. Rev. B. **45** 6479 (1992).

[109] T. Watanabe, H. Y. Okoyama, Y. Tanaka and J. Inoue, J. Phys. Soc. Jpn. **75** 074707 (2006).

[110] B. Kyung and A.-M. S. Tremblay, Phys. Rev. Lett. **97** 046402 (2006).

[111] J. Liu, J. Schmalian, and N. Trivedi, Phys. Rev. Lett. **94**, 127003 (2005).

[112] R. Pocha, *et al.*, J. Am. Chem. Soc. **127**, 8732 (2005).

[113] S. Jakob, *et al.*, J. Mat. Chem. **17**, 3833 (2007).

[114] M. M. Abd-Elmeguid, *et al.*, Phys. Rev. Lett. **93**, 126403 (2004).

[115] V. Ta Phuoc, *et al.*, Phys. Rev. Lett. **110**, 037401 (2013).

[116] T. Takenobu, T. Muro, Y. Iwasa, and T. Mitani, Phys. Rev. Lett. **85**, 381 (2000).

[117] M. Capone, M. Fabrizio, C. Castellani, E. Tosatti, Rev. Mod. Phys. **81**, 943 (2009).

[118] Alexey Y. Ganin, *et al*, Nature **466**, 221 (2010).

[119] Y. Ihara, H. Alloul, P. Wzietek, D. Pontiroli, M. Mazzani, and M. Ricco, Phys. Rev. Lett. **104**, 256402 (2010).

[120] B. D. Gaulin, J. N. Reimers, T. E. Mason, J. E. Greedan, and Z. Tun, Phys. Rev. Lett. **69**, 3244 (1992).

[121] M. J. P. Gingras, C. V. Stager, N. P. Raju, B. D. Gaulin, and J. E. Greedan, Phys. Rev. Lett. **78**, 947 (1997).

[122] S. Iguchi, N. Hanasaki, M. Kinuhara, N. Takeshita, C. Terakura, Y. Taguchi, H. Takagi, and Y. Tokura, Phys. Rev. Lett. **102**, 136407 (2009).

[123] S. Nakatsuji, *et al.*, Phys. Rev. Lett. **96**, 087204 (2006).

[124] K. Matsuhira, *et al.*, J. Phys. Soc. J. **76**, 043706 (2007).

[125] K. Ueda, J. Fujioka, Y. Takahashi, T. Suzuki, S. Ishiwata, Y. Taguchi, and Y. Tokura, Phys. Rev. Lett. **109**, 136402 (2012).

[126] F. F. Tafti, J. J. Ishikawa, A. McCollam, S. Nakatsuji, and S. R. Julian, Phys. Rev. B **85**, 205104 (2012).

[127] Y. Machida, S. Nakatsuji, Y. Maeno, T. Tayama, T. Sakakibara, and S. Onoda, Phys. Rev. Lett. **98**, 057203 (2007).

[128] D. Grensing, E. Marsch, and W. H. Steeb, Phys. Rev. B **17**, 2221 (1978).

[129] Subrat Kumar Das, Viveka Nand Singh, and Pinaki Majumdar, Phys. Rev. B **88**, 214428 (2013).

[130] J. Hubbard, Phys. Rev. Lett. **3** 77 (1959).

[131] H. J. Schulz, Phys. Rev. Lett. **65**, 2462 (1990).

[132] H. J. Schulz, Phys. Rev. Lett. **65**, 2462 (1990).

[133] S. Kumar and P. Majumdar, Eur. Phys. J. B, **50**, 571 (2006).

[134] P. B. Allen in *Conceptual Foundation of Materials V.2*, edited by Steven G. Louie, Marvin L. Cohen, Elsevier (2006).

[135] M. V. Gvozdikova, M. E. Zhitomirsky, JETP letters *51* 236, (2005).

[136] J. P. Ader, Phys Rev B, *65* 014411 (2001).

[137] J. P. Ader, Phys Rev B, **66** 174414 (2002).

[138] J. Sousa, J. A. Plascak Phys Rev B *77* 024419 (2008).

[139] M. Mayr, G. Alvarez, A. Moreo, and E. Dagotto, Phys. Rev. B. **73** 014509 (2006).

[140] Anderson, P. W. Science **235**, 11961198 (1987).

[141] Moessner, R. & Sondhi, S. L. Phys. Rev. Lett. **86**, 18811884 (2001). Kitaev, A. Ann. Phys. (Leipz.) **321**, 2111 (2006). Motrunich, O. I. & Senthil, T. Phys. Rev. Lett. **89**, 277004 (2002). Balents, L., Fisher, M. P. A. & Girvin, S. M. Phys. Rev. B **65**, 224412 (2002). Hermele, M., Fisher, M. P. A. & Balents, L. Phys. Rev. B **69**, 064404 (2004).

[142] H. Frhlich Phys. Rev. **79**, 845856 (1950)

[143] John Bardeen and David Pines, Phys. Rev. **99**, 11401150 (1955)

[144] J. Bardeen, L. N. Cooper, and J. R. Schrieffer Phys. Rev. **106**, 162164 (1957)

[145] A. H. Wilson, Proc. R. Soc. London Ser. **A133**, 458 (1931); Proc. R. Soc. London Ser. **A134**, 277 (1931). R. H. Fowler, Proc. R. Soc. London Ser. **A140**, 505 (1933); Proc. R. Soc. London Ser. **A141**, 56 (1933).

[146] P. Fazekas, *Lecture Notes on Electron Correlation and Magnetism*, Chapter 4.5, World Scientific (1999).

[147] N. Goldenfeld, L. Kadanoff, Science **284**, 87 (1999).

[148] Gaulin *et al*, *Phys. Rev. Lett.* **69**, 3244 (1992), Gingras *et al*, *Phys. Rev. Lett.* **78**, 947 (1997).

[149] Wiebe *et al*, *Phys. Rev.* B **65**, 144413 (2002), Aharen *et al*, *Phys. Rev.* B **80**, 134423 (2009), Aharen *et al*, *Phys. Rev.* B **81**, 064436 (2010).

[150] Elmeguid *et al.*, *Phys. Rev. Lett.* **93**, 126403 (2004), Phuoc, *et al.*, *Phys. Rev. Lett.* **110**, 037401 (2013).

[151] Capone *et al*, *Rev. Mod. Phys.* **81**, 943 (2009).

[152] Kanoda *et al*, Annu. Rev. Condens. Matter Physics. **2** 167 (2011), Powell *et al*, Rep. Prog. Phys. **74**, 056501 (2011).

[153] R. L. Stratonovich, Sov. Phys. Doklady **2**, 416 (1958), J. Hubbard, *Phys. Rev. Lett.* **3**, 77 (1959), H. J. Schulz, *Phys. Rev. Lett.* **65**, 2462 (1990).

[154] S. Lefebvre, *et al.*, Phys. Rev. Lett. **85** 5420 (2000), F. Kagawa, T. Itou, K. Miyagawa, and K. Kanoda, Phys. Rev. B. **69** 064511 (2004).

[155] Takashi Koretsune, Yukitoshi Motome, and Akira Furusaki J. Phys. Soc. Jpn. **76** 074719 (2007).

[156] E. Dagotto and T. Hotta and A. Moreo, Phys. Rep. **344** 1 (2001).

[157] Y. Dubi, Y. Meir and Y. Avishai, Nature, **449**, 876 (2007).

[158] B. J. Powell and R. H. McKenzie, Rep. Prog. Phys. **74**, 056501 (2011).

[159] K. Kanoda, J. Phys. Soc. Jpn. **75**, 051007 (2006).

[160] The effective 'pressure' can also be of chemical origin, driven by change in ionic radius.

[161] J. Hubbard, Phys. Rev. B **19**, 2626 (1979).

[162] R. L. Stratonovich, Sov. Phys. Doklady **2**, 416 (1958), J. Hubbard, Phys. Rev. Lett. **3**, 77 (1959).

[163] K. Binder and A. P. Young, Rev. Mod. Phys. **58**, 801 (1986).

[164] Y. Dubi, Y. Meir and Y. Avishai, Nature, **449**, 876 (2007).

[165] M. V. Gvozdikova and M. E. Zhitomirsky, JETP Lett., **81**, 236 (2005).

[166] R. Tiwari and P. Majumdar, arXiv:1301.5026.

[167] H. Y. Yang, A. M. Lauchli, F. Mila and K. P. Schmidt, Phys. Rev. Lett. **105**, 267204 (2010).

[168] R. Tiwari and P. Majumdar, unpublished.

[169] Weng, Z. Y. and Ting, C. S. and Lee, T. K., Phys. Rev. B **43** 3790 (1991)

[170] K. Borejsza and N. Dupuis, Europhys. Lett. **63** 722 (2003)

[171] H. Das, M. De Raychaudhury, and T. Saha-Dasgupta. Appl. Phys. Lett. 92, 201912 (2008).

[172] J. B. Philipp, P. Majewski, L. Alff, A. Erb, R. Gross, T. Graf, M. S. Brandt, J. Simon, T. Walther, W. Mader, D. Topwal, and D. D. Sarma. Phys. Rev. B 68, 144431 (2003).

[173] P. Majewski, S. Geprägs, A. Boger, M. Opel, A. Erb, R. Gross, G. Vaitheeswaran, V. Kanchana, A. Delin, F. Wilhelm, A. Rogalev, and L. Alff. Phys. Rev. B 72, 132402 (2005).

[174] S. Kumar and P. Majumdar. EPJ B50, 571 (2006).

[175] We have worked on $\Delta \in [-10, 10]$, so J has to be large compaired to it. We used J = 1000, as the atomic bands which, for finite J, are actually dispersive (of band-width $\sim \mathcal{O}(\frac{1}{\Delta})$) become actually atomic to required numerical accuracy.

[176] We campared ratio of the maximum of $(\delta E)^{FM}$ and maximum of $(\delta E)^{AF}$ in the density window, for $\Delta = 0$ and $t' = 0$

[177] J. Navarro, C. Frontera, L. Balcells, B. Martinez, and J. Fontcuberta, Phys. Rev. B**64**, 092411 (2001).

[178] B.-G. Park, Y.-H. Jeong, and J.-H. Park, J. H. Song, J.-Y. Kim, H.-J. Noh, H.-J. Lin and C. T. Chen, Phys. Rev. B**79**, 035105 (2009).

[179] V. Singh and P. Majumdar, Eur. Phys. J. B 83, 147 (2011).

[180] Wiebe, C. R. and Greedan, J. E. and Luke, G. M. and Gardner, J. S., Phys. Rev. B **65**, 144413 (2002)

[181] Aharen *et al*, Phys. Rev. B **81**, 064436 (2010)

[182] Aharen *et al*, Phys. Rev. B **80**, 134423 (2009)

[183] Asymptote: The Vector graphics Language, URL http://asymptote.sourceforge.net/